
*Institut Laue-Langevin*


*Università degli Studi di Perugia*

*Dottorato di Ricerca in Fisica e Tecnologie Fisiche*

*XXVI Ciclo*

# Boron-10 layers, Neutron Reflectometry and Thermal Neutron Gaseous Detectors

*Author:*
Francesco Piscitelli

*Supervisor:*
Prof. Francesco Sacchetti

*ILL Supervisors:*
Dr. Patrick Van Esch
Dr. Bruno Guérard

*Coordinator:*
Prof. Maurizio Busso

---

A.A. 2012/2013

*To my family.*

[...] *fatti non foste a viver come bruti,*
*ma per seguir virtute e canoscenza.*

[...] *you were not made to live as brutes,*
*but to follow virtue and knowledge.*

**Dante Alighieri - Divina Commedia,**
**Inferno Canto XXVI vv. 119-120**

*I would like to thank many people. Each Chapter starts with a special thank to who was decisive to finalize the work explained in such Chapter or I had important discussions with or, more simply, who taught me a lot on a specific subject. I thank my colleague Anton Khaplanov for what he taught me about the $\gamma$-ray physics. Philipp Gutfreund, Anton Devishvili, and Boris Toperverg for what concerns neutron reflectometry: experiments, theory and data analysis. Federica Sebastiani and Yuri Gerelli for the discussions we had on neutron reflectometry. Carina Höglund for the excellent work done on the boron layers. I want to thank also Jean-Claude Buffet and Sylvain Cuccaro for the amount of technical issues they solved for me and for what they taught me about the mechanics. I want also to thank my colleagues Anton Khaplanov and Jonathan Correa for the pleasant time spent together in our office and in the labs.*
*I wish to every PhD student to have a supervisor as Patrick Van Esch. A special thank goes to him for the huge amount of things he explained to me on the neutron scattering. For the help he gave me to develop the theory of neutron converters and for the time he spent with me to make this manuscript as it is presented now.*
*I thank my group leader, Bruno Guérard who believed in the success of the prototype concept, for having pushed me to construct the detector. I want to thank Bruno Guérard and Richard Hall-Wilton for the support they gave in the research of new technologies in thermal neutron detection.*
*I thank the SISN (Italian Society of Neutron Spectroscopy) and all its members, in particular Alessio De Francesco, for what I learned about neutrons and for all the occasions it gave me.*

*I would like to thank all the people that, even if they have not been directly involved in this thesis, I think they have contributed somehow.*
*The entire "Italian lunch community" for the time spent together eating, drinking and playing sports, in particular skiing and playing football. I want to thank the "Tresette" players for the pleasant time spent after lunch to get back the concentration to work.*
*I thank Giuliana Manzin and John Archer because they had care of me when I came in Grenoble for the first time and because of our well-established "eating-friendship".*
*I would like to thank "Los Latinos" football group for the matches we played together that really helped me to discharge the stress of writing a thesis.*
*I thank my friends, that I left in Italy, to be always interested in how my life is going.*

*I thank my family for its strong support. For the moral and concrete means I received from them over the years.*
*I would also to thank my family as I conceive it now including Federica's family for the convivial time spent together.*

*I thank Federica Sebastiani to be always present.*

October 29, 2013

# Boron-10 layers, Neutron Reflectometry and Thermal Neutron Gaseous Detectors

**Francesco Piscitelli**

# Contents

# Introduction

## Institut Laue-Langevin

The Institut Laue-Langevin (ILL) is an international research center at the leading edge of neutron science and technology. It is situated in Grenoble, France, among some other important research centers like C.E.A. [1] or E.S.R.F. [2]
ILL was funded and it is managed by the governments of France, Germany and the United Kingdom, in partnership with 9 other European countries [3]. Every year, more than 1200 researchers from 30 countries visit the ILL. Over 700 experiments selected by a scientific review committee are performed annually and research focuses mainly on fundamental science in a variety of fields; this includes condensed matter physics, chemistry, biology, nuclear physics and materials science.
The institute operates the most intense neutron source in the World [4], feeding beams of neutrons to a suite of 40 high-performance instruments that are constantly upgraded. From a technical point of view, neutrons are created by the fission of $^{235}U$ in a nuclear reactor of about 58 $MW$ of power. Thanks to different procedures, neutrons with different energies can be produced. They are guided to the different apparatus in the Guide Halls where the experiments take place.

Figure 1: Panoramic view of ILL

[1] Commissariat à l'Ènergie Atomique
[2] European Synchrotron Radiation Facility
[3] Italy, Spain, Switzerland, Austria, the Czech Republic, Sweden, Hungary, Belgium and Poland
[4] $1.5 \cdot 10^5$ neutrons per second per $cm^2$

## Outline

By using neutrons we can determine the relative positions and motions of atoms in a bulk sample of solid or liquid. Neutrons make us able to look inside the sample with a suitable magnifying glass. They have no charge, and their electric dipole moment is either zero or too small to be measured. For these reasons, neutrons can penetrate matter far better than charged particles and it is also why they are relatively hard to be detected. Available neutron beams have inherently low intensities. The combination of weak interactions and low fluxes make neutron scattering a signal-limited technique, which is practiced only because it provides information about the structure of materials that cannot be obtained in simpler, less expensive ways.

Nowadays neutron facilities are going toward higher fluxes, e.g. the European Spallation Source (ESS) in Lund (Sweden), and this translates into a higher demand in the instrument performances: higher count rate capability, better timing and smaller spatial resolution are requested amongst others. Moreover, existing facilities, such as ILL, need also a continuous updating of their suite of instruments.
Because of its favorable properties, $^3He$ (a rare isotope of $He$) has been the main actor in thermal neutron detection for years. $^3He$ is produced through nuclear decay of tritium, a radioactive isotope of hydrogen. By far the most common source of $^3He$ in the United States is the US nuclear weapons program, of which it is a byproduct. The federal government produces tritium for use in nuclear warheads. Over time, tritium decays into $^3He$ and must be replaced to maintain warhead effectiveness. Until 2001, $^3He$ production by the nuclear weapons program exceeded the demand, and the program accumulated a stockpile. In the past decade $^3He$ consumption has risen rapidly. After the terrorist attacks of September 11, 2001, the federal government began deploying neutron detectors at the US border to help secure the nation against smuggled nuclear and radiological material. Thus, starting in about 2001, and more rapidly since about 2005, the stockpile has been declining.
The World is now experiencing the shortage of $^3He$. This makes the construction of large area detectors (several squared meters) not realistic anymore. A way to reduce the $^3He$ demand for those applications is to move users to alternative technologies. Some technologies appear promising, though implementation would likely present technical challenges.
Although scintillators are also widely employed in neutron detection, they show a higher $\gamma$-ray sensitivity compared to gaseous detectors that makes their use in strong backgrounds difficult.
Many research groups in Europe and in the World are exploring different alternative ways to detect neutrons to assure the future of the neutron scattering science. They focus mainly on the $^3He$ replacement because this expensive gas, in large quantities, is not available anymore. Although it is absolutely necessary to replace $^3He$ for large area applications, this is not the main issue for what concerns small area detectors ($\sim 1\,m^2$) for which the research is focused on improving their performances.
There are several aspects that must be investigated in order to validate those new technologies. E.g. their detection efficiency is one of the main concerns because it is in principle relatively limited compared to $^3He$ detectors. The detection of a $\gamma$-ray instead of a neutron can give rise to misaddressed events. The level of discrimination between neutrons and background events (e.g. $\gamma$-rays) a neutron detector can attain is then another key feature to be studied.

This PhD work was carried out at Institut Laue-Langevin (ILL) in Grenoble (France) in the Neutron Detector Service group (SDN) which is mainly in charge of the maintenance of the

neutron detectors of the instruments. This group is also involved in the development of new technologies for thermal neutron detection.
At ILL we tackled both the problem of $^3He$ replacement for large area applications and the performance problem for small area detectors. Both solutions are based on $^{10}B$ layers. $^{10}B$ is about 20% of the natural abundance of Boron, and thanks to its large neutron absorbtion cross-section, it is a suitable material to be employed in neutron detection as a neutron converter. In particular we used thin layers of magnetron sputtered $^{10}B_4C$ produced by the Linköping University (Sweden).
Although the physical process involved in neutron detection via layers of solid converter (such as $^{10}B$) is well known, there a great interest in expanding the theory toward new models and equations that can help to develop such a technology.
The Multi-Grid gaseous neutron detector was developed at ILL to face the problem arising for large area applications. We also implemented the Multi-Blade detector, already introduced at ILL in 2005, but never implemented until 2012, to go beyond the intrinsic limit in performances of the actual small area detectors. The Multi-Blade is a small area detector for neutron reflectometry applications that exploits $^{10}B_4C$-films employed in a proportional gas chamber. In a $^3He$-based detector the counting rate and spatial resolution are both limited. The instruments dedicated to neutron reflectometry studies need detectors of high spatial resolution ($< 1\,mm$) and high counting rate capability.
There is a great interest in expanding the performances of neutron reflectometry instruments, but due to practical limits in actual detector resolution and collimation, the technique is probably not practical. The principal investment is an area detector with $0.2\,mm$ spatial resolution required in one dimension only.

The Multi-Grid exploits up to 30 $^{10}B_4C$-layers in a cascade configuration. For large area applications the main concern about the $^{10}B$-based technology is the detection efficiency. While in $^3He$ tubes a $2\,cm$ detection volume assures an efficiency beyond 70% (at 2.5Å); a 30-layer $^{10}B$ detector is needed to reach about 50% efficiency for the same neutron wavelength. Since those layers are arranged in cascade, there is a strong interest in studying their arrangement in order to improve the efficiency and the neutron to $\gamma$-ray discrimination.
We elaborated a pure analytical study, proved by experiments, on the layer arrangement to increase the detector efficiency. We developed a suite of equations to help the detector construction, i.e. we derived analytical formulae to optimize the $^{10}B$-coating thicknesses. Those results can be also applied to other kinds of solid neutron converter, such as $^6Li$, and not only to $^{10}B$-films.
This theoretical study has also demonstrated that the magnetron sputtering is a suitable technique to make optimized converter layers. We also derived the analytical expression for the Pulse Height Spectrum (PHS) that helps to predict the neutron to $\gamma$-ray discrimination.

For a standard neutron detection efficiency, less than $10^{-6}$ $\gamma$-ray sensitivity can be easily achieved in $^3He$ detectors. The discrimination procedure is also easy to be applied and it is based on the distinction of the energy deposited in the gas volume. While there is a good separation in energy between neutron and $\gamma$-ray events for $^3He$ detectors, this is not the case for solid-converter-based detectors. We investigated deeply the $\gamma$-ray sensitivity of $^{10}B$-based detector and we compared with $^3He$ detectors. We exposed $^{10}B$ and $^3He$ detectors to the same calibrated $\gamma$-ray background in order to quantify their sensitivity, when the same energy discrimination

method is used.
Since there is always a certain loss of neutron detection efficiency for $^{10}B$ detectors, we investigated one more method to perform the neutron to $\gamma$-ray discrimination for those detectors.
In order to quantify the $\gamma$-ray background a detector is exposed to on a real instrument we measured the typical background on the time-of-flight spectrometer IN6 at ILL.
We elaborated a procedure to measure both the PHS and the counting curve of $^{10}B$-based detectors free from $\gamma$-rays that can be compared with the theoretical model we developed.

The Multi-Blade prototype is a small area detector for neutron reflectometry applications. It is a Multi Wire Proportional Chamber (MWPC) operated at atmospheric pressure. The Multi-Blade prototype uses $^{10}B_4C$ converters at grazing angle with respect to the incoming neutron beam. The inclined geometry improves the spatial resolution and the count rate capability of the detector. Moreover, the use of the $^{10}B_4C$ conversion layer at grazing angle also increases the detection efficiency.
While detection efficiency increases as the inclination decreases, the reflection of neutrons at the surface can be an issue. We studied this potential problem by developing a theoretical model about neutron reflection by strong absorbing materials such as $^{10}B_4C$.
We characterized $^{10}B_4C$ layers deposited on several types of substrates by using neutron reflectometry. We quantified the loss by reflection of such a layer as a function of the hitting angle and neutron wavelength. We investigated which properties of the layer and its substrate influence the reflection that has to be minimized. Our analytical model helped to investigate the data and to get information about the neutron converter itself.
The Multi-Blade prototype is conceived to be modular in order to be adaptable to different applications. A significant concern in a modular design is the uniformity of detector response. Several effects might contribute to degrade the uniformity and they have to be taken into account in the detector concept: overlap between different substrates, coating uniformity, substrate flatness and parallax errors.
We studied several approaches in the prototype design: number of converters, read-out system and materials to be used.
We built two versions of the Multi-Blade prototype focusing on its different issues and features. We measured their detection efficiency and uniformity on our test beam line. We quantified their spatial resolution and dead time.
We investigated a different deposition method for the $^{10}B$ converters which is not magnetron sputtering but $^{10}B$ glue-based painting.

We hope that in our work we have laid a solid theoretical basis, confirmed by experiments, for the understanding of the main aspects of solid converter layers employed in neutron detectors. We also explored practically, by the construction and characterization of prototypes, a specific type of solid-converter-based neutron detector, the Multi-Blade, especially suited for application in neutron reflectometry.

# Chapter 1

# Interaction of radiations with matter

This chapter summarizes the prerequisites needed for the comprehension of the material aboarded in this manuscript. We present notions of interactions between particles and matter, and we introduce some neutron physics. We pay especially attention to the meaning of coherent and incoherent scattering lengths, and to the meaning of the imaginary part of the scattering length. The main sources of the material for this Chapter are: the books [1], [6], [7], [8], [9] and the articles [5], [10], [12].

## 1.1 Definition of cross-section

The collision or interaction of two particles is generally described in terms of the *cross-section* [1]. This quantity essentially gives a measure of the probability for a reaction to occur. Consider a beam of particles incident on a target particle and assume the beam to be broader than the target (see Figure 1.1). Suppose that the particles in the beam are randomly distributed in space and time. We can define $\Phi$ to be the flux of incident particles per unit area and per unit time. Now look at the number of particles scattered into the solid angle $d\Omega$ per unit time. By *scattering* we mean any reaction in which the outgoing particle is emitted in the solid angle $\Omega$. If we average, the number of particles scattered in a solid angle $d\Omega$ per unit time will tend toward a fixed value $dN_s$. The *differential cross-section* is then defined as:

$$\frac{d\sigma}{d\Omega}(E,\Omega) = \frac{1}{\Phi} \cdot \frac{dN_s}{d\Omega} \tag{1.1}$$

that is, $\frac{d\sigma}{d\Omega}$ is the the average fraction of particles scattered into $d\Omega$ per unit time per unit incident flux $\Phi$ for $d\Omega$ infinitesimal. Note that because of $\Phi$, $d\sigma$ has the dimension of an area. We can interpret $d\sigma$ as the geometric cross sectional area of the target intercepting the beam. In other words, the fraction of flux incident on this area will interact with the target and scatter into the solid angle $d\Omega$ while all those missing $d\sigma$ will not.

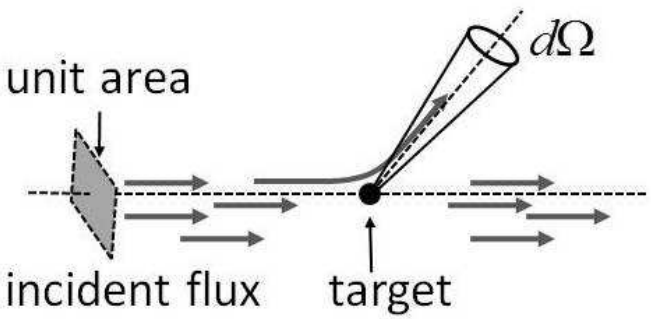


Figure 1.1: Definition of the scattering cross-section for a single scattering center.

In general the differential cross-section of a process varies with the energy of the reaction and with the angle at which the particle is scattered. We can calculate a *total cross-section*, for any scattering whatsoever at an energy $E$, as the integral of the differential cross-section over all solid angles as follows:

$$\sigma(E) = \int \frac{d\sigma}{d\Omega}(E,\Omega)\, d\Omega \tag{1.2}$$

Consider now a real target, which is usually a slab of material containing many scattering centers. We want to know how many interactions occur on average when that target is exposed to a beam of incident particles. Assuming that the slab is not too thick so that the likelihood of interaction is low, the number of centers per unit perpendicular area which will be seen by the beam is then $n \cdot \delta x$ where $n$ is the volume density of centers and $\delta x$ the thickness of the material along the direction of the beam (see Figure 1.2). If $A$ is the perpendicular area of the target and the beam is broader than the target, the number of incident particles which are eligible for

an interaction per unit of time is $\Phi \cdot A$. The average number of scattered particles into $d\Omega$ per unit time is:

$$N_s(\Omega) = \Phi \cdot A \cdot n \cdot \delta x \cdot \frac{d\sigma}{d\Omega} \cdot d\Omega \tag{1.3}$$

The total number of scattered into all angles is similarly:

$$N_{tot} = \Phi \cdot A \cdot n \cdot \delta x \cdot \sigma \tag{1.4}$$

In the case the beam is smaller than the target, we need only to set $A$ equal to the area covered by the beam. We can take another point of view; that is the probability of an incident particle of the beam to be scattered. If we divide Equation 1.4 by the total number of incident particles per unit time ($\Phi \cdot A$), we have the probability for the scattering of a single particle in a thickness $\delta x$:

$$P_{\delta x} = n \cdot \sigma \cdot \delta x \tag{1.5}$$

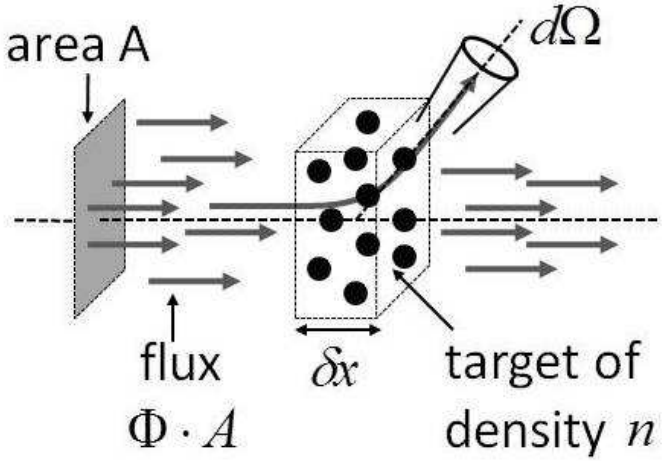


Figure 1.2: Definition of the scattering cross-section for an extended target.

Note that the probability for interaction is proportional to the distance traveled, $dx$ in first order.
Let us consider now a more general case of any thickness $x$. We ask what is the probability for a particle not to suffer an interaction over a distance $x$ traveled in the target. This can be interpreted as the probability for a particle to *survive* the interaction process. Let's denote with $P(x)$ the probability of not having an interaction after a distance $x$ (hence the probability to survive to the interaction process after a distance $x$ traveled) and with $w\,dx$ the probability to have an interaction in the interval $(x, x + dx)$. From Equation 1.5 we define $\Sigma = n \cdot \sigma$ the macroscopic cross-section. The probability of not having an interaction up to $x + dx$ is given

by:

$$\begin{aligned} &P(x+dx) = P(x)\cdot(1-\Sigma\,dx) \quad \Rightarrow \\ &P(x) + \frac{dP}{dx}dx = P(x) - P(x)\,\Sigma\,dx \quad \Rightarrow \\ &\frac{dP(x)}{P(x)} = -\Sigma\,dx \quad \Rightarrow \\ &P(x) = C\cdot e^{-\Sigma\,x} = e^{-\Sigma\,x} \end{aligned} \tag{1.6}$$

where $C$ is an integration constant. Note that $C = 1$ because we require that $P(x = 0) = 1$. From Equation 1.6 we can immediately deduce the probability to have an interaction over a distance $x$:

$$P_{int}(x) = 1 - P(x) = 1 - e^{-\Sigma\,x} \tag{1.7}$$

We can define the mean distance $\eta$ traveled by a particle without interacting; this is known as the *mean free path* that a particle can travel across the target without suffering any collision, thus:

$$\eta = \frac{\int xP(x)dx}{\int P(x)dx} = \frac{1}{\Sigma} = \frac{1}{n\cdot\sigma} \tag{1.8}$$

The survival probability of a trajectory of length $x$ becomes:

$$P(x) = e^{-\Sigma x} = e^{-\frac{x}{\eta}} \tag{1.9}$$

and the probability of interaction:

$$P_{int}(x) = 1 - e^{-\Sigma x} = 1 - e^{-\frac{x}{\eta}} \tag{1.10}$$

## 1.2 Charged particles interaction

In general two principal features characterize the passage of charge particles through matter: a loss of energy by the particle and the deflection of the particle from its incident direction [1]. Mainly these effects are the result of two processes:

- electromagnetic interactions with the atomic electrons of the material;
- elastic scattering from nuclei.

These reactions almost occur continuously in matter and it is their cumulative result which accounts for the principal effects observed. Other processes include the emission of Cherenkov radiation, nuclear reaction (this is the case for neutrons) and bremsstrahlung.
It is necessary to separate charged particles into two classes: electrons and positrons on one side and heavy particles, i.e., particles heavier than the electron, on the other.

### 1.2.1 Heavy charged particles

The inelastic collisions with the electrons of the material are almost solely responsible for the energy loss of heavy particles in matter. In these collisions energy is transferred from the particle to the atom causing an ionization or excitation of the latter. The amount of energy transferred in each collision is generally a very small fraction of the particle's total kinetic energy; however,

in normally dense matter, the number of collisions per unit path length is so large, that a substantial cumulative energy loss is observed in relatively thin layers of material.
Elastic scattering from nuclei also occurs although not as often as interactions with the bound electrons. In general very little energy is transferred in these collisions since the masses of the nuclei of most materials are usually large compared to the incident particle.
The inelastic collisions are statistical in nature, occurring with a certain quantum mechanical probability. However, because their number per macroscopic unit of path length is generally large, the fluctuations in the total energy loss are small and one can meaningfully work with the average energy loss per unit path length. This quantity, often called *stopping power* or $\frac{dE}{dx}$, was first calculated by Bohr using classical arguments and later by Bethe and Bloch using quantum mechanics.
The classical derivation, that is shown in details in the Appendix A, helps to clarify the line of reasoning which stands behind the result.
Even Bohr's classical formula gives a reasonable description of the energy loss for very heavy particles; the correct quantum-mechanical calculation leads to the Bethe-Bloch formula (see Appendix A).
Software packages are freely available which simulate the energy loss, from which one can deduce the stopping power. They give a similar result as the Bethe-Bloch calculation. We use SRIM [2], [3] to calculate the stopping power.
It is clear from the behavior in $E$ that as a heavy particle slows down in matter, its rate of energy loss will change as it loses its kinetic energy. More energy per unit length will be deposited towards the end of its path rather than at its beginning. This effect is more clear in the central plot in Figure 1.3 which shows the amount of ionization created by a heavy particle as a function of its position along its slowing-down path. This is known as a *Bragg* curve, and most of the energy is deposited close to the end of the trajectory.

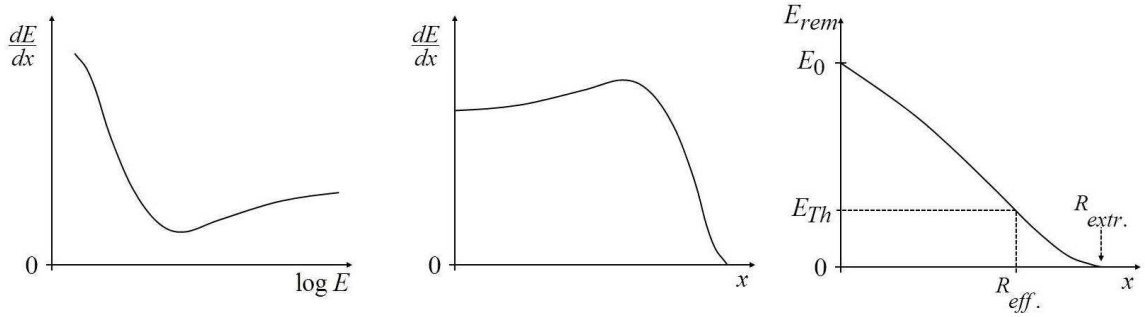


Figure 1.3: The stopping power as a function of $E$ (left) and $x$ (center). Remaining energy $E_{rem}$ as a function of $x$ (right).

If we assume the energy loss to be a continuous function, we can define the particle *range* which is the average distance a particle can travel inside a material before stopping. The latter depends on the type of material, the kind of particle and its energy. In reality, the energy loss is not continuous but statistical; two identical particles, with the same initial energy, will not suffer the same number of collisions and hence the same energy loss.
There are various ways to define the actual range of a particle. In order to clarify the definition of the range we refer to Figure 1.3. The right plot represents the energy a particle still owns as a function of the distance it has traveled in the material that can be calculated from the stopping

power function according to:

$$E_{rem}(x) = E_0 - \int_0^x \frac{dE}{d\xi}\, d\xi \tag{1.11}$$

where $E_0$ is the particle initial energy. Note that, in our model, a particle that has slowed down, below the minimum energy necessary to create a ion-pair, is considered stopped. As a result we define *extrapolated range* the average distance a particle can travel until it carries an energy below the minimum needed to ionize an atom. In Figure 1.3 the extrapolated range corresponds to a threshold energy of about $E_{Th} \sim 0$.
An alternative definition of range can be the *effective range*; this corresponds to the distance a particle on average has traveled in order to conserve at most the threshold energy $E_{Th}$. In general this definition is useful when dealing with particle detectors. Furthermore, if a particle detection system is sensitive to the particle energies until a minimum detectable threshold (or LLD - *Low Level Discrimination* [4]), it is meaningful to consider the effective range, that is associated only to particles that carry a minimum threshold energy necessary to activate the detector.

### 1.2.2 Electrons and Positrons

Like heavy charged particles, electrons and positrons also suffer a collisional energy loss when passing through matter. However, because of their small mass an additional energy loss mechanism comes into play: the emission of electromagnetic radiation arising from scattering in the electric field of a nucleus (bremsstrahlung). Classically, this can be understood as radiation arising from the acceleration of the electron as it is deviated from its straight trajectory by the electrical attraction of the nucleus.
The total energy loss of electrons and positrons, therefore, is composed of two parts:

$$\left(\frac{dE}{dx}\right)_{tot} = \left(\frac{dE}{dx}\right)_{rad} + \left(\frac{dE}{dx}\right)_{coll} \tag{1.12}$$

In Figure 1.4 the energy loss in radiative and collisional contributions are plotted for electrons in common Aluminium ($\rho = 2.7\, g/cm^3$). At energies of a few $MeV$ or less, the radiative loss is still a relatively small factor. However, as energy increases, the probability of bremsstrahlung rises and it is comparable to or greater than collision loss.
The Bethe-Bloch formula is still essentially valid, but we have to take into account two issues. Due to their small mass, the assumption the incident particle remains undeflected during the collision process is not valid. Second, for electrons, we are dealing with interactions between identical particles, and the quantum-mechanical calculation has to take into account their indistinguishability.
Because of electron's greater susceptibility to multiple scattering by nuclei, the actual range of electrons is generally very different from the calculated one obtained from the stopping power function integration.

## 1.3 Photon interaction

The behavior of photons in matter is different from that of charged particles. The probability of single interaction is much lower, but their effect is much more important. The main interactions of x-rays and $\gamma$-rays in matter are:

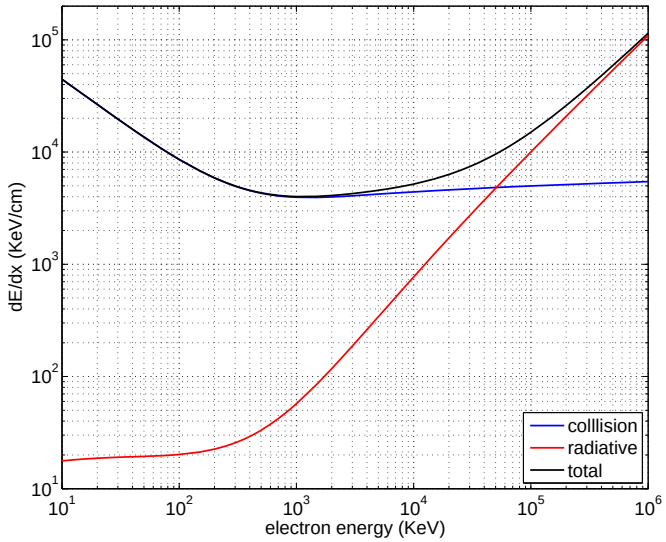


Figure 1.4: The stopping power for electrons in Aluminium $\rho = 2.7 g/cm^3$.

- photoelectric effect;
- Compton scattering;
- pair production.

X-rays and $\gamma$-rays are many times more penetrating in matter than charged particles and a beam of photons is not degraded in energy as it passes through a thickness of matter but it is only attenuated in intensity.
The first feature is due to the small cross-section of the three processes, the second is due to the fact that the three listed processes remove photons from the beam entirely, either by absorption or scattering. As a result the photons which pass straight through are only those which have not suffered any interactions all. The attenuation suffered by a photon beam can be expressed by Equation1.9:

$$I(x) = I_0 \, e^{-\mu \, x} \tag{1.13}$$

where $I_0$ is the incident intensity, $x$ is the absorber thickness and $\mu$ the linear attenuation coefficient.
The linear attenuation coefficient is characteristic of a material and it is directly related to the total interaction cross-section.

### 1.3.1 Photoelectric effect

The photoelectric effect involves the absorption of a photon by an atomic electron with the subsequent ejection of the electron from the atom. The energy of the outgoing electron is:

$$E_e = \hbar\omega - E_b \tag{1.14}$$

where $\hbar\omega$ is the photon energy and $E_b$ is the electron binding energy.
A free electron can not absorb a photon because of conservation laws, therefore the photoelectric effect always occurs on bound electrons with the nucleus absorbing the recoil momentum.
Figure 1.7 shows the linear attenuation coefficient $\mu$ for lead ($\rho = 11.34\, g/cm^3$) as a function of the incident photon energy. The red curve is the contribution given by the photoelectric effect. In general, rather than the linear attenuation coefficient $\mu$, one gives the absorption coefficient $\xi$ or the cross-section $\sigma$; one can be calculated from the other by using [5]:

$$\mu\left[\frac{1}{cm}\right] = \frac{\sigma\left[cm^2\right] \cdot N_A\left[\frac{1}{mol}\right] \cdot \rho\left[\frac{g}{cm^3}\right]}{A\left[\frac{g}{mol}\right]} = \xi\left[\frac{cm^2}{g}\right] \cdot \rho\left[\frac{g}{cm^3}\right] \tag{1.15}$$

where $\rho$ is the material mass density, $A$ its atomic mass and $N_A$ is Avogadro's number.
Still referring to Figure 1.7, the photoelectric coefficient value shows discontinuities due to the atomic energy shells. From the highest energy down to smaller energies, the shells are called K, L, M, etc. At energies above the highest electron binding energy of the atom (K-shell), the cross-section is relatively small but increases as the K-shell energy is approached. By lowering the energy, the cross-section drops drastically since the K-electrons are no longer available for the photoelectric effect. Below this energy, the coefficient $\mu$ rises again and dips as the L, M, etc. levels, are passed.
In general when a photon knocks-out an electron this leaves a vacancy in a specific atomic orbital. The higher electrons tend to relax to the minimum atomic energy with a consequent emission of an x-ray owning the electron binding energy $E_b$. Since the probability for an x-ray to undergo the photoelectric effect is even lager than for a $\gamma$-ray, in most cases it is absorbed again. Hence, if a $\gamma$-ray energy spectrum is measured through a scintillator, the energy measured will be the full incoming $\gamma$-ray energy because the x-ray will be reabsorbed.

### 1.3.2 Compton scattering

Compton scattering is the scattering of photons on free electrons. In matter the electrons are bound; however, if the photon energy is high with respect to the electron binding energy $E_b$, this latter can be neglected and the electrons can be considered as essentially free.

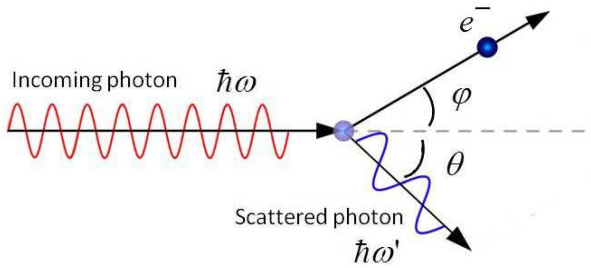


Figure 1.5: Compton scattering kinematic.

Figure 1.5 shows the scattering process. By applying the energy and momentum conservation, the following relation can be obtained:

$$\hbar\omega' = \frac{\hbar\omega}{1 + \gamma\,(1 - \cos\theta)} \tag{1.16}$$

where $\gamma = \hbar\omega/m_e c^2$. The kinetic energy the knocked electron gains in the process is:

$$E_e = \hbar\omega - \hbar\omega' = \hbar\omega \frac{\gamma\,(1-\cos\theta)}{1+\gamma\,(1-\cos\theta)} \tag{1.17}$$

Figure 1.7 shows, in black, the linear absorption coefficient for Compton scattering in lead as a function of the incoming photon energy.
Note from Equation 1.17 that the maximum energy is transferred from the photon to the knocked electron when $\theta = \pi$, that results into $E_{e(max)} = \hbar\omega \frac{2\gamma}{1+2\gamma}$; this is called the Compton edge. The latter is always smaller than the energy an electron can acquire if a photoelectric interaction occurs. As a result, the continuous spectra due to Compton interactions and the peak shaped spectrum due to photoelectric interactions will always be well separated in energy. Figure 1.6 shows a $\gamma$-ray energy spectrum when a NaI scintillator is exposed to three different $\gamma$-ray sources: a neutron induced source of 480 $KeV$ photons, a $^{60}Co$ source that emits almost only two radiations above 1 $MeV$ and a $^{22}Na$ source that emits at 511 $KeV$ and 1274 $KeV$.

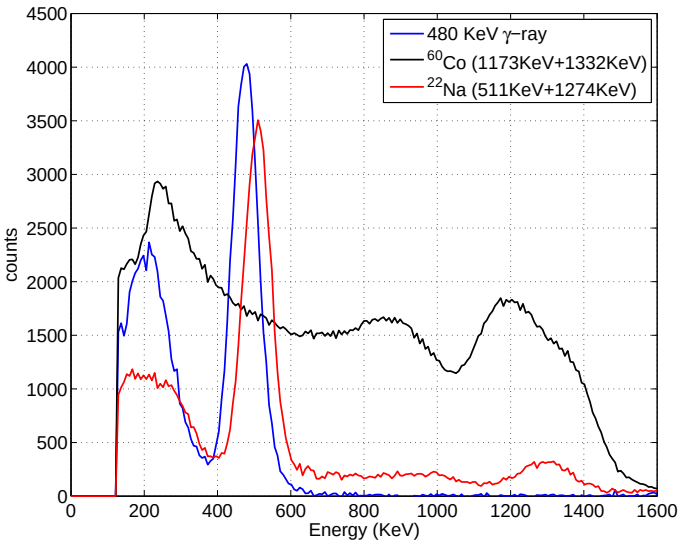


Figure 1.6: Measured $\gamma$-ray spectra with a NaI scintillator.

In the spectra are clearly visible the photo-peaks and the continuous spectrum extended until the relative Compton edge.
The scintillator energy calibration can be performed by exposing it to a $\gamma$-ray source. A calibration source should present at least two photons of well defined and well distinguished energies. $^{22}Na$ is a suitable calibration source thanks to its 511 $KeV$ and 1274 $KeV$ $\gamma$-rays. The calibration is done by applying a linear scaling between the two photo-peaks.

### 1.3.3 Pair production

The process of pair production involves the transformation of a photon into an electron-positron pair. In order to conserve momentum, this can only occur in presence of a third body, usually a nucleus. Moreover, to create the pair, the photon must have at least the energy of 1022 $KeV$;

being $511\,KeV$ the rest mass of an electron (or positron). In Figure 1.7 the pair production coefficient is plotted in green, and indeed it vanishes at $1022\,KeV$.

### 1.3.4 Total absorption coefficient and photon attenuation

The total probability for a photon to interact with matter is the sum of the individual linear attenuation coefficients (or cross-sections, or absorption coefficients) we mentioned above.

$$\mu_{tot} = \mu_{ph.el.} + \mu_{Compt.} + \mu_{pair} \tag{1.18}$$

In Figure 1.7 the total linear attenuation coefficient is plotted in blue. From Figure 1.7 we

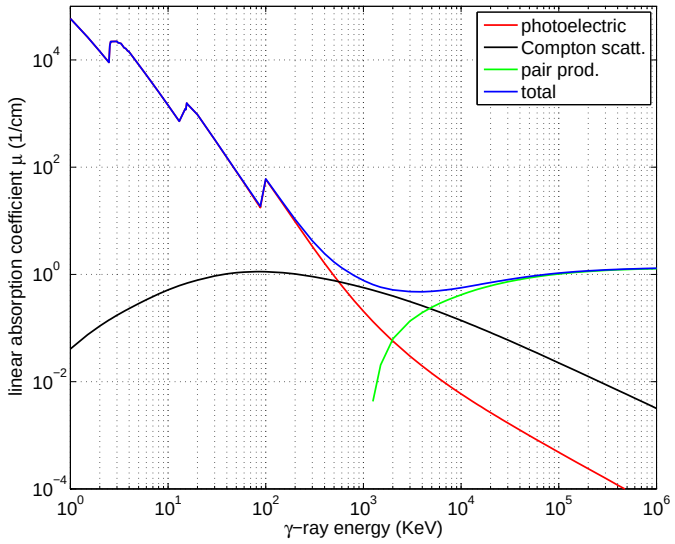


Figure 1.7: The linear absorption coefficient $\mu$ in lead as a function of the $\gamma$-ray energy for different processes.

notice that the three possible interactions of photons dominate in three different energy regions. At low energies the photoelectric effect is dominant, Compton scattering is the main effect at energies around $1\,MeV$, and pair production prevails at higher energies.

## 1.4 Sources, activity and decay

### 1.4.1 Activity

The activity of a radioisotope source is defined as its rate of decay where $\lambda_d$, the decay constant, is the probability per unit time for a nucleus to decay [6]:

$$A(t) = \left|\frac{dN(t)}{dt}\right| = |-\lambda_d\, N(t)| \quad \Longrightarrow \quad N(t) = N_0 e^{-\lambda_d\, t} \tag{1.19}$$

where $N$ and $N_0$ is the number of radioactive nuclei at the time $t$ and $t = 0$ respectively. Activity can be measured in $Ci$, defined as $3.7 \cdot 10^{10}$ disintegrations per second, or in $Bq$ which is its SI equivalent and that is 1 disintegration per second. Equivalently the activity can be expressed as

a function of the decay constant $\lambda_d$, the average lifetime $\tau = 1/\lambda_d$ or the half-life $t_{1/2} = \tau \cdot \ln 2$. By knowing the activity at time $t = 0$ ($A_0$) it is possible to calculate the activity at the time $t$ by:

$$A(t) = \lambda_d \cdot N(t) = \lambda_d \cdot N_0 e^{-\lambda_d t} = A_0 \cdot e^{-\lambda_d t} \tag{1.20}$$

It should be emphasized that activity measures the source disintegration rate, which is not synonymous with the emission rate of radiation produced in its decay. Frequently, a given radiation will be emitted in only a fraction of all the decays, thus a knowledge of the decay scheme of the particular isotope is necessary to infer a radiation emission rate from its activity. Moreover, the decay of a radioisotope may lead to a daughter product whose activity also contributes to the radiation yield from the source.
Figure 1.8 shows the decay scheme for $^{60}Co$, in green is shown its half life (in days), in black the radioisotopes and the energy of the levels (in $KeV$) and in blue the characteristic $\gamma$-ray energies and their probability.

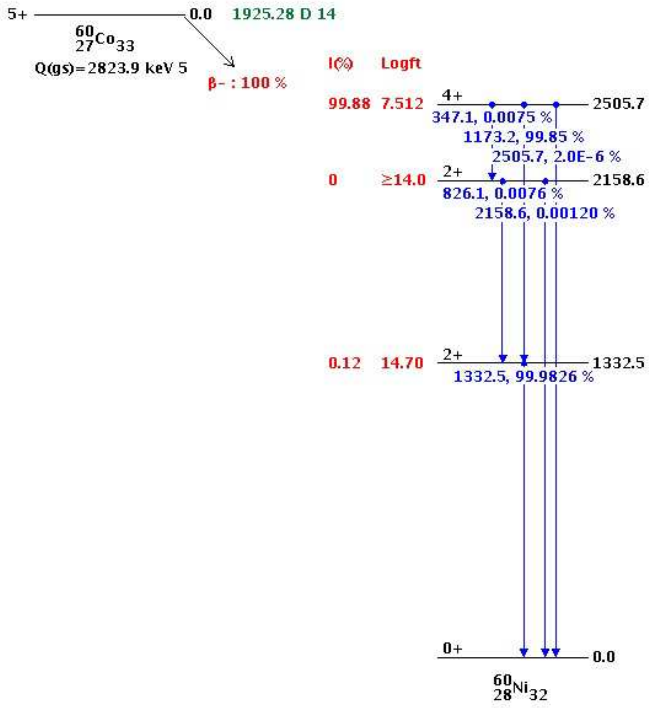


Figure 1.8: $^{60}Co$ decay level scheme.

E.g. if we imagine to deal with a source of activity $A = 10^4\,Bq$ at the present time, its emission rate of $\gamma$-rays of energy $1173.2\,KeV$ is given by $0.9985 \cdot 10^4\,Bq$.

### 1.4.2 Portable neutron sources

The most common portable source of neutrons is obtained by the bombardment of $Be$ with $\alpha$-particles emitted by an other element, e.g. $Am$. $\alpha$-particles emitted by the $^{241}Am$ have an energy greater than $5\,MeV$ that is sufficient to overcome the Coulomb repulsion between the particle and the nucleus (Beryllium is used because of its low Coulomb force). The reaction is

the following:

$$\alpha +^{9} Be \rightarrow \quad ^{12}C + n \tag{1.21}$$

The resulting neutrons emitted are fast and they have to be slowed down if thermal neutrons are needed. Most of the $\alpha$-particles are simply stopped in the target, and only 1 in about $10^4$ reacts with a $Be$ nucleus. About 70 neutrons are produced per $MBq$ of $^{241}Am$. This process to produce neutrons is very inefficient and an AmBe source has a $\gamma$-ray emission which is orders of magnitude higher than the neutron yield.
The slowing down of fast neutrons is known as moderation. When a fast neutron enters into matter it scatters on the nuclei, both elastically and inelastically, losing energy until it comes into thermal equilibrium with the surrounding atoms. At this point it diffuses through matter until it is captured or enters into other type of nuclear reaction. Elastic scattering is the principal mechanism of energy loss for fast neutrons. If we consider a single collision between a neutron, of unity atomic mass, with velocity $v_0$ and a rest nucleus with an atomic mass $A$; in the center-of-mass system, the average velocity of the neutron $v_n$ after the collision is:

$$v_n = \frac{A}{A+1} v_0 \tag{1.22}$$

Note that the maximum velocity loss is attained when the neutron scatter on light nuclei, i.e. protons ($A = 1$). Intuitively, the lighter the nucleus the more recoil energy it absorbs from the neutron. This implies the slowing down of neutrons is most efficient when light nuclei are used. With $^{12}C$ as a moderator of $1\,MeV$ neutrons slowing down to thermal energies would require about 110 collisions. For $H$, instead, only 17.
When thermal neutron sources are needed, the AmBe core is surrounded by polyethylene in order to moderate fast neutrons.

## 1.5 Neutron interaction

### 1.5.1 Neutron interactions with matter

Because of their lack of electric charge, neutrons are not subject to Coulomb forces. Their principal means of interaction is through the strong force with nuclei. These interactions are much rarer, in comparison with charged particles, because of the short range of this force. Purely from a classical point of view, neutrons must come within $\sim 10^{-15}\,m$ of the nucleus before anything can happen, and since matter is mainly empty space, it is not surprising that neutrons are very penetrating particles. Figure 1.9 shows the penetration depth of a beam of electrons, x-rays, or thermal neutrons as a function of the atomic number of the element. The main characteristic of charged particles which distinguishes them from photons and neutrons is that their penetration into a material cannot be described by an exponential function. Although there is a finite probability that a photon or neutron, however low in energy, can penetrate to a large depth, this is not the case for a charged particle. There is always a finite depth beyond which a charged particle will not travel.
The peculiarity of neutrons to be weakly absorbed by most materials makes it a powerful probe for condensed matter research. On the other hand, this is also the reason why it is rather difficult to build efficient neutron detectors, particularly if position sensibility is required.

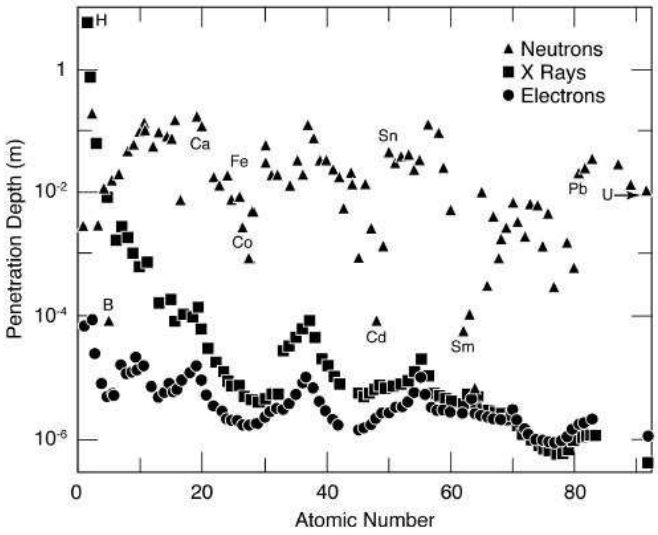


Figure 1.9: The plot shows how deeply a beam of electrons, x-rays, or thermal neutrons (1.4Å) penetrates a particular element in its solid or liquid form before the beam intensity has been reduced by a factor $1/e$.

The energy $E$ of a neutron, in the non-relativistic limit, can be described in terms of its wavelength $\lambda$ through the De Broglie relationship:

$$\lambda = \frac{2\pi\hbar}{m_n v} \qquad \Rightarrow \qquad E = \frac{1}{2} m_n v^2 = \frac{\pi\hbar^2}{m_n \lambda^2} \tag{1.23}$$

where $\hbar$ is the Planck's constant and $m_n$ is the mass of the neutron. In this manuscript we will talk about neutron velocity $v$, kinetic energy or wavelength equivalently. The energy classification of neutrons is shown in Table 1.1.

| Energy classification | kinetic energy E (eV) | wavelength (Å) | velocity (m/s) |
|---|---|---|---|
| ultra cold (UCN) | $E < 3 \cdot 10^{-7}$ | $\lambda > 520$ | $v < 7.5$ |
| very cold (VCN) | $3 \cdot 10^{-7} < E < 5 \cdot 10^{-5}$ | $520 > \lambda > 40$ | $7.5 < v < 99$ |
| cold | $5 \cdot 10^{-5} < E < 0.005$ | $40 > \lambda > 4$ | $99 < v < 990$ |
| thermal | $0.005 < E < 0.5$ | $4 > \lambda > 0.4$ | $990 < v < 9900$ |
| epithermal | $0.5 < E < 10^3$ | $0.4 > \lambda > 0.01$ | $9900 < v < 4.4 \cdot 10^5$ |
| intermediate | $10^3 < E < 10^5$ | $0.01 > \lambda > 0.001$ | $4.4 \cdot 10^5 < v < 4.4 \cdot 10^6$ |
| fast | $10^5 < E < 10^{10}$ | $0.001 > \lambda > 3 \cdot 10^{-6}$ | $4.4 \cdot 10^6 < v < 1.3 \cdot 10^9$ |

Table 1.1: Energy classification of neutrons.

Neutron states of motion owe their name to the temperature because they carry energies that are comparable with the daily life temperatures. E.g. thermal neutrons are those with energies around $k_B T$ (where $k_B$ is the Boltzmann constant and $T$ is the absolute temperature corresponding to $20\,^\circ C$) or about $25meV$.
When the neutron interacts with an individual nucleus, it may undergo a variety of nuclear processes depending on its energy. Among these are:

- Elastic scattering from nuclei, i.e. $A(n,n)A$. This is the principal mechanism of energy loss for neutrons.

- Inelastic scattering, e.g. $A(n,n')A^*$. In this reaction, the nucleus is left in an excited state which may later decay by $\gamma$-ray or some other form of radiative emission. In order for the inelastic reaction to occur, the neutron must have sufficient energy to excite the nucleus, usually order of $1\,MeV$ or more. Below this energy threshold, only elastic scattering may occur.

- Radiative neutron capture, i.e. $n + (Z,A) \rightarrow \gamma + (Z, A+1)$. In general, the cross-section for neutron capture goes approximately as $1/v$ with $v$ the neutron velocity. Therefore, absorption is most likely at low energies. Depending on the element, there may also be resonance peaks superimposed upon the $1/v$ dependence. At these energies the probability of neutron capture is greatly enhanced.

- Other nuclear reactions, such as $(n,p)$, $(n,d)$, $(n,\alpha)$, $(n,t)$, etc. in which the neutron is captured and charged particles are emitted. These generally occur in the $eV$ to $KeV$ region. Like the radiative capture reaction, the cross-section falls as $1/v$. Resonances may also occur depending on the element.

- Fission, i.e. $(n,f)$. Again this is most likely at thermal energies.

- High energy hadron shower production. This occurs only for very high energy neutrons with $E > 100\,MeV$.

The neutron has a net charge of zero and a rest mass slightly greater than that of the proton. $\beta$ decay is therefore possible according to $n \rightarrow p + e^- + \bar{\nu_e}$. The maximum electron energy is $781.32\,KeV$ and half-life in free space is $(11.7 \pm 0.3)$ minutes.
The total probability for a neutron to interact in matter is given by the sum of the individual cross-sections listed above (as long as interference effects are not significant), i.e.:

$$\sigma_{tot} = \sum_i \sigma_i = \sigma_{elastic} + \sigma_{inelastic} + \sigma_{capture} + \cdots \tag{1.24}$$

If we multiply $\sigma_{tot}$ by the atomic density we obtain the macroscopic cross-section $\Sigma$ of which the inverse is the mean free path length $\eta$ as indicated in Equation 1.9:

$$\frac{1}{\eta} = \Sigma_{tot} = n \cdot \sigma_{tot} = \frac{N_A \cdot \rho}{A} \sigma_{tot} \tag{1.25}$$

where $\rho$ is the material mass density, $A$ its atomic number and $N_A$ the Avogadro's number. In general $\Sigma$ is a function of $\lambda$ because $\sigma$ depends on the neutron energy and it has units of an inverse length.
In analogy with photons, a beam of neutrons passing through matter will be exponentially attenuated. The probability for a neutron of wavelength $\lambda$ to interact with a nucleus of the matter at depth $x$ in a slab of thickness $dx$, is given by:

$$K(x,\lambda)\,dx = \Sigma\, e^{-x\Sigma(\lambda)}\,dx \tag{1.26}$$

Consequently, by integration over a finite distance $d$, we obtain the number of neutrons that have interacted:

$$\frac{N(d)}{N_0} = \int_0^d dx\, K(x) = \int_0^d dx\, \Sigma e^{-x\Sigma} = 1 - e^{-d\Sigma} \tag{1.27}$$

with $N_0$ the initial incoming neutron flux. The percentage of neutrons which pass the layer of thickness $d$ is then $e^{-d\Sigma}$.

### 1.5.2 Elastic scattering

We consider now the neutron elastic scattering by a single nucleus in a fixed position. From general scattering theory [7], [8] the incoming particle can be described by a plane wave which interacts, through a potential $V(\bar{r})$, with the nucleus. The resulting wave-function will be a superposition of the incoming wave and a spherically diffused wave. This is a solution of the stationary Schrödinger equation.

$$\left[-\frac{\hbar^2}{2m}\nabla^2 + V(\bar{r})\right]\Psi = E\Psi \tag{1.28}$$

In a scattering experiment one wants to determine the probability, i.e. the cross-section, for the diffusion process to happen. Hence, one is interested in the asymptotic ($\bar{r} \to \infty$) behavior of such a solution:

$$\Psi_{(\bar{r}\to\infty)} \sim e^{ikz} + f(\theta,\phi)\,\frac{e^{ikr}}{r} \tag{1.29}$$

where $f(\theta,\phi)$ is the diffusion amplitude and it depends on the interaction potential $V(\bar{r})$. One can wonder whether there are constraints on the form of $f(\theta,\phi)$ for $\Psi$ to be a solution of the Schrödinger equation.
In order to evaluate the cross-section of the process one should study the diffusion of a wave-packet hitting a potential $V(\bar{r})$. A simpler way is to calculate the cross-section from the incident and diffused probability currents:

$$\bar{J}(\bar{r},t) = -\frac{i\hbar}{2m}\left(\Psi^*\frac{d\Psi}{d\bar{r}} - \Psi\frac{d\Psi^*}{d\bar{r}}\right) \tag{1.30}$$

For the incident plane wave and for the scattered wave individually, it results in:

$$\bar{J}_i = \frac{\hbar k}{m}\,\hat{u}_z, \qquad \bar{J}_s = \frac{\hbar k}{m}\frac{1}{r^2}|f(\theta,\phi)|^2\,\hat{u}_r \tag{1.31}$$

which can be interpreted as the number of particles flowing through a unity surface per unity time. The scattered wave probability current, for $\bar{r} \to \infty$, can be considered only radial.
The cross-section per unity of solid angle is the ratio between the number of particles that have been scattered over the number of incoming particles per unity time over the surface $d\bar{S} = r^2\,d\Omega$:

$$d\sigma = \frac{\frac{\hbar k}{m}\frac{1}{r^2}|f(\theta,\phi)|^2\,r^2 d\Omega}{\frac{\hbar k}{m}} = |f(\theta,\phi)|^2\,d\Omega \quad \Rightarrow \quad \frac{d\sigma}{d\Omega} = |f(\theta,\phi)|^2 \tag{1.32}$$

No assumptions on the potential have been made so far. We consider now the case of a central potential, $V(\bar{r}) = V(r)$. The hamiltonian commutes with the angular momentum operator, hence there exist stationary states of well defined energy and angular momentum, i.e. a common

eigenfunction base for both operators. The angular dependence of these functions will be the spherical harmonics. A plane wave can be written as a superposition of spherical waves:

$$e^{ikz} = \sum_{l=0}^{\infty} i^l \sqrt{4\pi\,(2l+1)} j_l(kr) Y_l^0(\theta) \tag{1.33}$$

where the functions $j_l(kr)$ are the spherical Bessel functions and the $Y_l^0(\theta)$ are the spherical harmonics with $m = 0$ because $\bar{k}$ has been chosen along $z$, hence they do not depend on $\phi$. For large $r$:

$$j_l(kr) \sim \frac{1}{kr} \sin\left(kr - l\frac{\pi}{2}\right) \tag{1.34}$$

When a plane wave interacts with a central potential, it introduces a phase shift in the scattered wave amplitudes of each of the harmonic terms. This can be shown as follows. The asymptotic behavior of the radial stationary Schrödinger equation with a central potential, assuming $V(r \to \infty) = 0$, is:

$$\left[-\frac{d^2}{dr^2} + k^2\right] u_{k,l}(r) = 0 \tag{1.35}$$

with solutions

$$u_{k,l}(r) = Ae^{ikr} + Be^{-ikr} \tag{1.36}$$

for large $r$. This solution contains as well the incoming as the outgoing particle flux. Unitarity requires $|A| = |B|$, as there is in a stationary case no destruction or creation of particles within a large sphere. Hence:

$$u_{k,l}(r) = |A| \left(e^{ikr} e^{i\varphi_A} + e^{-ikr} e^{i\varphi_B}\right) = C \sin\left(kr - l\frac{\pi}{2} + \delta_l\right) \tag{1.37}$$

with $\delta_l = l\frac{\pi}{2} - \frac{\varphi_B - \varphi_A}{2}$ chosen to have $\delta_l = 0$ when $V(r) = 0$, to find the asymptotic behavior of the spherical Bessel functions of the plane wave expansion as given in Equation 1.34. Note that $\delta_l$ is a real quantity.

The Equation 1.37 is the solution to the radial part of Schrödinger's equation; the complete asymptotic solution, for $r \to \infty$ and considering the spherical waves is:

$$\Phi_{k,l,m}(\bar{r}) = D\,\frac{\left(e^{-ikr} e^{il\frac{\pi}{2}} - e^{ikr} e^{-il\frac{\pi}{2}}\right) + e^{ikr} e^{-il\frac{\pi}{2}} \cdot \left(1 - e^{2i\delta_l}\right)}{2ikr} Y_l^m(\theta, \phi) \tag{1.38}$$

We can interpret the two terms as follows: the incoming wave is a free particle, as it approaches the region where the potential increases, it is more and more perturbed by the potential. When it is scattered, i.e. is the outgoing wave, it has accumulated a phase shift $2\delta_l$ with respect to the outgoing free wave that it would be if the potential were $V = 0$.

By comparing Equation 1.29 and Equation 1.38, and using Equation 1.33, the diffusion amplitude $f(\theta, \phi)$, in terms of spherical waves, is:

$$f(\theta) = \frac{1}{k} \sum_{l=0}^{\infty} i^l \sqrt{4\pi\,(2l+1)} e^{i\delta_l} \sin(\delta_l) Y_l^0(\theta) \tag{1.39}$$

The differential scattering cross-section is:

$$\frac{d\sigma}{d\Omega} = |f(\theta)|^2 = \frac{1}{k^2} \left| \sum_{l=0}^{\infty} \sqrt{4\pi\,(2l+1)} e^{i\delta_l} \sin(\delta_l) Y_l^0(\theta) \right|^2 \tag{1.40}$$

Note that for the wave-function in Equation 1.29 to be a solution of the Schrödinger's equation $f(\theta)$ has to satisfy Equation 1.39. Not all the forms for $f$ are admitted.
We consider now the interaction of neutrons with nuclei. The nuclear forces which cause the scattering, we recall, have a range of about $10^{-15}\,m$ while the wavelength of a thermal neutron is of the order of $10^{-10}\,m$, thus much larger than the range of those forces. On the scale of a wavelength the potential is non zero only in a very small region. The potential is central and can be written as a three-dimensional Dirac's delta of intensity $a$, which is a real constant:

$$V(\bar{r}) = a\,\delta(\bar{r}) \tag{1.41}$$

The multi-pole development of a $\delta$-distribution being limited to $l = 0$, we can consider the only spherical wave to undergo a phase shift to be the component $Y_0^0(\theta) = \frac{1}{2\sqrt{\pi}}$. Hence, the scattering amplitude and the cross-section become (Equations 1.39 and 1.40):

$$f = \frac{1}{k} e^{i\delta} \sin(\delta), \qquad \frac{d\sigma}{d\Omega} = \frac{1}{k^2} \sin^2(\delta) \tag{1.42}$$

The outgoing scattered wave amplitude has to satisfy the Equation 1.42 with $\delta \in \Re$. Not all the complex plane is accessible for $f$, but only the circle $e^{i\delta}\sin(\delta)$, shown in red in Figure 1.10.

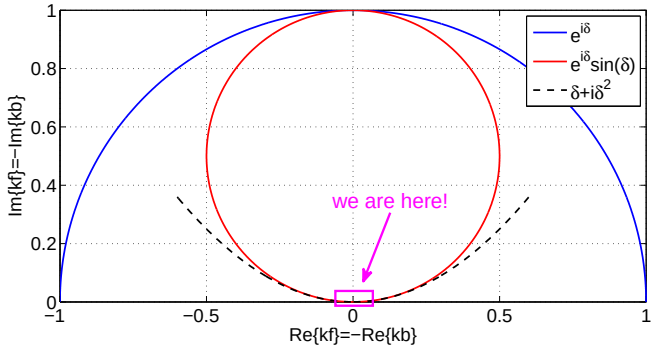


Figure 1.10: The value of the diffusion amplitude $f \cdot k$ in the complex plane for $\delta \in [0, \pi]$ (in red). $e^{i\delta}$ in blue and the parabola $\delta + i\,\delta^2$ in black.

In neutron scattering the incoming neutron can be described as a plane wave and the wave-function of the scattered neutrons at the point $\bar{r}$ can be written in the form:

$$\Psi^{scatt.}_{(\bar{r}\to\infty)} \sim e^{ikz} - b\,\frac{e^{ikr}}{r} \tag{1.43}$$

where $r$ is the module of the vector $\bar{r}$ and $b$ is a constant independent of the polar angles. The minus sign is a standard convention. If one considers the Fermi pseudo-potential:

$$V(\bar{r}) = \frac{2\pi\hbar^2}{m_n}\, b\,\delta(\bar{r}) \tag{1.44}$$

and one uses the Born approximation one will find Equation 1.43 as the solution.
The quantity $b$ is known as the *scattering length* [1] and depends on the nucleus. Even though

[1] The scattering length relates to a fixed nucleus and it is known as the bound scattering length. If the nucleus is free, the scattering must be treated in the center-of-mass system.

in strict potential scattering, $b$ should be independent of incident neutron energy, in general scattering theory, it can: this happens when there are nuclear resonances. The scattering length are experimentally determined and most $b$ values are of the order of a few $fm$.
The value of $b$ does not only depend on the particular nucleus, but on the spin state of the nucleus-neutron system. The neutron has spin $\frac{1}{2}$. Suppose the nucleus has spin $I$, not zero. Hence the spin of the system can be either $I + \frac{1}{2}$ or $I - \frac{1}{2}$. Each spin state has its own value of $b$. Every nucleus with non-zero spin has two values of the scattering length. If the nucleus spin is zero, the system nucleus-neutron can only have spin $\frac{1}{2}$, there is only one value of $b$.
The values for $b$ are determined experimentally, because the lack of a proper theory.
The $b$ is an empirical quantity known for most nuclei, varying strongly across the periodic table and often varying sharply between isotopes of the same element. Most materials have a positive $b$; therefore in a positive potential a neutron has less kinetic energy and hence a longer wavelength (opposite to light where the wavelength shortens). This quantity defines the nature of the neutron-nucleus interaction: whether it is attractive or repulsive and it also determine the strength of the interaction. Moreover, this is a specific quantity that strongly depends on the target nucleus and it can even depend on the neutron energy, e.g. in the case of $^{113}Cd$ resonances occur as well.
All the neutron scattering theory is based on this simple assumption that the neutron-nucleus interaction can be considered a Dirac's delta potential and all the information a scattering experiment can reveal is all related to the quantity $b$.
By comparing Equations 1.29 and 1.43, $-b$ is the diffusion amplitude $f$:

$$f = \frac{1}{k} e^{i\delta} \sin(\delta) = -b \quad \Rightarrow \quad k\, b = -e^{i\delta} \sin(\delta) \tag{1.45}$$

$b \sim 10^{-15}\, m$ and, for thermal neutrons $k = 10^{10}\, m^{-1}$, thus the product $k\, b \sim 10^{-5}$ and $e^{i\delta} \sin(\delta) << 1$. Expanding Equation 1.45 at the first order for $\delta << 1$ we obtain:

$$-k\, b = e^{i\delta} \sin(\delta) = (\cos(\delta) + i\, \sin(\delta)) \cdot \sin(\delta) \sim \delta + i\, \delta^2 \sim -10^{-5} \tag{1.46}$$

The scattering length $b$ for thermal neutron scattering can be considered to be a real quantity because its imaginary part is always at least five orders of magnitude smaller. The values of $b$ make the scattering amplitude $f$ to vary in the small range $\delta \in [-10^{-5}, 10^{-5}]$, i.e. $f \in \Re$. In Figure 1.10 is shown the approximated behavior for $b$ in Equation 1.46 which results in a parabola in the complex plane ($k\, f = -k\, b$). We see that $b$ is essentially real.
The differential cross-section, Equation 1.42, becomes:

$$\frac{d\sigma}{d\Omega} = \frac{\delta^2}{k^2} = b^2 \tag{1.47}$$

From which the total scattering cross-section can be derived:

$$\sigma_s = 4\pi\, b^2 \tag{1.48}$$

Let us consider now the scattering by a general system of particles. Its potential is:

$$V = \sum_i V_i \left(\bar{r} - \bar{R}_i\right) = \sum_i V_i \left(\bar{x}_i\right) \tag{1.49}$$

where $\left(\bar{r}-\bar{R_i}\right)=\bar{x_i}$ and $V_i\left(\bar{r}-\bar{R_i}\right)$ is the potential the neutron experiences due to the $i-th$ nucleus. Explicitly it is:

$$V_i(\bar{x_i})=\frac{2\pi\hbar^2}{m_n}\,b_i\,\delta(\bar{x_i}) \tag{1.50}$$

where $b_i$ is the scattering length of the nucleus $i-th$.
One can define the average value of $b$ of the system and the average value of $b^2$ as:

$$\bar{b}=\sum_i \nu_i b_i, \qquad \overline{b^2}=\sum_i \nu_i b_i^2 \tag{1.51}$$

where $\nu_i$ is the frequency with which the value $b_i$ occurs in the system. Note that the system can be made up of the same element atoms and the $b_i$ would be different for each nucleus. We recall the scattering length value depends on the spin states of the neutron-nucleus system.
In a scattering experiment a neutron beam impinges on a target, which is a large amount of nuclei. Any combination of spins can occur, i.e. the value of $b_i$ is averaged over a large number of atoms. On the assumption of no correlation between the $b$ values of different nuclei:

$$\begin{aligned}\overline{b_i b_j}&=\bar{b}^2 \qquad \text{if } i\neq j\\ \overline{b_i b_j}&=\overline{b^2} \qquad \text{if } i=j\end{aligned} \tag{1.52}$$

we can calculate the scattering cross-section of a process averaging over all the nuclei.
It can be shown that the overall cross-section of the scattering on such a system consists of two terms: a term depending only on the correlation of the position of each center with itself (incoherent part) and a term depending on the correlation of position of pairs of centers (coherent part) [9]. The incoherent part will be proportional to $\sigma_i$ and the coherent to $\sigma_c$ where we have defined:

$$\sigma_c=4\pi\bar{b}^2, \qquad \sigma_i=4\pi\left(\overline{b^2}-\bar{b}^2\right) \tag{1.53}$$

the coherent and incoherent scattering cross-sections.
The physical interpretation is as follows: the actual scattering system has different scattering lengths associated to different nuclei. The coherent scattering is the scattering the same system would give if all the $b$ were equal to $\bar{b}$. The incoherent scattering is the fluctuation we must add to obtain the scattering due to the actual system. The latter arises from the random distribution of the deviations of the scattering lengths from their mean value. As it is completely random, all interference cancels in this incoherent part.
We define:

$$b_c^2=\left|\bar{b}^2\right|, \qquad b_i^2=\left|\overline{b^2}-\bar{b}^2\right| \tag{1.54}$$

Note that averages taken are defined over the system at hand. In general the scattering system consists of many spin states. We recall that the scattering length depends on the coupling of the neutron and nucleus spins. Let's denote with $I$, the nuclear spin of the system made up of a single isotope. The resulting spin for the system neutron-nucleus can be either $I+1/2$ or $I-1/2$. We associate to the two compositions of spins the scattering length $b_+$ and $b_-$. If the system is unpolarized, all the possible combinations of spins can occur and $b_+$ gets a weight of $\frac{I+1}{2I+1}$ while $b_-$ gets a weight of $\frac{I}{2I+1}$ in the statistical ensemble.
If the neutron and the nuclei system are now both polarized the population over which we average is now defined and if only the coupling $I+1/2$ occurs, the average would be exactly

$\bar{b} = b_+$ with variance $\left(\overline{b^2} - \bar{b}^2\right) = 0$.
From the definition of the scattering length comes directly the definition of the various cross-sections already mentioned in Equation 1.24.
The actual total scattering cross-section is then given by the sum of the two contributions.

$$\sigma_s = \sigma_c + \sigma_i = 4\pi\overline{b^2} \tag{1.55}$$

If the neutron or the nucleus is unpolarized, the cross-section becomes:

$$\sigma_s = \sigma_c + \sigma_i = 4\pi \left|b_c\right|^2 + 4\pi \left|b_i\right|^2 \tag{1.56}$$

The scattering cross-section does not depend on the neutron energy if we have potential scattering ($b$ constant).
The mixture of isotopes or different nuclei, denoted by $j$, is an additional source of incoherence in the scattering of neutrons. The average scattering length of such a system is:

$$b = \frac{\sum_j b_j n_j}{\sum_j n_j} \tag{1.57}$$

where $n_j$ is the number density of each isotope or nucleus and spin state.

### 1.5.3 Absorption

Let us consider now the possibility for a neutron to be absorbed. Let assume the interactions responsible for the absorption to be invariant under rotation around the origin. As a result, the scattering amplitude $f$ can still be decomposed in spherical waves. The phase shift method has to be modified in order to take into account the absorption. We demonstrated that an incoming plane wave is shifted by a factor $e^{i\delta}\sin(\delta) = (e^{2i\delta} - 1)/2i$ by the potential action. We recall $\delta$ is a real number. Since $|e^{2i\delta}| = 1$, the incoming and outgoing wave amplitudes are the same: the total probability flux for the plane wave and the scattered wave is conserved. The total number of particles is conserved in the scattering process. This was the requirement of unitarity.
In order to consider absorption this probability is not any more conserved and we need to add an imaginary part to the phase shift that results in: $|e^{2i\delta}| < 1$. The amplitude of the scattered wave is smaller than the one of the incoming wave. In Equation 1.36, $|A| = |B|$ signified that there was no source or no sink (unitarity) in the large $r$ sphere. Absorption means that there is a sink, thus $|A| < |B|$: $|\eta| = |A/B|$.
Since $\delta$ is a complex quantity we can denote $\eta = e^{2i\delta}$ with $|\eta| \leq 1$. The asymptotic solutions of Schrödinger's equation (Equation 1.38) become:

$$\Phi_{k,0,0}(r) = A\,\frac{e^{-ikr}e^{il\frac{\pi}{2}} - \eta e^{ikr}e^{-il\frac{\pi}{2}}}{2ikr} \tag{1.58}$$

where we focus only on the component $l = 0$ because, for the neutron-nucleus interaction, we assume the potential to be central and a Dirac's delta.
The scattering amplitude and the differential scattering cross-section (Equation 1.42) are:

$$f = \frac{1}{k}\frac{\eta - 1}{2i}, \qquad \frac{d\sigma}{d\Omega} = |f|^2 = \frac{1}{k^2}\left|\frac{\eta - 1}{2i}\right|^2 \tag{1.59}$$

Note that even for a perfect absorbing material, with $\eta = 0$, elastic scattering can and will still occur. The effect is called *shadow diffusion* and it is a purely quantum effect [7].
The absorption cross-section can be defined in a way similar to the scattering cross-section, as the number of particles absorbed, i.e. that have suffered the interaction, over the incident flux per unit time.
To calculate this cross-section we need to quantify the probability that a particle disappears, $\Delta P$, per unit time which is given by the difference between the integrals of the probability current that enters and exits a given volume of the space, that we take at $r \to \infty$ to use the asymptotic solutions of the Schrödinger's equation (Equation 1.38).
By using Equation 1.30 we calculate the probability current for the asymptotic solution in Equation 1.38.

$$\bar{J}_{r\to\infty} = -\frac{\hbar k}{m_n}\frac{\pi}{k^2 r^2}\left(1 - |\eta|^2\right) \tag{1.60}$$

We integrate the current to obtain the missing probability:

$$\Delta P = -\int_{r>>1} \bar{J}_{r\to\infty} r^2 \, d\Omega = \frac{\hbar k}{m_n}\frac{\pi}{k^2}\left(1 - |\eta|^2\right) \tag{1.61}$$

The absorption cross-section we normalize to the incident current of the plane wave (Equation 1.31):

$$\sigma_{abs} = \frac{\pi}{k^2}\left(1 - |\eta|^2\right) \tag{1.62}$$

The absorption cross-section is zero only when $|\eta| = |e^{2i\delta}| = 1$, i.e. when $\delta \in \Re$.
We can still put:

$$b = b' - i\, b'' = -f \tag{1.63}$$

We may distinguish three types of nucleus. In the first type $b$ is complex and varies rapidly with the neutron energy. The scattering of such nuclei is associated with the resonant absorption and or scattering of the neutron. In the second type the neutron is not absorbed, the imaginary part of the scattering length is small and the scattering length is independent of the neutron energy. For such a nuclei the scattering length can be considered to be a real quantity. In the third type there is absorption and scattering but the complex scattering length is constant.
In most cases the scattering length $b$ can be considered a real number. We demonstrated that, for thermal neutrons, the product $\delta \sim k\, b \sim 10^{-5}$ (Equation 1.46) and the scattering cross-section is, under these circumstances, given by Equation 1.47:

$$\sigma_s = \frac{4\pi}{k^2}\sin(\delta) \sim \frac{4\pi}{k^2}\delta^2 = 4\pi b^2 \tag{1.64}$$

which is independent from $k$, i.e. the neutron energy in as much we can consider it to be potential scattering.
For absorbing materials we have $Re\{b\} \sim Im\{b\} \sim 10^{-15}\, m$ and $k \sim 10^{10}\, m^{-1}$. Hence:

$$|\eta|^2 = |2ikb + 1|^2 = |2ikb' + 2kb'' + 1|^2 = 4k^2 b'^2 + 4k^2 b''^2 + 4kb'' + 1 \sim 4kb'' + 1 \tag{1.65}$$

because we can neglect the quadratic terms which are at least five order of magnitudes smaller than the first power term. Substituting in Equation 1.62:

$$\sigma_{abs} = \frac{\pi}{k^2}\left(1 - |\eta|^2\right) \sim \frac{\pi}{k^2} 4kb'' = \frac{4\pi}{k} b'' = \frac{4\pi}{k} Im\{b\} \tag{1.66}$$

The absorption cross-section is therefore uniquely given by the imaginary part of the scattering length. However, the scattering cross-section depends on both the real and imaginary parts. The absorption cross-section depends on the neutron energy, it scales as $1/k \sim 1/v$, the neutron velocity. It should be emphasized that in the regions where this dependence does not follow the law $1/v$, the imaginary part of the scattering length $b''$ as well depends on the neutron energy, which is typically the case for resonance scattering and absorption.
To be more precise as value for $b''$ one should take the statistical average over the neutron and nuclear spins. As for scattering, absorption as well depends on the specific spins coupling at the moment of the interaction between the neutron and the nucleus. There are then the coherent and the incoherent imaginary parts for absorption as well. $Im\{b_c\}$ is the average of absorption we would obtain on a non-polarized system;

$$\sigma_{abs} = \frac{4\pi}{k} Im\{b_c\} \tag{1.67}$$

It is only when the neutron and the nucleus are both polarized that the imaginary part of the bound incoherent scattering length $Im\{b_i\}$ contributes to the value of $\sigma_{abs}$.
It should be pointed out that the actual absorption cross-section is defined as follows:

$$\sigma_a = \sigma_{capt} + \sigma_f \tag{1.68}$$

where $\sigma_f$ is the fission cross-section typical for fissile elements, e.g. $U$. For fissile materials $\sigma_a$ is mostly given by $\sigma_f$ and for light atoms by $\sigma_{capt}$. The absorption cross-section we have discussed so far is more properly $\sigma_{capt}$. Fissile elements do not show imaginary part in their scattering lengths because the capture and the fission are two different physical processes.
Table 1.2 shows scattering lengths and partial cross-sections for several elements, where the absorption cross-section is tabulated for neutron of $k = 3.49\text{Å}^{-1}$ ($\lambda = 1.8\text{Å}$). In this Table the sign of $b_i$ is given by the sign of $(b_+ - b_-)$, the difference between the spin up $(I + 1/2)$ and the spin down $(I - 1/2)$ values for $b$. We defined $b_i$ somewhat different in Equation 1.54, as the standard deviation of the $b$ for a general population of neutron-target system, and not for a single isotope.
We notice that all the isotopes that own an imaginary part in their scattering length have also a large absorption cross-section.
Figure 1.11 shows the partial cross-sections for $^1H$, $^2H$ and $^3He$ as a function of the incoming neutron energy. We recall that elastic cross-section stands for a processes such as $A(n,n)A$; and its contribution is implicit in $\sigma_s$. Moreover, processes like $(n,\gamma)$ or $(n,p)$ can be considered as implicit in $\sigma_{capt}$.
Since $^3He$ is a strong neutron absorber, its total cross-section is entirely dominated by $\sigma_{capt}$ and only at very high energies the elastic scattering prevails. Below $1\,KeV$ the $^3He$ capture cross-section behaves as $1/v$ then the proportionality is lost.
On the other hand, hydrogen is a great neutron scatterer and its total cross-section is entirely given by the elastic contribution. Moreover, in a wide range, its $\sigma_{tot}$ does not depend on energy.
In neutron detection, the material with high $\sigma_{abs}$ are the most interesting because of their property to commute the neutron into a charged particle that can be detected, this will described more in details in Chapter 2.
Figure 1.11 shows the $\sigma_{capt}$ for several elements employed as neutron converter in neutron detectors.

| Isotope | $b_c(fm)$ | $b_i(fm)$ | $\sigma_c(b)$ | $\sigma_i(b)$ | $\sigma_s(b)$ | $\sigma_a(b)$ |
|---|---|---|---|---|---|---|
| $^1H$ | $-3.74$ | 25.27 | 1.76 | 80.27 | 82.03 | 0.33 |
| $^2H$ | 6.67 | 4.04 | 5.59 | 2.05 | 7.64 | 0.00052 |
| $^3He$ | $5.74 - 1.48i$ | $-2.5 + 2.57i$ | 4.42 | 1.6 | 6 | 5333 |
| $^4He$ | 3.26 | 0 | 1.34 | 0 | 1.34 | 0 |
| $^6Li$ | $2 - 0.26i$ | $-1.89 + 0.26i$ | 0.51 | 0.46 | 0.97 | 940 |
| $^7Li$ | $-2.22$ | $-2.49$ | 0.62 | 0.78 | 1.40 | 0.045 |
| $^{10}B$ | $-0.1 - 1.07i$ | $-4.7 + 1.23i$ | 0.14 | 3 | 3.1 | 3835 |
| $^{11}B$ | 6.65 | $-1.3$ | 5.56 | 0.21 | 5.77 | 0.0055 |
| $^{12}C$ | 6.65 | 0 | 5.56 | 0 | 5.56 | 0.0035 |
| $^{16}O$ | 5.80 | 0 | 4.23 | 0 | 4.23 | 0.0001 |
| $^{27}Al$ | 3.45 | 0.26 | 1.49 | 0.0082 | 1.5 | 0.231 |
| $^{28}Si$ | 4.11 | 0 | 2.12 | 0 | 2.12 | 0.171 |
| $^{113}Cd$ | $-8 - 5.73i$ | 0 | 12.1 | 0.3 | 12.4 | 20600 |
| $^{157}Gd$ | $-1.14 - 71.9i$ | $\pm 5 - 55.8i$ | 650 | 394 | 1044 | 259000 |
| $^{235}U$ | 10.47 | $\pm 1.3$ | 13.78 | 0.2 | 14 | 680.9 |
| $^{238}Pu$ | 14.1 | 0 | 25 | 0 | 25 | 558 |

Table 1.2: Neutron scattering lengths and partial cross-sections [10]. Absorption cross-section is tabulated for $k = 3.49\text{Å}^{-1}$ ($\lambda = 1.8\text{Å}$).

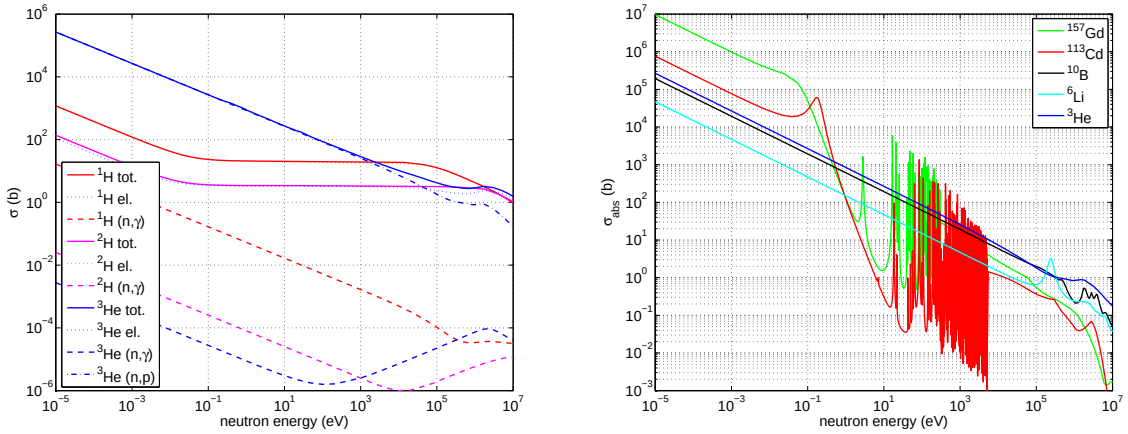


Figure 1.11: Several partial cross-section (expressed in barn) for $^1H$, $^2H$ and $^3He$ as a function of the neutron energy (left). Capture cross-sections for $^3He$, $^{10}B$, $^6Li$, $^{113}Cd$ and $^{157}Gd$ (right).

The $1/v$ dependence of the capture cross-section corresponds to the imaginary part of the scattering length $b''$ being independent on the neutron energy. We notice that for $Cd$ or $Gd$ the $1/v$ dependence is broken by nuclear resonances that occur at precise energies.
The most common neutron reactions for neutron converter elements are listed in Table 1.69. The associated energy that is liberated at the moment of the absorption is also indicated. At the moment of the creation of the two fragments, the atomic electrons are dispersed, thus the two fragments carry a net electric charge.

$$
\begin{array}{lll}
n +^3 He \rightarrow & ^3H + p + 770KeV & \\
n +^{10} B \rightarrow & ^7Li + \alpha + 480KeV\,\gamma\text{-ray} & +2300KeV\,(94\%) \\
\rightarrow & ^7Li + \alpha & +2780KeV\,(6\%) \\
n +^6 Li \rightarrow & ^3H + \alpha + 4790KeV & \\
n +^{157} Gd \rightarrow & Gd^* \rightarrow \gamma\text{-ray spectrum} \rightarrow \text{conversion } e^-(< 182KeV) & \\
n +^{235} U \rightarrow & \text{fission fragments} + \sim 80MeV &
\end{array}
\tag{1.69}
$$

The energies carried by the individual fragments can be calculated from the energy and momentum conservation. We can neglect the incoming neutron energy in this calculation because it is several orders of magnitude smaller than the absorption reaction energy: as a result the two fragments can be considered emitted back-to-back. In the thermal range neutrons have energies between $5\,meV$ and $500\,meV$ to be compared with typical energies of the $MeV$ order carried by the neutron absorption reaction. Hence the energies carried by the fragments in Table 1.69 are:

$$
\begin{array}{lll}
n +^3 He \rightarrow & ^3H(193\,KeV) + p(577\,KeV) & \\
n +^{10} B \rightarrow & ^7Li(830\,KeV) + \alpha(1470\,KeV) + 480KeV\,\gamma\text{-ray} & (94\%) \\
\rightarrow & ^7Li(1010\,KeV) + \alpha(1770\,KeV) & (6\%) \\
n +^6 Li \rightarrow & ^3H(2740\,KeV) + \alpha(2050\,KeV) &
\end{array}
\tag{1.70}
$$

It is important for a neutron converter, used to reveal thermal neutrons, to have a large absorption cross-section and for its capture reaction to yield a large amount of energy available to be detected. This will be treated in details in the next chapter.

### 1.5.4 Reflection of neutrons by interfaces

The reflection of light from surfaces is a well-known phenomenon caused by the change of refractive index across the interface. The mirror neutron reflection was demonstrated by Fermi and Zinn in 1944 [11] and they observed the total reflection of thermal neutrons below the critical angle. Neutron reflection follows the same fundamental equations as optical reflectivity but with different refractive indices. The optical properties of neutron propagation arise from the fact that quantum-mechanically the neutron is described by a wave-function. **The potential in the Schrödinger equation, which is the averaged density of the scattering lengths of the material, plays the role of a refractive index.** The neutron refractive index is given by the scattering length density of its constituent nuclei and the neutron wavelength. As with light, total reflection may occur when neutrons pass from a medium of higher refractive index to one of lower refractive index.
Neutron reflection is different from light reflection because the neutron refractive index of most of materials is slightly less than that of air or vacuum. As a result total external reflection is more commonly observed instead of the total internal reflection experienced with light. The angle where no neutrons penetrate the surface, hence all of them are reflected, is called *critical*

*angle*: the reflectivity of neutrons of a given wavelength from a bulk interface is unity at smaller angles (ignoring absorption effects) and falls sharply at larger angles. As with light, interference can occur between waves reflected at the top and at the bottom of a thin film, which gives rise to interference fringes in the reflectivity profile [12].
Neutron reflection is used as an analytical tool and offers many advantages over traditional techniques and to x-ray reflection. In particular, because of the short wavelengths available, it has a resolution of a fraction of a nanometer, it is nondestructive and it can be applied to buried interfaces, which are not easily accessible to other techniques.
Neutron reflection is now being used for studies of surface chemistry (surfactants, polymers, lipids, proteins, and mixtures adsorbed at liquid/fluid and solid/fluid interfaces), surface magnetism (ultrathin Fe films, magnetic multilayers, superconductors) and solid films (Langmuir-Blodgett films, thin solid films, multilayers, polymer films) [12].
Neutron reflection can be described using the Schrödinger equation:

$$-\frac{\hbar^2}{2m_n}\nabla^2\Psi + V\Psi = E\Psi \tag{1.71}$$

where $V$ is the potential to which the neutron is subject and $E$ its energy. $V$ represents the net effect of the interactions between the neutron and the scatterers in the medium through which it moves. We model $V$ as the smeared-out potential of all nuclei, instead of looking at the individual scattering centers [13]. From Equation 1.44, we average out the Fermi pseudo-potential:

$$V = \frac{2\pi\hbar^2}{m_n}N_b \tag{1.72}$$

where $N_b$ is the *scattering length density* of the medium the neutron is crossing defined as:

$$N_b = \sum_i b_i n_i \tag{1.73}$$

where $n_i$ is the number of nuclei per unit volume and $b_i$ is the coherent scattering length of nucleus $i$, because we take the spin-average (unpolarized beam or sample).
As already mentioned in Section 3.1, most materials have a positive scattering length $b$; therefore in a positive potential a neutron has less kinetic energy and hence a longer wavelength (light usually behaves in the opposite way). Moreover, some materials, such as $^{10}B$, present a complex $b$, of which the imaginary part represents the power for that material to absorb neutrons. In this Section, we only consider real $b$; the reflection of neutrons by strong absorbers will be treated in details in Chapter 4.
Referring to Figure 1.12, we consider a neutron beam approaching a surface with a bulk potential $V$. The only potential gradient and hence force is perpendicular to the surface; this will be not the case when the reflection surface is not ideally flat and its roughness will play a role in the reflection process.
Since we are considering a specular reflection only elastic scattering has to be taken into account. This implies $k_{r\perp} = k_{i\perp}$.
The solution of the Schrödinger equation for this specific two-dimensional case can be factorized as two plane waves, one orthogonal to the surface and one parallel:

$$\begin{aligned} \Psi(x,z) &= \left(e^{+i\,k_{i\perp}z} + r\,e^{-i\,k_{i\perp}z}\right)\cdot e^{+i\,k_{i\parallel}x} && \text{if } z<0 \\ Y(x,z) &= t\,e^{+i\,k_{t\perp}z}\cdot e^{+i\,k_{t\parallel}x} && \text{if } z>0 \end{aligned} \tag{1.74}$$

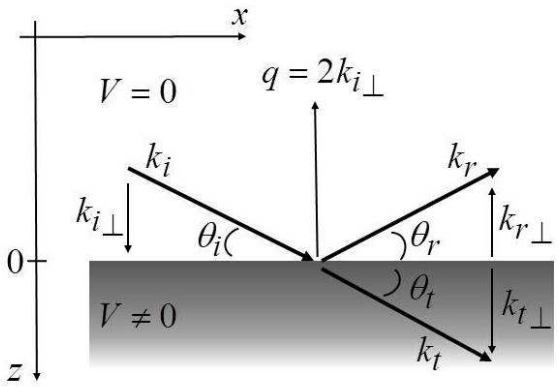


Figure 1.12: Reflection of an incident neutron beam from an ideally flat interface, $k_i$ and $k_r$ are the incident and scattered wave vectors, $q$ is the wave vector transfer; and $V$ is the potential of the semi-infinite substrate.

where $r$ and $t$ are the probability amplitudes for reflection and transmission. By substituting the solutions into the Schrödinger equation 1.71 we obtain the total energy conservation:

$$H\Psi = E\Psi \qquad \Longrightarrow \qquad \frac{\hbar^2}{2m_n}\left(k_{t\perp}^2 + k_{t\parallel}^2\right) = \frac{\hbar^2}{2m_n}\left(k_{i\perp}^2 + k_{i\parallel}^2\right) - V \qquad (z=0) \tag{1.75}$$

Continuity of wavefunctions and their derivatives at boundaries lead to:

$$\begin{cases} \Psi(x,z) = Y(x,z) & \Longrightarrow & (1+r)\,e^{+i\,k_{i\parallel}x} = te^{+i\,k_{t\parallel}x} & \Longrightarrow & 1+r=t \\ \frac{\partial\Psi(x,z)}{\partial z} = \frac{\partial Y(x,z)}{\partial z} & \Longrightarrow & k_{i\perp}\,(1-r)\,e^{+i\,k_{i\parallel}x} = t\,k_{t\perp}e^{+i\,k_{t\parallel}x} & \Longrightarrow & k_{i\perp}\,(1-r) = t\,k_{t\perp} \\ \frac{\partial\Psi(x,z)}{\partial x} = \frac{\partial Y(x,z)}{\partial x} & \Longrightarrow & k_{i\parallel}\Psi(x,z) = k_{t\parallel}Y(x,z) & \Longrightarrow & k_{i\parallel} = k_{t\parallel} \end{cases} \tag{1.76}$$

The potential the neutrons experience affects only the normal component of the momentum. Without loss of generality we can deal with a one-dimensional problem considering only the orthogonal solution of the Schrödinger equation, with $k_{t\parallel} = k_{i\parallel}$ in Equation 1.75:

$$\begin{aligned} \Psi_z &= e^{+i\,k_{i\perp}z} + r\,e^{-i\,k_{i\perp}z} && \text{if } z<0 \\ Y_z &= t\,e^{+i\,k_{t\perp}z} && \text{if } z>0 \end{aligned} \tag{1.77}$$

In the case of an ideally flat interface only the normal component of the incoming wave vector $k_i$ is altered by the barrier potential. It is "the normal component of the kinetic energy $E_{i\perp}$", that determines whether the neutron is totally reflected.

$$E_{i\perp} = \frac{p_{i\perp}^2}{2m_n} = \frac{(\hbar k_\perp)^2}{2m_n} = \frac{(\hbar\,k_i\,\sin(\theta_i))^2}{2m_n} = \frac{\hbar^2 q^2}{8m_n} \tag{1.78}$$

where $\theta_i$ is the incoming neutron angle with respect to the surface. $q = 2k_{i\perp} = 2k_i\sin(\theta_i)$ is the momentum transfer, as shown in Figure 1.12. If the normal component of the kinetic neutron energy does not exceed the barrier potential ($E_{i\perp} < V$), total reflection occurs and no neutrons penetrate into the layer. This happens when the momentum transfer $q$ is smaller than the critical value of wave vector transfer $q_c$, deduced by the condition $E_{i\perp} = V$ from Equations 1.72 and 1.78 we obtain:

$$q_c = \sqrt{16\pi N_b} \tag{1.79}$$

Conservation of momentum implies that $\theta_i = \theta_r$ where $\theta_r$ is the reflected beam angle; i.e. the reflection is specular. Off-specular scattering is elastic as well but occurs in presence of in-plane structures, mixing parallel and normal components. We do not treat it here.
On the other hand if the perpendicular neutron kinetic energy is $E_{i\perp} > V$, neutrons can penetrate into the layer, thus reflection is not total and the neutron can be either reflected or transmitted into the bulk of the material. As for light the transmitted beam $k_t$ must change direction because its normal component of kinetic energy is reduced by the potential; i.e. it is refracted. The change in the normal wave-vector is given by $E_{t\perp} = E_{i\perp} - V$, and it equals:

$$k_{t\perp}^2 = k_{i\perp}^2 - 4\pi N_b \tag{1.80}$$

The latter relation allows to define the refractive index $n$:

$$n^2 = \frac{k_t^2}{k_i^2} = \frac{k_{i\parallel}^2 + \left(k_{i\perp}^2 - 4\pi N_b\right)}{k_i^2} = 1 - \frac{4\pi N_b}{k_i^2} = 1 - \frac{\lambda^2 N_b}{\pi} \tag{1.81}$$

where $\lambda$ is the neutron wavelength. For most materials $N_b << 1$, hence Equation 1.81 can be approximated up in the thermal neutron energy range as $n \approx 1 - \frac{\lambda^2 N_b}{2\pi}$. This result confirms that the wavelength change in the bulk is opposite to that of light (for positive $b$, $n$ is less than 1). It can be important to notice that materials with constant $N_b$ are naturally dispersive ($n$ depends on $\lambda$) [14].
Referring to the solution of the Schrödinger equation (Equation 1.77), if the potential is real and $E_{i\perp} < V$ (see Equation 1.86), then $k_{t\perp}$ is imaginary and the solution for $z > 0$ in Equation 1.77 is an evanescent wave (an exponential decay).
From Equation 1.76 we can solve the classical Fresnel coefficients as it is in optics:

$$r = \frac{k_{i\perp} - k_{t\perp}}{k_{i\perp} + k_{t\perp}} \qquad\qquad t = \frac{2\,k_{i\perp}}{k_{i\perp} + k_{t\perp}} \tag{1.82}$$

The continuity equation considered for the stationary case $\frac{\partial P(\bar{r},t)}{\partial t} = 0$ where $P(\bar{r},t) = |\Psi(\bar{r},t)|^2$, and using unitary (no absorption):

$$\frac{\partial P(\bar{r},t)}{\partial t} + \nabla \cdot \bar{J}(\bar{r},t) = 0 \qquad \Longrightarrow \qquad \nabla \cdot \bar{J}(\bar{r},t) = 0 \tag{1.83}$$

where $\bar{J}(\bar{r},t)$ is the quantum probability current defined in Equation 1.30. Assuming $E_{i\perp} > V$, the probability for a neutron to be reflected or transmitted into the layer, given by the ratio of the reflected or transmitted flux over the incoming flux, is:

$$R = \frac{k_{i\perp}}{k_{i\perp}} r^2 = r^2 \qquad\qquad T = \frac{k_{t\perp}}{k_{i\perp}} t^2 \tag{1.84}$$

By using the Equations 1.79, 1.80 and 1.82 the reflectivity $R$ can be also written as:

$$R = r^2 = \left(\frac{q - \sqrt{q^2 - q_c^2}}{q + \sqrt{q^2 - q_c^2}}\right)^2 \qquad \text{for} \quad q > q_c \tag{1.85}$$

When $q >> q_c$, Equation 1.85 at the air-solid interface can be approximated as $R \approx \frac{16\pi^2}{q^4} N_b^2$.
$Y_z$, using Equation 1.80, is a real solution when $E_{i\perp} < V$ (or $q < q_c$):

$$Y_z = t\, e^{+i\, k_{t\perp} z} = t\, e^{+i\left(k_{i\perp}^2 - 4\pi N_b\right)^{1/2} z} = t\, e^{-\frac{1}{2}\left(q_c^2 - q^2\right)^{1/2} z} \tag{1.86}$$

When the potential barrier is higher than the particle energy normal to the surface it can still penetrate to a characteristic depth of $D_{ev} = \left(q_c^2 - q^2\right)^{-1/2}$, but there is no quantum probability current associated to it. This *evanescent* wave travels along the surface with wave vector $k_{\|}$ and after a very short time it is ejected out of the bulk in the specular direction. Taking as example the value of $N_b$ for Si this penetration is on the order of 100Å at $q = 0$, rising rapidly to infinity at $q = q_c$. No conservation laws are broken, as the reflectivity is still unity due to the fact that this wave represents no flux transmitted into the bulk.
The interface between materials may be rough over a large range of length scales. A boundary may be smooth but with one material diffused into the other. It turns out that in both the rough and diffuse cases the specular reflectivity is reduced as $q^{-4}$. The resulting density profiles are the same. Equation 1.85 in the case of $q >> q_c$ is affected in the manner:

$$R \approx \left(\frac{16\pi^2}{q^4} N_b^2\right) \cdot e^{-q^2\sigma^2} \qquad \text{for} \quad q >> q_c \tag{1.87}$$

where $\sigma$ is a characteristic length scale of the layer imperfection, the surface roughness. In the case of the diffuse interface the lost intensity given by the factor $e^{-q_z^2\sigma^2}$ goes into the transmitted beam as there are no potential gradients in any other direction than normal to the surface. This is not the case for the rough interface where intensity is lost by local reflections in directions away from the specular direction or off-specular scattering. If the in-plane structure is regular as in an optical grating then the off-specular can be quite dramatic.
The objective of a specular neutron reflection experiment is to measure the reflectivity as a function of the wave vector perpendicular to the reflecting surface, $q$. The measurement can be done by varying either the angle of incidence $\theta$ at constant wavelength or measuring the time-of-flight, hence varying wavelength, at constant $\theta$. The corresponding incoming intensity must also be measured. The reflectivity is simply the ratio of these two intensities, as a function of $\theta$ or $\lambda$ which is converted to $q$ by:

$$q = \frac{4\pi}{\lambda} \sin(\theta) \tag{1.88}$$

# Chapter 2

# Neutron gaseous detector working principles

An overview of the state of the art in neutron detection is discussed after we are going to describe the working principles of neutron gaseous detectors.
The main sources of the material for this Chapter are the books [1] and [6].

## 2.1 Principles of particle detectors

### 2.1.1 Introduction

Many types of detector have been developed so far, all are based on the same fundamental principle: the transfer of part or all of the radiation energy to the detector matter where it is converted into some other form more accessible to human perception [1]; usually an electrical signal. In Chapter 1 we discussed the interaction of charged particles and photons with matter. They transfer their energy to matter through direct collisions with the atomic electrons, thus excitation or ionization of the atoms.
The way to produce the electrical signal output is different for gaseous detectors, scintillators or semiconductors.
Gaseous detectors are based on the direct collection of the ionization electrons and ions produced in a gas by passing radiation. During the first half of the $20^{th}$ century ionization chambers, proportional counters and Geiger counters were developed. During the late 1960's the multi-wire proportional chamber was invented.
The scintillation detector makes use of the fact that certain materials, when struck by a radiation, emit a small flash of light, i.e. a scintillation. When coupled to an amplifying device such as a photomultiplier, these scintillations can be converted into electrical pulses. They detect the passing radiation trough the indirect process of light detection.
Semiconductors are based on crystalline semiconductors materials, most notably $Si$ and $Ge$. These detectors are also referred to as solid-state detectors. The basic operational principle is analogous to gas ionization devices. Instead of gas, the medium is a semiconductor. The passage of ionizing radiation creates electron-hole pairs which are then collected by an electric field. The advantage of semiconductors is that the average energy required to create a pair is an order of magnitude smaller than that required for gas ionization. On the other hand, being crystalline materials, they also have a greater sensitivity to radiation damage.
The neutron lack of charge and the fact that it is weakly absorbed by most materials are properties which have contributed to its powerfulness as a probe for condensed matter research. On the other hand, these properties make the construction of efficient neutron detectors difficult. Neutral radiation must first undergo some sort of reaction in the detector producing charged particles, which in turn ionize and excite the detector atoms.
As mentioned in Section 1.4.2, elastic scattering is the principal mechanism of energy loss for fast neutrons. A fast neutron, hitting a light atom target, can transfer its energy and generate an energetic charged particle by recoil.
For thermal neutrons the energy is too low to generate fast charged particles by elastic scattering. Thermal neutrons are detected indirectly by exploiting a capture reaction. Those reactions produce either prompt $\gamma$-rays or heavy charged particles such as protons, tritons, $\alpha$ or fission fragments. Those secondary radiations have sufficient energy to be directly detected. The processes used to detect those secondary particles can be ionization, excitation or scintillation.

### 2.1.2 Gas detectors

#### Charged particles in gas

A common method to detect a charged particle is based on sensing the ionization produced when it passes through a gas. As described in Section 1.2, the primary interaction of charged particles

is to ionize and excite the gas molecules along their tracks. After a neutral molecule is ionized, the resulting positive ion and free electron is called an *ion pair*. The ionization generated by the heavy charged particles is called *primary ionization*. The free electrons and ions created may diffuse. Some of the electrons may also have enough energy to be an ionizing charged particle themselves and to produce a *secondary ionization*. We define $n_{pair}$ as the total number of ion pairs created by the passage of a charged particle, both considering primary and secondary ionization.
With secondary ionization several different processes are intended. In this manuscript, we always refer to it as the ionization induced by electrons that have been created, though primary ionization, by the passage of a charged particle. In Section 2.1.2 we will introduce the multiplication process which is another kind of ionization performed by electrons in strong electric field; we refer to this ionization as avalanche process.
As already explained in Chapter 1, the energy loss of a charged particle in matter is essentially given by two types of reactions: ionization and excitation. In Table 2.1 the excitation and ionization potential for several gases are listed. It should be emphasized that the actual energy transfer needed, on average, to create a ion pair is $w_i$. $I_i$ is the ionization potential. The difference is due to excitation which costs energy to the particle but which does not create ion pairs. The average energy lost by a charged particle in the formation of an ion pair is about $w_i = 30\,eV$ and it is not strongly dependent on the type of molecule or charged particle. The number $n_{pair}$ of ion pairs created is given by [15]:

$$n_{pair} = \frac{\Delta E}{w_i} \tag{2.1}$$

where $\Delta E$ is the charged particle energy loss. The net charge created by the passage of a charged particle in a medium is directly proportional to the energy it deposits. E.g. for an $\alpha$-particle of $1\,MeV$ the process ends up with the creation of a net charge of a few $fC$.

| gas | $I_{ex}(eV)$ | $I_i(eV)$ | $w_i(eV)$ |
|---|---|---|---|
| $H_2$ | 10.8 | 15.4 | 37 |
| $He$ | 19.8 | 24.5 | 41 |
| $N_2$ | 8.1 | 15.5 | 35 |
| $O_2$ | 7.9 | 12.2 | 31 |
| $Ne$ | 16.6 | 21.6 | 36 |
| $Ar$ | 11.6 | 15.8 | 26 |
| $CO_2$ | 5.2 | 13.7 | 33 |
| $CH_4$ | 9.8 | 13.1 | 28 |
| $CF_4$ | 12.5 | 15.9 | 54 |

Table 2.1: Excitation and ionization potential for several gases [15].

The occurrence of the ionizing reactions is statistical in nature, thus two identical particles will not, in general, produce the same number of ion pairs. Hence, $n_{pair}$ has to be considered as the average number of ion pairs created by a ionization process.
While the number of ion pairs created is important for the efficiency and energy resolution of the detector, it is equally important that these pairs, or at least the electrons, remain in a free state long enough to be collected. Two processes contribute to diminish the net charge created:

*recombination* and *electron attachment* [6]. In absence of electric field, ions and electrons can only diffuse and they will generally recombine under the force of their electric attraction, emitting a photon in the process. Electron attachment is the capture of free electrons by electronegative atoms to form negative ions. The presence of electronegative gases in the detector severely diminishes the efficiency of electron collection by trapping the electrons before they can reach the electrodes. Some well known electronegative gases are $O_2$, $H_2O$ and $CO_2$. It has been observed that a small amount of $CO_2$ does not dramatically affect the detector performances but helps to stop more efficiently the ionizing particles. In contrast, noble gases $He$, $Ar$, etc. have negative electron affinities and are suitable for application in gaseous detectors.
In the absence of electric field, electrons and ions liberated by the passage of the charged particle diffuse uniformly outward from their point of creation. It is important to distinguish the words: *diffusion*, which is the free motion of ions and *drift*, which is the motion due to an external force, e.g. an electric field.
In the diffusion process the electrons and ions suffer multiple collisions with the gas molecules and come quickly into thermal equilibrium with the gas. The charges velocities distribution can be described by using the Maxwelian distribution.
In Figure 2.1 we plot the charge created by ionization, that eventually can entirely be collected, as a function of the voltage applied to two electrodes immerse into the gas volume, through which we apply the electric field. When $V = 0$, the electric field between ions and electrons causes a drift which leads to recombination. Only thermal diffusion occurs and no net charge can be collected.

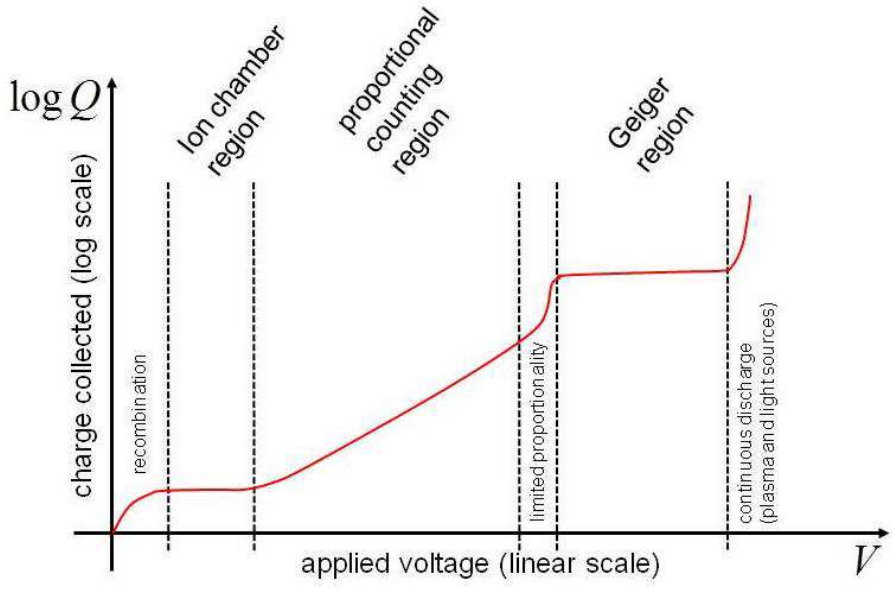


Figure 2.1: Practical gaseous ionization detector regions.

As the potential applied to the gaseous detector increases, several operational modes occur:

- ionization mode;
- proportional mode;

- Geiger mode.

Before describing in details the detector operational modes, we are going to explain how the charge created into the gas is translated into a readable signal.

### The Shockley-Ramo theorem

The signal from a detector is a current signal read from electrodes. It arises from the *motion* of charge carriers and not from their physical collection. This statement is valid for gas-filled detectors as well as for semiconductor detectors. The output pulse begins to form immediately when the carriers start their motion toward the electrodes. When the charge carriers deposit their electrical charge on the electrodes the process is over and no output signal is induced anymore [6]. The time evolution of the signal is fundamental for understanding the timing properties of detectors.
The method to calculate the induced charge on electrodes due to the motion of charges in a detector makes use of the Shockley-Ramo theorem [16], [17], [18] and the concept of the *weighting field*.
Referring to Figure 2.2, consider a volume where there are some, in this case three, conductors. Each conductor is maintained at his fixed potential $V_i$ through a generator. We take the volume surrounded by a conductor maintained at ground potential. Let's imagine a net charge $q$ has been created, e.g. from the passage of a radiation.

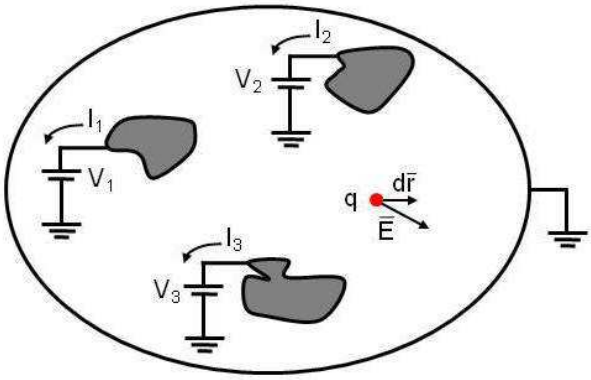


Figure 2.2: Three conductors are polarized through a generator and a charge $q$ moves along $d\bar{r}$ in the resulting electric field generated by the conductors.

The resulting electric field $\bar{E}$ in a generic point of the space can be calculated as the superimposition of the single electric field generated by each conductor.

$$\bar{E} = \sum_i V_i \, \bar{E}_i = V_1 \, \bar{E}_1 + V_2 \, \bar{E}_2 + V_3 \, \bar{E}_3 \tag{2.2}$$

where $E_i$ is the weighting field associated to the $i-th$ conductor. It is measured in $1/m$ and can be interpreted as the electric field that would be generated by the $i-th$ conductor if its generator is set to $V_i = 1V$ and all the other conductors are at ground potentil. The actual electric field generated by a conductor can be obtained by setting each potential to zero apart from the one under interest. E.g. $\bar{E}_i^{real} = V_i \bar{E}_i$.

Let's imagine the charge $q$ to move over an interval $d\bar{r}$. The work done by the electric field on the charge is:

$$dW_q = q\bar{E} \cdot d\bar{r} \tag{2.3}$$

Since the volume is closed, and assuming that the charge $q$ does not perturb the electric field generated by the conductors, we assume the conservation of energy in the volume, i.e. $dW_q = dW$. Where we denote with $dW$ the work done by the sources:

$$dW = -\sum_i V_i \, I_i \, dt = -\left(V_1 \, I_1 + V_2 \, I_2 + V_3 \, I_3\right) dt \tag{2.4}$$

By comparing Equations 2.3 and 2.4 we obtain:

$$-\left(V_1 \, I_1 + V_2 \, I_2 + V_3 \, I_3\right) = q\bar{E} \cdot \frac{d\bar{r}}{dt} = q\bar{E} \cdot \bar{v} = q\left(V_1 \, \bar{E}_1 + V_2 \, \bar{E}_2 + V_3 \, \bar{E}_3\right) \cdot \bar{v} \tag{2.5}$$

where $\bar{v}$ is the charge velocity.
By differentiating with respect to the $i-th$ potential $V_i$ the Equation 2.5, we obtain the current $I_i$ that flows through the $i-th$ generator to compensate the motion of the charge $q$:

$$I_i = -q\bar{E}_i \cdot \bar{v} \tag{2.6}$$

which in its differential form, by using $I = \frac{dQ}{dt}$, is:

$$dQ_i = -q\bar{E}_i \cdot \bar{v} \, dt \tag{2.7}$$

$dQ_i$ is the instantaneously induced charge on the $i-th$ conductor. Note that, from Equation 2.7, when the charge $q$ reaches one electrode, i.e. $\bar{v} = 0$, there is no more charge induced $dQ$.
The total amount of charge induced on the $i-th$ conductor is:

$$Q_i = -q \int \bar{E}_i \cdot \bar{v} \, dt \tag{2.8}$$

Let us consider now two plane electrodes facing each other at a distance $D$. The first is polarized at $V_1 = V_0$, i.e. the anode, and the second at ground, $V_2 = 0$, i.e. the cathode. In this configuration the actual electric field, neglecting side effects is uniform $E = V_0/D$ and orthogonal to the electrodes. We denote its direction with $x$. The charge $q$ is created at a distance $d$ from the anode (a distance $D - d$ from the cathode). The weighing filed associated to the anode is $E_1 = 1/D$. The current and charge induced on the first electrode, Equations 2.6, 2.7 and 2.8, by a negative charge ($q < 0$) going to the anode, is:

$$I_1 = -\frac{q}{D} v_x, \qquad dQ_1 = -\frac{q}{D} v_x \, dt, \qquad Q_1 = -q \int \frac{1}{D} v_x \, dt = \frac{q}{D} \int_d^0 dx = \frac{q}{D} d \tag{2.9}$$

where $v_x$ is the component of the charge $q$ velocity parallel to the electric field. A negative charge induces a negative charge on the anode.
From Equation 2.9 we notice that the total induce charge does not depend on how the charge $q$ moved but only from the starting and ending points of its path: i.e. the electric field is conservative. This is not the case for the current which depends on the charge velocity. The current depends on the path traveled by the charge and not only on the starting and ending points.
The charge induced on the cathode is the same as the one induced on the anode, except for the sign.

### Signal read-out

The detector read-out can be essentially carried out in two ways: *continuous current mode* or *current pulse mode*.
In continuous current mode, the induced current is measured at the detector electrode. Because in strong irradiation conditions the detector response time is often long compared with the average time between events, the effect is to average out many fluctuations and the output depends on the product of the interaction rate and the charge per interaction.
In the current pulse mode, the current pulse due to a single event is measured. The transimpendence amplifier, connected to the electrode, has a bandwidth corresponding to a time constant $\tau$. $t_c$ is the time of the charge collection in the gas volume. If $\tau << t_c$ (short integration time), the voltage output will follow the instantaneous value of the current flowing in the detector. On the contrary, if $\tau >> t_c$ the current flow is integrated over a time $\tau$. The amplitude of the voltage output will be proportional to the integral of the current flow, i.e to the charge generated in the detector.
Common values for charge amplifier gains are $G = 5\,V/pC$ with integration time of $\tau = 2\,\mu s$. A standard charge amplifier presents a sensitivity of about $10\,fC$, below that charge level a low-noise amplifier should be used. For example, if a neutron is converted by $^{235}U$, its fission fragments carry about $80\,MeV$ that translates into about $3 \cdot 10^6$ ion pairs in $Argon$, i.e. $500\,fC$, which is a sufficient charge to be amplified electrically. On the other hand, the proton of the $^3He$-capture reaction carries $577\,KeV$ that turns into a net charge of about $3\,fC$.

### Ionization chambers

In the presence of an electric field, the electrons and ions created by the radiation are accelerated along the field lines toward the anode and cathode respectively. This acceleration is interrupted by collisions with the gas molecules which limits the maximum average velocity which can be attained by the charge carriers. The average velocity is called *drift velocity* of charges and it is superimposed on their random diffusion movement. Compared with the thermal speed, the drift speed of ions is slow, however, for electrons can be much higher since they are much lighter.
The mobility of a charge is defined as:

$$\mu = \frac{u}{E} \tag{2.10}$$

where $u$ is the drift velocity and $E$ is the electric field strength. For positive ions $u$ is found to depend linearly on the ratio $E/P$ (with $P$ gas pressure) with relatively large field values. At constant pressure it implies that mobility is constant and, for e given $E$, mobility varies as the inverse of the pressure. The usual mobility of a positive ion in a noble gas is about $1\,\frac{cm^2}{V\,s}$.
The recombination process decreases the net charge seen by electrodes; it is then necessary to increase the applied voltage, i.e. the electric field strength, until it is large enough to avoid recombination. In Figure 2.1 when the voltage is sufficient to collect the whole charge a plateau is attained (ion saturation). A detector operates in ionization mode when the whole charge created by a ionizing radiation is collected at the electrodes.
As mentioned in the previous section, neutrons that have been converted by $^{235}U$ into charged particles lead to induced charge of about $0.5\,pC$ which is a readable by using a standard amplifier; hence $^{235}U$ is suitable to build an ionization chamber working in *pulse mode* because of its reaction energy yield.
Generally ionization chambers work in *continuous current mode*.

**Proportional counters**

Not all neutron capture reactions can lead to fragments that, carrying hundreds of $KeV$, produce enough charge to be amplified by standard amplifiers.
In order to increase the ion pair yield of limited energy fragments, one can exploit the gas multiplication process. At low values of the electric field the electrons and ions created simply drift toward their collection electrodes, as in the case of an ionization chamber. During the migration ions collide with neutral gas molecules and, because of their low mobility, they achieve very little average kinetic energy between collisions. If the electric field is risen to a sufficient high value, free electrons, on the other hand, can be accelerated to get enough kinetic energy to produce further ionizations. Because the average energy of the electron between collisions increases with the electric field, there is a threshold value for the field above which this further ionization occurs. In typical gases, at atmospheric pressure, the threshold field required is of the order of $10^7\, V/m$.
The liberated electrons are accelerated as well and they can create additional ionization. The gas multiplication process therefore takes the form of a cascade, known as *Townsend avalanche*. The number of electrons per unit path length is governed by the Townsend equation:

$$\frac{dn}{n} = \alpha\, dx \tag{2.11}$$

where $\alpha$ is the first Townsend coefficient of the gas. Its value is zero when the electric field is below the threshold value and generally increases very rapidly as the electric field increases. In a spatially constant field the electron density grows exponentially with the distance as the avalanche progresses:

$$n(x) = n(0)\, e^{\alpha\, x} \tag{2.12}$$

where $n(0)$ is the original charge at the point $x = 0$.
In the proportional counter, the avalanche terminates when all free electrons are collected at the anode. As a result, the number of electrons created by the gas multiplication is proportional to the number of initial ion pairs created by the incident radiation, i.e. the net charge created, or read-out, is proportional to the incoming radiation energy. Referring to Figure 2.1, as the applied voltage rises, the actual electric field increases, hence the Townsend coefficient increases and the charge created grows exponentially.
This charge amplification reduces the signal to noise requirement of the amplifiers and significantly improves the signal-to-noise ratio compared with pulse-type ion chambers.
The formation of an avalanche involves many energetic electron-atom collisions in which the variety of excited atomic or molecular states may be formed. The performance of proportional counters is therefore much more sensitive to the composition of trace impurities of the fill gas than in the case of ion chambers.
Increasing further the electric field introduces nonlinear effects. Although free electrons are quickly collected, the positive ions move much more slowly, and during the time it takes to collect electrons, they barely move at all. Therefore, each pulse within the counter creates a cloud of positive ions which is slow to disperse and represents a space charge that can significantly alter the shape of the electric field within the detector.
The actual electric field necessary to produce gas multiplication can be problematic to be realized from a practical point of view of power supplies or electrical and mechanical constraints. E.g., in order to increase the electric field up to $2 \cdot 10^7\, V/m$ in a planar geometry detector,

where the two electrodes are faced one to the other and they stand at a distance $d_g = 10\,mm$, a potential of $200\,KV$ has to be applied. A way to address this problem is to use anodes of small radius. The electric field in a cylindrical geometry is given by:

$$|E| = \frac{V_0}{|\bar{r}|} \frac{1}{\ln\left(\frac{r_C}{r_A}\right)} \tag{2.13}$$

where $r_C$ and $r_A$ are the cathode and anode radius respectively; $V_0$ is the potential difference between them. Note that if $r_C \gg r_A$, the electric field rises in a region close to the wire, say up to $\sim 5 \cdot r_A$. This latter is the so-called *multiplication region*. The number of pairs created in the multiplication region rises as we approach the anode and also the Townsend coefficient increases strongly. Most of pairs are formed close to the anode surface. The exponential growth (Equation 2.12) predicts that half of the charge is created in one path $\lambda = 1/\alpha$. At atmospheric pressure, for $Ar$, $\lambda = 2\,\mu m$. In reality, because of the rising $\alpha$, the growth is faster than exponential.
As example we take a tube of radius $r_C = 5\,mm$ (at ground potential) in which center is placed an anode wire $r_A = 10\,\mu m$. By only applying $V_0 = 1000\,V$ we can easily obtain a strong electric field of $1.6 \cdot 10^7\,V/m$.
The main contribution to the signal formation on electrodes is due to positive ions. The multiplication occurs in the multiplication region, i.e. around the anode wire. Let's take the previous example of a cylindrical detector. Denote with $q = |n \cdot e|$ the net charge created by the avalanche process ($n$ is the number of pairs created) and let us assume for simplicity that it is placed at $\lambda = 2\,\mu m$ from the wire surface, thus at $r = r_A + \lambda$.
By using the Schokley-Ramo theorem, the charge induced on the anode is given by Equation 2.8:

$$Q_{anode} = -q_i \int_{r_1}^{r_2} \bar{E}_{anode} \cdot \bar{v}\, dt = -\frac{q_i}{\ln\left(\frac{r_C}{r_A}\right)} \int_{r_1}^{r_2} \frac{dr}{|\bar{r}|} = -\frac{q_i}{\ln\left(\frac{r_C}{r_A}\right)} \ln(r) \,|_{r_1}^{r_2} \tag{2.14}$$

where we use as weighting field $|E|/V_0$ as defined in Equation 2.13. The charge induced on the cathode, in presence of only two electrodes, is $Q_{cath.} = -Q_{anode}$. $r_1$ and $r_2$ are the integration limits different for electrons ($q_i = q_e = -q$) and ions ($q_i = q_{ion} = +q$). From the point where the charge is created, electrons will travel toward the anode ($r_1 = r_A + \lambda = 12\,\mu m$ and $r_2 = r_A = 10\,\mu m$) and ions toward the cathode ($r_1 = r_A + \lambda = 12\,\mu m$ and $r_2 = r_C = 5\,mm$). Hence:

$$\begin{aligned} Q^e_{anode} &= -\frac{q_e}{\ln\left(\frac{r_C}{r_A}\right)} \ln(r) \,|_{r_A+\lambda}^{r_A} = -\frac{q_e}{\ln\left(\frac{r_C}{r_A}\right)} \ln\left(\frac{r_A}{r_A+\lambda}\right) \simeq +0.03\, q_e = -0.03\, q \\ Q^{ion}_{anode} &= -\frac{q_{ion}}{\ln\left(\frac{r_C}{r_A}\right)} \ln(r) \,|_{r_A+\lambda}^{r_C} = -\frac{q_{ion}}{\ln\left(\frac{r_C}{r_A}\right)} \ln\left(\frac{r_C}{r_A+\lambda}\right) \simeq -0.97\, q_{ion} = -0.97\, q \end{aligned} \tag{2.15}$$

where we denoted with $Q^e_{anode}$ and $Q^{ion}_{anode}$ the charge induced by electrons and ions on the anode. Note that the ions contribution is larger on the signal formation than the electrons' one.
Proportional counters are generally operated in *pulse mode* because they suffer from space charge effects before the count rate is high enough to have continuous current mode.

### Geiger counters

Referring to Figure 2.1, if the applied voltage is made sufficiently high, the space charge created by positive ions can become completely dominant in determining the subsequent history of the

pulse. Under these conditions, the avalanche proceeds until a sufficient number of positive ions have been created to reduce the electric field below the point at which additional gas multiplication can take place. The process is then self-limiting and will terminate when the same number of positive ions have been formed regardless of the number of initial ion pairs created by the incident radiation. Thus, each output pulse from the detector is on average of the same amplitude and no longer reflects any properties of the incident radiation. This is called the Geiger-Mueller region of operation [6].
In a proportional counter each original electron leads to an avalanche that is basically independent of all other avalanches formed from other electrons associated with the original ionizing event. Because all the avalanches are nearly identical, the collected charge remains proportional to the number of original electrons. On the other hand, in a Geiger tube, the higher electric field enhances the intensity of each avalanche; but as well each avalanche can itself trigger a second avalanche at different position within the tube and the process becomes rapidly divergent creating a discharge. In a typical avalanche many excited gas molecules are formed by electron collisions. Within few $ns$ those molecules return to their ground state through the emission of a photon, generally in the UV region. These photons are the key element in the avalanche chain propagation that makes up the discharge.
A typical pulse from a Geiger tube represents a large amount of charge collected, about $10^9$ ion pairs. Therefore, the output pulse is so intense that in principle no amplifier electronics is needed; thus a Geiger tube is often an inexpensive choice when a simple counting system is needed.

**Quencher and stopping gas**

As mention for the Geiger counters, for proportional counters as well, the gas multiplication process creates many excited molecules from the collisions of electrons and neutral molecules. These excited molecules do not contribute directly to the avalanche process but decay to their ground state through the emission of a photon, generally an UV-photon. Under certain circumstances these de-excitation photons could create additional ionization elsewhere in the fill gas or at the cathode. Although such photon-induced events are important in the Geiger region of operation, they are generally undesirable in proportional counters because they can lead to a loss of proportionality and/or spurious pulses. Furthermore they can cause avalanches which spread in time and space and, consequently, they reduce the spatial and time resolutions.
The addition of a small amount of polyatomic gas, such as methane, to many of the common fill gases, e.g. Argon, will suppress the photon-induced effects by absorbing the photons in a mode that does not lead to further ionization. This additional gas is often called *quench gas*.
Noble gases are commonly used as main gas fill, however for specific applications the sole use of such a gas can be not enough to guarantee a certain time or spatial resolution. E.g. neutron counters are filled with $^3He$, which does not only convert neutrons but it is as well a suitable gas fill for the detector operation. Usually to reduce dead time it is recommended to add a second element, i.e. the *stopping gas* as $CF_4$, to the gas mixture to increase its global stopping power. In such way the detector time response improve because ions are stopped on shorter tracks.

## 2.2 Thermal neutron gas detectors

### 2.2.1 The capture reaction

Mechanisms for detecting thermal neutrons in matter are based on indirect methods [19]. The process of neutron detection begins when neutrons, interacting with various nuclei, initiate the release of one or more charged particles or $\gamma$-rays. The electrical signal produced by this secondary radiation can then be processed by the detection system. Thermal neutrons carry a too small amount of energy to be transferred to a recoil nucleus and to produce ionization. As introduced in Chapter 1, neutrons can cause nuclear reactions. The products from these reactions, such as protons, alpha particles, $\gamma$-rays, and fission fragments, can initiate the detection process. Detectors employing the reaction mechanism can use solid, liquid, or gas-filled detection media. The choice of reactions is limited and most of the suitable materials, for their large neutron absorption cross-section, are listed in Equation 1.69.
The commonest capture process is one which results in the emission of a prompt $\gamma$-ray. Although these $(n, \gamma)$ reactions occur for most nuclides, the resulting photons, being uncharged, are also difficult to detect directly.
Hence, most thermal neutron detectors, with prompt read-out, are based on the few absorption reaction that result into heavy charged particles or fission fragments: $^3He$, $^6Li$, $^{10}B$, $^{235}U$, $Gd$, etc.
In the thermal neutron detection process the information on the initial neutron energy is completely lost. Once a neutron is captured, the energy available, to be detected, is the one of the capture reaction. Thus, in general, neutron detectors provide information only on the number of neutrons detected and not on their energy. The only effect of the neutron energy is via the absorption cross-section which usually follows the $1/v$ law. The latter influences the probability of the neutron to be detected by the detector medium.
We focus now on thermal neutron gaseous detectors. To detect a thermal neutron we need a converter and a stopping gas to be ionized by the charged particles originated by the neutron capture. Only fission fragments from $^{235}U$ have enough energy to operate the detector in ionization mode, usually $^3He$ and $^{10}B$-based gaseous detectors are operated in proportional regime. Since $^6Li$ is solid at room temperature and does not produce any $\gamma$-ray after the neutron capture, is a suitable material to be embedded in a scintillator.
$^3He$, which is a gas at room temperature, is both a powerful converter of neutrons and a stopping gas. Its capture reaction produces a proton and a triton (see Table 1.70). At $1\,bar$ ($\rho = 1.3 \cdot 10^{-4}\,g/cm^3$) and room temperature the $577\,KeV$ proton is stopped within about $55.3\,mm$; at $10\,bar$ in $5.5\,mm$. The track length can be too long to efficiently localize the interaction point of the neutron (see Section 2.2.3). Usually a variable amount of a more efficient stopping gas is added to $^3He$ to reduce the particle traces, e.g. $CF_4$. In a mixture $^3He/CF_4$ in the ratio 80/20 at $1\,bar$ the proton track length is reduced to $12.2\,mm$, at $10\,bar$ to $1.2\,mm$.
In addition to stopping gas can be added a quencher to absorb UV photons. In neutron detection any quenching gas containing a large amount of Hydrogen should be avoided because they can cause a strong neutron scattering.
Another gaseous converter exploited in thermal neutron detection is $^{10}BF_3$, but for its toxicity its use is limited.
For solid converters, such as $^{10}B$ or $^{10}B_4C$, the gaseous material acts only as stopping medium. The neutron is converted in the solid converter and escaping particles ionize the gas. The

description of such a detector will be discussed in details in Chapter 3.

### 2.2.2 Pulse Height Spectrum (PHS) and counting curve (Plateau)

In many applications of radiation detectors, the object is to measure the energy distribution of the incident radiation. This is not the case for thermal neutron detectors because the information on the neutron energy is completely lost in the conversion process of a neutron into charged particles. The energy information we can access is always the neutron capture fragment energy. An important detector aspect is to make it able to distinguish between real events and background events, e.g. between neutron events and $\gamma$-rays. As a result, energy resolution is required on the fragment energies and it is an important feature to be able to discriminate between particles.
When operating a detector in pulse mode, each individual pulse amplitude carries the information on the charge generated in the gas volume, i.e. on the energy deposited. The amplitudes will not all be the same. The pulse height distribution is a fundamental property of the detector output that is routinely used to deduce information about the incident radiation, or, in the case of neutrons, on the neutron capture reaction. This distribution is more commonly known as *differential pulse height distribution* and in this manuscript we will always refer to it as *PHS* or *Pulse Height Spectrum*. Figure 2.3 shows a typical PHS of a $^3He$-based gaseous detector, in which we recall the capture reaction yields about $770\,KeV$ of which $577\,KeV$ goes to the proton and $193\,KeV$ to the triton. When a neutron is converted by $^3He$ the two fragments immediately release their energy into the gas volume, consequently an amount of charge proportional to the total reaction energy will be created. A pulse of amplitude proportional to the energy will be readable at the detector output. Let's imagine now that a neutron is converted so close to the detector wall that one of the two fragments hits the wall without releasing its energy into the gas. The related output pulse will have a smaller amplitude. Obviously the energy loss by wall effect is a continuous process because neutrons can be converted at any distance from the wall and fragments can be emitted with a random angle. The effect of the walls is then visible on the PHS as a tail energy distribution toward smaller energies from the full energy peak.
Generally a neutron detector can be sensitive as well to other radiations, more commonly $\gamma$-rays. Events generated by $\gamma$-rays, according to the detector construction, generally deposit a small amount of energy in the gas volume compared with capture fragments, hence they are well separated in energy on the PHS (see Figure 2.3).
A better energy resolution, which is defined as the FWHM (Full Width Half Maximum) of the full energy peak, would improve the distinction between real events (neutrons) and spurious events ($\gamma$-rays).
In practice, the PHS is measured by accumulating the pulses using an integrating amplifier that is characterized by a given electronic noise. In order to measure properly the PHS a threshold in amplitude should be set just above the electronic noise to avoid false triggers.
In the proportional counting region (see Figure 2.1), the charge created in the detector can be set by changing the operational voltage and it grows exponentially with it. As a result, in pulse mode, the amplitude of the output from the detector varies as a function of the operational voltage. In Figure 2.4 we show three PHS corresponding to three operational voltages applied, with $V_A < V_B < V_C$. As the voltage increases, events with smaller energy are amplified over the noise level threshold of the amplifier and give rise to events on the PHS. We define the *counting curve* (or *Plateau*) as the integral of the counts over a given threshold (set by the electronics

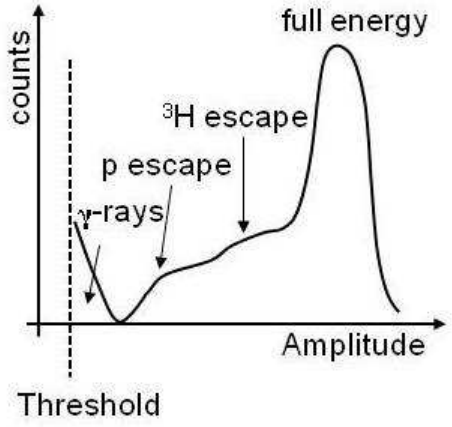


Figure 2.3: Typical PHS of an $^3He$-proportional tube.

used) on the PHS, plotted as a function of the operational voltage. Its behavior with the voltage $V$ is strictly related to the PHS shape and an example is shown in Figure 2.5. As the voltage increases, according to the PHS shape, the counting curve can vary its slope.
Generally, once the plateau is attained, it starts to rise again at higher voltages because of $\gamma$-ray events.
Once a detector geometry and electronics is defined, a detector should be operated in a stable regime where a small change in parameters (voltage, threshold, gas pressure, ...) does not affect efficiency. Referring to Figure 2.5, the best operating voltage would be $V_B$. Below this voltage the detector is not counting the totality of events, hence is less efficient; above this voltage, we are mixing up neutron events with other events at low energy.
It should be emphasized that the plateau depends on the detector geometry and read-out system, e.g. amplifier gain, thus the operational voltage chosen to operate the detector is related to the detector working configuration.

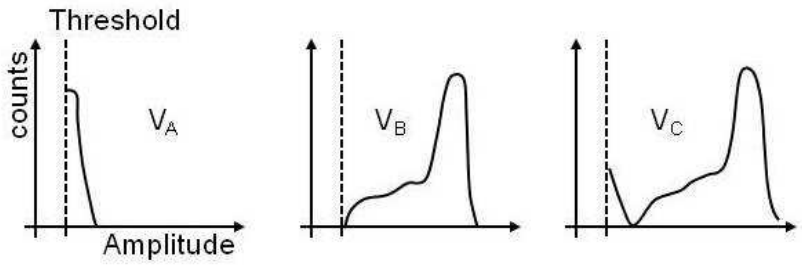


Figure 2.4: Examples of $^3He$-based counter tube PHS as a function of an increasing operational voltage applied to the detector.

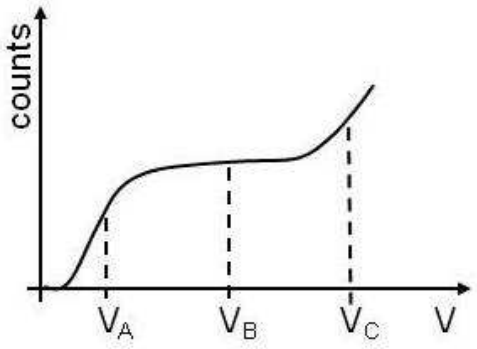


Figure 2.5: Example of counting curve plot (plateau) for an $^3He$-based counter tube.

### 2.2.3 Gas spatial resolution

In neutron scattering science it is often crucial to determine the neutron impact position on the detector. For such application a PSD (Position Sensitive Detector) is needed. The detector operational modes explained are valid for PSD, and an easy way to get the positional information is to place more anode wires in a gas chamber (Multi Wire Proportional Chamber - MWPC). Those wires act as individual detectors hence give the position of the neutron interaction point. To get the second dimension information a X-Y coincidence, a delay-line read-out, a charge division read-out, etc. Those are explained in details in Section 2.3.
The spatial resolution $\Delta x$ is defined as a distance and represents the ability for a detector to distinguish between two events that occur at a distance $\Delta x$, for a given confidence level. A widely used criterion, to define the spatial resolution, is to give the FWHM (Full Width Half Maximum) of the image of a point. If the image is a gaussian, it corresponds to 88% probability to properly distinguish between two events at that distance.
In the slowing down of a charged particle the charge is generated all along the particle path, thus what it is measured at the electrodes is the charge centroid [20]. The neutron capture reaction is asymmetric because of the difference in masses of the two fragments. For $^3He$, most of the energy will be carried by the proton and it will have a longer path with respect to the triton. Consequently the charge centroid does not correspond to the neutron interaction point.
If we use charge centroid read-out the gas spatial resolution is proportional to the charged particle range in the converter. The interaction point and the charge centroid approach as the particle ranges diminish. The higher the gas pressure, the lower are the particle ranges.
In $^3He$-based neutron detectors the spatial resolution is limited by mechanical constraints on the vessel containing the detector which limits the maximal pressure.
For a given neutron interaction point the direction the two capture fragments are emitted is isotropically distributed. The detector response, depending on its geometry, will be different according to the particle ejection direction. What is measured, when the detector is exposed to a point source, is an average over all the possibilities that results into a distribution with its own FWHM that defines the resolution due to the gas.
In Figure 2.6 the stopping power for the the two $^3He$ capture reaction fragments in $1\,bar$, $T = 300\,K$, $^3He/CF_4$ in the ratio 80/20 is shown. The resulting gas mixture density is $\rho = 8.8 \cdot 10^{-4}\,g/cm^3$. At atmospheric pressure in such a gas mixture, the extrapolated range for

the $577\,KeV$ proton is $1.22\,cm$ and for the $193\,KeV$ triton is $0.44\,cm$. The charge centroid is shown in Figure 2.6, and the error committed between the actual neutron conversion position and the detector read-out position is about $0.48\,cm$. This limits the actual spatial resolution the detector can attain and it can be improved by increasing the gas pressure. Since the stopping power is directly proportional to the density, thus the gas pressure, the particle range is inversely proportional to pressure. At $10\,bar$, in the same gas mixture just taken as example, the particles ranges are diminished by a factor 10. The charge centroid, thus the maximum spatial resolution achievable, would be around $0.5\,mm$.

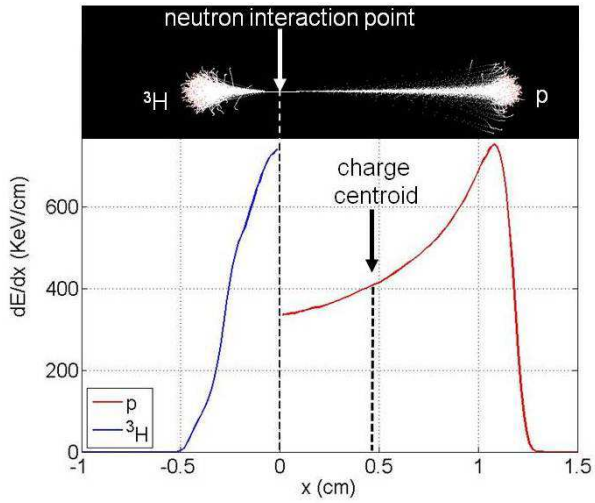


Figure 2.6: Stopping power for the $^3He$ capture reaction fragments in a gas mixture of $^3He/CF_4$ (80/10) ($\rho = 8.8 \cdot 10^{-4}\,g/cm^3$) at $1\,bar$.

It has to be pointed out that modern electronics allows to perform the reconstruction of the fragment tracks in order to determine the neutron interaction point. In this case the gas pressure in $^3He$-based detectors is needed only to increase the detection efficiency. Pressure remains an issue if the detector is operated in vacuum. We will not use such electronics.

### 2.2.4 Timing of signals

The time response of a gaseous detector is related to the time differences over which the different moving charges generate their signals on one hand, and the time of the signal development of a single charge on the other hand.
The stopping time of a charge in gases is a few nanoseconds. Hence, this time is not the bottleneck of the time response of a detector and it can often be neglected.
What limits the detector time performance is instead the time the charges, created by the ionization, need to be collected at the electrodes and the time duration of the signal induction. This latter depends on the strength of the electric field the detector is operated at and, according to the geometry, to the mobility of charges. This latter can be tuned by playing with the gas composition. Generally, in $^3He$-based neutron detectors the simple $^3He$ would be enough to assure a correct gas ionization and collection of charges. On the other hand, a fraction of other gases, such as $CF_4$, are added to it to form a mixture that increases the stopping power of the particles, in order to get faster responses and better resolution.

For example, according to Equation 2.10, the time for a general ion ($\mu = 1\frac{cm^2}{V\,s}$) to drift over $1\,cm$ at $1\,bar$ in an uniform electric field of $10^5\,V/m$ results in $t = \frac{1\,cm}{10^3\,cm/s} = 1\,ms$. This time for electrons generally is about three orders of magnitude smaller; i.e. $1\,\mu s$.

### 2.2.5 Efficiency

Detection efficiency is defined as the ratio between the detected events by the detector and the total amount of incident radiation.
In general, for neutron detectors, the detection efficiency is related to the absorption probability of a neutron but it is not strictly the same. The absorption probability increases with the converter density $\rho$, i.e. pressure for gases, because it follows the neutron absorption exponential law (see Equation 1.27) with $\Sigma(\lambda)$ macroscopic cross-section. Detection efficiency is the number of converted neutrons that give rise to a signal output over the total. It can happen that not all the converted neutrons give fragments that release sufficient energy over the noise level into the gas. Hence some neutrons can be absorbed without that a signal output is generated above the threshold. Usually this loss can be neglected and detection efficiency as well follows the neutron absorption exponential law. We recall, that since $\sigma_{abs}$ depends on the neutron energy as $1/v$ the detection efficiency increases with the neutron wavelength.
By keeping the detector volume constant, a way to increase the neutron detection efficiency is to increase the converter gas pressure.
For solid neutron converter based detectors efficiency does not depend in such a simple way on the neutron wavelength as for gas converters.
A full explanation of that will be given in Chapter 3.

## 2.3 Read-out and dead time

### 2.3.1 Read-out techniques

If position sensitivity is required a PDS (Position Sensitive Detector) is needed. A PSD allows to identify the point of interaction of the radiation in one direction or in a two-dimensional plane. The segmentation of the anodes or cathodes in a gas detector allows to get the positional information. We can imagine to segment a single cathode plane into strips and to place many wires close to each other to make an anode plane, i.e. MWPC. Each wire acts as a single detector. The read-out works in the same way for cathodes as for anodes. Once an ionization and gas multiplication occur there will be only a region in a gas chamber interested by the induction of the signal; there could be one or more wires where the signal is induced. The *individual read-out* can be performed by connecting each wire to a single charge amplifier. To get the second dimension information, a second wire plane, orthogonal to the first, can be placed in the gas volume and read-out in the same way. Equivalently, the cathode can be segmented and read-out by an individual amplifier for each strip. The number of read-out channels can diverge rapidly for a large detector. The large amount of electronics required can be expensive and unwieldy.
In order to reduce the number of read-out channels we discuss here the delay line and charge division approaches.
Figure 2.7 shows the schematic for a delay line and for charge division. In a delay line $N$ wires (or strips) are connected in a chain through inductances, say $L$. Each wire has an intrinsic capacitance to ground ($C$). Usually it is $100\,pF/m$. The circuit we obtain is a discrete trans-

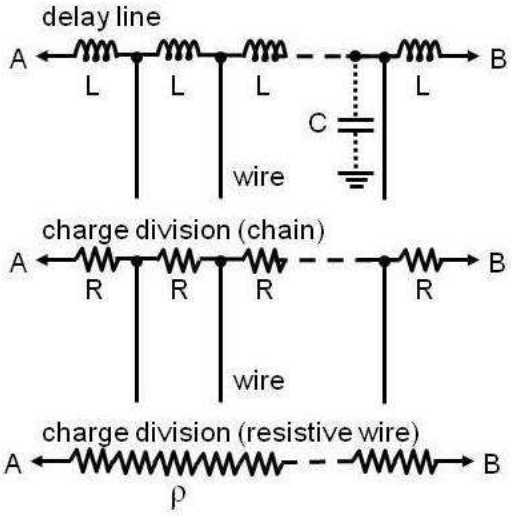


Figure 2.7: Delay line read-out, charge division on several wires and charge division on a single resistive wire.

mission line where signals travel at the velocity $v = 1/\sqrt{L_m\, C_m}$, where $L_m$ and $C_m$ are the inductance and capacitance per unity of length. At the two outputs, A and B, we measure the difference in the arrival time of the signals. The position along the delay chain is calculated as:

$$x = \frac{t_A - t_B}{\Delta t_{max}} \tag{2.16}$$

where $\Delta t_{max}$ is the maximum delay possible. The position $x$ is normalized between $-1, +1$ along the chain. The amplitude of the two outputs signals, neglecting the resistivity of the chain, is the same at both ends.
The delay line approach is widely used in radiation detectors in which the development of the signal is very fast. If the development of the signal is slow and variable from event to event, this introduces an error on the determination of the two arrival times and, consequently, on $x$. This is the case for neutron detectors where the particle track orientation in the gas introduces a large jitter on the signals.
Charge division consists of connecting several wires through resistors or using resistive wires of resistivity $\rho$ (see Figure 2.7). The charge induced in one wire (for the chain) or at certain position along the resistive wire, will split according to the total resistance seen toward the two terminations A and B. The amplitude of the signals at the two outputs ($Q_A$ and $Q_B$ proportional to the charge) is decreased proportionally to the resistance seen from the induction point. The position, normalized between $[0, 1]$, is:

$$x = \frac{Q_A}{Q_A + Q_B} \tag{2.17}$$

where $Q_A + Q_B$ is the total charge induced.
By neglecting any parasite capacitance, the two signals at both ends arrive at the same time.
By using resistive wires we avoid the use of a second wire plane in a MWPC because the two-dimensional information is given by the number of the wire fired and the charge division at its outputs.

A single wire can not be used as a single delay line as for charge division. The propagation velocity of the signal on the wire is of the order of the speed of light, and the delay too short to be of any use.
Johnson noise is inversely proportional to resistance. While in an ideal delay line there is no problem of noise, in a resistive chain its is necessary to increase the gas avalanche gain at which the detector operates in order to increase the signal to noise ratio. For this reason, neutron detectors read-out in charge division are operated at higher gain with respect to the same detector with individual read-out.

### 2.3.2 Dead time

The *dead time* is the minimum amount of time that must separate two events in order that they can be recorded as two separate pulses [6]. It can be limited by the processes in the detector itself or by the associated electronics. Usually the detector is not susceptible of the incoming radiation in a interval of a dead time and the information is then lost.
The read-out system also affects the detector dead-time.
A detector can be characterized by a *paralyzable* or *non-paralyzable* behavior. In a non-paralyzable detector, an event happening during the dead time of the previous event, is simply lost. With an increasing event rate the detector will reach a saturation rate equal to the inverse of the dead time. In a paralyzable detector, an event happening during the dead time will not just be missed, but will restart the dead time. With increasing rate the detector will reach a saturation point where it will be not capable to record any event at all. A semi-paralyzable detector exhibits an intermediate behavior, in which the event arriving during dead time does extend it, but not by the full amount, resulting in a detection rate that decreases when the event rate approaches saturation.

## 2.4 The $^3He$ crisis

### 2.4.1 The $^3He$ shortage

Scintillators, gaseous detectors and semiconductors are the main technologies to detect neutrons. Neutron detection is a key element for applications in homeland security, industry, and science [21]. Other uses are for commercial instruments, dilution refrigerators, for targets or cooling in nuclear research, and for basic research in condensed matter physics [22].
One of the principal thermal neutron converter materials is $^3He$, that has been the main actor for years because of its favorable properties. $^3He$ is a gas with high absorption cross-section and no electronegativity. $^3He$ is an isotope of helium, an inert, nontoxic, nonradioactive gas. Most helium is $^4He$. The natural abundance of $^3He$, as a fraction of all helium, is very small: only about 1.37 parts per million. Rather than rely on natural abundance, one usually manufactures $^3He$ through nuclear decay of tritium (see Equation 2.18), a radioactive isotope of hydrogen. The supply of $^3He$ comes almost entirely from US and Russia. By far the most common source of $^3He$ in the United States is the US nuclear weapons program, of which it is a byproduct. The federal government produces tritium for use in nuclear warheads. Over time, tritium decays into $^3He$ and must be replaced to maintain warhead effectiveness. From the perspective of the weapons program, the extracted $^3He$ is a byproduct of maintaining the purity of the tritium supply. This means that the tritium needs of the nuclear weapons program, not demand for

$^3He$ itself, determine the amount of $^3He$ produced.

$$^3H\ \left(t_{1/2} = 12.3y\right) \quad \rightarrow \quad ^3He + e^- + \bar{\nu_e} \tag{2.18}$$

$^3He$ does not trade in the marketplace as many materials do. It is accumulated in a stockpile from which supplies are either transferred directly to other agencies or sold publicly at auction. Despite declining supply and increasing demand, the auction price of $^3He$ has been relatively steady, at less than 100$ per liter.
Until 2001, $^3He$ production by the nuclear weapons program exceeded the demand, and the program accumulated a stockpile. In the past decade $^3He$ consumption has risen rapidly. After the terrorist attacks of September 11, 2001, the federal government began deploying neutron detectors at the US border to help secure the nation against smuggled nuclear and radiological material. Thus starting in about 2001, and more rapidly since about 2005, the stockpile has been declining. By 2009, the US government and others recognized that ongoing demand would soon exceed the remaining supply.
Nowadays, the world is experiencing a shortage of $^3He$ [21]. US federal officials have testified that the shortage is acute and, unless alternatives are found, will affect federal investments in homeland security, scientific research, and other areas. Scientists have expressed concern that the shortage may threaten certain fields of research.
The $^3He$ stockpile grew from roughly 140000 liters in 1990 to roughly 235000 liters in 2001. Since 2001, however, $^3He$ demand has exceeded production. By 2010, the increased demand had reduced the stockpile to roughly 50000 liters (see Figure 2.8).

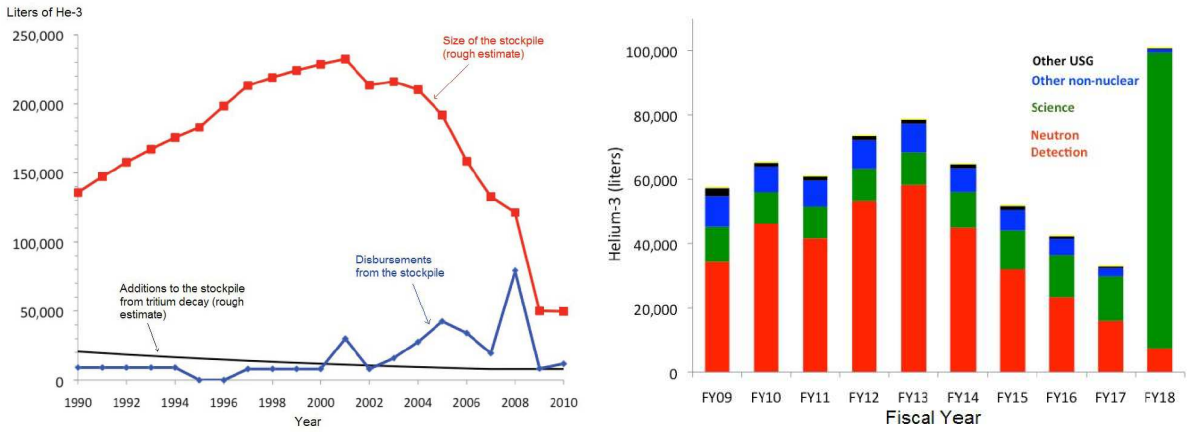


Figure 2.8: Size of the $^3He$ stockpile 1999 - 2010, the size of the stock in red and the demand in blue (left). Projected $^3He$ demand 2009 - 2018 (right). Adapted from [21].

The US weapons program currently produces tritium by irradiating lithium in a light-water nuclear reactor. Before 1988, the program used heavy-water reactors at the DOE Savannah River Site in South Carolina. In 1988, the last operating Savannah River Site reactor, the K reactor, was shut down for safety reasons. For the next several years, reductions in the nuclear weapons stockpile meant that tritium recycling met the weapons programs needs without additional tritium production. Over time, as the tritium produced before 1988 decayed into $^3He$, the total amount of remaining tritium decreased. The annual rate of $^3He$ production from the remaining tritium declined commensurately. The DOE restarted tritium production for the

weapons program in 2003.
Prior to 2001, the demand was approximately 8000 liters per year, which was less than the new supply from tritium decay. After 2001, the demand increased, reaching approximately 80000 liters in 2008. The projections, shown in Figure 2.8, show demand continuing at above the available new supply for at least the next several years. These projections contain many variables and are therefore considerably uncertain.
Given such a large mismatch between supply and demand, users are likely to seek out alternative technologies, reschedule planned projects, and make other changes that reduce demand below what it would be in the absence of a shortage.
One way to address the $^3He$ shortage would be to reduce demand by moving $^3He$ users to alternative technologies. Some technologies appear promising, though implementation would likely present technical challenges. For other applications, alternative technologies may not currently exist. It is unclear whether federal agencies and the private sector can reduce demand sufficiently to match the current $^3He$ supply and still meet priorities for security, science, and other applications.

### 2.4.2 Alternatives to $^3He$ in neutron detection

Because of its detection performance, nontoxicity, and ease of use, $^3He$ has become the material of choice for neutron detection. Nevertheless, other materials also have a long history of use. With the current shortage of $^3He$, researchers are reexamining past alternatives and investigating new ones. Existing alternative neutron detection technologies have significant drawbacks relative to $^3He$, such as toxicity or reduced sensitivity. A drop-in replacement technology does not currently exist. The alternatives with most short-term promise as $^3He$ replacements are boron trifluoride, boron-lined tubes, lithium-loaded glass fibers, and scintillatorcoated plastic fibers. A new scintillating crystal composed of cesium-lithium-yttrium-chloride (CLYC) also appears promising. Other materials, less suitable in the short term, show promise for the long term. Before the $^3He$ shortage became apparent, most neutron detection research was directed toward long-term goals such as improving sensitivity, efficiency, and other capabilities, rather than the short-term goal of matching current capabilities by alternative means. The neutron detectors used for homeland security present both an opportunity and a challenge. The large base of already deployed equipment, if retrofitted with an alternative technology, could be a substantial source of recycled $^3He$ for other uses. At the same time, the scale of planned future deployments presents a potentially large future demand for $^3He$ if suitable alternatives are not identified. For retrofitting, any alternative would need to match the dimensions, power requirements, and other characteristics of the existing technology. For future deployments, especially beyond the near term, some of these requirements might be relaxed or altered. In either case, the large number of systems means that any alternative would need to be relatively inexpensive. In addition, because of how and where the equipment is used, any alternative would need to be rugged, safe, and reliable.
In the last years several efforts have been made to address the $^3He$ shortage. $^{10}B$ technologies have been investigated in gaseous detectors for neutron science [23], [24], [25], [26], [27], [28] and for homeland security applications [29], [30]. $^{10}B$ in solid junction detectors and GEMs as [31], [4] and [32].
In this work, we will concentrate on $^{10}B$ solid converters in gas detectors.

# Chapter 3

# Theory of solid neutron converters

This chapter is born from the collaboration between Patrick Van Esch and me. I want to really thank him for the precious discussion we had on the subject [33].
Here are explained the principles of neutron detection via solid converters and how such detectors have to be optimized.

## 3.1 Introduction

Using powerful simulation software has the advantage of including many effects and potentially results in high accuracy. On the other hand it does not always give the insight an equation can deliver.
The calculations we are going to show originate from the necessity to understand both the Pulse Height Spectra (PHS) given by solid neutron converters employed in thermal neutron detectors as in [23], [27], [29], and from the investigation over such a detectors efficiency optimization.
When a neutron is converted in a gaseous medium, such as $^3He$ detector, the neutron capture reaction fragments ionize directly the gas and the only energy loss is due to the wall effect. As a result, such detectors show a very good $\gamma$-rays to neutron discrimination because $\gamma$-rays release only a small part of their energy in the gas volume and consequently neutron events and $\gamma$-rays events are easily distinguishable on the PHS. Moreover, the detector efficiency is essentially given by the absorption probability.
On the other hand, when dealing with hybrid detectors, as in [23], [34], [35], where the neutron converter is solid and the detection region is gaseous, the efficiency calculation is more complex. Also the $\gamma$-ray to neutron discrimination for such a detector can be an issue [30], [36]. Indeed, once a neutron is absorbed by the solid converter, it gives rise to charged fragments which have to travel across part of the converter layer itself before reaching the gas volume to originate a detectable signal. As a result, those fragments can release only a part of their energy in the gas volume. The neutron PHS can thus have important low energy contributions, therefore $\gamma$-ray and neutron events are not well separated just in energy.
In this chapter we want to give an understanding of the important aspects of the PHS by adopting a simple theoretical model for solid neutron converters. We will show good agreement of the model with the measurements obtained with a $^{10}B$-based detector.
The analytical model can help us to optimize the efficiency for single and multi-layer detector as well as a function of incidence angle as neutron wavelength distribution.
The model we use is the same as implicitly used in many papers such as [4] or [26]. It makes the following simplifying assumptions:

- the tracks of the emitted particles are straight lines emitted back-to-back and distributed isotropically;
- the energy loss is deterministic and given by the Bragg curves without fluctuations;
- the energy deposited is proportional to the charge collected without fluctuations.

We will consider solid neutron converters deposited on an holding substrate. We consider the substrate and the layer indefinitely extended in the plane (no lateral border effects). Referring to Figure 3.1, we talk about a *back-scattering* layer when neutrons are incident from the gas-converter interface and the escaping particles are emitted backwards into the gas volume; we call it a *transmission* layer when neutrons are incident from the substrate-converter interface and the escaping fragments are emitted in the forward direction in the sensitive volume. We consider a neutron to be converted at a certain depth ($x$ for back-scattering or $d-y$ for transmission) in the converter layer and its conversion yields two charged particles emitted back-to-back.
For the moment, we consider perpendicular impact on a layer. We will later see that impact under an angle is easy to implement in the resulting expressions.

We recall that the probability density per unit of depth for a neutron of wavelength $\lambda$ to be absorbed by a converter at depth $x$ is given by:

$$K(x,\lambda) = \Sigma e^{-x\Sigma(\lambda)} \tag{3.1}$$

where $\Sigma(\lambda) = n \cdot \sigma(\lambda)$ is the macroscopic absorption cross-section as already demonstrate in Chapter 1; $n$ is the number density of the material and $\sigma(\lambda)$ the microscopic absorption cross-section (expressed in barn).

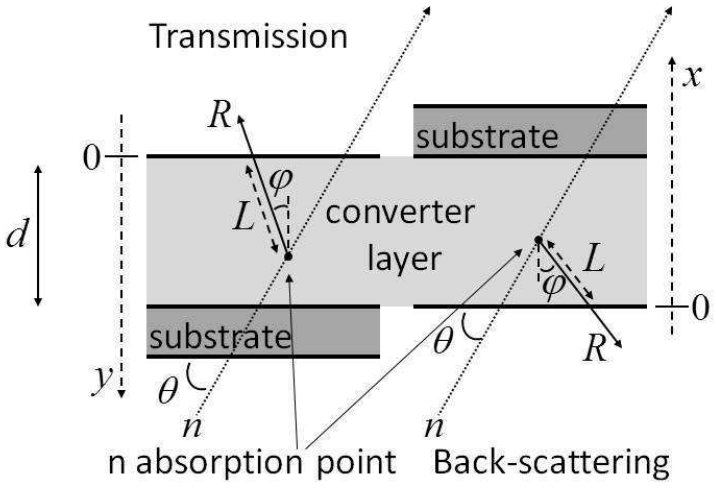


Figure 3.1: Variables definition for a *back-scattering* and *transmission* layer calculations.

Focusing on the back-scattering case in Figure 3.1, where we consider for the moment $\theta = \frac{\pi}{2}$, the neutron absorption coordinate is denoted by $x$, the escape probability for one particle, of range $R$, emitted isotropically at depth $x$, where the neutron is absorbed, is given by:

$$\xi(x) = \begin{cases} \frac{1}{2}\left(1 - \frac{x}{R}\right) & \text{if } x \leq R \\ 0 & \text{if } x > R \end{cases} \tag{3.2}$$

As a matter of fact, the ratio $2\pi \cdot \frac{x}{R} = 2\pi \cdot \cos(\varphi)$ is the solid angle of unity sphere coming out of the layer (see Figure 3.2). There are two particles emitted by the neutron reaction and they are emitted back-to-back. Each time a neutron is absorbed one of the two fragments is lost because of the holding substrate. The escape probability in this case is:

$$\xi(x) = \begin{cases} \frac{1}{2}\left(2 - \frac{x}{R_1} - \frac{x}{R_2}\right) & \text{if } x \leq R_2 < R_1 \\ \frac{1}{2}\left(1 - \frac{x}{R_1}\right) & \text{if } R_2 < x \leq R_1 \\ 0 & \text{if } R_2 < R_1 < x \end{cases} \tag{3.3}$$

where $R_1$ and $R_2$ are the two particle ranges, with $R_2 < R_1$.
Still referring to Figure 3.1, in the case we consider the *Transmission mode* the variable $x$ has to be replaced by $y$, therefore the neutron is absorbed at depth $d - y$.
As already mentioned in Section 1.2 of Chapter 1, since we are interested in particle detection,

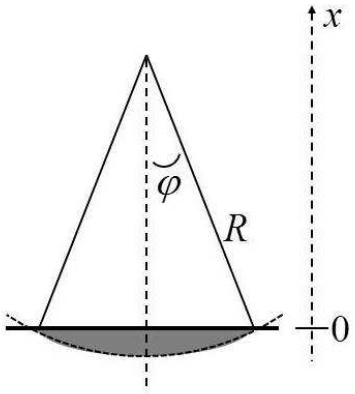


Figure 3.2: Geometric interpretation of Equation 3.2.

the range defined here is the effective range a particle has to travel through a material to still conserve an energy $E_{Th}$ which is the minimum detectable energy. As an example we take the four fragments originated by the neutron capture in $^{10}B$ (see Table 1.70). Their stopping powers and remaining energies $E_{rem}$ (Equation 1.11) are shown in Figure 3.3 [2]; e.g. one of the $^{7}Li$ particles, that carries $1010\,KeV$, presents an *extrapolated range* of about $2\,\mu m$ but if our minimum detectable energy is $E_{Th} = 200\,KeV$ the *effective range* is reduced to about $1.25\,\mu m$.

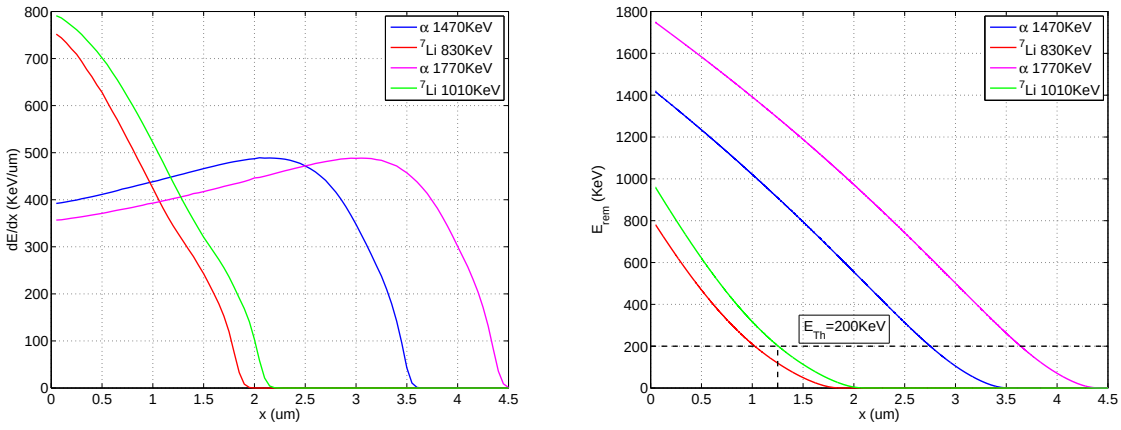


Figure 3.3: Stopping power and remaining energy $E_{rem}$ as a function of the distance traveled $x$ for the four $^{10}B$ neutron capture reaction fragments.

## 3.2 Theoretical efficiency calculation

### 3.2.1 One-particle model

Let's start by considering a neutron interaction with the material that generates one outgoing particle isotropically in $4\pi\,sr$.

Two cases could happen: either the range of the fragment is longer than the thickness of the layer or it is shorter.
In the first case ($d \leq R$) in the back-scattering case the efficiency is given by:

$$\varepsilon_{BS}(d) = \int_0^d dx K(x)\xi(x) = \int_0^d dx \Sigma e^{-x\Sigma}\left(\frac{1}{2} - \frac{x}{2R}\right) = \frac{1}{2}\left(1 - \frac{1}{\Sigma R}\right)\left(1 - e^{-d\Sigma}\right) + \frac{d}{2R}e^{-d\Sigma} \tag{3.4}$$

In the case of transmission:

$$\varepsilon_{T}(d) = \int_0^d dy K(d-y)\xi(y) = \int_0^d dy \Sigma e^{-(d-y)\Sigma}\left(\frac{1}{2} - \frac{y}{2R}\right) = \frac{1}{2}\left(1 + \frac{1}{\Sigma R}\right)\left(1 - e^{-d\Sigma}\right) - \frac{d}{2R} \tag{3.5}$$

In the second case ($d > R$) the back-scattering efficiency is:

$$\varepsilon_{BS}(d) = \int_0^R dx K(x)\xi(x) = \int_0^R dx \Sigma e^{-x\Sigma}\left(\frac{1}{2} - \frac{x}{2R}\right) = \frac{1}{2}\left(1 - \frac{1}{\Sigma R} + \frac{e^{-R\Sigma}}{\Sigma R}\right) \tag{3.6}$$

For transmission:

$$\varepsilon_{T}(d) = \int_0^R dy K(d-y)\xi(y) = \int_0^R dy \Sigma e^{-(d-y)\Sigma}\left(\frac{1}{2} - \frac{y}{2R}\right) = \frac{1}{2\Sigma R}e^{-d\Sigma}\left(e^{+R\Sigma} - R\Sigma - 1\right) \tag{3.7}$$

In Figure 3.4 the efficiencies, at 1.8Å, for the four particles of the $^{10}B$ neutron capture reaction are shown. We took $^{10}B_4C$ of density $\rho = 2.24\,g/cm^3$ for which the four fragments' effective ranges under a threshold of $100\,KeV$ are: $R_{Li(830KeV)} = 1.3\,\mu m$, $R_{\alpha(1470KeV)} = 3\,\mu m$, $R_{Li(1010KeV)} = 1.5\,\mu m$ and $R_{\alpha(1770KeV)} = 3.9\,\mu m$. The single particle efficiency is plotted for a layer in back-scattering mode and for one in transmission. The total efficiency for such a layer is also shown and it is obtained by adding the four particles efficiencies according to the relative branching ratio probability.

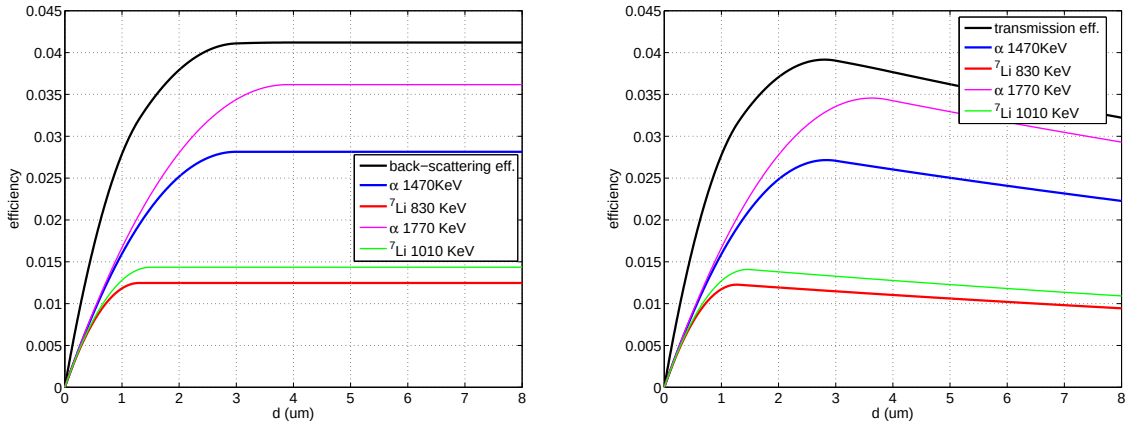


Figure 3.4: Efficiency per particle and for the whole reaction for a single back-scattering layer of $^{10}B_4C$ (left) and for a transmission layer (right). $\Sigma = 0.04\,\mu m^{-1}$ and $100\,KeV$ energy threshold applied.

From Figure 3.4 we can see that the maximum efficiency is attained at different thicknesses for the four fragments, this is due to the difference in the particle effective ranges. The maximum

efficiency position, considering the whole reaction, lays in between the four maxima.
A layer operated in back-scattering mode saturates its efficiency once attained the maximum. This is due to the fact that adding more material to the layer only gives rise to particles that can never escape the converter hence they can not deposit energy in the gas volume. The maximum is reached at the value of the effective range. On the other hand, the material added to a layer in transmission mode starts absorbing neutrons without any particle escaping as in the back-scattering layer but now the actual neutron flux the layer close to the gas volume can experience is diminished, consequently the efficiency drops.
In general, the direction of the incoming neutrons could be non-orthogonal to the converter layer. Referring to Figure 3.1, this angle is indicated by $\theta$ and it is measured starting form the layer surface. All the formulae deduced for the efficiency are still valid under an angle. It is sufficient to replace $\Sigma$ by $\frac{\Sigma}{\sin(\theta)}$. We demonstrate the validity only for the back-scattering case and $d \leq R$ (Equation 3.4). By inclining the layer the effective layer thickness (the path length of the neutron in the layer) will be $\frac{d}{\sin(\theta)}$ and the integration variable $x$ can be modified in the same way to $z = \frac{x}{\sin(\theta)}$. However, in $\xi$, the distance is still the perpendicular distance to the surface, $x = z\,\sin(\theta)$.

$$\begin{aligned}\varepsilon_{BS}(d,\Sigma,\theta) = &\int_0^{d/\sin(\theta)} dz K(z)\xi(z\cdot\sin(\theta)) = \int_0^{d/\sin(\theta)} dz\Sigma e^{-z\Sigma}\left(\frac{1}{2} - \frac{z\sin(\theta)}{2R}\right) = \\ =&\frac{1}{2}\left(1 - \frac{\sin(\theta)}{\Sigma R}\right)\left(1 - e^{-\frac{d\Sigma}{\sin(\theta)}}\right) + \frac{d}{2R}e^{-\frac{d\Sigma}{\sin(\theta)}} = \varepsilon_{BS}\left(d, \frac{\Sigma}{\sin(\theta)}, \theta = 90^\circ\right)\end{aligned} \tag{3.8}$$

Hence:

$$\Sigma \to \frac{\Sigma}{\sin(\theta)} \tag{3.9}$$

This result can be alternatively derived by considering that the absorption distance $x$ under an angle $\theta$ is equivalent to increase it by a factor: $x \to \frac{x}{\sin(\theta)}$.
**Moreover, this result points out that only the parameter $\Sigma$ plays a role in the efficiency determination, indeed the same value of $\Sigma$ can be obtained by changing either the inclination of the layer or the the neutron wavelength or the number density**. Furthermore, in the cold and thermal neutron energy region the microscopic neutron absorption cross-section can be approximated by a linear behavior in $\lambda$, hence:

$$\Sigma(\lambda,\theta) = n\cdot\frac{\sigma(\lambda)}{\sin(\theta)} = n\cdot\sigma_{1A}\cdot\frac{\lambda}{\sin(\theta)} \tag{3.10}$$

where the constant $\sigma_{1A}$ is the linear extrapolation of the neutron absorption cross-section from the value tabulated for 1.8Å. In the case of $^{10}B$: $\sigma_{1A} = \frac{3844}{1.8}[b/\text{Å}]$. As a result the same value for $\Sigma(\lambda,\theta)$, thus the same efficiency, can be obtained, for example, at 10Å under an angle of 80° or equivalently at 5Å under an angle of 30° as shown in Figure 3.5.

### 3.2.2 Two-particle model

Now we consider two fragments emitted back to back. The two particles have two different ranges, and hereafter we consider $R_2 < R_1$ without loss of generality.
For two particles we have three different cases: the layer is thinner than both ranges, it is in

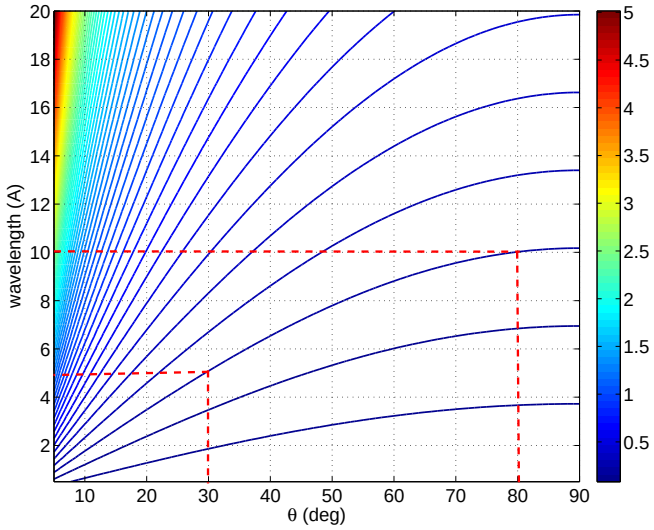


Figure 3.5: Value for the macroscopic neutron cross-section $\Sigma$ (expressed in $\mu m^{-1}$) for $^{10}B_4C$ ($n_{^{10}B} = 1.04 \cdot 10^{23}$ atoms/$cm^3$) as a function of neutron wavelength ($\lambda$) and neutron incidence angle ($\theta$).

between or it is thicker than both of them.
Case $d \leq R_2 < R_1$ for back-scattering:

$$\begin{aligned} \varepsilon_{BS}(d) &= \int_0^d dx K(x)\xi(x) = \int_0^d dx \Sigma e^{-x\Sigma}\left(1 - \frac{x}{2R_1} - \frac{x}{2R_2}\right) = \\ &= \left(1 - \frac{1}{2\Sigma R_1} - \frac{1}{2\Sigma R_2}\right)\left(1 - e^{-d\Sigma}\right) + \left(\frac{1}{2R_1} + \frac{1}{2R_2}\right) d e^{-d\Sigma} \end{aligned} \tag{3.11}$$

For transmission:

$$\begin{aligned} \varepsilon_T(d) &= \int_0^d dy K(d-y)\xi(y) = \int_0^d dy \Sigma e^{-(d-y)\Sigma}\left(1 - \frac{y}{2R_1} - \frac{y}{2R_2}\right) = \\ &= \left(1 + \frac{1}{2\Sigma R_1} + \frac{1}{2\Sigma R_2}\right)\left(1 - e^{-d\Sigma}\right) - \left(\frac{1}{2R_1} + \frac{1}{2R_2}\right) d \end{aligned} \tag{3.12}$$

Case $R_2 < d \leq R_1$ for back-scattering:

$$\begin{aligned} \varepsilon_{BS}(d) &= \int_0^{R_2} dx K(x)\xi(x) + \int_{R_2}^d dx K(x)\xi(x) = \\ &= \int_0^{R_2} dx \Sigma e^{-x\Sigma}\left(1 - \frac{x}{2R_1} - \frac{x}{2R_2}\right) + \int_{R_2}^d dx \Sigma e^{-x\Sigma}\left(\frac{1}{2} - \frac{x}{2R_1}\right) = \\ &= \left(1 - \frac{1}{2\Sigma R_1} - \frac{1}{2\Sigma R_2}\right) + \frac{e^{-R_2\Sigma}}{2R_2\Sigma} - \frac{e^{-d\Sigma}}{2}\left(1 - \frac{1}{R_1\Sigma} - \frac{d}{R_1}\right) \end{aligned} \tag{3.13}$$

For transmission:

$$\begin{aligned}\varepsilon_T(d) &= \int_0^{R_2} dyK(d-y)\xi(y) + \int_{R_2}^{d} dyK(d-y)\xi(y) = \\ &= \int_0^{R_2} dy\Sigma e^{-(d-y)\Sigma}\left(1 - \frac{y}{2R_1} - \frac{y}{2R_2}\right) + \int_{R_2}^{d} dy\Sigma e^{-(d-y)\Sigma}\left(\frac{1}{2} - \frac{y}{2R_1}\right) = \\ &= \frac{e^{(R_2-d)\Sigma}}{2R_2\Sigma} - \left(1 + \frac{1}{2\Sigma R_1} + \frac{1}{2\Sigma R_2}\right)e^{-d\Sigma} + \frac{1}{2}\left(1 + \frac{1}{R_1\Sigma} - \frac{d}{R_1}\right)\end{aligned} \tag{3.14}$$

Case $R_2 < R_1 < d$ for back-scattering:

$$\begin{aligned}\varepsilon_{BS}(d) &= \int_0^{R_2} dxK(x)\xi(x) + \int_{R_2}^{R_1} dxK(x)\xi(x) = \\ &= \int_0^{R_2} dx\Sigma e^{-x\Sigma}\left(1 - \frac{x}{2R_1} - \frac{x}{2R_2}\right) + \int_{R_2}^{R_1} dx\Sigma e^{-x\Sigma}\left(\frac{1}{2} - \frac{x}{2R_1}\right) = \\ &= \left(1 - \frac{1}{2\Sigma R_1} - \frac{1}{2\Sigma R_2}\right) + \frac{e^{-R_2\Sigma}}{2R_2\Sigma} + \frac{e^{-R_1\Sigma}}{2R_1\Sigma}\end{aligned} \tag{3.15}$$

For transmission:

$$\begin{aligned}\varepsilon_T(d) &= \int_0^{R_2} dyK(d-y)\xi(y) + \int_{R_2}^{R_1} duK(d-y)\xi(y) = \\ &= \int_0^{R_2} dy\Sigma e^{-(d-y)\Sigma}\left(1 - \frac{y}{2R_1} - \frac{y}{2R_2}\right) + \int_{R_2}^{R_1} dy\Sigma e^{-(d-y)\Sigma}\left(\frac{1}{2} - \frac{y}{2R_1}\right) = \\ &= e^{-d\Sigma}\left(-1 - \frac{1}{2\Sigma R_1} - \frac{1}{2\Sigma R_2} + \frac{e^{+R_2\Sigma}}{2R_2\Sigma} + \frac{e^{+R_1\Sigma}}{2R_1\Sigma}\right)\end{aligned} \tag{3.16}$$

## 3.3 Double layer

We put a double coated blade in a gas detection volume. A *blade* consists of a substrate holding two converter layers, one in back-scattering mode and one in transmission mode.
Starting from the analytical formulae derived in Section 3.2 and [4] we are going to derive properties that can help to optimize the efficiency in the case of a monochromatic neutron beam and in the case of a distribution of neutron wavelengths. E.g. since the sputtering technique [37] coats each side of each substrate with the same amount of converter material, one can wonder if this is optimal or if there exists a different optimal thickness for each side of the substrate to increase the neutron detection efficiency. The questions are: which are the two coatings thicknesses that maximize the efficiency of the blade for a given set of parameters ($\theta$, $\lambda$, ...)? And in the case the neutron beam is not monochromatic but it is a distribution of wavelength? By denoting with $d_{BS}$ the thickness of the coating for the back-scattering layer and with $d_T$ the transmission layer thickness, the efficiency of a blade is:

$$\varepsilon(d_{BS}, d_T) = \varepsilon_{BS}(d_{BS}) + e^{-\Sigma \cdot d_{BS}} \cdot \varepsilon_T(d_T) \tag{3.17}$$

where $\varepsilon_{BS}(d_{BS})$ and $\varepsilon_T(d_T)$ are the efficiencies for a single coating calculated as shown in Section 3.2. The relation $\nabla\varepsilon(d_{BS}, d_T) = 0$ determines the two optimal layer thicknesses.
In order to keep calculations simple, we consider only two neutron capture fragments yielded by the reaction. This approximation will not affect the meaning of the conclusion. In the case of $^6Li$ Equation 3.17 is exact, for $^{10}B$ the expression 3.17 should ideally be replaced by:

$$\varepsilon(d_{BS}, d_T) = 0.94 \cdot \left(\varepsilon_{BS}^{0.94}(d_{BS}) + e^{-\Sigma \cdot d_{BS}} \cdot \varepsilon_T^{0.94}(d_T)\right) + 0.06 \cdot \left(\varepsilon_{BS}^{0.06}(d_{BS}) + e^{-\Sigma \cdot d_{BS}} \cdot \varepsilon_T^{0.06}(d_T)\right)$$

where $\varepsilon^{0.94}$ means the efficiency calculated for the 94% branching ratio reaction with the right effective particle ranges. We will limit us to the 94% contribution as if it were 100%. As already defined in Section 3.2, $R_1$ and $R_2$, with $(R_2 < R_1)$, are the two ranges of the two neutron capture fragments. Those regions, delimited by the particle ranges, in the $\varepsilon(d_{BS}, d_T)$ plot, are marked by the blue lines in the Figures 3.7 and 3.8. In case of $^{10}B_4C$ ($\rho = 2.24 g/cm^3$), which is the converter used in [23], the two 94% branching ratio reaction particle ranges are $R_1 = 3\,\mu m$ ($\alpha$-particle) and $R_2 = 1.3\,\mu m$ ($^7Li$), when a $100\,KeV$ energy threshold is applied (as defined the minimum detectable energy in [4]). If one would like to use pure $^{10}B$ of density $\rho = 2.17 g/cm^3$, the two 94% branching ratio reaction particle ranges are $R_1 = 3.2\,\mu m$ ($\alpha$-particle) and $R_2 = 1.6\,\mu m$ ($^7Li$), when the same energy threshold is applied. We will take $^{10}B_4C$ as the coating material in our examples.
As $\varepsilon_{BS}(d)$ and $\varepsilon_T(d)$ have different analytical expressions according to whether $d \leq R_2 < R_1$, $R_2 < d \leq R_1$ or $R_2 < R_1 < d$ we need to consider 9 regions to calculate $\nabla\varepsilon(d_{BS}, d_T)$ as shown in Figure 3.6. If we were to include the four different reaction fragments we would have to consider 25 domain partitions (see Figure 3.6). We will see later that the most important regions, concerning the optimization process are the regions *square 11* (where $d_{BS} \leq R_2 < R_1$ and $d_T \leq R_2 < R_1$) and *square 22* (where $R_2 < d_T \leq R_1$, $R_2 < d_{BS} \leq R_1$).
In order to consider a non-orthogonal incidence of neutrons on the layers, it is sufficient to replace $\Sigma$ with $\frac{\Sigma}{\sin(\theta)}$, where $\theta$ is the angle between the neutron beam and the layer surface (see Figure 3.1). This is valid for both the single blade case and for a multi-layer detector. The demonstration was derived in Section 3.2.

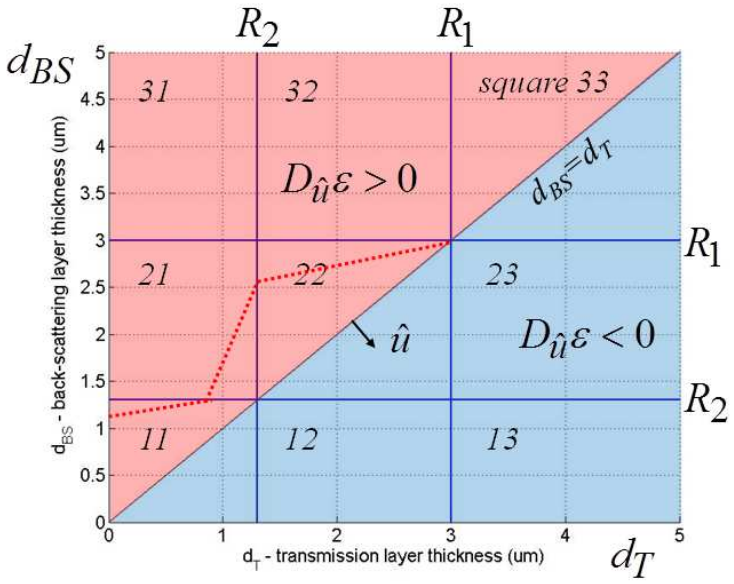


Figure 3.6: Domain for the blade efficiency function. The domain is divided into 9 partitions according to the neutron capture fragments ranges. In red and blue are the domain partition where the efficiency directional derivative along the unity vector $\hat{u}$ is respectively always positive or always negative. The red dotted line represents the case when the substrate effect is not negligible and the maximum efficiency can not be attained on the domain bisector.

### 3.3.1 Monochromatic double layer optimization

In the domain region called *square 11* the efficiency turns out to be:

$$\begin{aligned}\varepsilon_{11}(d_{BS}, d_T) &= \left(1 - \tfrac{1}{2\Sigma R_1} - \tfrac{1}{2\Sigma R_2}\right)\left(1 - e^{-\Sigma d_{BS}}\right) + d_{BS} \cdot \left(\tfrac{1}{2R_1} + \tfrac{1}{2R_2}\right) e^{-\Sigma d_{BS}} + \\ &+ e^{-\Sigma d_{BS}} \left(\left(1 + \tfrac{1}{2\Sigma R_1} + \tfrac{1}{2\Sigma R_2}\right)\left(1 - e^{-\Sigma d_T}\right) - \left(\tfrac{1}{2R_1} + \tfrac{1}{2R_2}\right) d_T\right) = \\ &= A \cdot \left(1 - e^{-\Sigma d_{BS}}\right) + d_{BS} \cdot C \cdot e^{-\Sigma d_{BS}} + e^{-\Sigma d_{BS}} \left(B \cdot \left(1 - e^{-\Sigma d_T}\right) - C \cdot d_T\right)\end{aligned} \tag{3.18}$$

where we have called:

$$\begin{aligned} A &= \left(1 - \frac{1}{2\Sigma R_1} - \frac{1}{2\Sigma R_2}\right) \\ B &= \left(1 + \frac{1}{2\Sigma R_1} + \frac{1}{2\Sigma R_2}\right) \\ C &= \left(\frac{1}{2R_1} + \frac{1}{2R_2}\right) \end{aligned} \tag{3.19}$$

From Equation 3.19, we obtain the useful relations: $\Sigma\,(A - B) = -2C$, $\Sigma A = \Sigma - C$ and $\Sigma B = \Sigma + C$. By calculating $\nabla\varepsilon_{11}(d_{BS}, d_T) = 0$, we obtain the result that $d_{BS} = d_T$ and

$$d_{BS} = d_T = -\frac{1}{\Sigma} \cdot \ln\left(\frac{C}{\Sigma B}\right) \tag{3.20}$$

We repeat the procedure for the *square 22* in which the efficiency is:

$$\begin{aligned}\varepsilon_{22}(d_{BS}, d_T) &= \left(1 - \frac{1}{2\Sigma R_1} - \frac{1}{2\Sigma R_2}\right) + \frac{e^{-\Sigma R_2}}{2\Sigma R_2} - \frac{e^{-\Sigma d_{BS}}}{2} \cdot \left(1 - \frac{1}{\Sigma R_1} - \frac{d_{BS}}{R_1}\right) + e^{-\Sigma d_{BS}} \cdot \\ &\cdot \left(-e^{-\Sigma d_T}\left(1 + \frac{1}{2\Sigma R_1} + \frac{1}{2\Sigma R_2}\right) + \frac{1}{2}\left(1 + \frac{1}{\Sigma R_1} - \frac{d_T}{R_1}\right) + \frac{e^{-\Sigma(d_T - R_2)}}{2\Sigma R_2}\right) = \\ &= A + \frac{e^{-\Sigma R_2}}{2\Sigma R_2} - \frac{e^{-\Sigma d_{BS}}}{2} \cdot \left(1 - \frac{1}{\Sigma R_1} - \frac{d_{BS}}{R_1}\right) + e^{-\Sigma d_{BS}} \cdot \\ &\cdot \left(-B \cdot e^{-\Sigma d_T} + \frac{1}{2}\left(1 + \frac{1}{\Sigma R_1} - \frac{d_T}{R_1}\right) + \frac{e^{-\Sigma(d_T - R_2)}}{2\Sigma R_2}\right)\end{aligned} \tag{3.21}$$

We obtain again $d_{BS} = d_T$ and

$$d_{BS} = d_T = -\frac{1}{\Sigma} \cdot \ln\left(\frac{R_2}{R_1}\left(\frac{1}{2R_2\Sigma B - e^{+\Sigma R_2}}\right)\right) \tag{3.22}$$

Naturally each result of Equations 3.20 and 3.22 is useful only if it gives a value that falls inside the region it has been calculated for.
The points defined by Equations 3.20 and 3.22 define a *maximum* of the efficiency function in the regions either *square 11* or *square 22* because the Hessian matrix in those points has a positive determinant and $\frac{\partial^2 \varepsilon}{\partial d_{BS}^2}$ is negative. It is easy to demonstrate there are no extreme

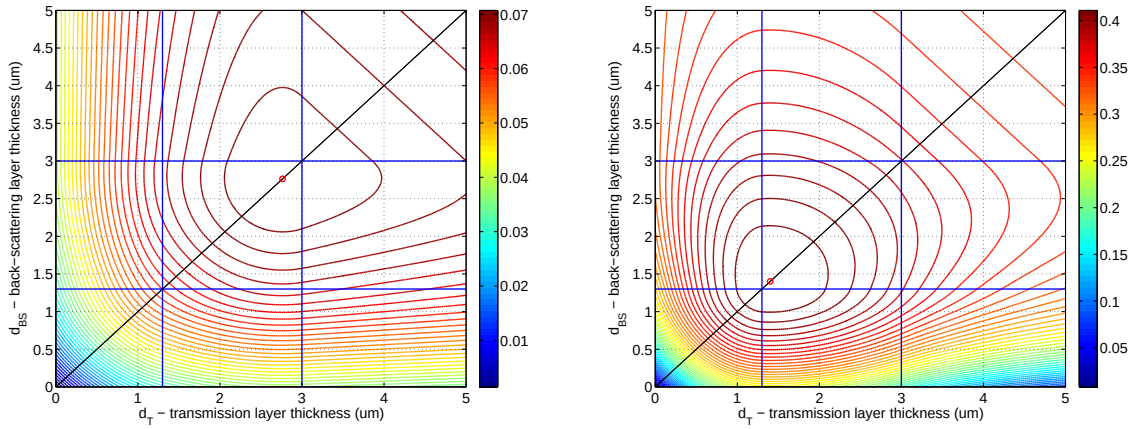


Figure 3.7: Efficiency plot for a double coated substrate with $^{10}B_4C$ at $\theta = 90°$ incidence at 1.8Å (left) and 20Å (right).

points outside the domain regions where either $d_{BS} > R_1$ or $d_T > R_1$, i.e. *square jk* with $j = 3$ or $k = 3$ or both. This outcome is also intuitive. In back-scattering mode when the converter thickness becomes thicker than the longest particle range ($R_1$) there is no gain in efficiency by adding more converter material. In the transmission case, increasing the thickness above $R_1$ will add material that can only absorb neutrons without any particle escaping.
For the cases of *squares 12* and *21*, we obtain that $\nabla\varepsilon(d_{BS}, d_T) = 0$ has no solution; thus the efficiency maximum can never fall in these domain regions.
In Figures 3.7 and 3.8 the efficiency for four different cases are plotted. The red circle identifies the point of maximum efficiency calculated by using Equations 3.20 or 3.22; it stands out immediately that even though the efficiency function is not symmetric relatively to the domain bisector (drawn in black) the maximum nevertheless always lies on it.

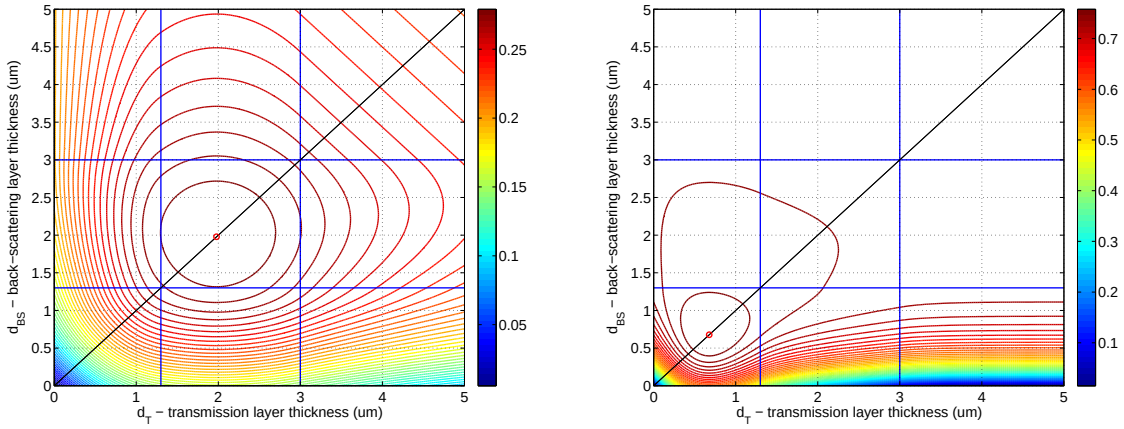


Figure 3.8: Efficiency plot for a double coated substrate with $^{10}B_4C$ at $\theta = 10°$ incidence at 1.8Å (left) and 20Å (right).

**This is a very important result because the sputtering deposition method [37] coats both sides of the substrate with the same thickness of converter material and it is also suited to make optimized blades.**

### 3.3.2 Effect of the substrate

If we consider the neutron loss due to the substrate, the Equation 3.17 has to be modified as follows:

$$\varepsilon(d_{BS}, d_T) = \varepsilon_{BS}(d_{BS}) + e^{-\Sigma_{sub} \cdot d_{sub}} \cdot e^{-\Sigma \cdot d_{BS}} \cdot \varepsilon_T(d_T) = \varepsilon_{BS}(d_{BS}) + \delta(\lambda) \cdot e^{-\Sigma \cdot d_{BS}} \cdot \varepsilon_T(d_T) \quad (3.23)$$

where $\Sigma_{sub}$ and $d_{sub}$ are the macroscopic cross-section and the thickness of the substrate.
If we optimize the layer thicknesses, we find the same result of Equations 3.20 and 3.22 for the transmission layer thickness $d_T$ but, on the other hand, the back-scattering layer thickness does not equal the transmission layer thickness anymore. It becomes:

$$d_{BS} = \begin{cases} \frac{1}{C} \cdot (1-\delta) + \delta \cdot d_T & \text{for } \textit{square 11} \\ R_1 \cdot (1-2\delta) + \delta \cdot \left(1 + \frac{R_1}{R_2}\right) \cdot d_T & \text{for } \textit{square 21} \\ R_1 \cdot (1-\delta) + \delta \cdot d_T & \text{for } \textit{square 22} \end{cases} \quad (3.24)$$

The maximum efficiency can now also lie in *square 21* but not in *square 12*, because $\delta \in [0, 1]$. The dotted line in *squares 11, 21* and *22*, in Figure 3.6, are Equations 3.24. The slope of the line in *squares 11* and *22* is equal to $\delta(\lambda) < 1$. The maximum efficiency, when $\delta(\lambda)$ is different from 1, now lies on the dotted lines right above the optimum without substrate effect.
From Equation 3.24 we can observe that when $\delta$ is close to zero, i.e. the substrate is very opaque to neutrons, the thickness of the back-scattering layer tends to the value $R_1$. On the other hand, when $\delta$ is close to one, $d_{BS}$ tends to $d_T$. The factor $\delta(\lambda)$ is usually very close to one for many

materials that serve as substrate. We define the relative variation between $d_{BS}$ and $d_T$ as:

$$\Delta_d = \left|\frac{d_T - d_{BS}}{d_T}\right| = \begin{cases} \frac{(1-\delta)\cdot\left|d_T - \frac{1}{C}\right|}{d_T} & \text{for } \textit{square 11} \\ \frac{\left|\left(1+\delta+\delta\frac{R_1}{R_2}\right)\cdot d_T - R_1(1-2\delta)\right|}{d_T} & \text{for } \textit{square 21} \\ \frac{(1-\delta)\cdot|d_T - R_1|}{d_T} & \text{for } \textit{square 22} \end{cases} \tag{3.25}$$

Still considering the $^{10}B$ neutron capture reaction for the 94% branching ratio, we list in Table 3.1 the values for $\delta(\lambda)$ and $\Delta_d$ for a $0.5\,mm$ and $3\,mm$ thick Aluminium substrate of density $\rho = 2.7\,g/cm^3$ at 1.8Å. In case the substrate is inclined under an angle of 10° a substrate of $0.5\,mm$ looks like a substrate of about $3\,mm$. We consider a neutron to be lost when it is either scattered or absorbed, therefore, the cross-section used [10] is: $\sigma_{Al} = \sigma_{Al}^{abs}(\lambda) + \sigma_{Al}^{scatt} = 0.2\,b$(at 1.8Å)$+1.5\,b = 1.7\,b$.

| $d_{sub}(mm)$ | $\delta$ (1.8Å) | $\Delta_d$ (1.8Å) |
|---|---|---|
| 0.5 | 0.995 | 0.0004 |
| 3 | 0.970 | 0.0026 |

Table 3.1: Neutron loss factor $\delta$ for an Aluminium substrate and percentage difference between the two coating thicknesses held by the substrate for 1.8Å.

Even though the substrate effect can be neglected in most cases when dealing with a small amount of blades, its effect in a multi-layer detector can strongly differ from the results obtained for the ideal case of completely transparent substrate. A further step is to take its effect into account.

### 3.3.3 Double layer for a distribution of neutron wavelengths

The result of having the same optimal coating thickness for each side of a blade has been demonstrated for monochromatic neutrons. We want to prove it now for a more general case when the neutron beam is a distribution of wavelengths and when the substrate effect can be neglected ($\delta(\lambda) \approx 1$).
We will prove a property that will turn out to be useful. We will show that the directional derivative of $\varepsilon(d_{BS}, d_T)$, when descending along the unit vector $\hat{u} = \frac{1}{\sqrt{2}}(1,-1)$, is positive up to the bisector $d_{BS} = d_T$ and it changes sign only there. This vector identifies the orthogonal direction to the bisector (see Figure 3.6).
In the *square 11*:

$$D_{\hat{u}}\varepsilon(d_{BS}, d_T) = \hat{u} \times \nabla\varepsilon(d_{BS}, d_T) = \frac{C\Sigma}{\sqrt{2}} \cdot e^{-\Sigma d_{BS}}\,(d_{BS} - d_T) \tag{3.26}$$

In the *square 22*:

$$D_{\hat{u}}\varepsilon(d_{BS}, d_T) = \frac{\Sigma}{2\sqrt{2}R_1} \cdot e^{-\Sigma d_{BS}}\,(d_{BS} - d_T) \tag{3.27}$$

which are both positive above the bisector and negative below. In the other domain regions the demonstration is equivalent. E.g. in the *square 12*:

$$D_{\hat{u}}\varepsilon(d_{BS}, d_T) = -\frac{\Sigma}{2\sqrt{2}} \cdot e^{-\Sigma d_{BS}} \left(1 - \frac{d_{BS}}{R_2} - \frac{d_{BS}}{R_1} + \frac{d_T}{R_1}\right) \tag{3.28}$$

which is strictly negative in the *square 12* where $d_{BS} \leq R_2 < R_1$ and $R_2 < d_T \leq R_1$ except on the bisector where $d_{BS} = d_T = R_2$. The following theorem is therefore proved.

**Theorem 3.3.1** *The efficiency function defined by the Equation 3.17 is strictly monotone in the two half-domains identified by the bisector $d_{BS} = d_T$ (see Figure 3.6).*

In a general instrument design one can be interested in having a detector response for a whole range of $\lambda$. An elastic instrument can work a certain time at one wavelength and another time at another wavelength. In a Time-Of-Flight instrument one can be interested in having a sensitivity to neutrons of a certain energy range including or excluding the elastic peak. One can define a normalized weight function $w(\lambda)$, such as $\int_0^{+\infty} w(\lambda)\, d\lambda = 1$, that signifies how much that neutron wavelength is important compared to others. I.e. the price we want to spend in a neutron scattering instrument to be able to detect a neutron energy with respect to an other one. We can also consider an incident beam of neutrons, whose wavelength distribution is $w(\lambda)$, and we want to maximize the efficiency given this distribution.
The efficiency for a blade exposed to a neutron flux which shows this distribution is:

$$\varepsilon_w(d_{BS}, d_T) = \int_0^{+\infty} w(\lambda)\, \varepsilon(d_{BS}, d_T, \lambda)\, d\lambda \tag{3.29}$$

where $\varepsilon(d_{BS}, d_T, \lambda)$ is the efficiency in Equation 3.17.
In order to optimize the efficiency defined by the Equation 3.29, its gradient relative to $d_{BS}$ and $d_T$ has to be calculated:

$$\nabla\varepsilon_w(d_{BS}, d_T) = \nabla \int_0^{+\infty} w(\lambda)\, \varepsilon(d_{BS}, d_T, \lambda)\, d\lambda = \int_0^{+\infty} w(\lambda)\, \nabla\varepsilon(d_{BS}, d_T, \lambda)\, d\lambda \tag{3.30}$$

Both gradient components have to cancel out ($\frac{\partial\varepsilon_w}{\partial d_{BS}} = \frac{\partial\varepsilon_w}{\partial d_T} = 0$), this leads to $D_{\hat{u}}\varepsilon_w = 0$. E.g. in *square 11*: $\int_0^{+\infty} w(\lambda) \left(e^{-\Sigma d_{BS}} (d_T - d_{BS})\, C\Sigma\right) d\lambda = 0$. As a result, in order for the efficiency to attain a maximum, necessarily (but not sufficiently), its directional derivative along the unity vector $\hat{u} = \frac{1}{\sqrt{2}}(1, -1)$:

$$D_{\hat{u}}\varepsilon_w(d_{BS}, d_T) = \int_0^{+\infty} w(\lambda)\, D_{\hat{u}}\varepsilon(d_{BS} = d_T, d_T, \lambda)\, d\lambda \tag{3.31}$$

has to be zero. More explicitly, the condition $\nabla\varepsilon_w = 0$ also implies that $\hat{u} \cdot \nabla\varepsilon_w = D_{\hat{u}}\varepsilon_w = 0$.
For a general family of functions $f(d_{BS}, d_T, \lambda)$ for which the maximum always lies on the domain bisector it is not true that the function defined by their positively weighted linear combination must have the maximum on $d_{BS} = d_T$, because in general $\nabla f(d_{BS}, d_T, \lambda)$ can be positive, null or negative, thus there are many ways to accomplish $\nabla f_w(d_{BS}, d_T) = 0$. However, thanks to Theorem 3.3.1, $D_{\hat{u}}\varepsilon_w = 0$ is satisfied only on the bisector. Below the bisector, $D_{\hat{u}}\varepsilon_w$ is always negative, as it is a positively weighted integral of strictly negative values; similarly, above the bisector, $D_{\hat{u}}\varepsilon_w$ is always positive. The only place where it can be zero, is on the bisector. Hence, the maximum of $\varepsilon_w$ can only be attained on the bisector.
The gradient can hence be replaced by $\frac{\partial}{\partial d_T}$ and the function maximum has to be searched on the bisector, therefore:

$$\nabla\varepsilon_w(d_{BS}, d_T) = \int_0^{+\infty} w(\lambda)\, \frac{\partial}{\partial d_T}\varepsilon(d_{BS} = d_T, d_T, \lambda)\, d\lambda \tag{3.32}$$

**In the end the same layer thickness for both sides of a blade has to be chosen in order to maximize its efficiency, even if it is exposed to neutrons belonging to a general wavelength distribution** $w(\lambda)$.

Equations for the optimal thickness (like in the case of a single wavelength, Equations 3.20 and 3.22) can be obtained from Equation 3.32 once a neutron wavelength distribution has been established. At first $\frac{\partial}{\partial d_T}\varepsilon(d_{BS} = d_T, d_T, \lambda)$ has to be calculated, furthermore it has to be integrated over $d\lambda$ before searching for its solutions.
The integration over $\lambda$ can be alternatively executed in the variable $\Sigma$; indeed $\Sigma$ is just a linear function in $\lambda$ because $\sigma_{abs}$ is proportional to $\lambda$ in the thermal neutron region. Moreover, as indicated previously, $\Sigma$ is also a function of $\theta$ and this is the only appearance of $\theta$ in the efficiency function. **Hence, we can just as well consider a weighting in $\lambda$ and $\theta$ which results in just a weighting function over $\Sigma$.** In other words, all the results that have been derived for a wavelength distribution also hold for an angular distribution or both.

### Flat neutron wavelength distribution example

As a simple example we take a flat distribution between two wavelengths $\lambda_1$ and $\lambda_2$ defined as follows:

$$w(\lambda) = \frac{1}{\lambda_2 - \lambda_1} \tag{3.33}$$

In *square 11* we obtain:

$$\frac{\partial}{\partial d_T}\varepsilon(d_{BS} = d_T, d_T, \lambda) = 2e^{-\Sigma d_T}\left(B\Sigma e^{-\Sigma d_T} - C\right) \tag{3.34}$$

We call $\Sigma_1 = \Sigma(\lambda_1)$ and $\Sigma_2 = \Sigma(\lambda_2)$. We recall that A and B are function of $\Sigma(\lambda)$.

$$\begin{aligned}\nabla\varepsilon_w(d_{BS}, d_T) &= \frac{1}{M(\lambda_2 - \lambda_1)}\int_{\Sigma_1}^{\Sigma_2}\frac{\partial}{\partial d_T}\varepsilon\left(d_{BS} = d_T, d_T, \Sigma\right)\, d\Sigma = \\ &= \frac{1}{(\Sigma_2 - \Sigma_1)}\left[\frac{e^{-2\Sigma d_T}}{d_T}\left(2Ce^{+\Sigma d_T} - C - \Sigma - \frac{1}{2d_T}\right)\right]_{\Sigma_1}^{\Sigma_2} = 0\end{aligned} \tag{3.35}$$

Where the relation $B\Sigma = \Sigma + C$ and $\Sigma(A - B) = -2C$ were used.
In the same way the solution in *square 22* can be determined.

$$\frac{\partial}{\partial d_T}\varepsilon(d_{BS} = d_T, d_T, \lambda) = e^{-\Sigma d_T}\left(e^{-\Sigma d_T}\left(2B\Sigma - \frac{e^{+\Sigma R_2}}{R_2}\right) - \frac{1}{R_1}\right) \tag{3.36}$$

By integrating we finally obtain:

$$\nabla\varepsilon_w(d_{BS}, d_T) = \frac{1}{(\Sigma_2 - \Sigma_1)}\left[\frac{e^{-2\Sigma d_T}}{d_T}\left(\frac{e^{+\Sigma d_T}}{R_1} - C - \Sigma - \frac{1}{2d_T} - \frac{d_T\, e^{+\Sigma R_2}}{R_2\left(R_2 - 2d_T\right)}\right)\right]_{\Sigma_1}^{\Sigma_2} = 0 \tag{3.37}$$

The solution of Equations 3.35 and 3.37 gives the optimum value for the thickness of the two converter layers in the region of the domain called *square 11* and *square 22* respectively for a uniform neutron wavelength distribution between $\lambda_1$ and $\lambda_2$. E.g. for a uniform neutron

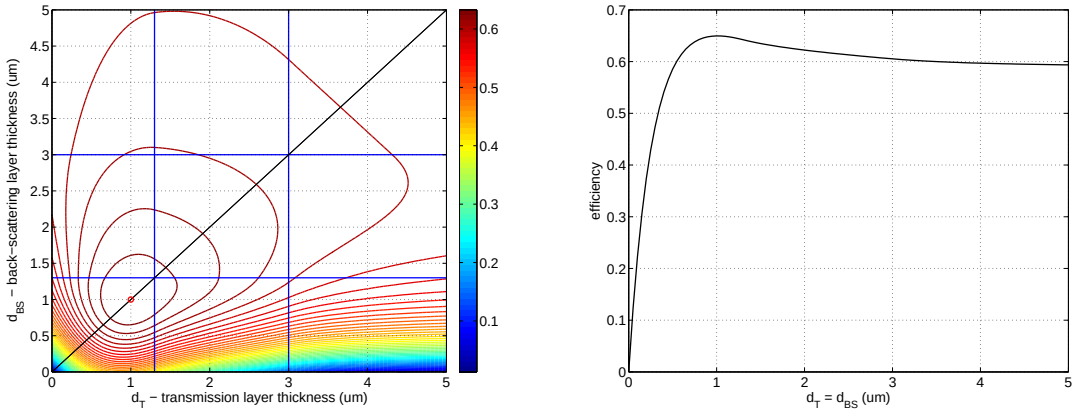


Figure 3.9: Efficiency plot for a double coated substrate with $^{10}B_4C$ at $\theta = 10°$ for a flat distribution of neutron wavelengths between 1Å and 20Å (left). Efficiency on the bisector which attains its maximum at $1\,\mu m$ (right).

wavelength distribution between 1Å and 20Å the optimal thickness of coatings on both sides of the blade inclined at 10° is $1\,\mu m$ (see Figure 3.9).
Note that in Figure 3.9 the asymptotic efficiency for thick layers is not much lower than the optimum at $1\,\mu m$. Thus at an incidence angle of 10° between 1Å and 20Å, a very thick piece of $^{10}B_4C$ is almost as efficient as a double layer.

## 3.4 The multi-layer detector design

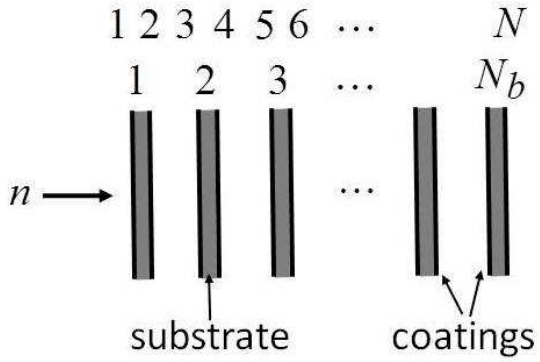


Figure 3.10: A multi-layer detector schematic. $N_b$ blades, holding $N = 2 \cdot N_b$ converters layers, are placed in cascade alternate with detection regions.

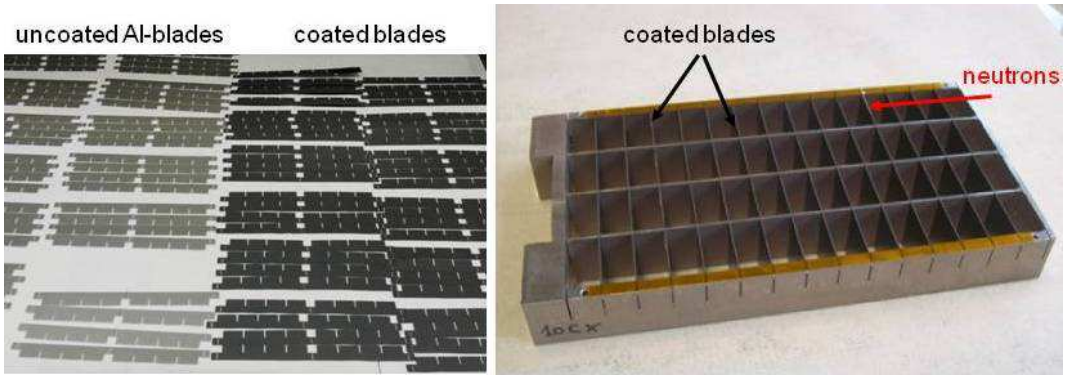


Figure 3.11: The Multi-Grid detector [23]. 15 blades coated with $^{10}B_4C$, are placed in cascade alternate with gaseous detection regions.

In a detector like that presented in [23] (see Figure 3.11), [38], or in [25], all the substrates have the same coating thickness. The actual working principle of the Multi-Grid will be explained in details in Chapter 5.
One can ask if it is possible to optimize the coating thicknesses for each layer individually in order to gain in efficiency. This is also applicable to neutron detectors which use solid converters coupled with GEMs [31].
In Section 3.3 we demonstrated that, for a single substrate holding two converter layers (blade), efficiency is optimized when both layers have the same thickness such as naturally happens with a sputtering technique. In general, this property is not preserved in a multi-layer detector of which we can see the sketch in Figure 3.10. In a multi-layer detector, composed by $N$ layers or $N_b = \frac{N}{2}$ blades, the efficiency can be written as follows:

$$\varepsilon_{tot}(N_b) = \varepsilon_1(d_{BS1}, d_{T1}) + \sum_{k=2}^{N_b} \varepsilon_1(d_{BSk}, d_{Tk}) \cdot e^{-\left(\sum_{j=1}^{(k-1)}(d_{BSj}+d_{Tj})\right)\cdot\Sigma} \tag{3.38}$$

Where $\varepsilon_1(d_{BSk}, d_{Tk})$ represents the efficiency for a single blade already defined by the Equation 3.17; $d_{BSk}$ and $d_{Tk}$ are the coating thicknesses of the $k-th$ blade.
If the detector is assembled with blades with all coatings of the same thickness, i.e. $d_{BSk} = d_{Tk} = d,\ \forall k = 1, 2, \ldots, N_b$, Equation 3.38 can be simplified as follows:

$$\varepsilon_{tot}(N_b) = \varepsilon_1(d) + \sum_{k=2}^{N_b} \varepsilon_1(d) \cdot e^{-2\left(\sum_{j=1}^{(k-1)} d\right)\cdot\Sigma} = \varepsilon_1(d) \cdot \sum_{k=1}^{N_b} e^{-2(k-1)d\cdot\Sigma} = \varepsilon_1(d) \cdot \frac{1 - e^{-2d\Sigma N_b}}{1 - e^{-2d\Sigma}} \quad (3.39)$$

Therefore, $\frac{d\varepsilon_{tot}}{dd} = 0$ optimizes the efficiency for one single neutron wavelength for a detector containing blades of same coating thicknesses:

$$\frac{d\varepsilon_{tot}}{dd} = \frac{\varepsilon_1(d) \cdot 2\Sigma}{\left(1 - e^{-2d\Sigma}\right)^2} \left( N e^{-2d\Sigma N_b} - e^{-2d\Sigma} - (1 - N_b)\, e^{-2d\Sigma(N_b+1)} \right) + \frac{d\varepsilon_1}{dd} \cdot \frac{1 - e^{-2d\Sigma N_b}}{1 - e^{-2d\Sigma}} = 0 \quad (3.40)$$

where $\varepsilon_1(d)$ and $\frac{d\varepsilon_1}{dd}$ are expressed in Equations 3.18 and 3.21 where we impose $d_{BS} = d_T = d$ and Equations 3.34 and 3.36 respectively if we are calculating in the *Square 11* or *Square 22*.
From Equation 3.40, we notice that the maximum efficiency for a multi-layer detector made up of identical coating thickness blades, depends explicitly on $N_b$. This means that the optimal coating thickness for a multi-layer detector depends on how many blades it is composed of.

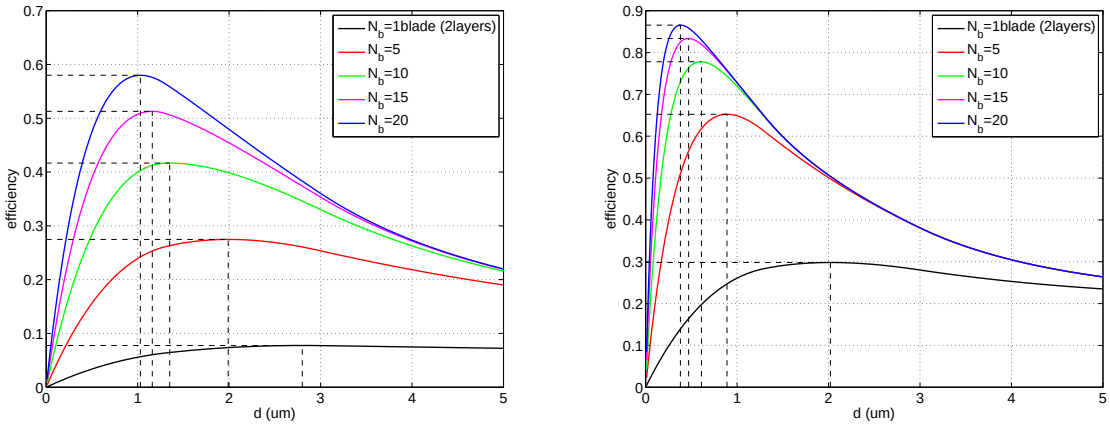


Figure 3.12: Multi-layer detectors containing blades of same coating thickness optimized for 1.8Å (left) and for 10Å (right).

Figure 3.12 shows the optimization of several multi-layer detectors containing 1, 5, 10, 15, 20 blades, done for both 1.8Å and for 10Å. Note that the longer the neutron wavelength, the thinner is the thickness of the layers has to be chosen.
In Figure 3.13 the efficiencies and the coating thicknesses, given for each blade, of the five multi-layer detectors already described are plotted as a function of the neutron wavelength. There, each detector is optimized for each neutron wavelength and consequently the coating thickness changes with $\lambda$. The values at 1.8Å and at 10Å correspond to the maxima already shown in Figure 3.12.
We consider now a neutron wavelength distribution defined by $w(\lambda)$ (with $\int_0^{+\infty} w(\lambda)\, d\lambda = 1$)

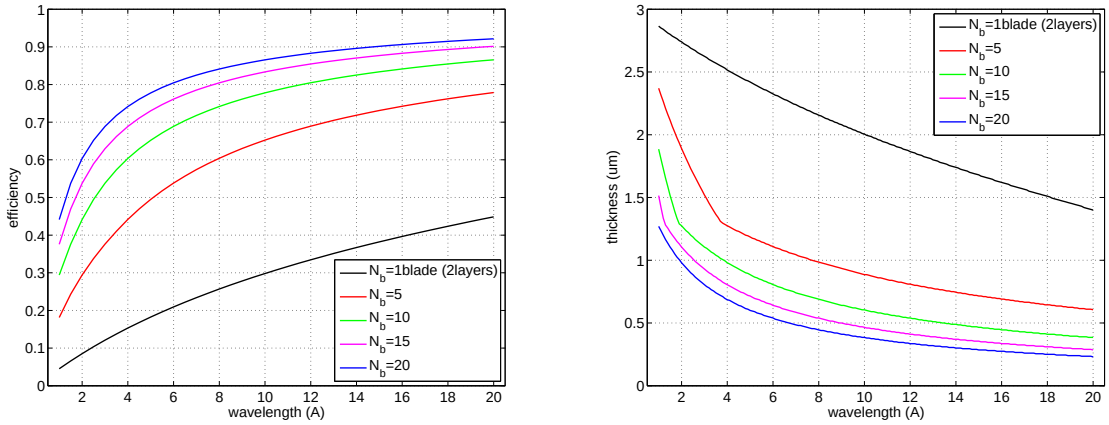


Figure 3.13: Efficiency (left) and optimal thickness of the identical blades (right) as a function of neutron wavelength for a 2, 10, 20, 30 and 40 layers multi-layer detector. Solid lines indicate the optimized efficiency, for each wavelength, for a detector made up for blades of identical thicknesses.

as in Section 3.3.3 for a single blade. In this case the efficiency for such a detector can be written as follows:

$$\varepsilon_{tot}^{w}(N_b, d) = \int_0^{+\infty} w\left(\lambda\right) \varepsilon_{tot}(N_b, \lambda)\, d\lambda = \int_0^{+\infty} w\left(\lambda\right) \varepsilon_1(d, \lambda) \cdot \frac{1 - e^{-2d\Sigma(\lambda)N_b}}{1 - e^{-2d\Sigma(\lambda)}}\, d\lambda \tag{3.41}$$

where $\varepsilon_1(d, \lambda)$ is Equation 3.18. We considered the optimal efficiency of a multi-layer detector with all-identical layer thicknesses. If we relax this constraint (that is, if we allow different layers to have different thicknesses) we can in principle achieve still higher efficiencies.

If individual layer thicknesses have to be optimized for the maximum efficiency for a multi-layer detector, the approach to follow is different if we want to optimize for a single neutron wavelength or for a wavelength distribution. Indeed, for a single lambda, we can start by optimizing the last layer and, hereafter, we go backward up to the first layer. If the wavelength if fixed, we are requiring the layer we are considering to be at its maximum efficiency. On the other hand, if we deal with a distribution of lambda, the previous layers to the one we are optimizing will change the distribution it is receiving. Hence the optimization process has to take into account the whole detector at once. The Multi-Grid detector optimization for a given wavelength and for a distribution will be elucidated.

### 3.4.1 Monochromatic multi-layer detector optimization

As already mentioned the way to optimize the layers in multi-layer detector for a given neutron wavelength is to maximize the last layer efficiency for this wavelength. Once that is done, we can go backward until the first layer. Each time we find the optimal thickness of a layer we fix it and we move on to optimize the previous one.

By expanding Equation 3.38 we obtain:

$$\begin{aligned}\varepsilon_{tot}(N_b) &= \varepsilon_1(d_{BS1}, d_{T1}) + e^{-(d_{BS1}+d_{T1})\Sigma} \cdot \varepsilon_1(d_{BS2}, d_{T2}) + \\ &+ e^{-(d_{BS1}+d_{T1})\Sigma} \cdot e^{-(d_{BS2}+d_{T2})\Sigma} \cdot \varepsilon_1(d_{BS3}, d_{T3}) + \dots \\ &\dots + e^{-(d_{BS1}+d_{T1})\Sigma} \cdot e^{-(d_{BS2}+d_{T2})\Sigma} \cdot \dots \cdot e^{-(d_{BS(N_b-1)}+d_{T(N_b-1)})\Sigma} \cdot \varepsilon_1(d_{BSN_b}, d_{TN_b}) = \\ &= \varepsilon_1(d_{BS1}, d_{T1}) + e^{-(d_{BS1}+d_{T1})\Sigma} \cdot \Big[\varepsilon_1(d_{BS2}, d_{T2}) + e^{-(d_{BS2}+d_{T2})\Sigma} \cdot \\ &\cdot \Big[\varepsilon_1(d_{BS3}, d_{T3}) + e^{-(d_{BS3}+d_{T3})\Sigma} \cdot \dots \cdot \Big[\dots \cdot \Big[\varepsilon_1(d_{BS(N_b-1)}, d_{T(N_b-1)}) + \\ &+ e^{-(d_{BS(N_b-1)}+d_{T(N_b-1)})\Sigma} \cdot \varepsilon_1(d_{BSN_b}, d_{TN_b})\Big] \dots \Big]\Big]\Big]\end{aligned} \tag{3.42}$$

Note that the variable $d_{N_b}$ appears only once, in the efficiency function $\varepsilon_1(d_{BSN_b}, d_{TN_b})$. In the case of a single wavelength, its optimal value can be determined without taking the other layers into account. We can optimize the detector starting from the last blade and going backward till the first. Any change on the previous blades will only affect the *number* of neutrons that reach the last blade, and we require the last blade to be as efficient as possible for that kind of neutron. As the layer thickness optimum of each blade does not depend on the previous ones, the system of equations is triangular.
This will be not true for the wavelength distribution case and it will be clarified in Section 3.4.3. Intuitively, for a distribution, the gradient of Equation 3.42 is in addition integrated over $\lambda$, thus all the blades have to be taken into account simultaneously in the optimization process.
Looking carefully into the Equation 3.42, we can see that the optimization process involves each time a function of structure:

$$f_k = \begin{cases} \varepsilon_1(d_{BSk}, d_{Tk}) + e^{-(d_{BSk}+d_{Tk})\Sigma} \cdot \alpha_{k+1} & \text{if } k < N_b \\ \varepsilon_1(d_{BSk}, d_{Tk}) & \text{if } k = N_b \end{cases} \tag{3.43}$$

In fact, if the $k-th$ layer it is going to be optimized, all the following layers up to $N = 2 \cdot N_b$ have been already optimized, hence $\alpha_{k+1}$ is a fixed number and represents the cumulative efficiency of the detector from the blade $(k+1)-th$ to the end. As a result, the optimization is an iterative process where a function like 3.43 has to be optimized each time, taking into account that $\alpha_{k+1}$ is always a fixed number and not a function of the thicknesses to be determined, because their optimal values have been already found.
The two gradient components of Equation 3.43 are:

$$\frac{\partial f_k}{\partial d_{BSk}} = \begin{cases} \frac{\partial}{\partial d_{BSk}}\varepsilon_1(d_{BSk}, d_{Tk}) - \Sigma\, e^{-(d_{BSk}+d_{Tk})\Sigma} \cdot \alpha_{k+1} & \text{if } k < N_b \\ \frac{\partial}{\partial d_{BSk}}\varepsilon_1(d_{BSk}, d_{Tk}) & \text{if } k = N_b \end{cases} \tag{3.44}$$

$$\frac{\partial f_k}{\partial d_{Tk}} = \begin{cases} \frac{\partial}{\partial d_{Tk}}\varepsilon_1(d_{BSk}, d_{Tk}) - \Sigma\, e^{-(d_{BSk}+d_{Tk})\Sigma} \cdot \alpha_{k+1} & \text{if } k < N_b \\ \frac{\partial}{\partial d_{Tk}}\varepsilon_1(d_{BSk}, d_{Tk}) & \text{if } k = N_b \end{cases} \tag{3.45}$$

Note that the only difference between Equation 3.44 and Equation 3.45 is the partial derivative variable.
Thus, the condition $\nabla f_k = 0$ turns out to be:

$$\begin{cases} \frac{\partial}{\partial d_{BSk}}\varepsilon_1(d_{BSk}, d_{Tk}) = \frac{\partial}{\partial d_{Tk}}\varepsilon_1(d_{BSk}, d_{Tk}) \Rightarrow D_{\hat{u}}\varepsilon_1(d_{BSk}, d_{Tk}) = 0 & \text{if } k < N_b \\ \frac{\partial}{\partial d_{BSk}}\varepsilon_1(d_{BSk}, d_{Tk}) = \frac{\partial}{\partial d_{Tk}}\varepsilon_1(d_{BSk}, d_{Tk}) = 0 & \text{if } k = N_b \end{cases} \tag{3.46}$$

The condition in Equation 3.46 is exactly what was demonstrated in Section 3.3. The Theorem 3.3.1 implies that the directional derivative along the unity vector $\hat{u} = \frac{1}{\sqrt{2}}(1,-1)$ of the function $\varepsilon_1(d_{BSk}, d_{Tk})$ can only be zero on the bisector domain, in the case of $k < N_b$. Hence, the maximum efficiency can only be found, again, on the domain bisector. On the other hand, in the case of $k = N_b$ the Equation 3.46 requires the gradient of the efficiency function to be zero, property which was also demonstrated in Section 3.3 (Equations 3.20 and 3.22) for these kind of functions.

**As a result, even in a Multi-Grid like detector, that is optimized for a given neutron wavelength with variable layer thicknesses, it turns out that all the blades have to hold two layers of the same thickness. On the other hand, thicknesses of different blades can be distinct.**

Thanks to the latter derived property, we can denote with $d_k$ the common thickness of the two layers held by the $k-th$ blade ($d_{BSk} = d_{Tk} = d_k$). The detector efficiency function can be redraft as follows:

$$\begin{aligned}
\varepsilon_{tot}(N, \bar{d}) &= \varepsilon_1(d_1) + e^{-2d_1\Sigma} \cdot \varepsilon_1(d_2) + e^{-2d_1\Sigma} \cdot e^{-2d_2\Sigma} \cdot \varepsilon_1(d_3) + \dots \\
&\quad \cdots + e^{-2d_1\Sigma} \cdot e^{-2d_2\Sigma} \cdot \dots \cdot e^{-2d_{N_b-1}\Sigma} \cdot \varepsilon_1(d_{N_b}) = \\
&= \varepsilon_1(d_1) + e^{-2d_1\Sigma} \cdot \Big[\varepsilon_1(d_2) + e^{-2d_2\Sigma} \cdot \Big[\varepsilon_1(d_3) + e^{-2d_3\Sigma} \cdot \dots \\
&\quad \cdots \Big[\varepsilon_1(d_{(N_b-1)}) + e^{-2d_{(N_b-1)}\Sigma} \cdot \varepsilon_1(d_{N_b})\Big] \dots \Big]\Big] = \\
&= \varepsilon_1(d_1) + \sum_{k=2}^{N_b} \varepsilon_1(d_k) \cdot e^{-2\left(\sum_{j=1}^{(k-1)} d_j\right)\cdot\Sigma}
\end{aligned} \tag{3.47}$$

where $\bar{d}$ is the vector of components $d_k$ for $k = 1, 2, \dots, N_b$. The condition $\nabla f_k = 0$ can be simplified by searching for the maximum on the domain bisector, thus Equations 3.44 and 3.45 turns into:

$$\frac{df_k}{dd_k} = \left\{ \begin{array}{ll} \frac{d}{dd_k}\varepsilon_1(d_k) - 2\Sigma\, e^{-2d_k\Sigma} \cdot \alpha_{k+1} & \text{if } k < N_b \\ \frac{d}{dd_k}\varepsilon_1(d_k) & \text{if } k = N_b \end{array} \right\} = 0 \tag{3.48}$$

We recognize into the expression $\frac{d}{dd_k}\varepsilon_1(d_k)$ the derivative in Equations 3.34 and 3.36 that have already been calculated according to the region domain in Section 3.3. In the domain region called *square 11* as defined in Section 3.3, we obtain:

$$\frac{df_k}{dd_k} = \begin{cases} 2e^{-\Sigma d_k}\left(\left(B - \alpha_{k+1}\right)\Sigma e^{-\Sigma d_k} - C\right) & \text{if } k < N_b \\ 2e^{-\Sigma d_k}\left(B\Sigma e^{-\Sigma d_k} - C\right) & \text{if } k = N_b \end{cases} \tag{3.49}$$

And in the *square 22*:

$$\frac{df_k}{dd_k} = \begin{cases} e^{-\Sigma d_k}\left(e^{-\Sigma d_k}\left(2\left(B - \alpha_{k+1}\right)\Sigma - \frac{e^{+\Sigma R_2}}{R_2}\right) - \frac{1}{R_1}\right) & \text{if } k < N_b \\ e^{-\Sigma d_k}\left(e^{-\Sigma d_k}\left(2B\Sigma - \frac{e^{+\Sigma R_2}}{R_2}\right) - \frac{1}{R_1}\right) & \text{if } k = N_b \end{cases} \tag{3.50}$$

Where we recall $B = \left(1 + \frac{1}{2\Sigma R_1} + \frac{1}{2\Sigma R_2}\right)$ and $C = \left(\frac{1}{2R_1} + \frac{1}{2R_2}\right)$.
Equations 3.49 and 3.50 have solutions similar to Equations 3.20 and 3.22 apart from the fact

that they are a recursive form with $\alpha_{k+1}$. In the *square 11* the solution is:

$$d_k^{opt} = \begin{cases} -\frac{1}{\Sigma} \cdot \ln\left(\frac{C}{(B-\alpha_{k+1})\Sigma}\right) & \text{if } k < N_b \\ -\frac{1}{\Sigma} \cdot \ln\left(\frac{C}{B\Sigma}\right) & \text{if } k = N_b \end{cases} \tag{3.51}$$

In the *square 22*:

$$d_k^{opt} = \begin{cases} -\frac{1}{\Sigma} \cdot \ln\left(\frac{R_2}{R_1}\left(\frac{1}{2R_2\Sigma(B-\alpha_{k+1})-e^{+\Sigma R_2}}\right)\right) & \text{if } k < N_b \\ -\frac{1}{\Sigma} \cdot \ln\left(\frac{R_2}{R_1}\left(\frac{1}{2R_2\Sigma B-e^{+\Sigma R_2}}\right)\right) & \text{if } k = N_b \end{cases} \tag{3.52}$$

As already mentioned in Section 3.3, these solutions are valid if the result they return is included in the domain region they are defined on.
The optimization method is a recursive procedure that employs the Equations 3.51 and 3.52; we start from the last blade, and we find its optimal thickness $d_{N_b}^{opt}$, then we calculate $\alpha_{N_b}$ as the last layer efficiency using the optimal thickness found. Now we can calculate $d_{N_b-1}^{opt}$ from Equations 3.51 or 3.52 and $\alpha_{N_b-1}$ and so on until the first layer. By definition $\alpha_{k+1}$ is the detector cumulative efficiency starting from the $k+1$ blade to the end ($N_b$); hence:

$$\alpha_{k+1} = \begin{cases} \varepsilon_1(d_{k+1}) + e^{-2d_{k+1}\Sigma} \cdot \varepsilon_1(d_{k+2}) + e^{-2d_{k+1}\Sigma} \cdot e^{-2d_{k+2}\Sigma} \cdot \varepsilon_1(d_{k+3}) + \dots \\ \dots + e^{-2d_{k+1}\Sigma} \cdot e^{-2d_{k+2}\Sigma} \cdot \dots \cdot e^{-2d_{N_b-1}\Sigma} \cdot \varepsilon_1(d_{N_b}) = \\ = \varepsilon_1(d_{k+1}^{opt}) + \sum_{i=k+2}^{N_b} \varepsilon_1(d_i^{opt}) \cdot e^{-2\left(\sum_{j=k+1}^{(i-1)} d_j^{opt}\right)\cdot\Sigma} & \text{if } k+1 < N_b \\ \varepsilon_1(d_{k+1}^{opt}) & \text{if } k+1 = N_b \end{cases} \tag{3.53}$$

**Example of application**

We analyze a detector composed of 30 successive converter layers (15 blades) crossed by the neutron beam at 90° (like in Figure 3.10). We consider $^{10}B_4C$ ($\rho = 2.24\, g/cm^3$) as converter; we neglect again the 6% branching ratio of the $^{10}B$ neutron capture reaction. A $100\, KeV$ energy threshold is applied and the effective particle range turns out to be $R_1 = 3\,\mu m$ ($\alpha$-particle) and $R_2 = 1.3\,\mu m$ ($^7Li$), for the 94% branching ratio, which we take to be 100%.
Figures 3.14 and 3.15 show the optimization result for this multi-layer detector; for a monochromatic neutron beam of 1.8Å and 10Å. On the left, the optimal thickness given by either Equations 3.51 or 3.52 is plotted in red for each blade; for comparison we use two similar detectors suitable for short and for long wavelengths in which the blades are holding $1.2\,\mu m$ and $0.5\,\mu m$ thick coatings. Those values have been obtained by optimizing the Equation 3.39, the efficiency for a detector holding 15 blades of all equal thicknesses for 1.8Å and for 10Å. The detector with $1.2\,\mu m$ coatings is very close to the one presented in [23]. On the right, in Figures 3.14 and 3.15, the efficiency contribution of each blade is plotted, again for an optimized detector for 1.8Å and for an optimization done for 10Å. The expression of the efficiency as a function of the detector depth is given by Equation 3.47 for each blade by fixing the index $k$.
The whole detector efficiency is given in the end by summing all the blades' contributions. The whole detector efficiency is displayed in Table 3.2 for the detector of Figures 3.14 and 3.15. By optimizing the detector for a given neutron wavelength we gain only about 2% efficiency which is equivalent to add a few more layers to the detectors optimized to hold identical blades.

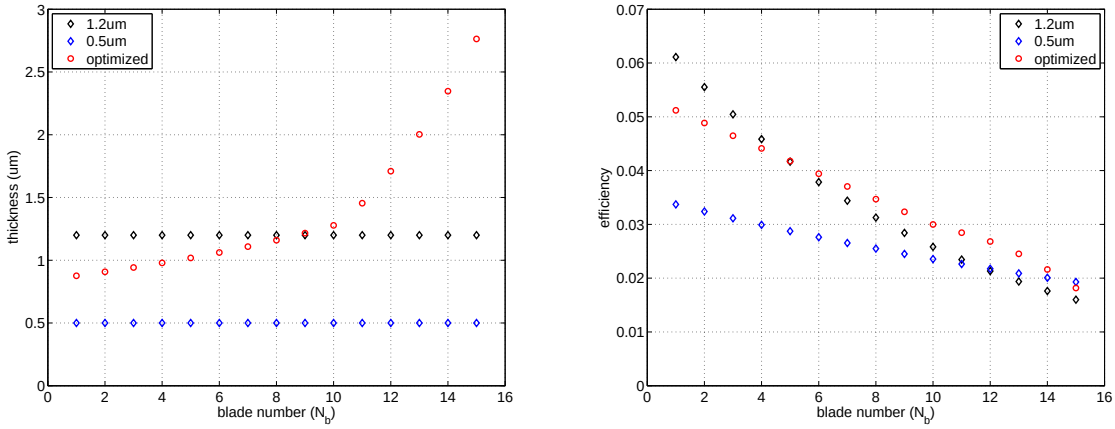


Figure 3.14: Thicknesses of the blades coatings (left) and their efficiency contribution (right), for a detector made up of 15 identical coating thickness blades of $1.2\,\mu m$, $0.5\,\mu m$ and for a detector optimized for 1.8Å.

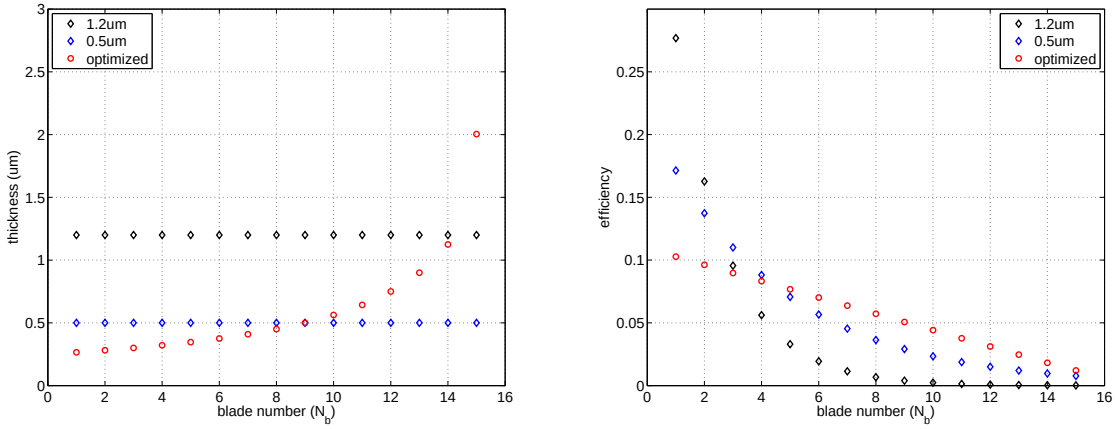


Figure 3.15: Thicknesses of the blades coatings (left) and their efficiency contribution (right), for a detector made up of 15 identical coating thickness blades of $1.2\,\mu m$, $0.5\,\mu m$ and for a detector optimized for 10Å.

| wavelength (Å) | opt. detect. | $0.5\,\mu m$ detect. | $1.2\,\mu m$ detect. |
|---|---|---|---|
| 1.8 | 0.525 | 0.388 | 0.510 |
| 10 | 0.858 | 0.831 | 0.671 |

Table 3.2: Efficiency for an optimized multi-layer detector and for a detector which contains 15 identical blades of $1.2\,\mu m$ and $0.5\,\mu m$.

In Figure 3.16 is shown the efficiency resulting from the monochromatic optimization process of the individual blade coatings and the optimization for a detector containing all identical blades (which thicknesses are shown on the right for each neutron wavelength), as already shown in Figure 3.12. Neutrons hit the layers at 90° and five cases have been taken into account with an increasing number of layers. We notice that about for all neutron wavelengths the gain in optimizing the detector with different blades, let us to gain few percent in efficiency. The values

in Table 3.2 are the values on the pink solid curve and the dashed one at 1.8Å and at 10Å in Figure 3.16.

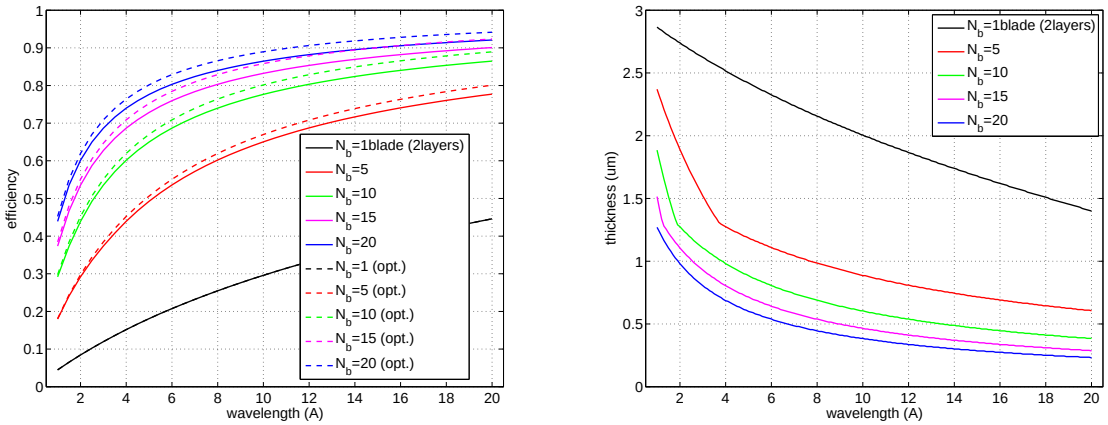


Figure 3.16: Efficiency (left) and optimal thickness of the identical blades (right) as a function of neutron wavelength for a 2, 10, 20, 30 and 40 layers multi-layer detector. Solid lines indicate the optimized efficiency, for each wavelength, for a detector made up for blades of identical thicknesses; the dashed one indicate the monochromatic optimization using different thicknesses inside the detector.

Still referring to Figure 3.16, we notice that a detector with 15 individually optimized blades (30 layers) has about the same efficiency (above 10Å) as a detector optimized to contain 20 blades (40 layers) of equal thickness. On the other hand for short wavelengths the difference is not very significant. Moreover, there is also a trade off between the constraints of the detector construction and the complexity of the blade production.

### 3.4.2 Effect of the substrate in a multi-layer detector

We are going to add the substrate effect in a multi-layer detector; as we have already treated the case for the single blade in Section 3.3.2. For simplicity we neglect the deviation from the rule $d_{BS} = d_T$ due to the substrate for each single blade. Hence we can start from Equation 3.47, where each blade has the same coating thickness for its back-scattering and transmission layer. The latter in the presence of the substrate becomes:

$$\varepsilon_{tot}^{sub}(N, \bar{d}) = \varepsilon_1^{sub}(d_1) + \sum_{k=2}^{N_b} \varepsilon_1^{sub}(d_k) \cdot e^{-(k-1)d_{sub}\cdot\Sigma_{sub}} \cdot e^{-2\left(\sum_{j=1}^{(k-1)} d_j\right)\cdot\Sigma} \tag{3.54}$$

where $\varepsilon_1^{sub}(d)$ is given by Equation 3.23. In the case of a detector made up of identical coating thickness blades we wrote the efficiency as shown in Equation 3.39 and considering the substrate it becomes:

$$\varepsilon_{tot}^{sub}(N_b) = \varepsilon_1^{sub}(d) \cdot \sum_{k=1}^{N_b} e^{-(k-1)d_{sub}\cdot\Sigma_{sub}} e^{-2(k-1)d\cdot\Sigma} = \varepsilon_1^{sub}(d) \cdot \frac{1 - e^{-(2d\Sigma + d_{sub}\Sigma_{sub})N_b}}{1 - e^{-(2d\Sigma + d_{sub}\Sigma_{sub})}} \tag{3.55}$$

where, again, $\varepsilon_1^{sub}(d)$ is given by Equation 3.23.
As an example we take an Aluminium substrate (density $\rho = 2.7\, g/cm^3$) of $0.5\, mm$ for each

blade. We consider a neutron to be lost when it is either scattered or absorbed, therefore, the cross-section used is: $\sigma_{Al} = \sigma_{Al}^{abs}(\lambda) + \sigma_{Al}^{scatt} = 0.2\,b(\text{at } 1.8\text{Å}) + 1.5\,b = 1.7\,b$. Absorption cross-sections at others neutron wavelengths have been extrapolated linearly in $\lambda$.
Figure 3.17 shows the five detector taken as example in Figure 3.16 when the detectors are made up for blades of identical thicknesses considering or not the substrate effect. The optimization is made for each neutron wavelength separately. Solid lines represent are the same as in Figure 3.16, dashed-dotted lines are made for the monochromatic optimization considering the substrate, i.e. optimizing Equation 3.55. On the right in Figure 3.17 is shown the optimal thickness of the identical blades contained in the detector. The effect of the substrate turns out to change slightly the optimal coating thickness in order to attain the maximum efficiency. Furthermore,

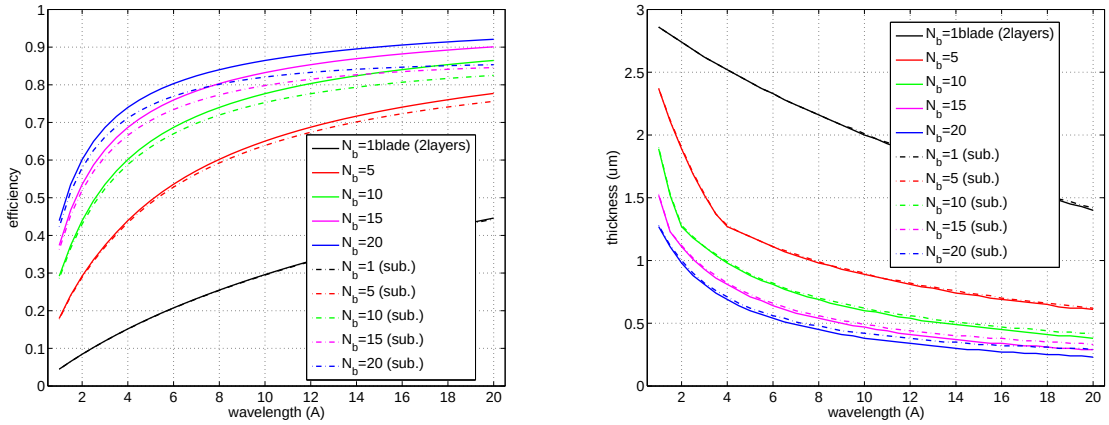


Figure 3.17: Efficiency (left) and optimal thickness of the identical blades (right) as a function of neutron wavelength for a 2, 10, 20, 30 and 40 layers multi-layer detector. Solid lines indicate the optimized efficiency, for each wavelength, for a detector made up for blades of identical thicknesses; the dashed-dotted ones indicate the same optimization considering the substrate.

the higher the number of layers, the bigger is the deviation between the efficiencies taking into account or not the effect of the substrate. At long wavelengths, the difference between a detector composed of 30 or 40 layers becomes smaller taking into account the substrate.
Moreover, the reasoning explained in Section 3.4.1, through which the efficiency of a multi-layer detector can be optimized by changing the individual blade coating thicknesses, can be applied also in presence of the substrate effect. We take a 30-layer detector that we optimize for 4 different cases. In Figure 3.18 the solid line represents the 30-layer detector optimized when it contains identical coating thickness blades without taking the substrate into account, as was the case of solid line in Figures 3.16 or 3.17. The dashed line represents the optimization done by changing the coating thicknesses without substrate effect, as dashed line in Figure 3.16. The dashed-dotted line, as in Figure 3.17, represents the detector efficiency when it is optimized considering the substrate and it contains identical blades. The dotted line represents a detector optimized taking the substrate effect into account allowing the coating thicknesses to change between different blades.
The substrate effect is to decrease the actual detector efficiency mainly at higher wavelengths. We can observe from Figure 3.18 that the optimization process helps to gain efficiency even when substrate plays a role.

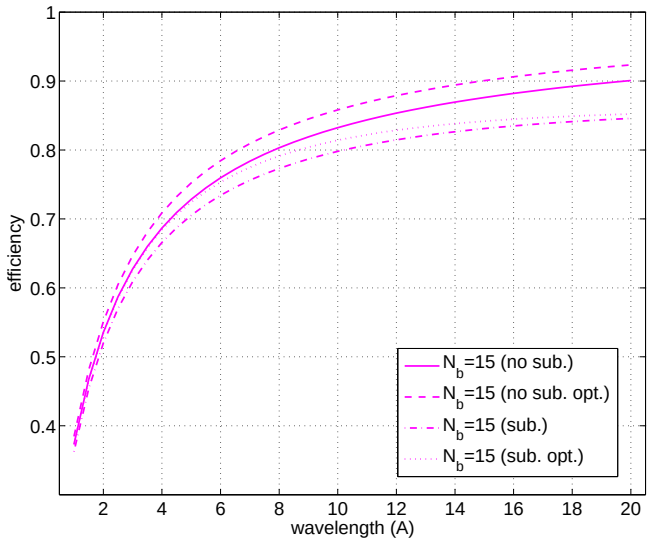


Figure 3.18: Efficiency as a function of neutron wavelength for a 30-layer detector. Solid lines indicate the optimized efficiency, for each wavelength, for a detector made up for blades of identical thicknesses. The dashed one indicates the monochromatic optimization using different thicknesses inside the detector. Dashed-dotted and dotted lines are the same as solid and dashed lines respectively when the substrate is cloistered.

### 3.4.3 Multi-layer detector optimization for a distribution of neutron wavelengths

Let's consider now a multi-layer detector operating on a neutron wavelength distribution defined by $w(\lambda)$ and normalized ($\int_0^{+\infty} w(\lambda)\, d\lambda = 1$). The efficiency for such a detector can be written as follows:

$$\varepsilon_{tot}^{w}(N_b, \bar{d}_{BS}, \bar{d}_T) = \int_0^{+\infty} w(\lambda)\, \varepsilon_{tot}(N_b, \lambda)\, d\lambda \tag{3.56}$$

where $\varepsilon_{tot}(N_b, \lambda)$ is the multi-layer detector efficiency for a single neutron wavelength defined as in Equation 3.38. The efficiency, in this case will be function of $N = 2 \cdot N_b$ variables; which can be denoted using the compact vectorial notation by the two vectors $\bar{d}_{BS}$ and $\bar{d}_T$ of $N_b$ components each.
The optimization problem, in the case of a neutron wavelength distribution, is the maximization of a $N$-dimensional function. Any change on the previous blades will change the actual *distribution* of wavelengths the last blade experiences. The neutron distribution a blade has to be optimized for depends on all the previous blade coatings.
Therefore, the $N$-dimensional equation $\nabla\varepsilon_{tot}^{w} = 0$ has to be solved; explicitly:

$$\nabla\varepsilon_{tot}^{w} = \int_0^{+\infty} w(\lambda)\, \nabla\left(\varepsilon_1(d_{BS1}, d_{T1}) + \sum_{k=2}^{N_b} \varepsilon_1(d_{BSk}, d_{Tk}) \cdot e^{-\left(\sum_{j=1}^{(k-1)}\left(d_{BSj}+d_{Tj}\right)\right)\cdot\Sigma}\right) d\lambda \tag{3.57}$$

The $k-th$ $N$-dimensional gradient component for back-scattering is:

$$\frac{\partial \varepsilon_{tot}(N_b,\lambda)}{\partial d_{BSk}} = \begin{cases} \frac{\partial \varepsilon_1(d_{BSk},d_{Tk})}{\partial d_{BSk}} - \Sigma \cdot \sum_{p=(k+1)}^{N_b} \varepsilon_1(d_{BSp},d_{Tp}) \cdot e^{-\left(\sum_{i=1}^{(p-1)}(d_{BSi}+d_{Ti})\right)\cdot\Sigma} \\ \text{if } \; k=1 \\ \\ \frac{\partial \varepsilon_1(d_{BSk},d_{Tk})}{\partial d_{BSk}} \cdot e^{-\left(\sum_{j=1}^{(N_b-1)}(d_{BSj}+d_{Tj})\right)\cdot\Sigma} + \\ -\Sigma \cdot \sum_{p=(k+1)}^{N_b} \varepsilon_1(d_{BSp},d_{Tp}) \cdot e^{-\left(\sum_{i=1}^{(p-1)}(d_{BSi}+d_{Ti})\right)\cdot\Sigma} \\ \text{if } \; 1<k<N_b \\ \\ \frac{\partial \varepsilon_1(d_{BSk},d_{Tk})}{\partial d_{BSk}} \cdot e^{-\left(\sum_{j=1}^{(N_b-1)}(d_{BSj}+d_{Tj})\right)\cdot\Sigma} \\ \text{if } \; k=N_b \end{cases} \tag{3.58}$$

Equivalently we find the same expression for the $k-th$ component of the gradient with respect to the transmission variable; we can substitute $\partial d_{BSk}$ with $\partial d_{Tk}$ in Equation 3.58.
The condition $\nabla \varepsilon^w_{tot} = 0$ implies that for each $k$ must hold $\frac{\partial \varepsilon_{tot}(N_b,\lambda)}{\partial d_{BSk}} = 0$ and $\frac{\partial \varepsilon_{tot}(N_b,\lambda)}{\partial d_{Tk}} = 0$ at the same time. From Equation 3.58 and the one for the transmission variable we finally obtain $(\forall k = 1,2,\ldots,N_b)$:

$$\begin{cases} \frac{\partial \varepsilon_1(d_{BSk},d_{Tk})}{\partial d_{BSk}} = \frac{\partial \varepsilon_1(d_{BSk},d_{Tk})}{\partial d_{Tk}} \Rightarrow D_{\hat{u}}\varepsilon_1(d_{BSk},d_{Tk}) = 0 & \text{if } \; k<N_b \\ \frac{\partial \varepsilon_1(d_{BSk},d_{Tk})}{\partial d_{BSk}} = \frac{\partial \varepsilon_1(d_{BSk},d_{Tk})}{\partial d_{Tk}} = 0 & \text{if } \; k=N_b \end{cases} \tag{3.59}$$

As for the monochromatic case, the condition in Equation 3.59 is exactly what was demonstrated in Section 3.3. The Theorem 3.3.1 implies that the directional derivative along the unity vector $\hat{u} = \frac{1}{\sqrt{2}}(1,-1)$ of the function $\varepsilon_1(d_{BSk},d_{Tk})$ can only be zero on the domain bisector, in the case of $k < N_b$. Hence, the maximum efficiency can only be found, again, on the bisector. On the other hand, in the case of $k = N_b$ the Equation 3.59 requires the gradient of the efficiency function to be zero, property which was also demonstrated for these kind of functions in Section 3.3 (Equations 3.20 and 3.22).

**In a Multi-Grid like detector, which has to be optimized for any distribution of neutron wavelengths, all the blades have to hold two layers of the same thickness. Naturally, thicknesses of different blades can be distinct.** In this case it is not possible to start the optimization from the last blade because the thicknesses of the previous layers will affect the neutron wavelength distribution reaching the deeper laying blades. We have in this case to optimize an $N_b$-dimensional function at once. Therefore, the $N_b$-dimensional equation $\nabla \varepsilon^w_{tot} = 0$ has to be solved.
Thanks to the property just derived, we can denote with $d_k$ the common thickness of the two layers held by the $k-th$ blade ($d_{BSk} = d_{Tk} = d_k$). In the detector efficiency function, expressed by Equation 3.56, we can substitute $\varepsilon_{tot}(N_b,\lambda)$ with its simpler expression shown in Equation 3.47.
For the optimization process the $k-th$ component of the gradient $\nabla_k \varepsilon^w_{tot}$ can be replaced with

$\frac{\partial \varepsilon_{tot}^{w}}{\partial d_k}$; because now $N_b = \frac{N}{2}$ unknown, instead of $N$, have to be found.

$$\nabla_k \varepsilon_{tot}^{w} = \int_0^{+\infty} w(\lambda) \frac{\partial \varepsilon_{tot}}{\partial d_k} d\lambda = \int_0^{+\infty} w(\lambda) \frac{\partial}{\partial d_k} \left( \varepsilon_1(d_1) + \sum_{k=2}^{N_b} \varepsilon_1(d_k) \cdot e^{-2\left(\sum_{j=1}^{(k-1)} d_j\right)\cdot\Sigma} \right) d\lambda \tag{3.60}$$

$\frac{\partial \varepsilon_{tot}}{\partial d_k}$ is an expression like Equation 3.58 provided that we impose $d_{BSk} = d_{Tk}\, \forall k = 1, 2, \ldots, N_b$. Finally, in order to optimize a detector for a given neutron wavelength distribution, the following system of $N_b$ equations in $N_b$ unknown ($d_k$) has to be solved:

$$\begin{cases} \int_0^{+\infty} w(\lambda) \left[ \frac{\partial \varepsilon_1(d_k)}{\partial d_k} - 2\Sigma \cdot \sum_{p=2}^{N_b} \varepsilon_1(d_p) \cdot e^{-2\left(\sum_{i=1}^{(p-1)} d_i\right)\cdot\Sigma} \right] d\lambda = 0 & \text{if } k = 1 \\ \int_0^{+\infty} w(\lambda) \left[ \frac{\partial \varepsilon_1(d_k)}{\partial d_k} \cdot e^{-2\left(\sum_{j=1}^{(N_b-1)} d_j\right)\cdot\Sigma} + \right. & \\ \left. - 2\Sigma \cdot \sum_{p=(k+1)}^{N_b} \varepsilon_1(d_p) \cdot e^{-2\left(\sum_{i=1}^{(p-1)} d_i\right)\cdot\Sigma} \right] d\lambda = 0 & \text{if } 1 < k < N_b \\ \int_0^{+\infty} w(\lambda) \left[ \frac{\partial \varepsilon_1(d_k)}{\partial d_k} \cdot e^{-2\left(\sum_{j=1}^{(N_b-1)} d_j\right)\cdot\Sigma} \right] d\lambda = 0 & \text{if } k = N_b \end{cases} \tag{3.61}$$

We recall that $\varepsilon_1(d_k)$ and $\Sigma$ are function of $\lambda$ and $\varepsilon_1(d_k)$ is the blade efficiency defined in Equations 3.18 and 3.21; its derivative $\frac{\partial \varepsilon_1(d_k)}{\partial d_k}$ was already calculated in the Equations 3.34 and 3.36 (Section 3.3).
The system of equations 3.61 can be easily solved numerically.
Comparing this result with the one found in the monochromatic case in Section 3.4.3, where the solution could be found iteratively starting from the last blade, we have now a system of $N_b$ equations in $N_b$ unknown. In Section 3.4.3, the system of equations 3.48 turned out to be upper triangular.
This is not the case for the distribution case in which the gradient of Equation 3.47 is in addition integrated over $\lambda$, thus all the blades have to be taken into account at once in the optimization process. The optimization problem will be the maximization of a $N$-dimensional function.
To better understand the meaning of that, we should figure out how the optimization process works. For a single wavelength, each layer efficiency has to maximize for that well defined neutron energy; all the previous layers only affect the number of neutrons that can reach the deeper blades. We require the last blade to be as efficient as possible on that kind of neutron. On the other hand, in the case of a wavelength distribution, any change on the previous blades will change the actual distribution the last blade experiences. There can be neutrons of a certain energy that can not get to a layer it was optimized for. Thus, the neutron distribution a blade has to be optimized for depends on all the previous blades coatings. In this case, the matrix does not end up to be triangular.

**Flat neutron wavelength distribution example**

We take a flat distribution $w(\lambda) = \frac{1}{\lambda_2 - \lambda_1}$ between the two wavelengths $\lambda_1 = 1\text{Å}$ and $\lambda_2 = 20\text{Å}$ as in Section 3.3 for the single blade case. In Figure 3.19 the thicknesses of each of the blade

coatings and each blade efficiency contribution for a 30-layer detector are shown. Three detectors are compared, the one of simplest construction is a detector holding 15 identical blades of $0.5\,\mu m$ coating thickness, the second is a detector optimized according to Equation 3.61 for that specific flat distribution and the last is a detector that has been optimized for a single neutron wavelength of 10Å conforming to Equations 3.51, 3.52 and 3.53. The fact to have a contribution of wavelengths shorter than 10Å in the case of the red line makes the coating thicknesses larger compared to the blue curve.
As a result, frontal layers are slightly more efficient for the distribution optimized detector than for the one optimized for 10Å; on the other hand, deep layers lose efficiency. Figure 3.20 shows

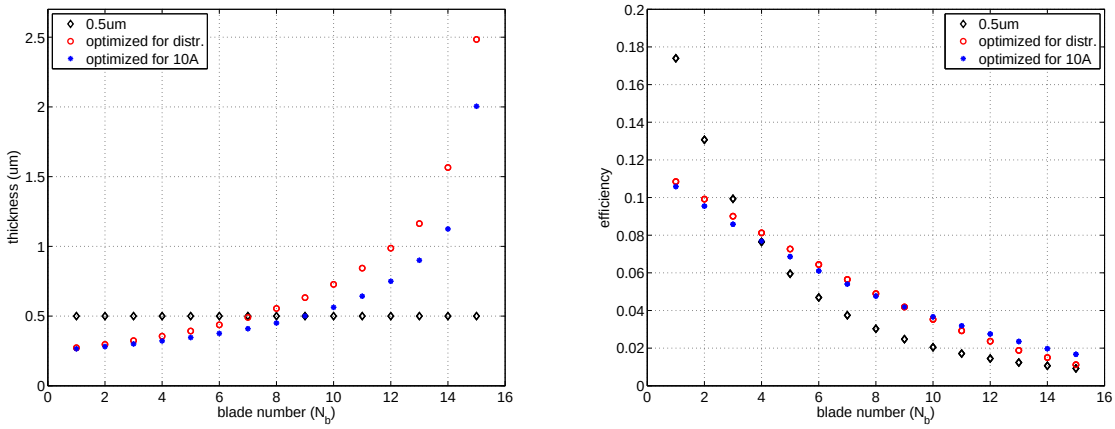


Figure 3.19: Thicknesses of the blades coatings (left) and their efficiency contribution (right), for a detector made up of 15 identical coating thickness blades of $0.5\,\mu m$, for a detector optimized for the flat distribution of wavelengths and for a detector optimized for 10Å.

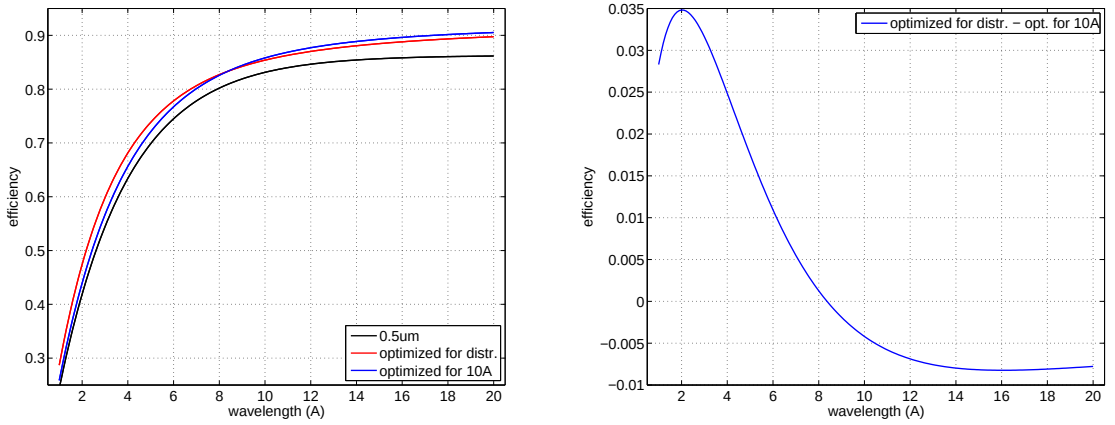


Figure 3.20: Efficiency as a function of neutron wavelength (left) for a detector made up of 15 identical coating thickness blades of $0.5\,\mu m$, for a detector optimized for the flat distribution of wavelengths and for a detector optimized for 10Å. Difference between the efficiencies for a detector optimized for a flat distribution and for 10Å as a function of neutron wavelength (right).

the three detector efficiencies as a function of neutron wavelength. By comparing red and blue

lines, of which the difference is plotted on the right plot, the optimized detector gains efficiency on shorter wavelengths but loses on longer. Moreover, we notice that the optimization process explained in this section let to gain at most 3.5% at short wavelengths while losing less than 1% on longer ones. The weighted efficiency over $w(\lambda)$ is shown in Table 3.3. We can conclude

| opt. detect. | opt. detect. for 10Å | $0.5\,\mu m$ detect. |
|---|---|---|
| 0.796 | 0.793 | 0.764 |

Table 3.3: Averaged efficiency over the flat neutron wavelength distribution (1Å-20Å) for a detector which contains 15 identical blades of $0.5\,\mu m$, for an optimized multi-layer detector for that specific flat distribution and for a detector optimized for 10Å. (Energy threshold $100\,KeV$ applied).

that if we are interested in optimizing a detector in a given interval of wavelengths without any preference to any specific neutron energy; optimizing according to Equation 3.61 does not give a big improvement in the average efficiency compared to optimizing for the neutron wavelength distribution barycenter (about 10Å).
Although the averaged efficiency for the optimized detector in the neutron wavelength range differs from the one optimized for 10Å only by 0.3% one can be interested to have a better efficiency for shorter wavelengths rather than for longer. It is in this case that the optimization process can play a significant role. On that purpose let's move to the following example.

**Hyperbolic neutron wavelength distribution example**

We consider a hyperbolic neutron wavelength distribution between $\lambda_1 = 1$Å and $\lambda_2 = 20$Å.

$$w(\lambda) = \frac{1}{\ln\left(\frac{\lambda_2}{\lambda_1}\right)} \cdot \frac{1}{\lambda} \tag{3.62}$$

This optimization aims for giving equal importance to bins on a logarithmic wavelength scale. The barycenter of the wavelength distribution corresponds to $\int_{\lambda_1}^{\lambda 2} w(\lambda)\,\lambda\,d\lambda = 6.34$Å.
In Figure 3.21 are shown the thicknesses of each blade coatings and the efficiency as a function of the depth direction in the detector for a 30-layer detector. Five detectors are compared, the one of $1.2\,\mu m$ coating thickness, a detector optimized according to Equation 3.61 for that specific hyperbolic distribution, a detector that has been optimized for a single neutron wavelength of 10Å, 1.8Å, and the barycenter of the distribution.

| opt. detect. | opt. 10Å | opt. 6.34Å | opt. 1.8Å | $1.2\,\mu m$ detect. |
|---|---|---|---|---|
| 0.671 | 0.641 | 0.664 | 0.639 | 0.597 |

Table 3.4: Averaged efficiency over the hyperbolic distribution defined in Equation 3.62 for a detector which contains 15 identical blades of $1.2\,\mu m$, for an optimized multi-layer detector for that specific distribution and for a detector optimized for 10Å, 6.34Å and for 1.8Å. (Energy threshold $100\,KeV$ applied).

By only comparing the averaged efficiencies, shown in Table 3.4, the distribution optimized detector shows only a gain of at most about 3% with respect to the detectors optimized for the distribution barycenter or other wavelengths. It seems that there is not a big improvement in the detector efficiency over the full neutron energy range.
Figure 3.22 shows the five detector efficiencies as a function of wavelength and their difference on

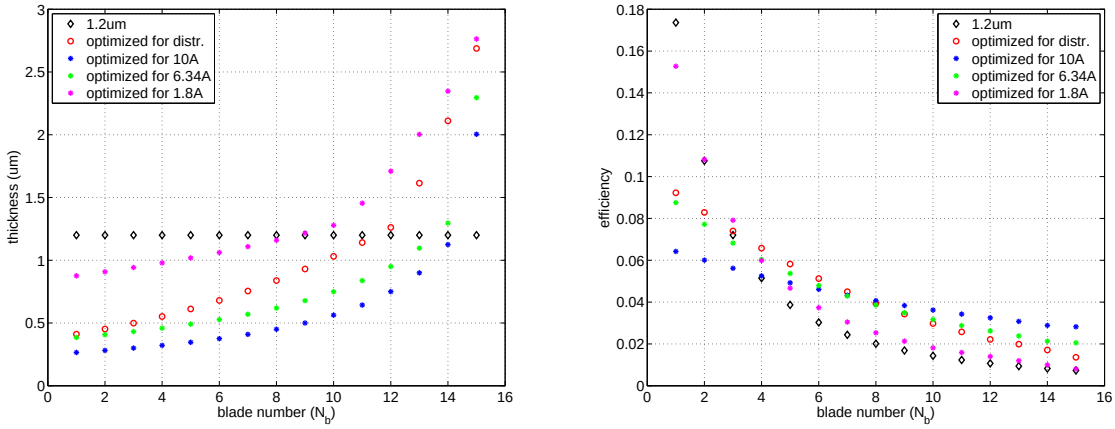


Figure 3.21: Thicknesses of the blades coatings (left) and their efficiency contribution (right), for a detector made up of 15 identical coating thickness blades of 1.2 $\mu m$, for a detector optimized for an hyperbolic distribution of wavelengths and for a detector optimized for 10Å, 6.34Å and for for 1.8Å.

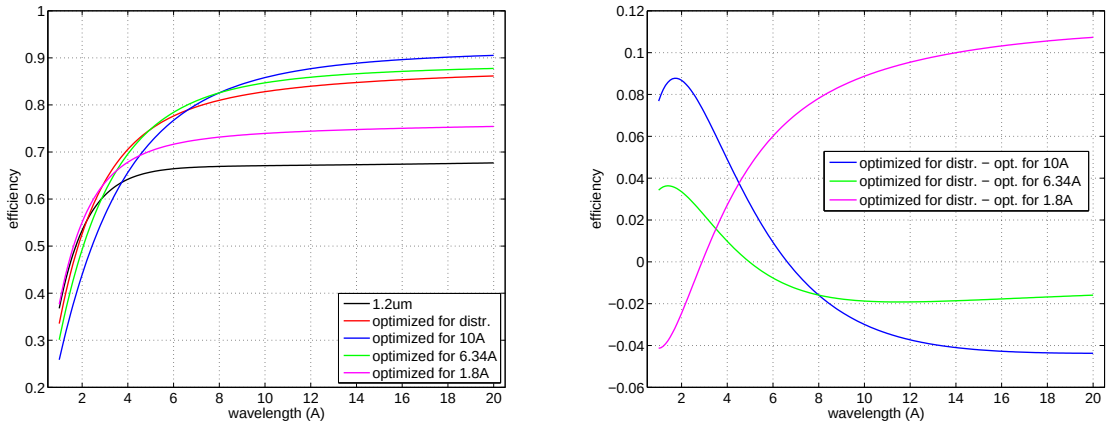


Figure 3.22: Efficiency as a function of neutron wavelength (left) for a detector made up of 15 identical coating thickness blades of 1.2 $\mu m$, for a detector optimized for an hyperbolic distribution of wavelengths and for a detector optimized for 10Å and for 1.8Å. Difference between the efficiencies for a detector optimized for a flat distribution and for 10Å, 6.34Å and for 1.8Å as a function of neutron wavelength (right).

the right plot. By comparing the red (distribution optimized detector) and the green (barycenter optimized detector) lines, of which the difference is plotted in green on the right plot, we notice that the detector optimized for such a distribution gains about 4% efficiency at short wavelengths and loses about 2% at high wavelengths. With respect to a detector conceived for higher wavelengths (blue curve), i.e. 10Å, the distribution optimized one gains about 9% at short wavelengths and loses about 4% at high wavelengths. A detector conceived for short wavelengths, such as the one represented by the pink line (1.8Å), has an opposite behavior instead. The distribution optimized detector gains efficiency for long wavelengths reaching about 11%.
Even if the the optimization procedure, explained in this section, shows that there is not a notable improvement over the full range of neutron wavelength, it can lead to a significant

efficiency improvement in certain neutron wavelength ranges. As in the case of a flat distribution, a detector optimized for a distribution according to Equations 3.61, does not show significant improvement in performances with respect to a detector just optimized for its barycenter.

## 3.5 Why Boron Carbide?

We are going to explain here why $^{10}B_4C$ is a suitable material for neutron detection in solid converter gaseous detectors.
A good solid converter material that can be employed in a thermal neutron detector should own features like sufficient electrical conductivity, high neutron absorption cross-section, low density, no toxicity and easy manipulation. We compare two neutron solid converters $^{10}B$ and $^{6}Li$ and their compounds $^{10}B_4C$ and $^{6}LiF$; their characteristics are listed in Table 3.5. We list their mass density, microscopic and macroscopic absorption cross-section $\Sigma$, $\eta = 1/\Sigma$ is the mean free path, and the electrical resistivity.
A good converter material should not be too resistive because, in general, it acts as a cathode in the gaseous detector. In order for the electric field to stay constant in time it should evacuate the charges in a reasonable time.
While $^{10}B$, $^{10}B_4C$ and $^{6}LiF$ do not present any strong reactivity, pure $^{6}Li$ reacts with water easily. It has to be manipulated and operated in a controlled atmosphere.
Among the features listed in Table 3.5, a converter material should offer a high density to maximize the number of neutron conversions per unit volume but, on the other hand, a low density to let the neutron capture reaction fragments escape easily from the layer to produce a detectable charge in the gas volume. While the microscopic absorption cross-section only plays a role in the neutron capture process; the mass density influences both the capture and the fragment escape processes. Hence, $\Sigma$, or equivalently $\eta$, represents the capture power of a material given its density and its absorption cross-section. The shorter $\eta$, the higher is the probability for a neutron to be captured. The energy the fragments own contributes to the escape probability, i.e. in their ranges. For that purpose $^{6}Li$ fragments carrying $4790\,KeV$ are more probable to escape.
Moreover, mass density plays in the escape process. In Table 3.6 the ranges for the $^{10}B$ and $^{6}Li$ reaction fragments (see Table 1.70) are listed for an energy threshold of $100\,KeV$.
It is true that pure $^{10}B$ has a slightly higher boron atom density and the fragments have somewhat longer ranges which makes the potential efficiency of a pure $^{10}B$ coated detector in principle higher. However, given that pure $^{10}B$ is about eight orders of magnitudes more electrically resistive than $^{10}B_4C$, therefore one opted in [23] to use $^{10}B_4C$.
Because the fragments in $^{6}Li$ have a very long range, although $\eta$ is shorter than the one in $^{6}LiF$, it could be a very powerful converter material but hygroscopicity makes it not a very good candidate.
We compare now $^{10}B_4C$ and $^{6}LiF$. Ranges in $^{6}LiF$ are longer, i.e. have higher escape efficiency; on the contrary, it is $^{10}B_4C$ that has a higher neutron conversion power because of its shorter mean free path $\eta$. From only these consideration it is not easy to figure out which one exhibits the highest detection efficiency.
A qualitative parameter to evaluate the goodness of a solid neutron converter is:

$$\chi(\lambda) = \langle R \rangle \cdot \Sigma(\lambda) = \frac{\langle R \rangle}{\eta(\lambda)} \tag{3.63}$$

| material | $\rho(g/cm^3)$ | $\Sigma(1/\mu m)\,at\,1.8$Å | $\eta(\mu m)\,at\,1.8$Å | $\sigma_{abs}(b)\,at\,1.8$Å | $\rho_e(\Omega \cdot m)$ |
|---|---|---|---|---|---|
| $^{nat}Li$ | 0.53 | $3.3 \cdot 10^{-4}$ | 3030 | 940 | $10^{-7}$ |
| pure $^{6}Li$ | 0.46 | $4.4 \cdot 10^{-3}$ | 227 | 940 | $10^{-7}$ |
| $^{nat}B$ | 2.35 | $1.0 \cdot 10^{-2}$ | 100 | 3835 | $10^{6}$ |
| pure $^{10}B$ | 2.17 | $5.0 \cdot 10^{-2}$ | 20 | 3835 | $10^{6}$ |
| $^{nat}LiF$ | 2.64 | $4.4 \cdot 10^{-4}$ | 2273 | 940 | $10^{-8}$ |
| 96% enriched $^{6}LiF$ | 2.54 | $5.8 \cdot 10^{-3}$ | 172 | 940 | $10^{-8}$ |
| $^{nat}B_4C$ | 2.52 | $8.4 \cdot 10^{-3}$ | 119 | 3835 | $10^{-3}$ |
| 98% enriched $^{10}B_4C$ | 2.37 | $4.2 \cdot 10^{-2}$ | 24 | 3835 | $10^{-3}$ |
| glass | | | | | $> 10^{9}$ |
| Si | | | | | 1 |
| graphite | | | | | $10^{-5}$ |
| Cu | | | | | $10^{-8}$ |

Table 3.5: Physical features of common neutron thermal neutron converter. $\eta = 1/\Sigma$ is the mean free path a neutron can travel across the material before being absorbed. $\sigma_{abs}$ is shown for the active nuclide; i.e. $^{6}Li$ or $^{10}B$. Natural compounds refer to 7.5% of $^{6}Li$ and 92.5% of $^{7}Li$ for Lithium and 19.4% of $^{10}B$ and 80.6% of $^{11}B$ for Boron.

| material | $R(\mu m)$ $\alpha(2050\,KeV)$ | $R(\mu m)$ $^{3}H(2740\,KeV)$ | | |
|---|---|---|---|---|
| pure $^{6}Li$ | 21 | 132 | | |
| 96% enriched $^{6}LiF$ | 5.2 | 32.8 | | |
| | $R(\mu m)$ $\alpha(1470\,KeV)$ | $R(\mu m)$ $^{7}Li(830\,KeV)$ | $R(\mu m)$ $\alpha(1770\,KeV)$ | $R(\mu m)$ $^{7}Li(1010\,KeV)$ |
| pure $^{10}B$ | 3.3 | 1.5 | 4.1 | 1.8 |
| 98% enriched $^{10}B_4C$ | 2.9 | 1.2 | 3.7 | 1.5 |

Table 3.6: Ranges of the capture reaction fragments in the material. An energy threshold of $100\,KeV$ is applied.

where as $\langle R \rangle$ we refer to the average particle range for a given capture reaction. $\chi$ is a dimensionless number that takes into account both the power of a material to convert neutrons of a given wavelength and the ease for the produced particle to escape. The higher $\chi$, the better is the converter. $\chi$-values are tabulated in Table 3.7.

| material | $\langle R \rangle(\mu m)$ | $\chi\,at\,1.8$Å |
|---|---|---|
| pure $^{6}Li$ | 76.5 | 0.34 |
| pure $^{10}B$ | 2.43 | 0.12 |
| 96% enriched $^{6}LiF$ | 19 | 0.11 |
| 98% enriched $^{10}B_4C$ | 2.08 | 0.09 |

Table 3.7: Average range for different neutron converters and the corresponding $\chi$ calculated for 1.8Å. An energy threshold of $100\,KeV$ is applied.

Figure 3.23 shows the detection efficiency for a single converter layer either in transmission mode or in back-scattering plotted as a function of the film thickness. We chose 1.8Å as neutron wavelength and an angle of incidence of neutrons of 10°. An energy threshold of $100\,KeV$ is applied.

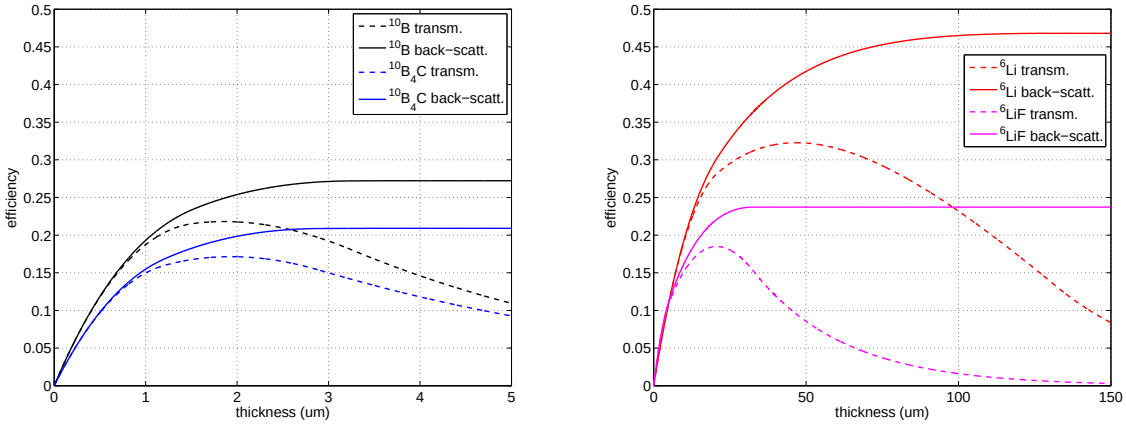


Figure 3.23: Comparison between the efficiencies of pure $^{10}B$, enriched $^{10}B_4C$, pure $^{6}Li$ and enriched $^{6}LiF$ plotted as a function of the layer thickness. Both efficiencies at 1.8Å for a single layer in transmission mode and in back-scattering mode at 10° incidence angle are plotted. An energy threshold of 100 $KeV$ is applied.

$^{10}B_4C$ and $^{6}LiF$, in back-scattering mode, attain their maximum efficiency, about 21% and 24% respectively, for a film of thickness $d = 3\,\mu m$ and $d = 30\,\mu m$ respectively. Even $^{6}LiF$ shows a slightly higher efficiency, the fabrication of layer of $30\,\mu m$ can be an issue in terms of costs and deposition time unless a single material block is used.

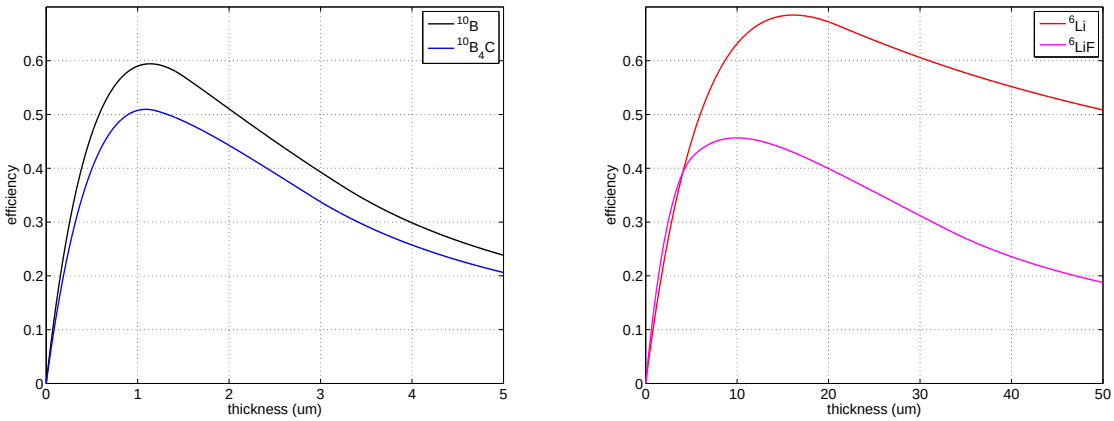


Figure 3.24: Comparison between the efficiencies of pure $^{10}B$, enriched $^{10}B_4C$, pure $^{6}Li$ and enriched $^{6}LiF$ plotted as a function of the single layer thickness. Efficiencies are calculated at 1.8Å for a multi-layer detector made up of 30 layers ($N_b = 15$ blades) at 90° incidence angle. An energy threshold of 100 $KeV$ is applied.

Figure 3.24 shows the efficiency for a multi-layer detector composed of $N_b = 15$ blades (30 layers) as a function of the single film thickness.
This time $^{10}B_4C$ presents a higher efficiency (about 50%) with respect to $^{6}LiF$ (about 45%). This makes it the best candidate for a multi-grid like detector [23].
An alternative to exploit the high escape probability of $^{6}Li$ fragments, is to coat a $^{6}Li$ layer with a very thin layer of $^{10}B_4C$ that acts as a protection and an additional converter material. The latter should be optimized to let $^{6}Li$ particles escape. Moreover, one can make self-supporting

layers out of $^6Li$ to be coated with $^{10}B_4C$; it will increase significantly the neutron detection efficiency.

## 3.6 Theoretical Pulse Height Spectrum calculation

The physical model taken into account in [4] and in [26] can be used as well to derive the analytical formula for the Pulse Height Spectra (PHS). A similar work was done in [26] (see Appendix C) where only Monte Carlo solutions were shown; here we want to use analytic methods to understand the structure of the PHS.
We make the approximation mentioned in the Introduction 3.1 and we assume either a simplified stopping power function (see Section 3.6.1) or one simulated with SRIM [2] for the neutron capture fragments.
Referring to Figure 3.1, we calculate the probability for a particle emitted from the neutron conversion point at certain depth ($x$ for back-scattering or $d-y$ for transmission) to travel exactly a distance $L$ on a straight line towards the escape surface. This distance $L$ is related to the charged particle remaining energy through the primitive function of the stopping power. The final electric signal will be proportional to the charge created by these charged fragments and, thus, to the energy they own after escaping the layer.
We will demonstrate that even under strong approximations of the stopping power function the model still predicts quite well the important physical features of the PHS.

### 3.6.1 Back-scattering mode

The probability for a neutron to be captured at depth $(x, x+dx)$ in the converter layer and for the capture reaction fragment (emitted isotropically in $4\pi\, sr$) to be emitted with an angle $\varphi = \arccos(u)$ (between $(u, u+du)$) is:

$$p(x,u)dx\,du = \begin{cases} \frac{1}{2}\cdot\Sigma e^{-\Sigma\cdot x}dx\,du & \text{if } x \le d \\ 0 & \text{if } x > d \end{cases} \tag{3.64}$$

where $\Sigma = n\cdot\sigma$ with $n$ number density of the conversion layer and $\sigma$ the neutron absorption cross section; $d$ is the layer thickness. The factor $\frac{1}{2}$ takes into account that half of the time the particle travels toward the layer substrate and it is therefore lost.
The fragment will travel a distance $L$ across the converter layer if $L = \frac{x}{u}$ and it is formally expressed by a Dirac delta function:

$$\delta\left(\frac{x}{u} - L\right) = \frac{x}{L^2}\cdot\delta\left(u - \frac{x}{L}\right) \tag{3.65}$$

By using the following delta function property $\delta(g(\xi)) = \sum_i \frac{\delta(\xi-\xi_i)}{|g'(\xi_i)|}$ where $\xi_i$ are the solutions of $g(\xi) = 0$.
The probability for a particle to travel a distance $(L, L+dL)$ across the layer is given by:

$$\begin{aligned} P(L)\,dL &= \int_0^d\int_0^1 \delta\left(\frac{x}{u} - L\right)p(x,u)\,dxdu = \frac{\Sigma}{2L^2}\int_0^d dx\,xe^{-\Sigma\cdot x}\int_0^1 du\,\delta\left(u-\frac{x}{L}\right) = \\ &= \frac{\Sigma}{2L^2}\int_0^d dx\,xe^{-\Sigma\cdot x}\left(H(x) - H(x-L)\right) = \begin{cases} \frac{1}{2L^2}\left(\frac{1}{\Sigma} - (\frac{1}{\Sigma}+L)e^{-\Sigma\cdot L}\right)dL & \text{if } L \le d \\ \frac{1}{2L^2}\left(\frac{1}{\Sigma} - (\frac{1}{\Sigma}+d)e^{-\Sigma\cdot d}\right)dL & \text{if } L > d \end{cases} \end{aligned} \tag{3.66}$$

where $H$ is the Heaviside step function.
It is sufficient to replace $\Sigma$ with $\frac{\Sigma}{\sin(\theta)}$ if neutrons hit the layer under the angle $\theta$ with respect to the surface (see Figure 3.1). In the PHS calculation $p(x,u)$ has to be changed as follows:

$$p(x,u,\theta)dx\,du = \begin{cases} \frac{1}{2}\cdot\Sigma e^{-\Sigma\cdot\frac{x}{\sin(\theta)}}\frac{dx}{\sin(\theta)}\,du & \text{if } x \le d \\ 0 & \text{if } x > d \end{cases} \tag{3.67}$$

The demonstration is identical to the one shown in Section 3.2 for the efficiency calculation.
Referring to Figure 3.5 in Section 3.2, this result means that the same PHS can be obtained, for example, at 10Å under an angle of 80° or equivalently at 5Å under an angle of 30°. If, for example, one is interested in measuring some PHS for a given neutron incidence angle and only a monochromatic beam is available, from Figure 3.5 it is possible to get the effect of having a different wavelength by changing the inclination instead. Every PHS measured on each equipotential line in Figure 3.5 is the same.
If $E(L)$ is the remaining energy of a particle that has traveled a distance $L$ into the layer, $\frac{dE(L)}{dL}$ is the stopping power or equivalently the Jacobian of the coordinate transformation between $L$ and $E$.
Once $P(L)dL$ is known we can calculate $Q(E)dE$, therefore:

$$P(L)dL = P(L(E))\cdot\left|\frac{dL}{dE}\right|\cdot dE = P(L(E))\cdot\frac{1}{\left|\frac{dE}{dL}\right|}\cdot dE \tag{3.68}$$

Therefore:

$$Q(E)dE = P(L(E))\cdot\frac{1}{\left|\frac{dE}{dL}\right|}\cdot dE \tag{3.69}$$

where $Q(E)dE$ is the probability that an incident neutron will give rise to a release of an energy $(E, E+dE)$ in the gas volume; hence it is the analytical expression for the PHS.

**PHS calculation using SRIM output files for Stopping Power**

We take the case of the $^{10}B$ reaction as example, however results can be applied to any solid neutron converter. We recall the energies carried for the 94% branching ratio is $E_0 = 1470KeV$ for the $\alpha$-particle and $E_0 = 830KeV$ for the $^7Li$; for the 6% branching ratio, $E_0 = 1770KeV$ for the $\alpha$-particle and $E_0 = 1010KeV$ for the $^7Li$. Referring to Equation 3.69, the stopping power $\frac{dE}{dL}$ used here was simulated with SRIM [2] (see Figure 3.27) and $L(E)$ obtained by numerical inversion of the stopping power primitive function, i.e. the remaining energy inverse function.
The full PHS that takes into account the full process can be obtained by adding the four PHS in the case of $^{10}B$ according to the branching ratio probability:

$$\begin{aligned} Q_{tot}(E)dE \quad &= (0.94\cdot(Q_{\alpha\,1470KeV}(E) + Q_{^7Li\,830KeV}(E)) + \\ &+0.06\cdot(Q_{\alpha\,1770KeV}(E) + Q_{^7Li\,1010KeV}(E)))\cdot dE \end{aligned} \tag{3.70}$$

Consequently the efficiency for a single layer can be calculated by:

$$\varepsilon\,(E_{Th}) = \int_{E_{Th}}^{+\infty} Q_{tot}(E)dE \tag{3.71}$$

where $E_{Th}$ is the energy threshold applied to cut the PHS. This result is fully in agreement with what can be calculated by using the Equations derived in Section 3.2.

In order to confirm our derived formulae a Monte Carlo simulator has been developed taking into account the same physical model exploited in this section. A random number generator simulates the probability for a neutron to be absorbed a certain depth in the conversion layer and with a random emission angle for the fragment. Using the SRIM files, we calculate the remaining energy after a straight path inside the layer for the fragment in question; this is the energy released into the gas volume.
Figure 3.25 shows the result of Equation 3.70 for the four single particles and the total PHS compared with the Monte Carlo PHS, for $1\,\mu m$ single back-scattering layer at 1.8Å and 90° incidence.

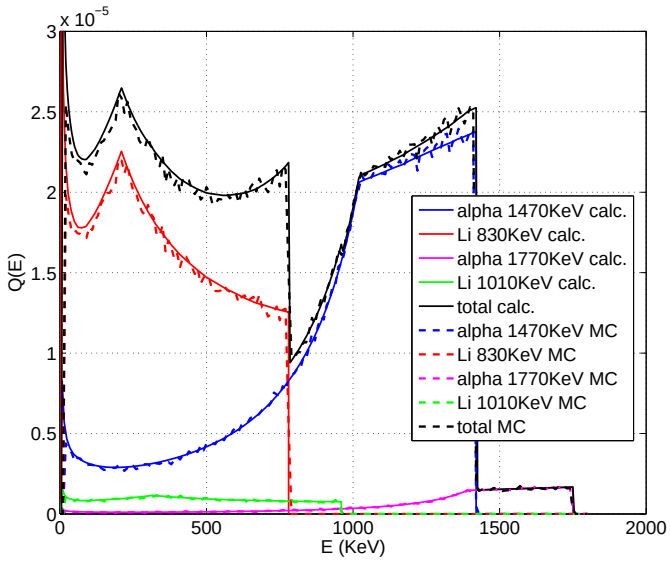


Figure 3.25: PHS calculated and MC simulated for $1\,\mu m$ back-scattering layer at 1.8Å and 90° incidence.

In order to check in practice the formulae derived, a direct measure on the neutron beam is necessary. A Multi-Grid-like detector [23] was used to collect the data we are going to show here. The data was collected on CT1 (Canal Technique 1) at the ILL where a monochromatic neutron beam of 2.5Å is available. This particular detector has the peculiarity that in each of its frames blades of different thickness coating were mounted; as a result the simultaneous PHS measurement for different layer thicknesses has been possible. The blades are made up of an Aluminium substrate of $0.5\,mm$ thickness coated [37] on both sides by an enriched $^{10}B_4C$ layer. Thicknesses available in the detector were: $0.50\,\mu m$, $0.75\,\mu m$, $1\,\mu m$, $1.5\,\mu m$, $2\,\mu m$ and $2.5\,\mu m$.
In our calculation we are not taking into account several processes, such as wall effects, gas amplification and fluctuations, space charge effects, electronic noise, etc. but only the neutron conversion and the fragment escape. Moreover, while the calculation has an infinite energy precision, this is not the case on a direct measurement because many processes give a finite energy resolution.
In order to be able to compare calculations and measurements, after the PHS were calculated for the thicknesses listed above, they were convoluted with a gaussian filter of $\sigma = 10\,KeV$. The measured PHS were normalized to the maximum energy yield ($1770\,KeV$). An energy threshold of $180\,KeV$ was applied to the calculation to cut the spectrum at low energies at the same level

the measured PHS was collected.
We compare calculated and measured PHS in Figure 3.26; we can conclude that the model gives realistic results in sufficient agreement with the experimental ones, to be able to describe its main features.

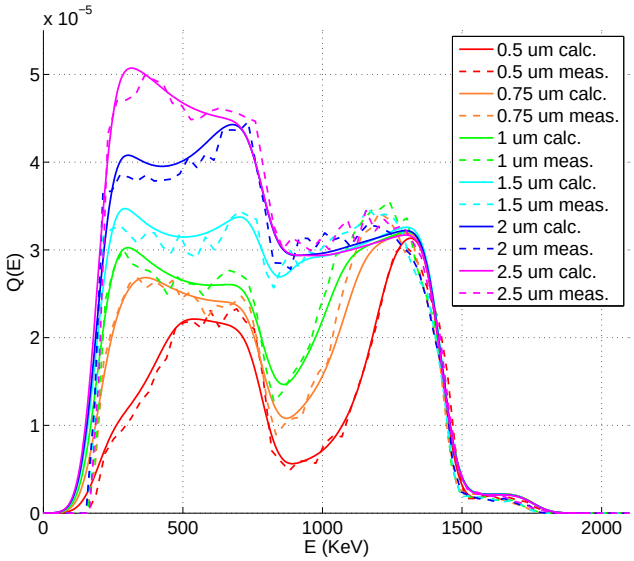


Figure 3.26: Comparison between a PHS calculated and one measured at ILL-CT2 on a 2.5Å neutron beam using a Multi-Grid like detector [23] where were mounted blades of different thicknesses.

### PHS calculation using a strong approximation

A fully analytical result that does not appeal to experimental or SRIM-calculated stopping power functions can be useful to understand the PHS structure and to determine its properties. The stopping power functions $\frac{dE}{dL}$ can be approximated by a constant in the case of an $\alpha$-particle and with a linear dependency in $L$ for a $^7Li$-ion. As a result the energy dependency as a function of the traveled distance $L$ is given by:

$$E_\alpha(L) = \begin{cases} -\frac{E_0}{R}(L-R) & \text{if } L \leq R \\ 0 & \text{if } L > R \end{cases} \tag{3.72}$$

And equivalently for the $^7Li$-fragment:

$$E_{Li}(L) = \begin{cases} \frac{E_0}{R^2}(L-R)^2 & \text{if } L \leq R \\ 0 & \text{if } L > R \end{cases} \tag{3.73}$$

Where $R$ is the particle range and $E_0$ its initial energy.
In Figure 3.27 are shown the stopping power functions $\frac{dE}{dL}$ for $^{10}B$-reaction fragments and their primitive $E(L)$, in the case of using SRIM (solid lines) and in the case we use the expression displayed in the Equations 3.72 and 3.73 (dashed lines). By substituting Expressions 3.72 and 3.73 into the Equation 3.69 we obtain a fully analytical formula for the PHS. It has to be pointed

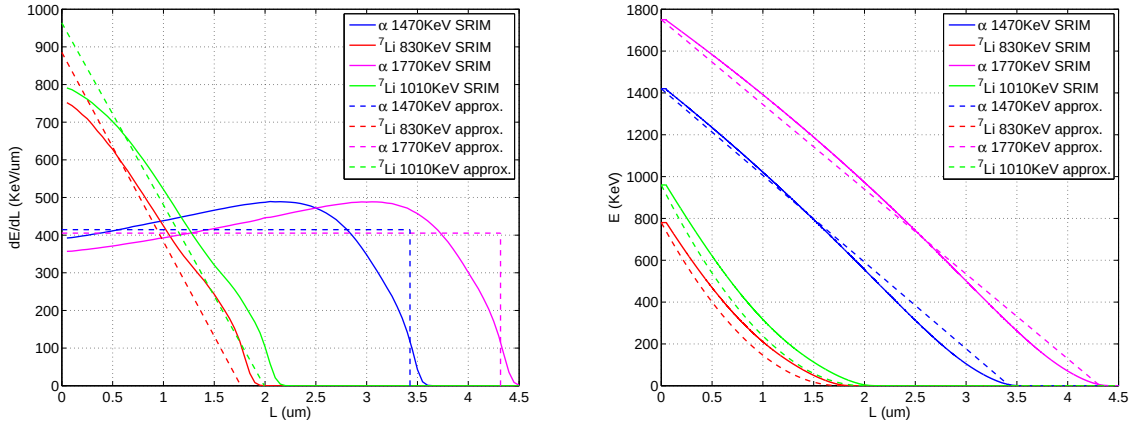


Figure 3.27: Stopping power and its primitive $E(L)$ for $^{10}B$-reaction fragments, solid curves are for functions obtained from SRIM, dashed lines are the approximated behaviors in the Equations 3.72 and 3.73.

out that each relation, valid for $L \leq R$, is valid in the range $E \leq E_0$. Hence Equations 3.74 and 3.75 hold for $E \leq E_0$. The two formulations in Equation 3.66 for $L \leq d$ and $L > d$, translate in two different analytical expressions for $Q(E)$ for $E < E^*$ and for $E \geq E^*$, with $d = L(E^*)$. For the $\alpha$-particle:

$$Q(E)\,dE = \begin{cases} \frac{1}{2E_0R\left(1-\frac{E}{E_0}\right)^2}\left(\frac{1}{\Sigma} - \left(\frac{1}{\Sigma}+d\right)e^{-\Sigma d}\right)\,dE & \text{if } E < E_0\left(1-\frac{d}{R}\right) \\ \frac{1}{2E_0R\left(1-\frac{E}{E_0}\right)^2}\left(\frac{1}{\Sigma} - \left(\frac{1}{\Sigma}+R\left(1-\frac{E}{E_0}\right)\right)\cdot e^{-\Sigma R\left(1-\frac{E}{E_0}\right)}\right)\,dE & \text{if } E \geq E_0\left(1-\frac{d}{R}\right) \end{cases} \tag{3.74}$$

Where the relation $E^* = E_0\left(1-\frac{d}{R}\right)$ is derived from $d = L(E^*)$.
For the $^7Li$:

$$Q(E)\,dE = \begin{cases} \frac{1}{4E_0R\sqrt{\frac{E}{E_0}}\left(1-\sqrt{\frac{E}{E_0}}\right)^2}\left(\frac{1}{\Sigma} - \left(\frac{1}{\Sigma}+d\right)e^{-\Sigma\cdot d}\right)\,dE & \text{if } E < E_0\left(1-\frac{d}{R}\right)^2 \\ \frac{1}{4E_0R\sqrt{\frac{E}{E_0}}\left(1-\sqrt{\frac{E}{E_0}}\right)^2}\left(\frac{1}{\Sigma} - \left(\frac{1}{\Sigma}+R\left(1-\sqrt{\frac{E}{E_0}}\right)\right)\cdot\right. & \\ \left.\cdot e^{-\Sigma R\left(1-\sqrt{\frac{E}{E_0}}\right)}\right)\,dE & \text{if } E \geq E_0\left(1-\frac{d}{R}\right)^2 \end{cases} \tag{3.75}$$

Where, again, the relation $E^* = E_0\left(1-\frac{d}{R}\right)^2$ is derived from the condition $d = L(E^*)$.
Figures 3.28, 3.29 and 3.30 show the calculated PHS obtained by using the SRIM stopping power functions and the approximated one displayed in the Expression 3.72 and 3.73 for $0.2\,\mu m$, $1\,\mu m$ and $4\,\mu m$ respectively, when neutrons hit at 90° the surface and their wavelength is 1.8Å. They show similar shapes that differ in some points; e.g. focusing on the $1470\,KeV$ $\alpha$-particle, the fact that the approximated $E(L)$ function (see Figure 3.27) differs from the SRIM one at high $L$ leads to a disappearance of the PHS rise at low energies; it is clearly visible in Figure 3.30. We see that as $d$ increases what looked like a single peak splits into two peaks. While one peak stays constant at the highest fragment energy $E_0$ the second one moves toward lower energies

when the layer thickness increases. This is important when trying to improve the neutron to gamma-rays discrimination by creating a valley that separates them in amplitude.

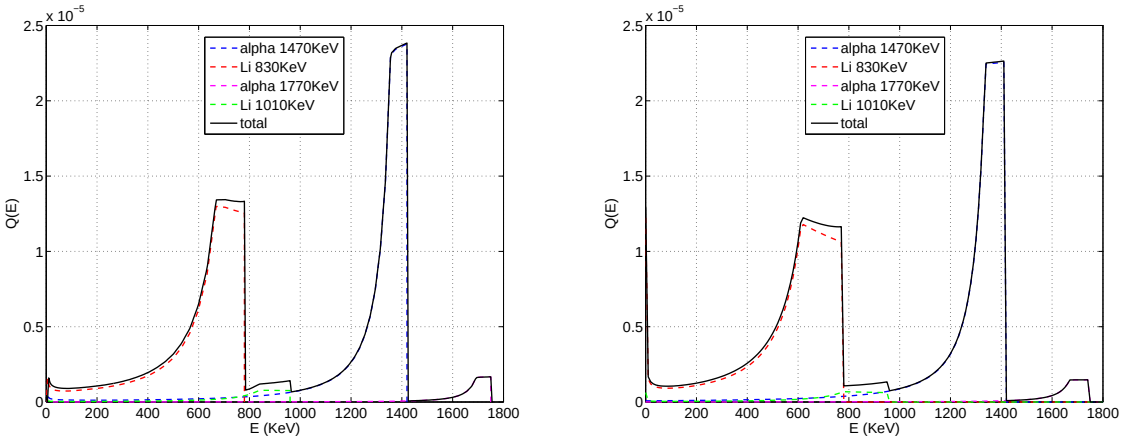


Figure 3.28: Calculated PHS using SRIM (left) and approximated (right) stopping power functions for a single back-scattering layer of $0.2\,\mu m$ for 1.8Å and 90° incidence.

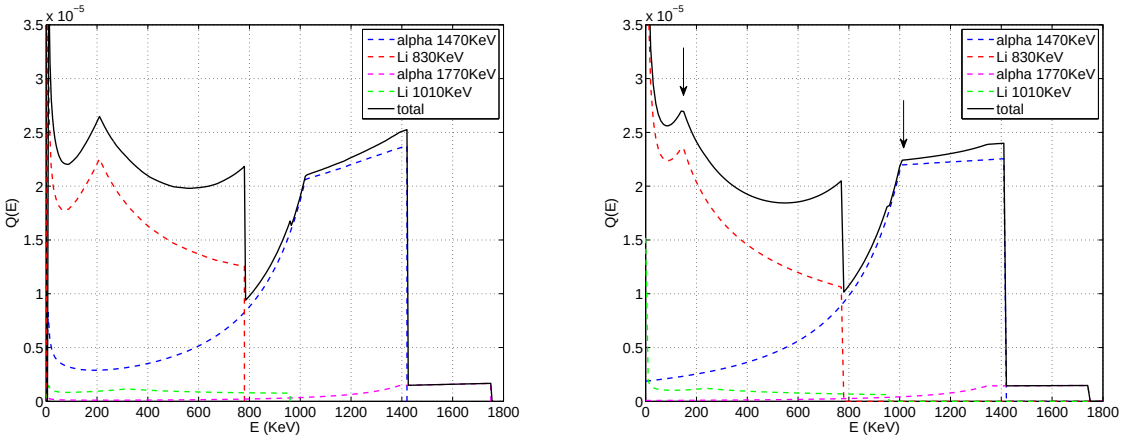


Figure 3.29: Calculated PHS using SRIM (left) and approximated (right) stopping power functions for a single back-scattering layer of $1\,\mu m$ for 1.8Å and 90° incidence.

In order to understand the PHS structure, we define the PHS *variable space*: on the abscissa axis is plotted $u = \cos(\varphi)$, where $\varphi$ is the angle the fragment has been emitted under, and, on the ordinates axis, is plotted the neutron absorption depth $x$. $u \in [0, 1]$; $x \in [0, d]$ if $d < R$ or $x \in [0, R]$ if $d \geq R$ because a neutron can only be converted inside the layer and, on the other hand, if a neutron is converted too deep into the layer, i.e. $x > R$ no fragments can escape whatever the emission angle would be. In Figure 3.31, on its left, the variable space is shown; an event in the A-position would be a fragment that was generated by a neutron converted at the surface of the layer and escape the layer at grazing angle. An event in the position B represents a fragment that escapes orthogonally to the surface and its neutron was converted at the surface. An event in C means a neutron converted deep into the layer with an orthogonal escaping

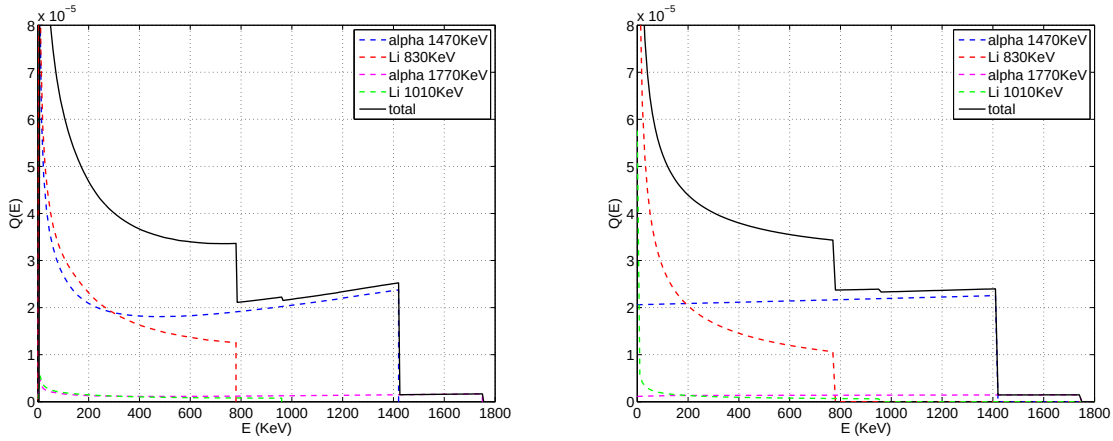


Figure 3.30: Calculated PHS using SRIM (left) and approximated (right) stopping power functions for a single back-scattering layer of $4\,\mu m$ for 1.8Å and 90° incidence.

fragment. The straight lines $x = L(E) \cdot u$ characterize the events with identical escape energy $E$, that contribute to the same bin in the PHS. The straight line characterized by $x = R \cdot u$ is the horizon for the particles that can escape the layer and release some energy in the gas volume. To be more precise events that give rise to the zero energy part of the PHS lie exactly on the line $\frac{x}{u} = L(E = 0) = R$ because they have traveled exactly a distance $R$ in the converter material. On the other hand, events that yield almost the full particle energy $E_0$, will lie on the line identified by $\frac{x}{u} = L(E = E_0) = 0$.
The events that generate the PHS have access to a region, on the variable space, identified by a triangle below the straight line $x = R \cdot u$ (see Figure 3.31).

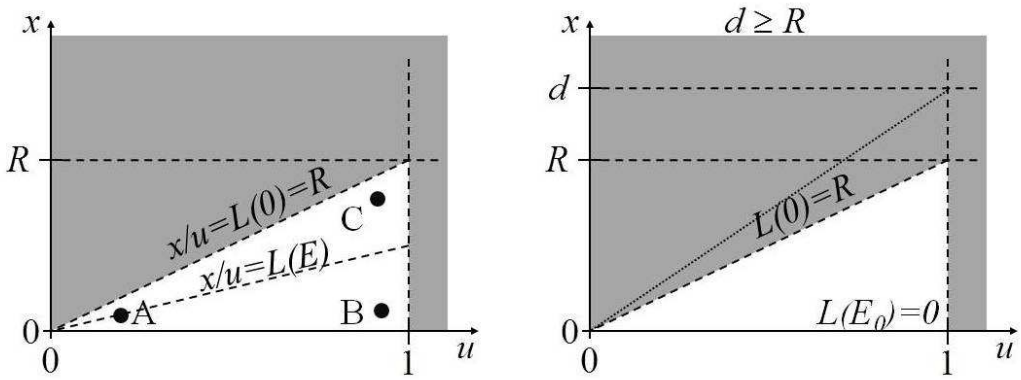


Figure 3.31: PHS *variable space* and PHS *variable space* when $d \geq R$.

If $d > R$ the variable $x$ can explore the interval $x \in [0, R]$. This is the case of the PHS in Figure 3.30, where $d = 4\,\mu m$, $R_{Li(830KeV)} = 1.7\,\mu m$ and $R_{\alpha(1470KeV)} = 3.4\,\mu m$. We take the two particles of the 94% branching ratio of $^{10}B$ reaction as example.
If $d < R$, the variable $x$ can explore the interval $x \in [0, d]$ (see Figure 3.32), thus the domain is now a trapezoid. The events near the line $\frac{x}{u} = L(E^*) = d$, which is the switching condition

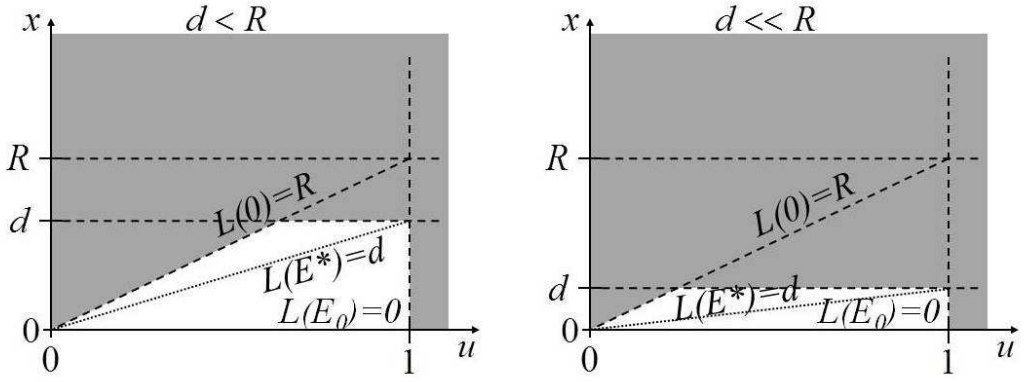


Figure 3.32: PHS *variable space* for $d < R$ and $d << R$.

found in the Equations 3.74 and 3.75, give rise to a peak because this line has the *maximum length available*. Thus, we expect a peak in the PHS around $E^*$. This is shown in Figure 3.29 where $d = 1\,\mu m$ and, again, $R_{Li(830KeV)} = 1.7\,\mu m$ and $R_{\alpha(1470KeV)} = 3.4\,\mu m$, the peaks that originate from the condition $\frac{x}{u} = L(E^*) = d$ for the two particles are indicated by the arrows.
If $d \geq R$, the peak occurs for $L(E^*) = R$, that is, zero energy. This is problematic for $\gamma$-ray to neutron discrimination.
If $d << R$, the variable space is compressed and the straight lines identified by $\frac{x}{u} = L(E^*) = d$ and $\frac{x}{u} = L(E) = 0$ become more and more similar. The two peaks approach and, the more $d$ is negligible compared to $R$, the more the two peaks appears as one single peak (see Figure 3.28).
If we want to avoid a strong presence of neutrons in the low energy range of the PHS, where we know the $\gamma$-rays contamination is strong, it is important to try to get the second peak higher than the energy threshold ($E_{Th}$). This implies that the thickness $d$ of any layer in the detector should obey $d < L(E_{Th})$ for the $L$ corresponding to the particle with the smallest range. This can be a contradictory requirement with efficiency optimization in which case a compromise between $\gamma$-rays rejection and efficiency has to be found.

### 3.6.2 Transmission mode

Equations for transmission mode can be calculated in the same way they have been determined for back-scattering mode by substituting $x$ with $d - y$ in the Expression 3.64 and $x$ with $y$ in the expression $\delta\left(\frac{x}{u} - L\right)$. As a result we obtain:

$$P(L)\,dL = \begin{cases} \frac{1}{2L^2}\left(\frac{1}{\Sigma}e^{-\Sigma\cdot d} + (L - \frac{1}{\Sigma})e^{-\Sigma\cdot(d-L)}\right)\,dL & \text{if } L \leq d \\ \frac{1}{2L^2}\left(\frac{1}{\Sigma}e^{-\Sigma\cdot d} + (d - \frac{1}{\Sigma})\right)\,dL & \text{if } L > d \end{cases} \tag{3.76}$$

Hence, $Q(E)dE$ can be calculated as shown already in Section 3.6.1.
However the same conclusions can be drawn concerning the qualitative aspects of the PHS especially the position of the two peaks.

# Chapter 4

# Converters at grazing angles

The ideas in this Chapter were born in October 2012, when a discussion between Philipp Gutfreund and me led us to the question: do the boron converters we are using in detectors reflect neutrons destroying any possibility to increase the layers' efficiency? A complete investigation has been made in the next 6 months and it has led to the discovery of the limits of the solid converter technology used at grazing angle. I want to thank Carina Höglund for the samples. I want to thank Philipp Gutfreund for the time he let me use the D17 reflectometer at ILL, I want to thank my colleague Anton Khaplanov, for the discussion and the support in this study. At last, I want to thank Anton Devishvili, Andrew Dennison and Boris Toperverg for the time spent on the reflectometer SuperAdam at ILL and for their important suggestions.

## 4.1 Introduction

In Chapter 3 we developed an analytical model to calculate the efficiency of a solid converter as a function of several parameters. We have already demonstrated that the two parameters $\theta$, the angle under which the neutrons hit the converter layer, and $\lambda$, their wavelength, enter in the calculations as a single parameter $\Sigma$ (Equation 3.10). This means that same features on the PHS or in the efficiency can be found either by acting on the neutron wavelength or on the angle $\theta$.
We can, for instance, fix the $\lambda$ and vary the angle. From the derivation of the physics of neutron conversion layer explained in Section 3.2.2 we can observe that, as $\theta$ decreases, the efficiency increases. Figure 4.1 shows the efficiency for a single back-scattering layer and for a single transmission layer as a function of $\theta$ for two neutron wavelengths: 1.8 Å, 10 Å and 25 Å. These neutron wavelengths were chosen to cover the usual neutron wavelength range used in a neutron reflectometer instrument. The layers are $1\,\mu m$ thick and consist of 100% enriched $^{10}B_4C$ ($\rho = 2.24 g/cm^3$). An energy threshold of $100\,KeV$ is applied.

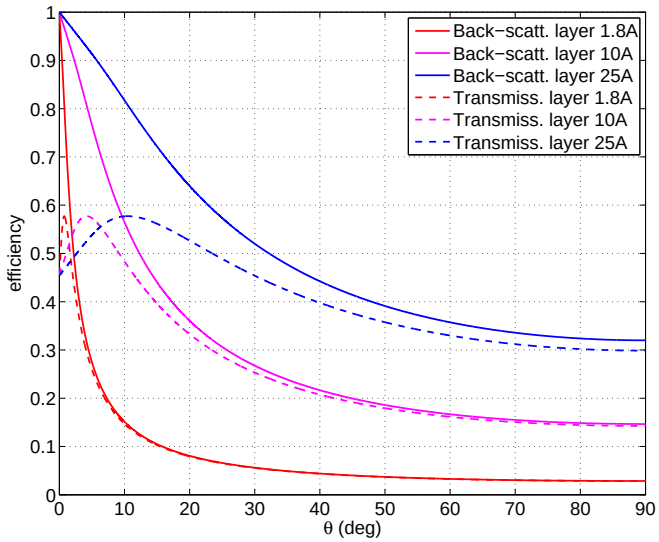


Figure 4.1: Efficiency for a single layer $1\,\mu m$ thick $^{10}B_4C$ as a function of the neutron incidence angle. Energy threshold of $100\,KeV$ is applied.

The efficiency for a back-scattering layer according to the theory can, in principle, reach 1 for a sufficiently small angle. When $\theta$ decreases (but not for $\theta = 0$) not only the effective layer thickness increases and consequently the absorption raises, but the source points where the charged particle are generated when a neutron is captured, are closer to the surface; therefore they have more chances to escape the layer.
On the other hand, for a transmission layer, as the angle decreases also the effective layer thickness increases starting absorbing neutrons without any increase in efficiency. In Figure 4.1, the transmission layer efficiency attains a maximum at low angle, and then starts decreasing again.
These calculations however do not take into account the potential reflection of the neutron by the conversion layer.

It is important to consider neutron reflection in the efficiency calculation when a detector involves converters at grazing angle.
Layer roughness has to be taken into account because it can affect the neutron reflection.

## 4.2 Reflection of neutrons by absorbing materials

Materials such as $Cd$ and $Gd$ or $^{10}B$, which are very strong absorbers of neutrons, can still have significant reflectivities. As shown in Section 1.5, the scattering and the absorbtion cross-sections depend both on the complex phase shift $\eta$. For absorbing materials $|\eta| < 1$. Referring to Equation 1.59, even for a perfect absorber ($\eta = 0$) there is a contribution to the scattering cross-section. This effect is what is *shadow diffusion* [7].
We discussed in Section 1.5.4 the principles of reflection of neutrons at interfaces. When dealing with neutron absorbers the theory describing the physical process of reflection has to be modified to take into account, not only the possibility for a neutron to be scattered, but also its absorption by nuclei. As introduced in Chapter 1, the scattering length of a nucleus is, in general, a complex quantity. Its real and imaginary parts can be associated to the scattering process but only its imaginary part to the absorption (see Equation 1.63).

$$b_{tot} = b_{coh} = b'_{coh} + i\, b''_{coh} \tag{4.1}$$

where we take only the coherent scattering length for both real and imaginary parts because we suppose either the sample or the neutrons to be unpolarized (Equation 1.62), and we will average over the bulk to obtain an effective potential description.
The scalar potential $V$ (Equation 1.72) in the Schrödinger equation will contain the contribution given by the absorption:

$$V = \frac{2\pi\hbar^2}{m_n}\left(N_b^{real} + i\, N_b^{im}\right) \tag{4.2}$$

The potential the neutron experiences at the interface is now complex. To model absorption we are violating unitarity in the Schrödinger equation: it is a trick that works.
The solutions of the Schrödinger equation, with a complex potential, can still be written as shown in Section 1.5.4. The wave-vectors will be complex quantities. Referring to Equation 1.80, the change in the normal wave-vector has an imaginary part given by the complex potential that results into an exponentially reduced amplitude of the wave-function [39]. Note that if $N_b$ is purely imaginary (a perfectly absorbent material) it still gives a contribution to the change in the normal wave-vector (the square root of a purely imaginary number does have a real part). With absorption, even in the total reflection regime ($q < q_c$), a neutron wave (this time not evanescent, see Equation 1.86) can penetrate inside the layer reducing the total reflection amplitude to less than 1.
In the absorbing regime the characteristic depth a neutron can penetrate the layer before being absorbed is given by:

$$D = \frac{1}{Im\left\{k_{t\perp}\right\}} \tag{4.3}$$

As example we take enriched $^{10}B_4C$ ($\rho = 2.24\, g/cm^3$) to which corresponds a scattering length density of $N_b = (1.62 - i\,1.11)\cdot 10^{-6}$ Å$^{-2}$. For simplicity we imagine a bulk of $^{10}B_4C$ of constant $N_b$. In Figure 4.2 the scattering length density profiles at the interface air/$^{10}B_4C$ are shown on the left and the corresponding reflectivities are shown on the right.

By neglecting the imaginary part of the $N_b$, reflectivity is 1 when $q < q_c$, and it behaves like $\propto 1/q^4$ for large $q$. When $N_b$ is, on the other hand, complex the reflectivity below $q_c$ is reduced. For those materials having a negligible absorption cross section, absorption does not significantly reduce the reflectivity.

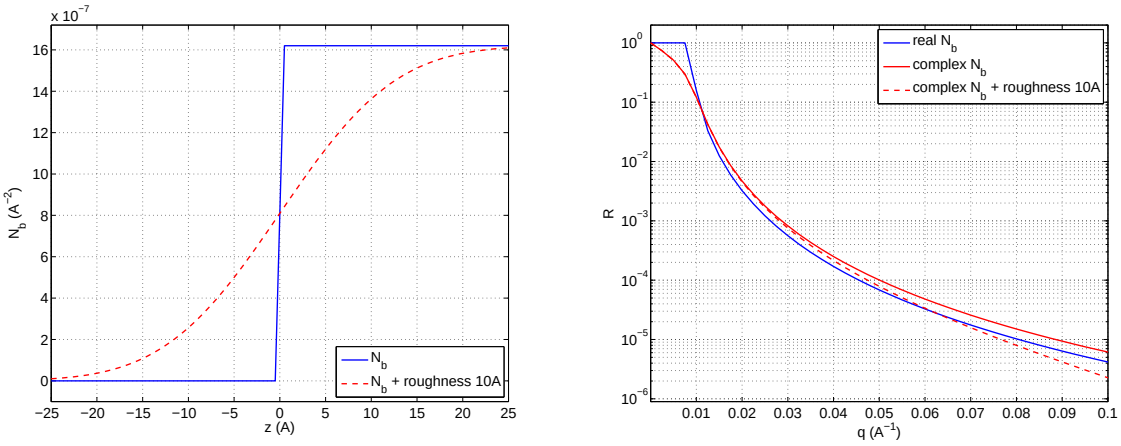


Figure 4.2: Scattering Length Density ($N_b$) for $^{10}B_4C$ omitting or not the interface roughness (left) and the corresponding reflectivities (right).

Figure 4.2 shows also what happens to the reflectivity when a roughness of $\sigma = 10$Å is considered at the air/$^{10}B_4C$ interface: intensity drops at high $q$. Note that the contribution given by the absorption affects the entire $q$-range while roughness has an influence only at high $q$.
The reflectivity profile can still be measured arbitrary in ToF or in monochromatic mode without affecting the results (if we can assume constant imaginary scattering length density, meaning there are no absorption resonances). We observe from Equation 1.76 that only the normal component of the wave-vector $k_{i\perp}$ is affected by the potential, for both complex and real cases. Moreover, excluding resonances, this potential does not depend on the neutron wavelength (Equations 1.72 and 1.73), because $b_{abs}$ does not depend on $\lambda$. The reflectivity then only depends on $\theta$ and $\lambda$ through $k_{i\perp} = \frac{q}{2}$, so whatever method (ToF or monochromatic) is used to get a value for the measured reflectivity the result is the same for same $q$, even if the material is a strong absorber. Neutron reflectometry at grazing angle by using thermal neutrons gives the same reflectivity profile as UCN (Ultra Cold Neutron) reflectometry at large angles if the resulting $k_{i\perp}$ is kept the same for both techniques.
The continuity equation 1.83 in the region where the material is an absorber has to be generalized as [8]:

$$\frac{\partial P(\bar{r},t)}{\partial t} + \nabla \cdot J(\bar{r},t) = -\frac{2}{\hbar} P(\bar{r},t) Im\{V\} \qquad \Longrightarrow \qquad \nabla \cdot J(\bar{r},t) = -\frac{4\pi\hbar}{m_n} P(\bar{r},t) N_b^{im} \quad (4.4)$$

assuming stationarity: $\frac{\partial P(\bar{r},t)}{\partial t} = 0$. The probability for a certain number of neutrons to be absorbed, $A$, is given by the integral over the entire volume of absorbing material, which in a one-dimensional case, reduces to:

$$A = \frac{m_n}{\hbar k_1} \int_0^d \nabla \cdot J(z,t)\, dz = -\frac{4\pi}{k_1} \int_0^d P(z,t) N_b^{im}\, dz = -\frac{4\pi}{k_1} \int_0^d |Y_z|^2 N_b^{im}\, dz \quad (4.5)$$

where $d$ is the thickness of the absorbing layer and $N_b^{im}$ is the imaginary part of the scattering length density of the absorbing medium.
Since we want to measure reflectivity of absorbers employed in neutron detectors; they are generally thin layers deposited on holding substrates.
Let us consider a finite thickness as in [40], $d$, of absorbing material deposited on a substrate, e.g. Silicon or Aluminium. Excluding resonances, the solutions of the Schrödinger equation can be written as shown in Section 1.5.4, and we can focus only on the normal components of the wave-functions:

$$\begin{aligned} \Psi_z &= e^{+i\,k_1 z} + r_1\, e^{-i\,k_1 z} && \text{if } z < 0 \\ Y_z &= t_2\, e^{+i\,k_2 z} + r_2\, e^{-i\,k_2 z} && \text{if } 0 < z < d \\ \Phi_z &= t_3\, e^{+i\,k_3 z} && \text{if } z > d \end{aligned} \tag{4.6}$$

where we have called $k_{n\perp} = k_n$ with $n = 1, 2, 3$, the normal component of the wave-vectors in the three regions defined by the potentials $V_n$ (see Figure 4.3).

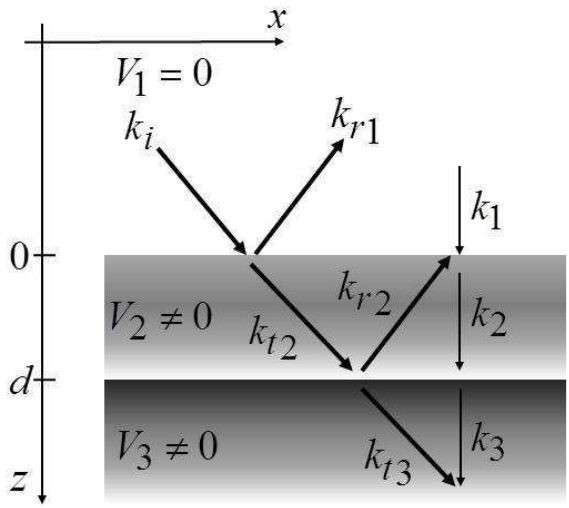


Figure 4.3: Reflection of an incident neutron beam from an ideally flat interface, $k_1$, $k_2$ and $k_3$ are the normal component of the wave-vectors in the three regions.

By imposing conservation of energy at the interfaces, as already shown in Section 1.5.4 (Equation 1.80), we obtain:

$$\begin{aligned} k_1 &= \frac{1}{2} q \\ k_2^2 &= k_1^2 - 4\pi N_b^{(2)} \\ k_3^2 &= k_1^2 - 4\pi N_b^{(3)} \end{aligned} \tag{4.7}$$

where $N_b^{(2)}$ and $N_b^{(3)}$ are the SLD (Scattering Length Density) of the absorbing layer and the substrate respectively.
Consequently, by imposing the continuity of the wave-function and its derivative at the two

boundaries ($z = 0$ and $z = d$), we obtain:

$$\begin{aligned} r_1 &= t_2 + r_2 - 1 \qquad & r_2 &= \frac{\alpha_{12}\beta_{23}\delta}{1+\beta_{12}\beta_{23}\delta} \\ t_2 &= \frac{\alpha_{12}}{1+\beta_{12}\beta_{23}\delta} \qquad & t_3 &= e^{-i(k_3+k_2)d} \cdot \frac{(1+\beta_{23})\,\alpha_{12}\delta}{1+\beta_{12}\beta_{23}\delta} \end{aligned} \tag{4.8}$$

where we have defined the Fresnel transmission coefficients as $\alpha_{ij} = \frac{2k_i}{k_i+k_j}$, the reflection coefficients $\beta_{ij} = \frac{k_i-k_j}{k_i+k_j}$ and $\delta = e^{+2ik_2d}$.
The reflection and transmission probabilities are given by:

$$R = \frac{|J_r|}{|J_i|}, \qquad T = \frac{|J_t|}{|J_i|} \tag{4.9}$$

with

$$|J_i| = \frac{\hbar\, k_1}{m_n}, \qquad |J_r| = \frac{\hbar\, k_1}{m_n}\,(r_1 \cdot r_1^*)\,, \qquad |J_t| = \frac{\hbar\, k_3}{m_n}\,(t_3 \cdot t_3^*) \tag{4.10}$$

Outside the absorbing regions the Equations 1.84 are still valid. Referring to Figure 4.3 if the first medium is air, the second is an absorber ($V_2$ is complex) and the third is a substrate such as Silicon ($V_3$ is real); the measured reflectivity, the transmission inside the substrate and the absorption in the layer are:

$$\begin{aligned} R &= r_1 \cdot r_1^* \\ T &= \frac{k_3}{k_1}\,(t_3 \cdot t_3^*) \\ A &= 1 - R - T = \frac{1}{k_1}\int_0^d \nabla \cdot J_2(z,t)\,dz = -\frac{4\pi}{k_1}\int_0^d |Y_z|^2 N_b^{im}\,dz \end{aligned} \tag{4.11}$$

where $J_2$ is the current probability calculated for $Y_z$.
As example we take the same absorber as in Figure 4.2; in this case the $^{10}B_4C$ is $d = 100\,nm$ thick and it is deposited on Si ($N_b = 2.14 \cdot 10^{-6}\,\text{Å}^{-2}$). In Figure 4.4, on the left we show reflectivity, transmission and absorption, as calculated in Equation 4.11 as a function of $q$. On the right we show the probability for a neutron, carrying a given $q$, to be absorbed at certain depth in the layer, i.e. the quantity $-\frac{4\pi}{k_1}|Y_z|^2 N_b^{im}$. We notice that absorption increases in proximity of the critical edge ($q_c$) that is, in this case about $q_c = 0.01\,\text{Å}^{-1}$.

## 4.3 Corrected efficiency for reflection

The neutron efficiency for a single layer of $1\,\mu m$ $^{10}B_4C$ has been measured as a function of the neutron incidence angle $\theta$ for a given neutron wavelength of 2.5 Å on our neutron test beam line CT2 at ILL.
The converter layer was mounted in a MWPC of about $100\,cm^2$ operated at $1bar$ of $CF_4$. After calibration and Plateau measurement we chose $1300V$ as the working voltage. A neutron beam of $2 \times 3\,mm^2$ was focused on the detector and a PHS was measured as a function of the incidence angle. In Figure 4.5 the measured PHS for a single back-scattering layer is shown.
The calculation assumes no reflection. The increase in detection efficiency can be calculated

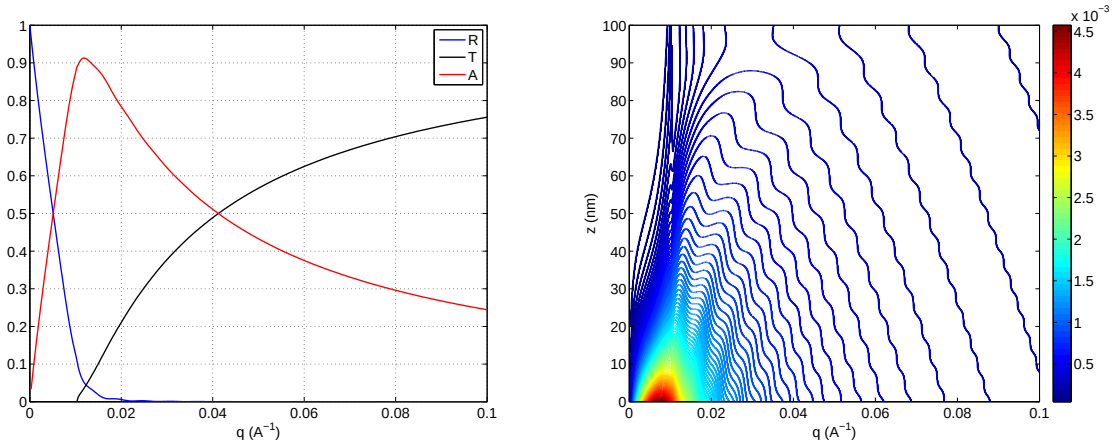


Figure 4.4: Reflectivity, Transmission and Absorption from a $d = 100\,nm$ $^{10}B_4C$ layer deposited on Si (left), probability for a neutron to be absorbed in the layer as a function of $z$ and $q$ (right).

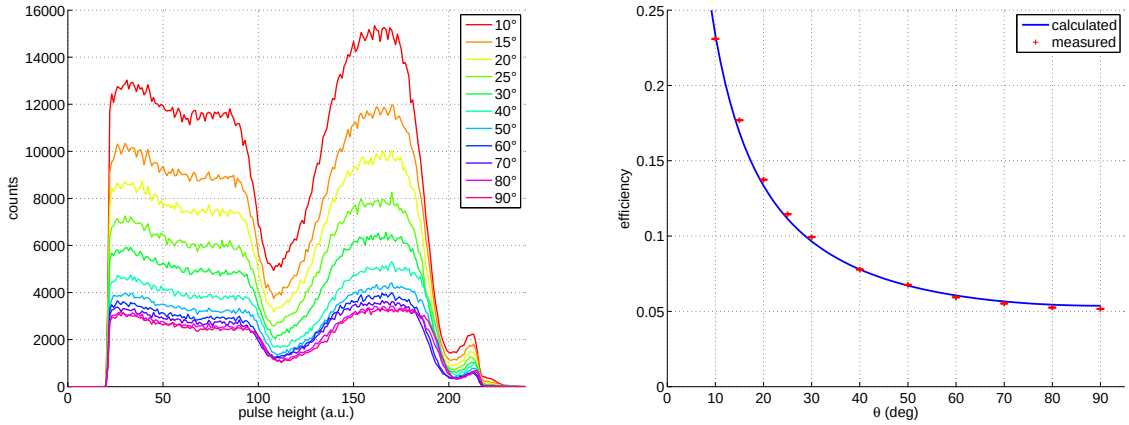


Figure 4.5: PHS and efficiency measured at 2.5 Å for a $1\,\mu m$ $^{10}B_4C$ back-scattering layer operated in a MWPC.

according to Equation 3.70 in Section 3.6.1. The resulting measured and calculated neutron detection efficiency is shown in Figure 4.5.
When we deal with detectors that involve converters at grazing angle, the formulae derived in Chapter 3 for the detection efficiency have to be replaced by:

$$\varepsilon_R\,(d,\theta,\lambda) = (1 - R(\theta,\lambda)) \cdot \varepsilon\,(d,\theta,\lambda) \tag{4.12}$$

where $R$ is the neutron reflectivity that becomes significant at cold neutron wavelength or at very small angle. In general for $\theta > 2°$ neutron reflection can be neglected ($R \approx 0$) in the thermal-cold neutron wavelength range. As we will discuss, there is a way to reduce the reflectivity factor ($R$) at smaller than 2° angles, by acting on the layer surface roughness.
In Figure 4.6 we plot the calculated factors $(1 - R(\theta,\lambda))$ according to the Equations 1.85 in Section 1.5.4 in Chapter 1 given that $q = \frac{4\pi}{\lambda}\sin(\theta)$. We take as example a $1\,\mu m$ $^{10}B_4C$ layer, that we can consider bulk, of Scattering Length Density $N_b = (1.6 - 1.11\,i) \cdot 10^{-6}$ Å$^{-2}$ ($\rho = 2.24 g/cm^3$).

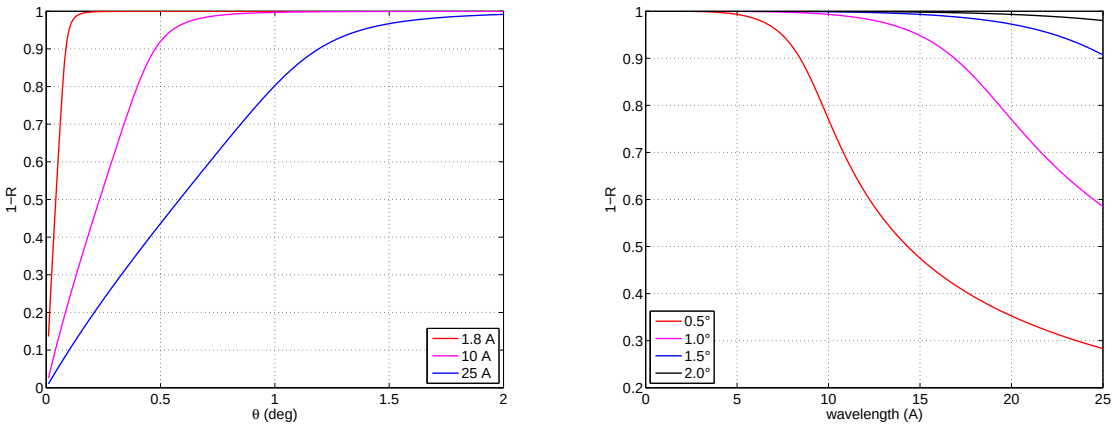


Figure 4.6: Factor $1-R$ for a $1\,\mu m$ $^{10}B_4C$ layer ($N_b = 1.6 - 1.11\,i$) as a function of $\theta$ (left) and as a function of neutron wavelength (right).

We notice that for application that involve cold neutron wavelength such as 25 Å the detection efficiency is limited to be at most 60% and not 1 if the detector employs 1° as converting angle. In order to study experimentally the neutron reflectivity of thin-films neutron converters, two sets of data have been recorded. The first set of data was taken using D17 [41] at ILL which is a ToF reflectometer to preliminary quantify the actual reflectivity of the coatings. A second experiment has been performed on SuperAdam [42] at ILL, which is a monochromatic reflectometer ($\lambda = 4.4\,$Å) in a more complete setup. The two experiments allowed to compare the two techniques (ToF and monochromatic) in addition to give information on neutron converter reflectivity. The comparison let us to verify the theoretical predictions in Section 1.5.4.
The coatings were fabricated in Linköping University by the Thin Film Physics Division [37], [43] by sputtering technique (PVD). The $^{10}B_4C$ layers have been deposited either on several $Al$ alloys or on $Si$ wafers for preliminary characterizations. Examples of those samples are shown in Figure 4.7. The $Si$ samples look shiny while the higher roughness of the $Al$ alloy makes the $Al$ samples matte. Moreover, we had two different $Al$-alloys for the $1\,\mu m$ sample with different layer roughness (see Figure 4.7).
Physical vapor deposition (PVD) is a technique for thin film synthesis under vacuum conditions, where a solid or liquid deposition material is vaporized and its condensation on a substrate forms a film. Chemical reactions are usually absent in the gas phase, due to the small probability for collisions of the vapor species under the applied pressures. The usual physical mechanisms for source atoms to enter the gas phase are high temperature evaporation or sputtering. $^{10}B_4C$ films were grown in high vacuum chambers by reactive magnetron sputter deposition.
To minimize the amount of impurities in the films it is necessary to have good vacuum conditions in the deposition chamber. All films we discuss here are deposited at base pressures of $0.1\,mPa$ [43].
Ion beam analysis is used for determination of the concentration of specific elements in a sample. Thickness, compositional gradients and depth positions of different elements can also be determined. Elastic recoil detection analysis (ERDA) was used. This technique is based on elastic scattering of incoming ions with the target atoms. In ERDA the energy of the knocked out target atom is detected. ERDA is good for depth profiling and analysis of elements with

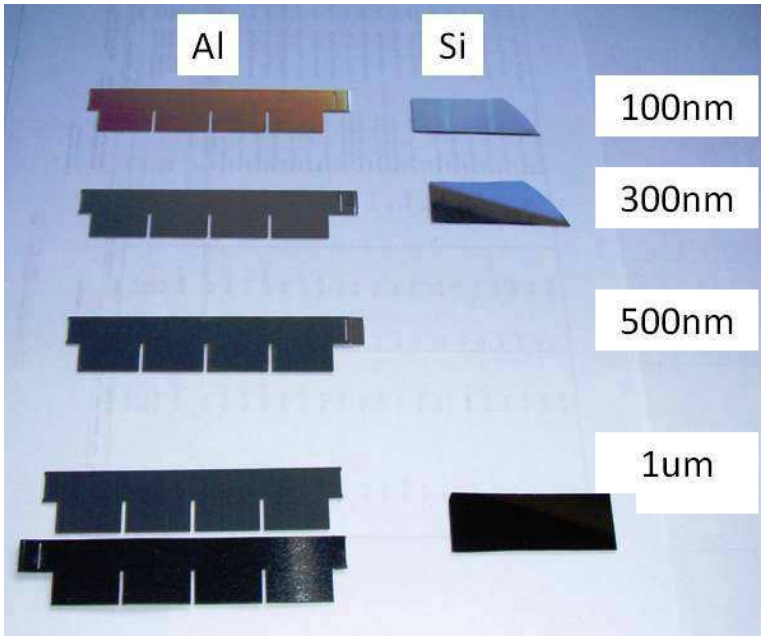


Figure 4.7: Samples of $Al$ and $Si$ coated with different thicknesses of $^{10}B_4C$ layer [37].

a mass smaller than the mass of the incoming heavy ions. In the present setup the relative concentrations of element was measured at $\sim 2\%$ in ERDA [43],[37].

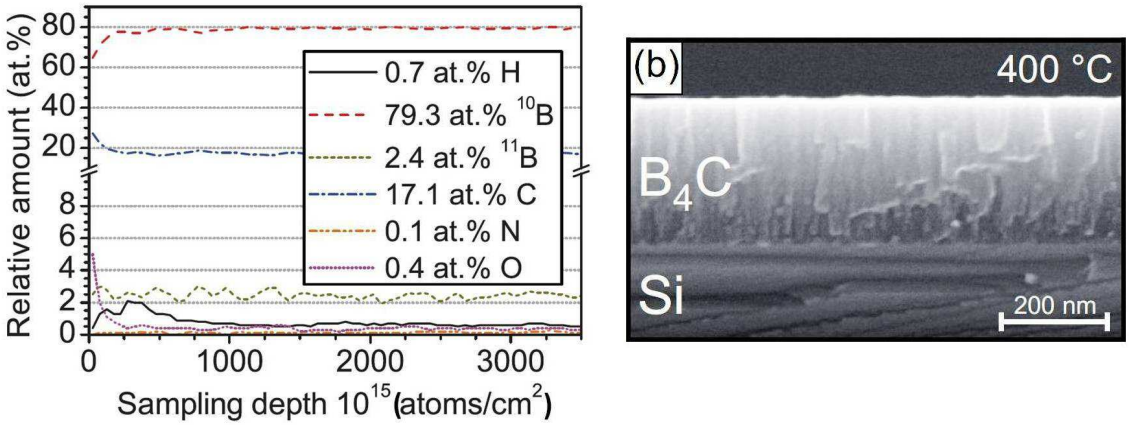


Figure 4.8: $^{10}B_4C$ film composition and a SEM image of a $^{nat}B_4C$ layer on $Si$. The x-axis correspond to about $270\,nm$ of sampling depth [37].

In Figure 4.8 the relative amount of elements in a typical $^{10}B_4C$ film is plotted as a function of the layer depth. The conversion between the x-axis and the actual depth is given by:

$$d = \frac{x \cdot M_r}{\rho \cdot N_A} \tag{4.13}$$

where $M_r$ is the molar mass of the $^{10}B_4C$ layer, $\rho$ its density and $N_A$ is the Avogadro's number. Referring to Figure 4.8 and using the Equation 4.13, we are sampling about $270\,nm$ on the full scale of x-axis.
According to Equation 1.73 and considering the composition given in Figure 4.8, the scattering length density of such a layer is: $N_b = \sum_i b_i n_i = (1.6 - 1.11\,i) \cdot 10^{-6}\,\text{Å}^{-2}$ ($\rho = 2.24 g/cm^3$). We use as scattering length density for $Si$ the standard value of $N_b = 2.14 \cdot 10^{-6}\,\text{Å}^{-2}$ and for $Al$ $N_b = 2.07 \cdot 10^{-6}\,\text{Å}^{-2}$.
The first experiment has been performed on the D17 instrument [41], a Time-of-Flight reflectometer at ILL, on $1\,\mu m$ samples deposited on both $Si$ and $Al$ (see Figure 4.7). Reflectivity profiles have been measured for three angles $\theta = 0.5°, 1°, 2°$ in ToF-mode between $\lambda = 2$Å and $\lambda = 25$Å. The resulting range in momentum transfer is from $q = 0.005\text{Å}^{-1}$ up to $q = 0.2\text{Å}^{-1}$ with a resolution of $\Delta q = 0.05\text{Å}^{-1}$ in the worst case. The reflected intensity (and the direct beam) in ToF can be measured without scanning in angle but just acquiring the neutron wavelength spectrum at once. The reflectivity is calculated as the ratio between the reflected and the direct wavelength spectra.
In ToF the background is uncorrelated with the instrument timing and it can be evaluated by looking at a region of the detector where we are sure there is no reflection and checking that it has no time structure. This background has been subtracted to the reflected and the direct beam spectra.
No specular reflection has been observed on all the $Al$-samples, on the other hand $Si$ has a strong reflectivity and it is shown in Figure 4.9 as a function of $q$ (pink curve).

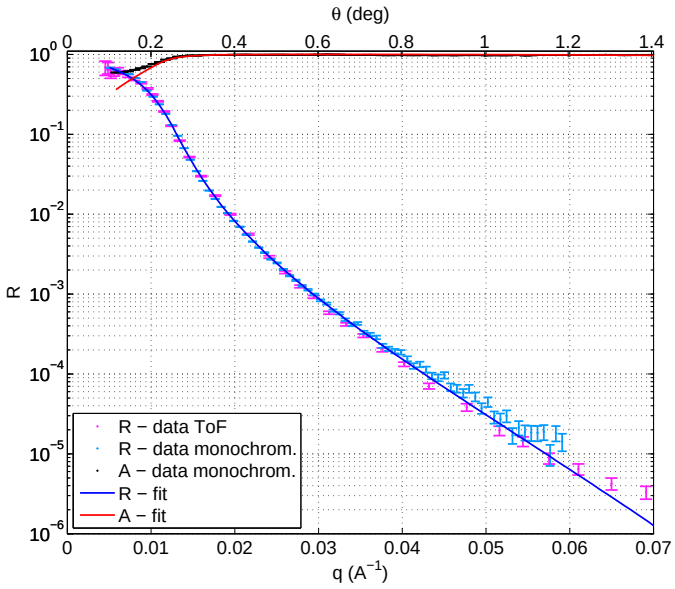


Figure 4.9: Measured reflectivity for the $1\,\mu m$ $^{10}B_4C$ sample on $Si$ as a function of $q$; pink curve has been obtained from a ToF measurement and cyan from monochromatic angular scan. Absorption was measured as well from the $\gamma$-ray yield.

We repeated the neutron reflectivity experiment by using the SuperAdam instrument [42] in monochromatic mode at $\lambda = 4.4$Å. A scan in angle has been performed to get the reflectivity profile in $q$. We measured in addition to the $1\,\mu m$ samples, one extra sample of $100\,nm$ deposited on a $Si$ substrate.

Not only neutron reflectivity has been measured but, neutron absorption has been measured as well, thanks to the $\gamma$-ray yield of $^{10}B$. We recall that in the 94% of the cases when a neutron is captured by a $^{10}B$-atom a $478\,KeV$ $\gamma$-ray is produced and emitted isotropically. In Figure 4.10 is shown a sketch of the experiment performed on SuperAdam. A Germanium detector was placed close to the sample in order to maximize the solid angle without affecting the neutron beam. Taking into account both the Ge-detector efficiency and the solid angle, we estimate the whole efficiency for the $478\,KeV$ $\gamma$-ray photo-peak detection to be around 5%. The Ge-detector has been calibrated in energy by using a $^{22}Na$ source.

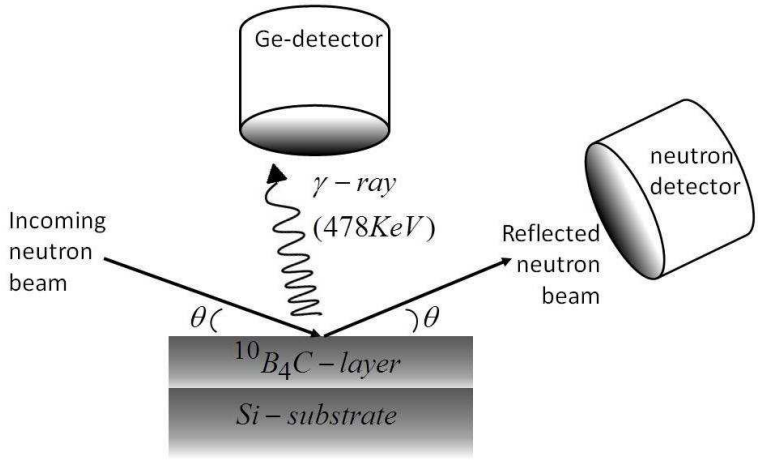


Figure 4.10: Schematic of the experiment on SuperAdam.

For a given sample we record for each angle during the scan a spectrum for the Ge-detector and a neutron detector image of the reflected neutrons knowing the actual normalization given by the direct beam.
Each point of the absorption curve has been obtained by fitting the Ge-detector spectrum, around the $478\,KeV$ $\gamma$-ray photo-peak, with a model that includes a linear background. The latter is subtracted from the actual number of counts and it takes into account a Compton background deriving from other $\gamma$-ray energies.
For small $q$ (small $\theta$), there is an overlap between the direct beam and the reflection images. The raw image is projected over the $x$-axis and fitted. Reflected intensities have been fitted using a double gaussian in order to decouple the reflected beam from the direct beam. Figure 4.11 shows an example of this fit for a given angle. The raw image of the detector shows the two peaks: on the left, it is the reflected beam and, on the right, the direct beam through the sample. The number of counts in the reflected peak is then obtained by the fitting parameters: $a$ the gaussian amplitude, $m$ its center and its standard deviation $\sigma$, through $\sqrt{2\pi}\,a\sigma$.
At higher $q$, higher $\theta$, the direct beam is far from the reflected beam on the detector. Usually the background is not symmetric under the reflected peak but it is more intense on the side of the direct beam. In order to subtract this contribution from the reflected intensity, it has been fitted with a single gaussian and a linear background fit. The intensity is again obtained from the fit parameters.
On a standard reflectivity measurement the angular scan starts from zero and rises up to one or few degrees; since the sample length is not infinite there will be a certain point in the scan when

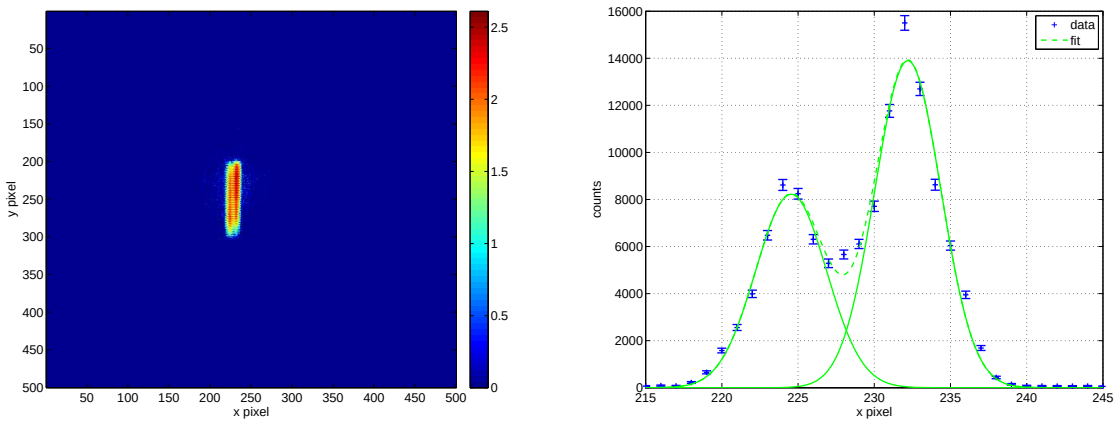


Figure 4.11: Raw image of the SuperAdam detector (left), projeceted intensities over the $x$-axis and the double gaussian fit (right).

the size of our beam coincides with the actual projected size of the sample, this is the so-called over-illumination angle ($\theta_{over}$). Therefore the raw intensity of the reflection rises until $\theta_{over}$ and then behaves as an absolute reflectivity profile. Hence a data correction has to be taken into account in order to transform the intensity of the reflection into reflectivity. Moreover, on SuperAdam the angles are known with an error of $0.2\,mrad$; thus a slight shift in the position of the angle is accepted and also the quantity $\theta_{shift}$ is a free fitting parameter.
The model considered to fit the data is the one explained in in Section 4.2 where a $^{10}B_4C$ layer is placed on a $Si$ substrate. This model is described in details in Appendix D.
The fitting routine is a standard reduced chi-square minimization that takes into account both absorption and reflectivity profiles at the same time. The measurements contain about 150 points for each curve and $\theta_{over}$, $\theta_{shift}$, $^{10}B_4C$ scattering length density (real and imaginary parts), layer roughness $\sigma_r$, thickness, and Ge-detector efficiency are the free fitting parameters.
Figure 4.12 shows the reflectivity and absorption profiles for the $100\,nm$ $^{10}B_4C$ sample on $Si$. In Table 4.1 the fitting parameters obtained are listed.
We suppose the fitting parameters to be independent of each other. We fix the complete set of parameters as obtained by the chi-square minimization. We modify one parameter at once until the chi-square increases by 1. We take this as the associated error in the parameter estimation.
Referring to Figure 4.9, we can observe that the reflectivity as measured in a ToF instrument or using angular scan in monochromatic mode is the same apart from a background tail at higher $q$ values. This is the experimental confirmation of what mentioned in Section 1.5.4, only the normal component of the wave-vector is affected by the layer independent of what $\theta$ and $\lambda$ combination is used, and even in the case of strong absorbing layers.
No layer thickness value has been found for the thicker film because it can be considered as bulk. Because of absorbtion not a single neutron can reach the substrate and can be reflected toward the detector. The thinner layer thickness parameter is estimated to be $(121 \pm 2)nm$ thick with a reduced $\chi^2$ of 1.2. The fitting routine on the $1\,\mu m$ sample ends up with a worse $\chi^2$ of about 20.
Referring to Figure 4.9, the absorption measured at low angles is higher than foreseen by the model because of the presence of more converter material exposed to the beam and that is not taken into account by the model used to fit the data. The presence of this additional $^{10}B_4C$, on

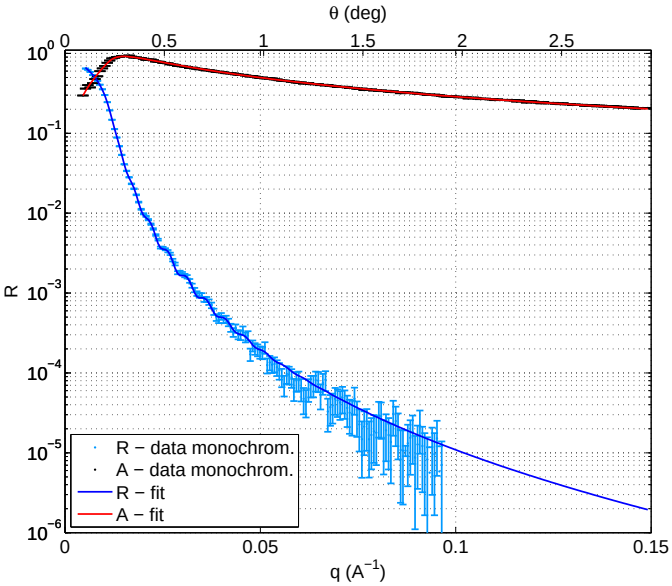


Figure 4.12: Measured reflectivity for the $100\,nm$ $^{10}B_4C$ sample on $Si$ as a function of $q$. Absorption was measured from the $\gamma$-ray yield.

the substrate back face and edge, is due to the deposition method.

| sample | d(nm) | $\theta_{over}(mrad)$ | $\theta_{shift}(mrad)$ | Ge eff.(%) | $\chi^2$ |
|---|---|---|---|---|---|
| $1\,\mu m$ $Si$ | bulk | $14.0 \pm 0.1$ | $0.22 \pm 0.02$ | $4.91 \pm 0.04$ | 20.7 |
| $100\,nm$ $Si$ | $121 \pm 2$ | $18.7 \pm 0.5$ | $0.74 \pm 0.04$ | $5.19 \pm 0.08$ | 1.2 |

| sample | $N_b(\text{Å}^{-2})$ | $\sigma_r(\text{Å})$ |
|---|---|---|
| $1\,\mu m$ $Si$ | $((2.48 \pm 0.02) - (1.01 \pm 0.02)i) \cdot 10^{-6}$ | $38 \pm 3$ |
| $100\,nm$ $Si$ | $((2.50 \pm 0.05) - (1.11 \pm 0.02)i) \cdot 10^{-6}$ | $45 \pm 9$ |

Table 4.1: Parameters found by the model fitting routine.

Expected SLD is $N_b = (1.6 - 1.11\,i) \cdot 10^{-6}\,\text{Å}^{-2}$, while the results for both samples is about $N_b = (2.5 - 1.1\,i) \cdot 10^{-6}\,\text{Å}^{-2}$. Note the significant difference in the real part and the good agreement for the imaginary part.
By neglecting minor contaminants in the sputtered layer, the imaginary part of the SLD is given entirely by $^{10}B$ while the real part is determined by $^{10}B$, $^{11}B$ and $^{12}C$ (see Table 1.2). The imaginary part of the fitted SLD corresponds to the calculated value based on the ERDA measurement which implies that the $^{10}B$ number density is in agreement and equals $n_{(^{10}B)} = 1 \cdot 10^{23} \frac{1}{cm^3}$ with an error of 6%.
Given that the scattering length of $^{11}B$ and $^{12}C$ are both equal to $6.65\,fm$, their ratio only matters in the mass density. The sum of their densities is determined by the real part of the SLD and the calculated density of $^{10}B$, itself determined by the imaginary part. Respecting the error bars on the SLD given by the fit, this results in a restriction on the interval of the $^{10}B$ fraction and the mass density. They are listed in Table 4.2.
The measured ERDA values are outside the given intervals, and imply higher levels of non $^{10}B$

| $\rho\,(g/cm^3)$ | $\%\,^{10}B$ | $\%\,^{11}B + \%\,^{12}C$ |
|---|---|---|
| $[2.34, 2.46]$ | $[70, 73.5]$ | $[30, 26.5]$ |

Table 4.2: Ranges of density and composition compatible with the fitted SLD.

atoms. We do not explain the difference.
We only considered a uniform layer consisting of $^{10}B$, $^{11}B$ and $^{12}C$ in our model. It is true that the ERDA analysis, in Figure 4.8, shows a thin oxygen rich layer of about $20\,nm$ at the surface and some presence of hydrogen both on the few percent level. A priori such a thin layer should give interference fringes in the reflectivity profile around $q = 0.016\,\text{Å}^{-1}$ and $q = 0.047\,\text{Å}^{-1}$ which are totally absent in the data shown in Figure 4.9. This is why we did not include such an extra thin layer in the model.
Values picked within these intervals and inspired by the ERDA measurement are shown in Table 4.3.

| | $\rho\,(g/cm^3)$ | $\%\,^{10}B$ | $\%\,^{11}B$ | $\%\,^{12}C$ | others |
|---|---|---|---|---|---|
| ERDA | 2.24 | 79 | 2.4 | 17 | 1.6 |
| Reflectometry | 2.40 | 71.5 | 2.5 | 26 | 0 |

Table 4.3: Density and composition of the sputtered layers.

The samples of $1\,\mu m$ deposited on $Al$ have been also measured, but no specular reflection has been observed while absorption is comparable to what was observed on the $Si$-sample.
Off-specular reflection is not observed in any sample ($Si$ or $Al$), it is always below the background level.
In order to diminish the reflection effect in a detector, it is sufficient to have a rough surface ($> 100\,nm$). This can be of importance if one wants to build a detector based on micro-strips and solid converters. Operated at small angle, the absorber deposition on glass could not have a large enough roughness to avoid significant reflection.
It has to be pointed out that an excessive roughness will also degrade the efficiency. When the roughness becomes comparable to the fragments path lengths in the converter ($\sim 1\,\mu m$ for $^{10}B_4C$) the surface can not be considered flat anymore. The theory of the efficiency for converters under an angle was drawn assuming the layer to be flat. This flatness is essential for the neutron to encounter a lot of $^{10}B$, and the conversion fragments to be close to the surface to be able to escape. If the roughness starts to be comparable to the conversion fragments ranges, this assumption does not work anymore. There is a drop in the expected efficiency.
We repeat, in Figure 4.13, the ToF measured reflectivities as a function of of the neutron wavelength $\lambda$ (while in Figure 4.9 they are shown as a function of $q$). In Figure 4.13 we notice that if we use a converter at 1° (red curve) about 30% or more of the neutrons are reflected, thus not converted, for wavelengths larger than 20Å.
According to Equation 4.12 we can calculate the corrected efficiency for reflection. The plot in Figure 4.1 has to be modified as shown in Figure 4.14. We calculate the corrected efficiency, for an energy threshold of $100\,KeV$, for a $1\,\mu m$ thick $^{10}B_4C$ single back-scattering layer for three neutron wavelengths: 1.8 Å, 10 Å and 25 Å. According to what we found from the fit and summarized in Table 4.1, the layer roughness used is about 40 Å and the scattering length density is $N_b = (2.5 - 1.1\,i) \cdot 10^{-6}\,\text{Å}^{-2}$.

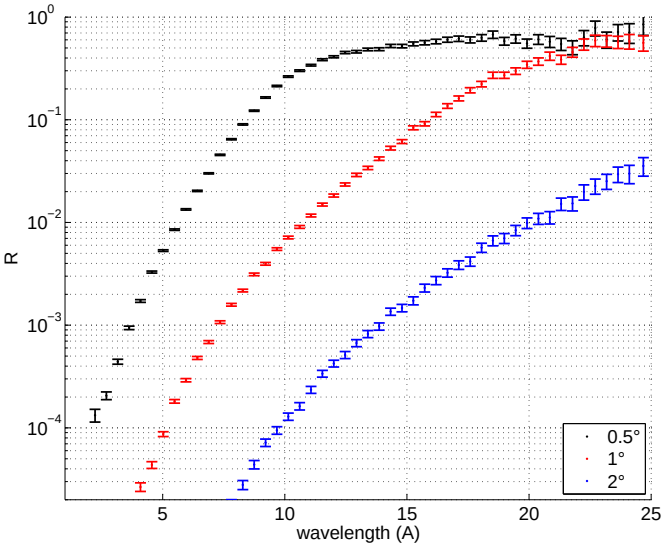


Figure 4.13: Measured reflectivity of $1\,\mu m$ $^{10}B_4C$ deposited on $Si$ as a function of $\lambda$ for 3 different angles.

We recall that, if the layer has a higher roughness, the effect of the reflection decreases. Aluminium is a suitable material to avoid neutron reflection instead of Silicon.

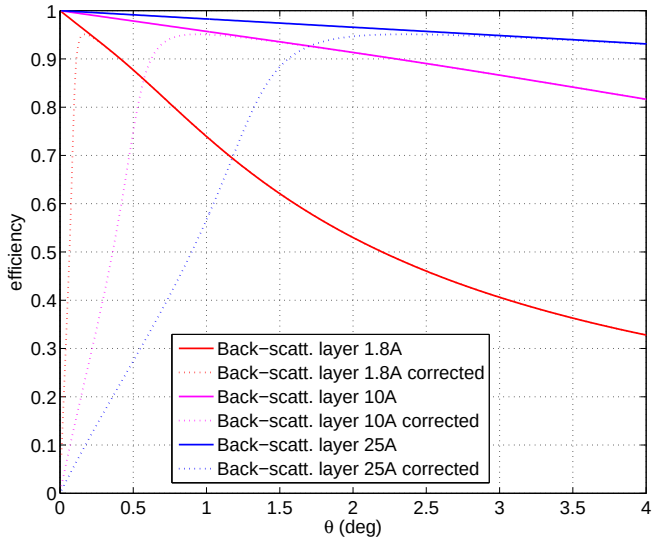


Figure 4.14: Corrected and not corrected efficiency for reflection calculated for a single layer $1\,\mu m$ thick $^{10}B_4C$ back-scattering layer at 1.8 Å, 10 Å and 25 Å as a function of the neutron incidence angle. Energy threshold applied: $100\,KeV$.

We observed a Doppler effect on the $478\,KeV$ $\gamma$-ray photo-peak due to the sample orientation. When a neutron is captured by $^{10}B$, it is the $^{7}Li$ fragment that, in the 94% branching ratio, goes in an excited state that emits the $\gamma$-ray. If $^{7}Li$ is emitted toward the substrate it is stopped

within about $120\,fs$, to be compared with the $^7Li^*$ half life of $t_{1/2} = 73\,fs$ before it goes to its ground state emitting the photon. A significant fraction of the $^7Li$ fragments will hence emit its photon when it is at rest. In a thin layer, if $^7Li$ is emitted toward the surface it travels in air for a much longer time. Then the $\gamma$-ray is also emitted when it is in motion. In a thick converter the volume to surface ratio is such that the fragment is almost always stopped, and a fraction of the photons are emitted when stopped. Referring to Figure 4.15, in the case A, a thick block of $B_4C$ rubber was placed in front of the Ge-detector. The spectrum measured is symmetric in energy. In Figure 4.15, the peak at $511\,KeV$ gives an indication of the Ge-detector energy resolution. All the measurements have been normalized to the intensity of the $478\,KeV$ $\gamma$-ray photo-peak to compare the peak shape.
When one of our samples is exposed to the beam, case B or C, the layer is thin enough to assure the fragments to always escape the layer. On average half of the times the $^7Li$ emits at rest and half of the times when travels either away from (B) (*red-shift*) or toward (C) (*blue-shift*) the Ge-detector. Consequently the $478\,KeV$ $\gamma$-ray photo-peak results asymmetric due to the Doppler shift.

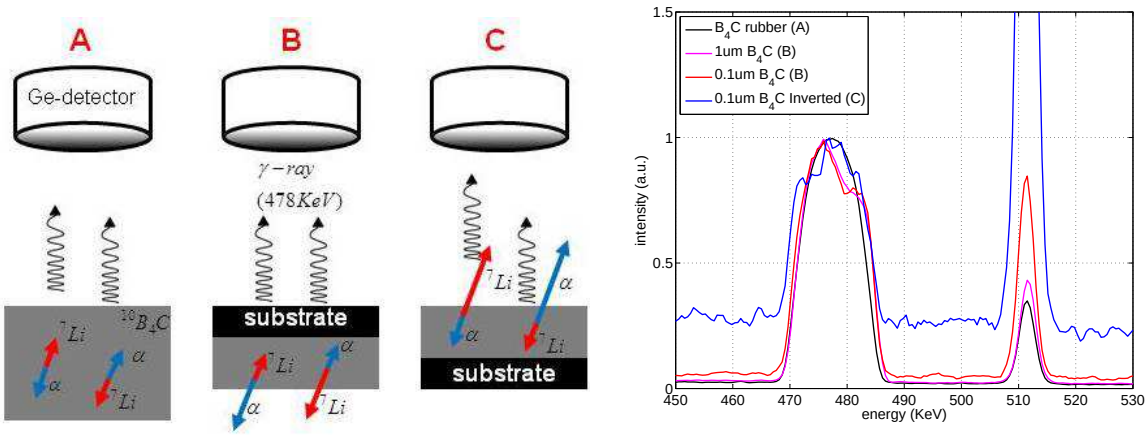


Figure 4.15: Setups used to measure the Doppler effect in the $478\,KeV$ $\gamma$-ray energy (left). Ge-detector spectrum: photo-peaks of $478\,KeV$ and $511\,KeV$ $\gamma$-rays (right).

# Chapter 5

# Gamma-ray sensitivity of neutron detectors based on solid converters

I want to thank Anton Khaplanov who taught me a lot about $\gamma$-rays. The work presented in this Chapter makes reference to the work in [44] and in [45].

## 5.1 Introduction

Any neutron detector is also a $\gamma$-ray detector. The aim of this Chapter is to individuate the characteristics that differentiate neutrons and background non-neutron events, e.g. $\gamma$-rays. In some cases it is possible to determine the origin of the electric signal, in other cases the two signals show the same time structure and same charge yield; hence it is not possible to distinguish them.
Different kinds of radiation can hit the detector and generate background, but $\gamma$-rays are the most common in neutron facilities. It is really likely for a neutron to excite any nucleus with the subsequent emission of $\gamma$-rays. Thus, a $\gamma$-ray background is always present in neutron facilities. Moreover at ILL, which is a reactor source, there is an important contribution that comes directly from the core.

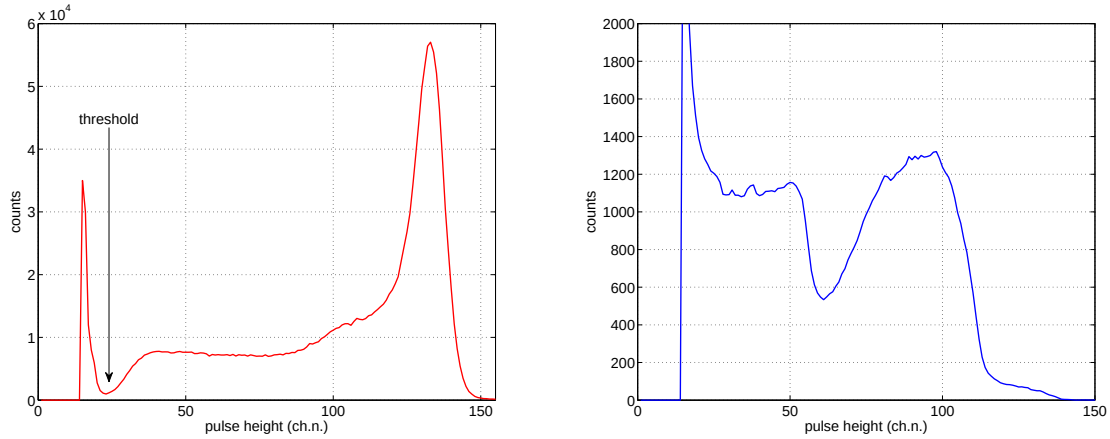


Figure 5.1: $^3He$ PHS (left) and $^{10}B$ PHS (right).

In $^3He$-based neutron detectors an efficient neutron to $\gamma$-ray discrimination can be easily done by applying an energy threshold. Figure 5.1 shows two PHS, one for $^3He$ and one for $^{10}B$. The standard discrimination of $\gamma$-ray and neutron events is by applying a threshold in the PHS. When a neutron is captured by $^3He$, the two fragments ionize directly the gas. Apart from the wall effect, they can always deposit their entire energy in the gas ($770\,KeV$), and even with the wall effect, a minimum energy is always deposited, equal to the triton energy.
Generally $\gamma$-rays can interact either with the wall of the detector or directly with the gas. Every time an electron is generated, by photoelectric absorption or Compton scattering, it ionizes the gas and gives rise to a net charge. As it will be shown in more details in Section 5.3, $\gamma$-rays deposit, on average, a smaller amount of energy in the gas than neutron capture fragments. Thus they appear at the lowest energies on the PHS. Of course there are interactions that give rise to higher energy events, but those are less likely. In the $^3He$ PHS in Figure 5.1, we notice how $\gamma$-rays originates the low energy rising on the PHS and how those events are well distinguished from neutron events. A simple amplitude threshold can be applied to discriminate against $\gamma$-rays. Naturally, there are some events that mix up with neutron events but their contribution for most applications can be neglected. The quantification of the misaddressed events using the energy threshold method to discriminate against background for $^3He$ and $^{10}B$ will be discussed in this chapter.

$^{10}B$ has in principle a better signal-to-noise ratio than $^{3}He$ because its energy yield is larger ($2300\,KeV$). A $^{10}BF_3$-based detector would behave as an $^{3}He$-based due to its conversion in the gaseous phase. The resulting PHS would have a wider valley between neutron and background events.
This is not the case for solid converters, e.g. $^{10}B_4C$.
In Figure 5.1 a $^{10}B$ PHS is also shown. The $^{10}B$ does not show a clear difference in the signal amplitude between a neutron event or a $\gamma$-ray. When a neutron is captured in solid $^{10}B$ it generates the capture fragments inside the layer. In order to reach the gas volume they have to travel toward the escaping surface, hence the energy deposition in the gas is a continuum down to zero or the minimum detectable energy (LDD [4] or $E_{Th}$). The rise at lower energy is then a mixture of neutron and background events. It is possible to diminish the neutron event contribution to the low energy part of the PHS. In Chapter 3 we notice that, given the neutron wavelength, playing with the layer thickness can improve the neutron to $\gamma$-rays energy separation, but this will affect the layer efficiency. Let us consider a Multi-Grid [23] like detector. The layer thickness has to be optimized to improve the detector efficiency. A very thin layer shows a better neutron to background separation, but several layers have to be added in order to keep the detector efficiency constant. This will increase the material inside the detector that can cause extra $\gamma$-ray interactions. On the other hand, thicker layers have a worse energy separation but the detector is more compact. For a single converter at grazing angle, the efficiency is maximized, in back-scattering, when it is very thick. This translates into no energy separation between neutrons and background on the PHS. Of course, one can still apply an energy threshold to eliminate $\gamma$-ray events, but contrary to a $^{3}He$-based detector this will now also lower the efficiency of the neutron detector. Hence, if one could find an efficient method to address the $\gamma$-ray discrimination, this would be of great interest. In this chapter we explore this possibility.

## 5.2 The Multi-Grid detector

The Multi-Grid detector is a prototype study over the alternatives to $^{3}He$ for large area detectors ($> 30\,m^2$) for ToF instruments.
The Multi-Grid detector [23], [24], is a solid neutron converter based gaseous detector. Neutron are converted by several $^{10}B_4C$ layers placed in cascade and alternated with gaseous detection regions. Neutrons hit each converter at normal incidence. It contains 15 blades, i.e. 30 converter layers. Each blade is a $0.5\,mm$ Aluminium substrate coated on both sides with $1\,\mu m$ $^{10}B_4C$ [37]. In order to get the two-dimensional event localization the Multi-Grid is segmented into grids. Figure 5.2 shows a grid equipped with 15 blades and the full mounted detector composed by 96 grids stacked to form 6 independent modules of 16 grids each. A stack of 16 grids is a column; 6 columns were placed one after the other in order to cover about $0.15\,m^2$ (see Figure 5.2).
Each grid acts as a cathode. They are insulated and read-out independently of each other. Each grid contains 15 blades in order to form $15 \times 4 = 60$ voxels of $2 \times 2 \times 1\,cm^3$ sides. Once the grids are stacked, they form 60 rectangular shaped tubes. An anode wire is placed all along them. A voxel is identified by the coincidence between a wire signal and a grid signal. This detector allows the three-dimensional localization of the neutron event with the voxel size spatial resolution.
Thanks to its 30 converter layers it shows an efficiency above 50% at 2.5Å. The multi-layer

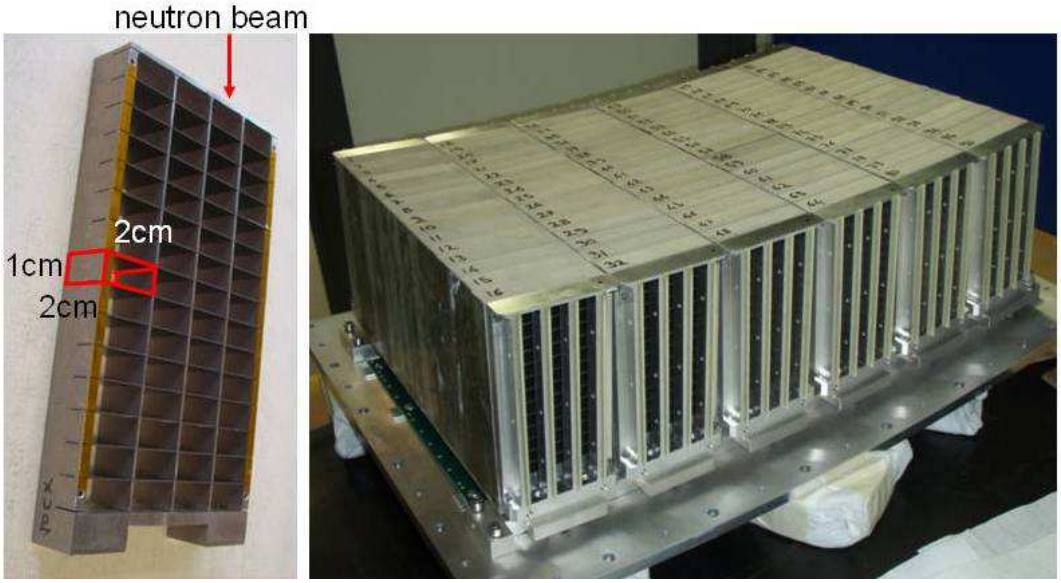


Figure 5.2: A grid containing 15 blades coated with $^{10}B_4C$ (left). The Multi-Grid detector [23] tested on IN6.

detector efficiency optimization was discussed in details in Chapter 3.
To reduce the number of read-out channels the wires were connected by resistors allowing a charge division read-out. The grids were connected together row by row. The detector is operated at atmospheric pressure. $Ar/CO_2$ (90/10) was flushed continuously in the detector.
The resulting detector was installed on IN6 at ILL to be tested and compared with $^3He$ detectors. The detector replaces 25 tubes of the standard compliance of IN6 [45].
A NaI scintillator was placed inside the chamber of the IN6 detector in order to measure the $\gamma$-ray background. The scintillator energy calibration was performed by using a $^{22}Na$ source as explained in Chapter 1 where we discussed the photon interactions. IN6 is ToF instrument, a chopper spectrometer more precisely, where a pulsed monochromatic neutron beam is obtained by a sequence of choppers that allow to determine the Time-of-Flight of neutrons, i.e. their energy. Neutrons arriving at the detector show a time structure. Those scattered elastically in the sample form a distinct peak in the time spectrum, while those scattered inelastically arrive earlier or later than the elastic peak depending on the energy transfer to or from the neutron. A large $\gamma$-ray background is also generated by the instrument itself by the surrounding equipment. The background originating in the instrument also shows a time structure. Figure 5.3 shows, on the left, the integral over all the photon energies of the NaI detector spectrum, recorded both when the neutron beam is opened and when the IN6 beam is shut off.
While the $\gamma$-ray background with the beam off is constant, we observe its time structure when the beam is on. Any interaction of the neutron beam with the instrument materials generates background. In Figure 5.3 we can distinguish when neutrons cross the collimators and the beam stop.
On the right plot in Figure 5.3 is shown the same time spectrum as for the NaI scintillator but for the Multi-Grid prototype for several bias voltage. The spectra have been normalized to the elastic neutron peak. We notice that as we increase the bias voltage in the detector the $\gamma$-ray background becomes more and more important with respect to the neutron contribution. The

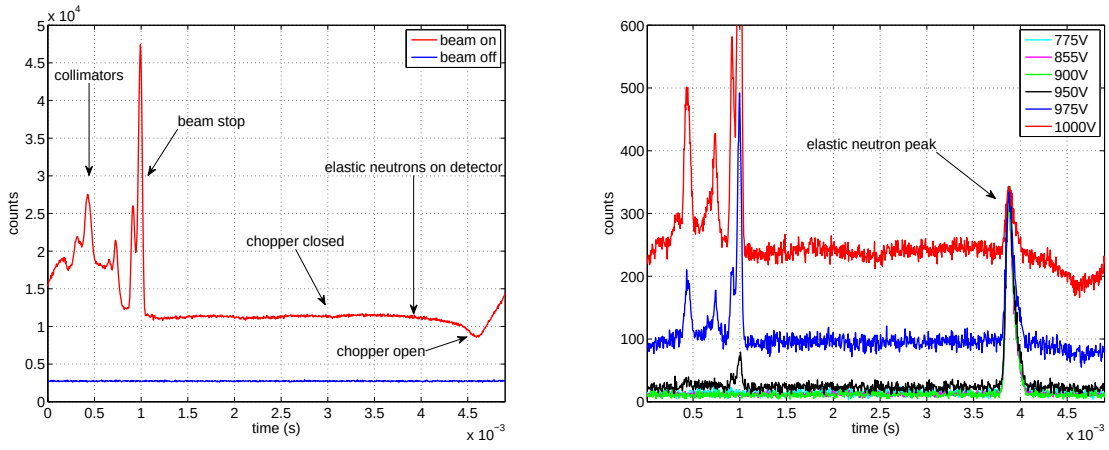


Figure 5.3: A NaI spectrum of the $\gamma$-ray background on IN6 at ILL temporized with the instrument timing (left). The Multi-Grid spectrum for several bias voltages. Courtesy of A. Khaplanov.

background shows the same time structure as for the NaI scintillator. From this measurement we understand that there exists an optimal operational voltage to get the best neutron to background discrimination. The best signal-to-noise ratio is obtained by setting the bias voltage to $900\,V$.

## 5.3 GEANT4 simulations of interactions

The energy threshold, applied on the PHS for a gaseous detector, is an efficient and simple method to discriminate between neutrons and background events. We mainly focus here on $\gamma$-rays as the background principally present in a neutron facility. The energy threshold method is efficient because of the low probability a $\gamma$-ray has to deposit its entire energy in the gas volume whatever energy it carries. A detector can be mainly decoupled in its solid part and its gas from the point of view of a photon.
Figure 5.4 shows the probability of interaction of photons with $Al$ ($\rho = 2.7\,g/cm^3$), $Ar$ and $^3He$ at room temperature and at two different pressures. The interaction probability is calculated from Equation 1.13 using the total attenuation coefficient considering Compton scattering, photo-electric absorption and pair production. On the left plot the interaction probability is plotted as a function of the photon energy and while the amount of material is fixed and vice versa on the right plot. The material thicknesses have been chosen according to commonly used in detectors and the photon energies according to widely employed sources, i.e. $^{241}Am$ and $^{60}Co$.

The probability for a photon to interact with the solid is higher than the probability of interaction with the gaseous part, for light gases. If a $\gamma$-ray interacts with the solid, the generated electron, either by Compton scattering or photo-electric effect, has to escape the solid in order to deposit its energy in the gas and to give rise to an electric signal. Intuitively, it is really unlikely an electron can deposit its entire energy in the gas, and it only happens if it was generated at the very surface of the solid facing the gas volume. On the other hand, if a photon has less chances to interact with the gas, it is also true that it can directly release its energy in the gas to generate a signal.

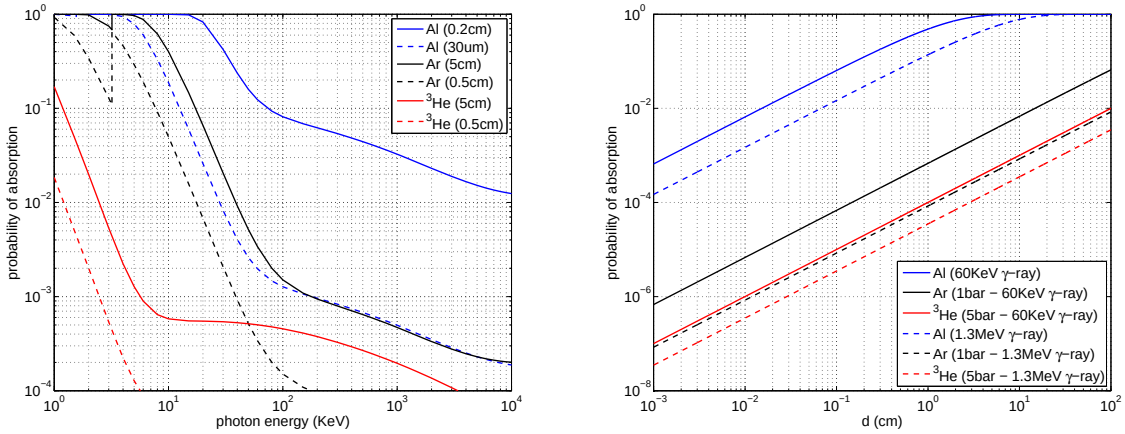


Figure 5.4: Probability of photon interaction with $Al$, $Ar$ and $^3He$ as a function of the photon energy (left) and of the traveled distance in matter (right).

Figure 5.5 shows the electron range in $Al$, $Ar$ and $^3He$ as a function of its energy. An electron can carry the full photon energy or less, either if it was generated by photo-electric absorption or by Compton scattering.

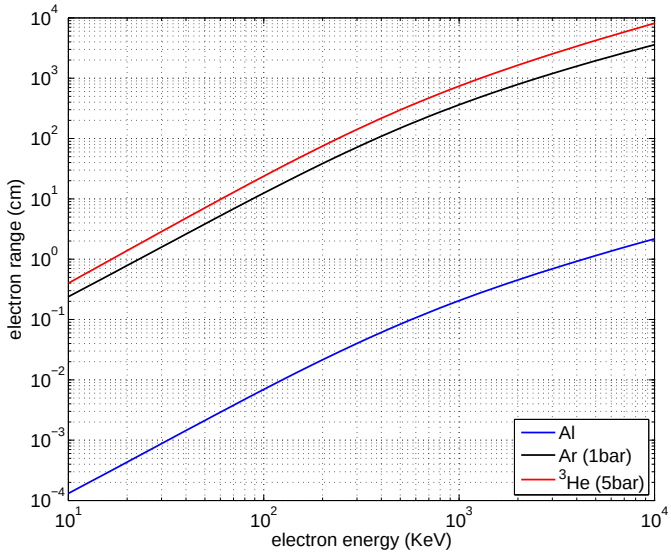


Figure 5.5: Electron range in $Al$, $Ar$ and $^3He$ as a function of its energy.

In a standard $^3He$ tube or in the Multi-Grid detector [23] the gas volume makes at most a few $cm$. Hence, if an electron carries a limited energy, e.g. $60\,KeV$, it will be stopped by the gas in few $cm$, thus it is likely to deposit its entire energy. On the other hand, if it carries higher energy, it can never deposit its full energy in the gas but will hit the wall of the vessel.
A simulation is needed to fully describe the physical process that gives rise to the low energy tail on the PHS and allows to find the energy threshold to be suited. A GEANT4 [46] simulation

has been developed. A volume of $2 \times 2 \times 1\,cm^3$ is filled with $Ar/Co_2$ (90/10) at $1\,bar$. The volume is a voxel of the Multi-Grid detector [23]. The gas volume is surrounded by $1\,mm$ thick $Al$ and an $Al$-window of $1\,mm$ is placed in front of the the detector entrance. Two $1\,\mu m$ $^{10}B_4C$ layers are at the front and a the bottom of the voxel.
A 2.5Å neutron beam is simulated to be compared with spread photon beams. Four energies have been simulated, $60\,KeV$, $662\,KeV$, $1332\,KeV$ and $10\,MeV$, in order to evaluate a wide energy range. These values have been chosen because the $\gamma$-ray sensitivity measurement has been performed using $\gamma$-ray sources. $60\,KeV$ emission represents an $^{241}Am$ source, $662\,KeV$ a $^{137}Cs$ source and $1332\,KeV$ a $^{60}Co$ source (see Table 5.2). The value $10\,MeV$ has been chosen to represent the $Cd$ neutron induced emission, which is widely extended in energy up to $10\,MeV$. The energy deposited in the gas is recorded and the Figure 5.6 shows the corresponding PHS. In the case of a neutron capture a $478\,KeV$ $\gamma$-ray is also emitted and it can consequently deposit its energy into the gas volume. The electron produced by this interaction always releases a small fraction of its energy before hitting the detector wall. A peak at small energies is visible on the PHS.

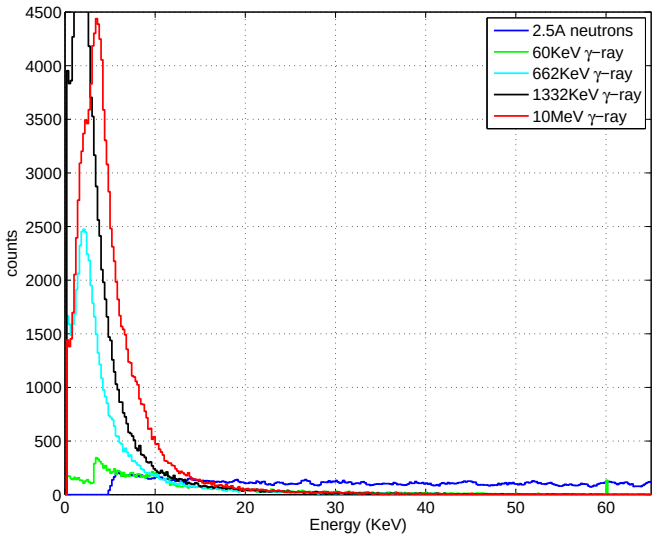


Figure 5.6: GEANT4 simulation of several energies photons interacting with a Multi-Grid [23] $Al$-voxel filled with $Ar/Co_2$ (90/10) at $1\,bar$.

As expected, only a small amount of the photon energy is deposited in the gas volume independently of the its initial energy.
Since the wide energy spectrum photons only generates a low energy tail on the PHS, the energy threshold method to discriminate against background remains a good method as well for solid converter based neutron detector, e.g. $^{10}B$. Even if the $^{10}B$ PHS is extended continuously down to low energy, one can obtain a good $\gamma$-ray rejection by losing only a few neutron events.
In the following sections the $\gamma$-ray sensitivity is quantified for the threshold method and alternatives methods, e.g. signal shape analysis, have been investigated to try to improve the discrimination quality.

## 5.4 $\gamma$-ray sensitivity measurements

We present here several measurements on the $\gamma$-ray sensitivity of both $^{10}B_4C$ and $^3He$-based neutron detectors. We define the detector sensitivity to $\gamma$-rays as its efficiency in counting background events in precise conditions. E.g. one can be interested in comparing the neutron detection efficiency with respect to the efficiency of measuring $\gamma$-rays in the same conditions. Since the background a detector is exposed can be high with respect to neutrons coming from the main beam, a very low $\gamma$-ray sensitivity is required; e.g. below $10^{-6}$.
The neutron to background contribution has been decoupled in the PHS and in the Plateau measurements in order to validate the simulations.
The absolute efficiency for neutrons and for $\gamma$-rays has been measured for both a $^{10}B_4C$ and $^3He$-based neutron detector.

### 5.4.1 $^{10}B_4C$-based detector PHS

The measurement of the actual contribution given by neutrons and by $\gamma$-rays to the PHS allows to validate the GEANT4 simulations and prove the background event contribution mainly concerns the low energy region of the PHS.
To decouple the neutron and the background contributions to the PHS one can measure the detector output, screening either one or the other radiation. This measurement was performed on CT2 at ILL with a 2.5Å neutron beam and with an AmBe source. The $^{241}Am$ available (see Table 5.2) has a too weak activity to perform a measurement in a reasonable time given the low detector sensitivity. Thus we opt for the AmBe of $3.7 \cdot 10^9\, Bq$ used as $\gamma$-ray source. In case of an AmBe source, the $\gamma$-ray counts greatly exceed neutron counts.
The PHS was measured with the Multi-Grid detector [23] in one of its voxels. To obtain the neutron contribution, the region of interest of the Multi-Grid was covered by a $5\, cm$ lead shield in order to screen the $\gamma$-rays. To obtain the $\gamma$-ray contribution, which is mostly given at $60\, KeV$ because of the $^{241}Am$, the AmBe source was shielded with polyethylene and $^{10}B_4C$ sheets to thermalize and stop neutrons. Since the background contribution is mainly given at low energy, we operated the detector at high gain in order to rise low energy events above the threshold. Moreover, the charge amplifier used has a limited dynamic range, hence high energy events are saturated.
Figure 5.7 shows the measured PHS and the integral of the number of counts which cross a given value of the threshold, both for neutrons and $\gamma$-rays. The neutron spectrum is saturated because of the neutron capture fragment higher energy yield. The long low energy tail of neutrons is extended down to zero inside the background. $\gamma$-ray contribution is extended under the high energy region of the spectrum.
The number of neutron counts as a function of the threshold is almost constant; in increasing the detector gain there is no actual raise of the neutron events. If a threshold of $200\, ch.n.$ or $100\, ch.n.$ is chosen, there is not much to gain in neutron efficiency. On the other hand, the behavior for background events is exponential. If a slightly different threshold is chosen there is a huge counting difference. A trade-off has to be found to maximize the signal to noise ratio of the detector.
The argument chosen is here arbitrary because the actual neutron and $\gamma$-ray flux is unknown. We will quantify accurately the detector sensitivity in Section 5.4.3.
In Section 4.3 of Chapter 4, we used the $480\, KeV$ $\gamma$-ray emitted by the $^{10}B$ neutron capture

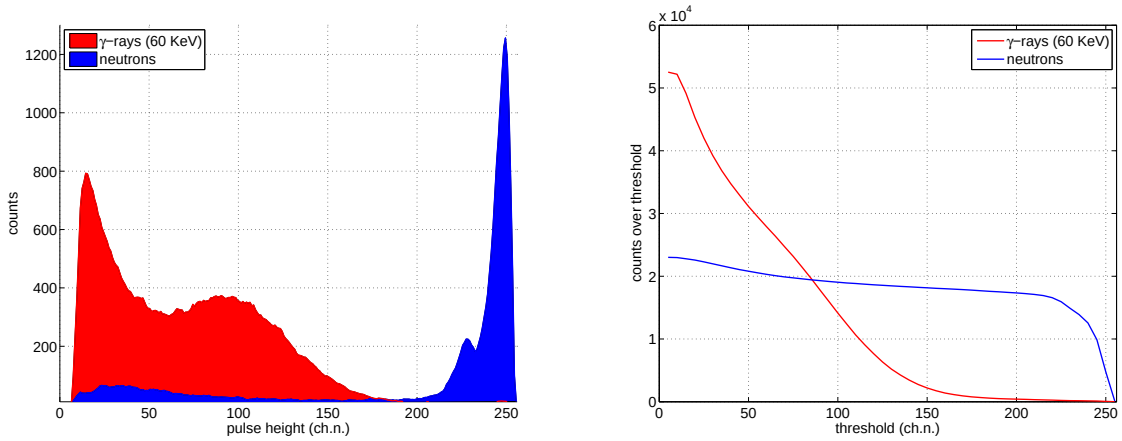


Figure 5.7: PHS measured for neutrons and $\gamma$-rays with the Multi-Grid detector (left). The evolution of the number of counts over a threshold as a function of the threshold (right).

reaction (see Table 1.69) to measure neutron absorption in the layer together with reflection. Similarly, in order to decouple properly the two contributions to the PHS given by neutrons and $\gamma$-rays, we exploit again the emission of this $480\,KeV$ photon. To measure the $480\,KeV$ $\gamma$-ray we used a $NaI$ scintillator. Its energy calibration can be obtained as explained in Chapter 1. Every time a $480\,KeV$ $\gamma$-ray is measured this is the signature that there was a neutron converted in the $^{10}B_4C$ layer or in other $B_4C$ (shielding, etc.).

Figure 5.8 shows the MWPC detector used and the setup of the experiment. The detector is operated at atmospheric pressure of $CF_4$. An $Al$-blade, coated with $1\,\mu m$ $^{10}B_4C$, was placed in a $20\times 8\,cm^2$ MWPC. The converter layer is facing the anode plane. All the anodes are connected together to a single charge amplifier. The bias voltage is applied through a decoupling capacitor and it is $1000\,V$.

The wide spectrum $\gamma$-ray background had to be shielded by a lead housing surrounding the NaI detector. Since most of the neutron shielding at ILL is made out of $Cd$ or $^{10}B_4C$ sheets, the contamination of our measurement involves as well the $480\,KeV$ region. It was really crucial to set up the shielding properly.

The MWPC and the NaI detectors were readout by the same data acquisition system and events were assigned a timestamp. This makes possible to examine both singles and coincident spectra in the same measurement. The total rate in the MWPC was $2.1\,KHz$ (neutrons and background $\gamma$-rays) and the rate of the NaI with the gate around the $480\,KeV$ photo-peak was $97\,Hz$. This rate is mostly given by the environment. Because of the small fraction of solid angle covered, only a few of those counts come from the MWPC. One coincidence is obtained by looking at an event in the $480\,KeV$ photo-peak by the NaI scintillator when the MWPC gives a signal over the threshold set over the electronic noise level. The coincidence rate is $8.3\,Hz$. The gate around the photo-peak was chosen to decrease the possibility to have a random coincidence with a background photon of different energy from $480\,KeV$.

The $^{10}B_4C$ detector was operated at a standard gain ($HV = 1000\,V$) and at a very high gain in order to make it more sensitive to photons.

Selecting the $480\,KeV$ peak in the NaI in coincidence with a signal in the MWPC allows to identify true neutron conversion events, even those whose energies normally make them indis-

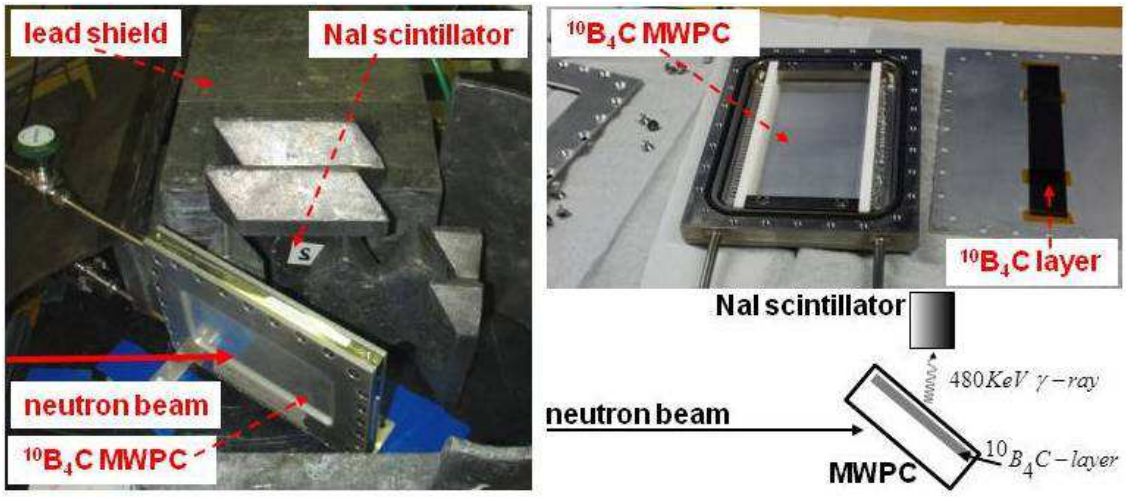


Figure 5.8: Setup used to measure the $^{10}B_4C$ PHS in coincidence with the emission of the $^{10}B$ neutron capture $\gamma$-ray.

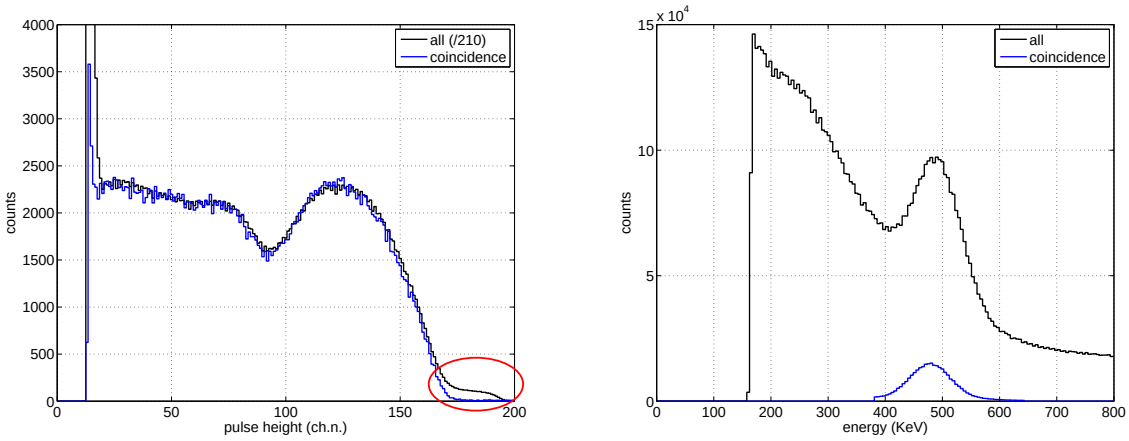


Figure 5.9: $^{10}B_4C$ detector PHS (left) and NaI scintillator energy spectrum (right) with and without 480 $KeV$ photon coincidence.

tinguishable from $\gamma$-rays. These are shown in blue in Figure 5.9. The probability to detect a 480 $KeV$ photon emitted from the boron layer is of course much smaller than one. However, since we know that for large energies essentially only neutrons contribute to the spectrum, scaling allows to match the coincident spectrum with the total spectrum. The best scaling factor turns out to be 210. The difference then corresponds to the spectrum due to all non-neutron events or neutrons converted in the 6% branching ratio of the $^{10}B$ capture reaction. In Figure 5.9, the contribution given by the 6% branching ratio $\alpha$-particle vanishes after coincidence.
The measurement was repeated at higher gain to increase the detector sensitivity to $\gamma$-rays. The neutron spectrum extends to much larger energies and only its lower part can be measured without saturation of the amplifier in these conditions. The measurement was operated on the neutron beam including or not a $\gamma$-ray source of high intensity, i.e. the AmBe source.
Figure 5.10 shows the results. Most of this difference spectrum vanishes when the AmBe source

is removed, which confirms that it corresponds to the $\gamma$-ray spectrum of $Am$: predominantly $60\,KeV$.

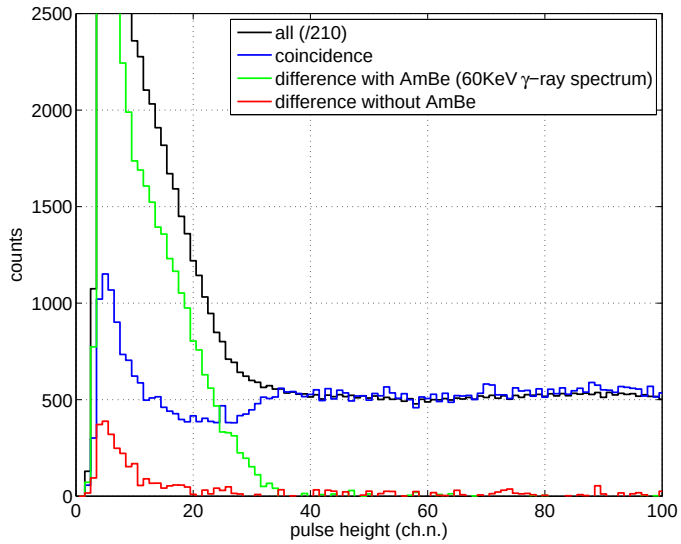


Figure 5.10: $^{10}B_4C$ detector PHS (lower energy tail) measured in coincidence with the $480\,KeV$ photon with and without an AmBe source.

We confirm the background energy spectrum mostly involves the low energy region.
The energy spectrum of neutron conversion fragments that reach the gas has no lower limit for a solid film detector. Therefore any lower level threshold will reject some neutron events. A minimum required threshold is determined by the end-point of the $\gamma$-ray spectrum.

### 5.4.2 $^{10}B_4C$-based detector Plateau

The fraction of neutrons rejected due to the overlap of the background and neutron spectra can be estimated in a counting curve measurement. In order to measure the background and the neutron components to the plateau, we have performed a set of measurements. The measurement has been repeated in several configurations in order to be able to subtract the single components. The plateau was measured on CT1 at ILL, with the MWPC containing a single $^{10}B_4C$ layer shown in Figure 5.8 and already used for the neutron to $480\,KeV$ $\gamma$-ray coincidence in Section 5.4.1.
Figure 5.11 shows the complete setup used to perform the measurements. A neutron beam (2.5Å) was collimated through two $^{10}B$ slits at $1.2\,m$ distance, to form a $5 \times 3\,mm^2$ footprint on the detector. An AmBe source, used as $\gamma$-ray source, was placed on the opposite window of the MWPC. The neutrons emitted were shielded by a polyethylene and a $B_4C$ sheet ($B_4C$ 3 in Figure 5.11). We can chose to add a second $B_4C$ sheet ($B_4C$ 1 in Figure 5.11) in order to stop the neutron beam and then measure the background without affecting the setup unless for the more $\gamma$-rays produced by the sheet. We can consider those $\gamma$-rays to be negligible because of the solid angle at $1.2\,m$. Moreover, the measurement was repeated with the $B_4C$ sheet after the second collimation slit and only a slight difference was observed at very high gain.
We performed measurements of the plateau in 5 different conditions. They are listed in Table

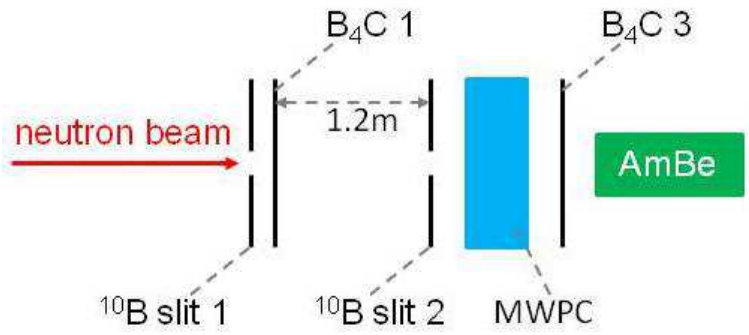


Figure 5.11: Setup used to measure the $^{10}B_4C$ detector plateau.

| Setup | beam | $B_4C$ 1 | $B_4C$ 3 | AmBe | Slit 1 | Slit 2 |
|---|---|---|---|---|---|---|
| $S1$ | x | | x | | x | x |
| $S2$ | x | | x | x | x | x |
| $S3$ | | | x | | x | x |
| $S4$ | x | x | x | x | x | x |
| $S5$ | x | x | x | | x | x |

Table 5.1: Setups used in the measurements (the x means that a specific element was used at the moment of the measurement).

5.1. $S1$ is the measurement of the neutron and the background contributions. $S2$ is as $S1$ with the addition of the AmBe background. $S3$ allows to measure the background without the beam. $S5$ is the background measurement with the beam on, and $S4$ with the additional AmBe contribution. All parts of the setup produced background that has to be subtracted. The collimation slits produce $\gamma$-rays when exposed to neutrons. We list here the single contribution to the counting curve:

$$\begin{aligned} S1 &= n \quad + S3 + \Gamma \quad + \gamma_{slit1} + \gamma_{slit2} \qquad\quad + \gamma_{B_4C3} \\ S5 &= \qquad S3 + \Gamma \quad + \gamma_{slit1} \qquad\quad + \gamma_{B_4C1} \end{aligned} \tag{5.1}$$

where $n$ is the pure neutron count, $\Gamma$ the unknown background coming from the environment due to the presence of the beam, e.g. $\gamma_{slit1}$ the $480\,KeV$ $\gamma$-rays coming from the $^{10}B$-slit 1. Moreover, $S2 = S1 + \gamma_{AmBe}$, $S4 = S5 + \gamma_{AmBe}$. Where $\gamma_{AmBe}$ are the $\gamma$-rays emitted by the AmBe, mostly $60\,KeV$.
The neutron beam was calibrated using the hexagonal detector according to the procedure in Appendix E. The neutron counting at the detector position was $(31850 \pm 20)\,Hz$. Knowing the neutron flux allows to normalize the counting curve to get the actual detection efficiency. The expected theoretical efficiency for a $1\,\mu m$ layer hit at 90° in back-scattering with no energy threshold ($E_{Th} = 0$) is 4.2% (red dashed curve in Figure 5.12).
Figure 5.12 shows the single measurements and the plateaux obtained by substraction. The plateau obtained in $S2$ shows a higher $\gamma$-ray rising at high voltage with respect to $S1$.
The AmBe source contribution can be highlighted by subtracting either $S2 - S1$ or $S4 - S5$.

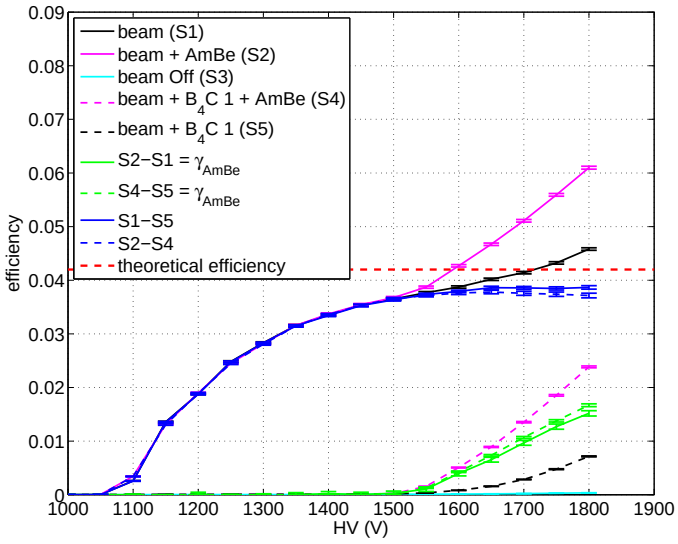


Figure 5.12: Plateau measured in the several configuration listed in Table 5.1.

The neutron contribution can be obtained by:

$$S1 - S5 = S2 - S4 = n + \gamma_{slit2} + \gamma_{B_4C3} - \gamma_{B_4C1} \tag{5.2}$$

apart from the background produced by the second collimation slit ($\gamma_{slit2}$) and if we assume $\gamma_{B_4C1} \simeq \gamma_{B_4C3}$. As already mentioned we moved the $B_4C1$ sheet after the second collimation slit and no appreciable difference is observed in the plateau.
We expect the pure neutron plateau to saturate to the theoretical efficiency.
Setting the high voltage at the point just before the rise of the $\gamma$-rays detection ($1500\,V$) results in approximately 6% fewer neutron counts compared to the maximum of the plateau. Note however, that a certain threshold level is required also to reject electronic noise. The loss of 6% compares to all neutron events where any finite part of the energy is deposited in the gas, not to those events that can be detected over the electronic noise level. The equivalent energy threshold of the noise level becomes smaller and smaller when the voltage and hence the gas gain rises. The plateau should approach the theoretical efficiency at high voltage.

### 5.4.3 $^{10}B_4C$ and $^3He$-based detectors $\gamma$-ray sensitivity

We quantify in this Section the actual sensitivity of both $^{10}B_4C$ and $^3He$-based detectors to $\gamma$-rays. The measurements have been performed in a wide range of $\gamma$-ray energy. The efficiency to detect $\gamma$-rays of a detector can be measured by using calibrated sources. By knowing the source activity and the solid angle subtended by the detector, the actual photon flux can be calculated. The efficiency is the ratio between the number of detection events and the incoming photon flux [47], [48].
Four $\gamma$-ray sources have been used and their activity, main photons emitted with their relative intensity are listed in Table 5.2. Those four sources allow to explore the energy range from $x$-rays up to $1\,MeV$. We can consider $^{241}Am$, $^{137}Cs$ and $^{60}Co$ three distinguished energy ranges

| source | photon energy (KeV) | intensity (%) |
|---|---|---|
| $^{133}Ba$ | 4 | 14.7 |
| ($A = 1.85 \cdot 10^5\, Bq$) | 30.6 | 31 |
| | 30.9 | 57 |
| | 34.9 | 15.4 |
| | 36 | 3 |
| | 53 | 2 |
| | 79 | 2.6 |
| | 81 | 32.9 |
| | 276 | 7 |
| | 303 | 18 |
| | 356 | 62 |
| | 383 | 9 |
| $^{241}Am$ | 13.9 | 14.3 |
| ($A = 3.5 \cdot 10^5\, Bq$) | 26 | 2.3 |
| | 60 | 35.9 |
| $^{137}Cs$ | 31 | 2 |
| ($A = 2 \cdot 10^5\, Bq$) | 32 | 3.8 |
| | 662 | 85 |
| $^{60}Co$ | 1173 | 99.85 |
| ($A = 2.31 \cdot 10^4\, Bq$) | 1332 | 99.98 |

Table 5.2: $\gamma$-ray sources activity, main photon emitted and their relative intensity.

from low energy up to above $1\, MeV$; while $^{133}Ba$ shows a low-medium energy range emission.
We compare two detectors: the $^{10}B_4C$-based Multi-Grid [23] and the $^3He$-based hexagonal detector used in Appendix E to quantify the neutron flux. The latter is filled with $3\, bar$ of $^3He$ and $1.5\, bar$ of $CF_4$. Multi-Grid was filled with $1\, bar$ of $CF_4$. The hexagonal detector is composed of 37 hexagonal tubes with a $7\, mm$ diameter arranged in a honeycomb formation.
Efficiencies or sensitivities to $\gamma$-rays are defined as the probability for a photon incident on a detector element (such as a tube) to result in an event confused with a neutron detection event. Plateau measurements have been used for this since in order to measure a pulse height spectrum, either the threshold needs to be set extremely low, or a high bias voltage needs to be used. At a typical gas amplification used in neutron detection, the threshold cannot be set low enough to study $\gamma$-ray signals due to electronic noise. Increasing the bias voltage results in a high gas gain but in turn leads to poor energy resolution.
Each detector was exposed to the sources and the actual photon flux was determined by calculating the solid angle the detector was subtended [49], [50], [51].
The normalized neutron plateau at 2.5Å for both detectors was measured for comparison. It was determined by knowing the actual neutron flux (see Appendix E).Figure 5.13 shows the results; where the efficiency is given per tube.
The disconnected points at the left ends of the curves are upper limits, sensitivity can be lower than the plotted points, where no statistically significant counts could be detected over background.
The $^{133}Ba$ and $^{241}Am$ source can be considered as low energy sources, whereas $^{137}Cs$ and $^{60}Co$

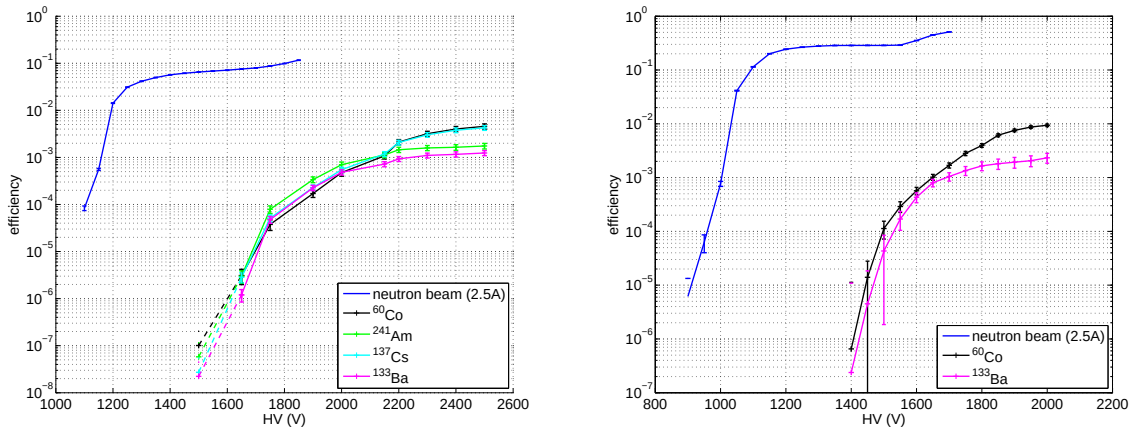


Figure 5.13: Plateau measurements with the Multi-Grid $^{10}B$ detector (left) and a Multi-Tube $^{3}He$ detector (right) with neutrons (2.5Å) and $\gamma$-ray sources. Detection efficiency per tube is shown. The nominal operating voltages are $1600\,V$ and $1400\,V$ respectively.

as high energy sources. Note that (see Figure 5.13) the difference between low and high energy photons is only visible at high gain for both detectors. As the bias voltage increases the count rate due to the $^{60}Co$ source exceeds that of $^{133}Ba$ since a larger number of interactions, primarily in the solid elements of the detector, contributes with higher energy electrons.
In a realistic configuration where a gas detector is set up to detect neutrons, the energy threshold should be set so that the signals from photons are rejected while those from neutrons are not. No sharp cut-off for the highest pulse height resulting from a specific primary particle energy exists due to the statistical nature of gas amplification and charge transport. The final contamination due to $\gamma$-ray signals will be due to those events where a $\gamma$-ray signal including statistical fluctuation is over the threshold. This is most likely to be due to a low-energy $\gamma$-ray (since the specific energy loss is then high), such as $60\,KeV$. At the first glance this fact is encouraging since it is much easier to shield low-energy photons. Note however, that interactions of high-energy photons as well as nuclear reactions, such as neutron capture or decay of activated materials, often result in emission of $x$-rays and internal conversion electrons which have just the energy that is most likely to contribute to background. It is therefore important to carefully consider the external radiation environment as well as the secondary sources that may exist in the immediate vicinity of the detectors.
The discrimination between neutron and photon signals presents a challenge in many types of neutron detectors. A high level of discrimination can be reached with the conventional $^{3}He$ tube. Concerning the $^{10}B$ thin film detectors, we have found that the $\gamma$-ray rejection need not be lower in these detectors than in $^{3}He$ tubes, if we allow for a small loss in neutron detection efficiency. Less than $< 10^{-6}$ is easily reached: one needs to lower the efficiency only by about 0.5%.

### 5.4.4 Pulse shape analysis for neutron to $\gamma$-ray discrimination

In this Section we want to investigate the possibility to achieve a greater neutron to $\gamma$-ray discrimination than just a PHS threshold by also processing the signals shapes.
While several methods have been developed in order to discriminate between neutrons and $\gamma$-

rays for neutron scintillators [52], [53]; it is not the case for neutron gaseous detectors. In a scintillator the time structure of the light output follows two completely different behaviors for neutrons and for $\gamma$-rays. The technique works well by virtue of the fact that for gamma initiated scintillations there is much more fast decay constant light output than slower decay constant light output as compared to the same relative intensities in light output from neutron induced scintillations [53].
In a gaseous detector the main difference between neutron and $\gamma$-ray signals is the space charge density created. While a neutron originates heavy particles which ionize the gas, a $\gamma$-ray produces a light electron. The way a particle or an electron ionizes the gas is different for two reasons: the electron generally carries less energy than the particles and its energy loss behaves differently. However, the tracks in gas, for electrons and capture fragments, can be both oriented randomly; this makes it difficult to find a discrimination criterion that is valid for the multiplicity of cases that can occur.
To study the shape of the output signals we use the same MWPC used previously and shown in Figure 5.8. We operate the detector at a high gain in order to have an intense $\gamma$-rays sensitivity: i.e. $1750V$ (see Figure 5.12). This voltage corresponds to a region of limited proportionality of the gas amplification which is in between the proportional and Geiger detector operational modes. For such a reason in Figures 5.15, 5.16, 5.17 and in Figures 5.18, 5.19 and 5.20 in the PHS we can not recognize the energy carried by the fragments.
Since we do not know a priori the signal time structure, two amplifiers have been chosen to perform the analysis: a fast one with $3\,ns$ integration time and a slower one of $1\,\mu s$.
We place a $5\,cm$ lead shield before the detector in order to decrease the $\gamma$-ray background originated from the collimation slits. We record 20000 signal traces each time. The signal processing was then done off-line.
We use in three different configurations, listed in Table 5.4.4: with and without the neutron beam and with and without the additional background originated by the AmBe source.

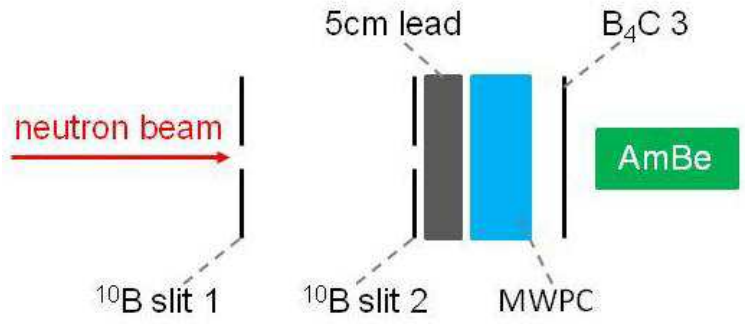


Figure 5.14: Setup used to perform the signal shape analysis.

We can assume that $S1$ is a measurement of mostly neutrons, $S2$ of mostly the $\gamma$-rays from the AmBe source and $S3$ of both contributions.
The off-line analysis was performed by looking at the signal structure in terms of charge yield and time-over-threshold (TOT). For what concerns the $1\,\mu s$ amplifier, the signal amplitude is proportional to the charge created in the gas volume because its integration time is longer than the physical charge collection in the detector. On the other hand, for the $3\,ns$ amplifier the charge is given by the integral of the signal over time. The time-over-threshold is the time a

| Setup | beam | Lead | $B_4C$ 3 | AmBe | Slit 1 | Slit 2 |
|---|---|---|---|---|---|---|
| $S1$ | x | x | | | x | x |
| $S2$ | | x | x | x | x | x |
| $S3$ | x | x | x | x | x | x |

Table 5.3: Setups used in the measurements (the x means that a specific element was used at the moment of the measurement).

signal stays above a given threshold. The latter was set at the lowest value possible according to the amplifiers noise level ($3\,mV$ for both).
In each figure that follows, is shown a charge spectrum on the top-left corner, a TOT spectrum on the top-right corner. A charge versus TOT is shown in each figure in the bottom plots: one scattered and one of intensity normalized to the total number of events.
Figures 5.15, 5.16 and 5.17 show the signal analysis for the three sets of measurements for the slow amplifier.

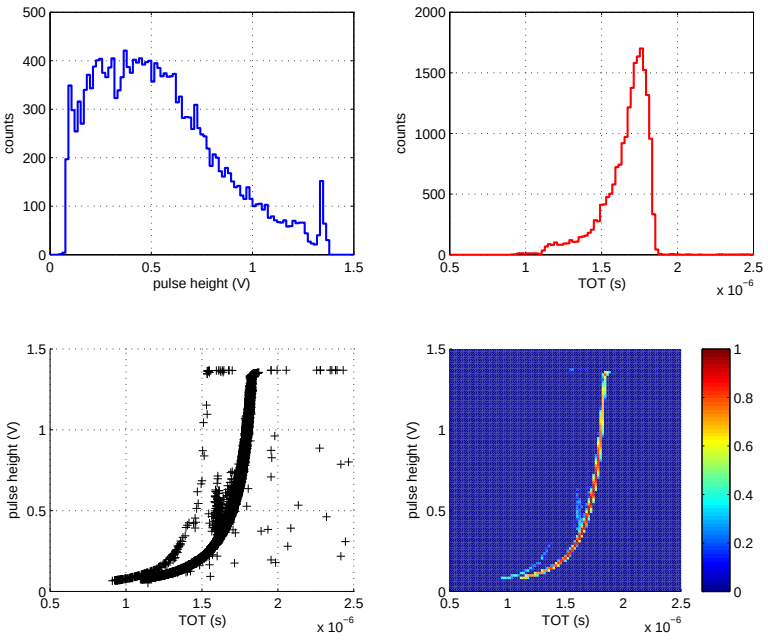


Figure 5.15: Measurement of $S1$ (beam only) - amplifier $1\,\mu s$.

By comparing Figure 5.15 with Figures 5.16 and 5.17; we note that in the correlation plot TOT-PH the $\gamma$-ray contribution is mixed with the neutron one as it is in the PHS. The low TOT events for neutrons and $\gamma$-rays (below $1.5\,\mu s$) are just as indistinguishable.
We repeat the analysis for the fast amplifier. Figures 5.18, 5.19 and 5.20 show the signal analysis for the three sets of measurements for the fast amplifier.
In Figures 5.18 the contribution is mostly given by neutrons. In the TOT spectrum we notice two peaks corresponding to the $\alpha$-particle and the $^7Li$-fragment as it is in the PHS.

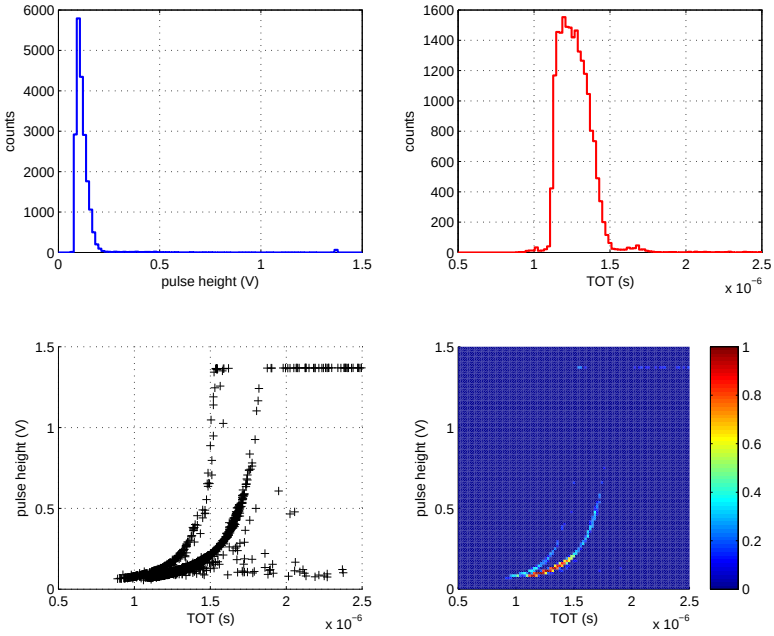


Figure 5.16: Measurement of $S2$ (AmBe source only) - amplifier $1\,\mu s$.

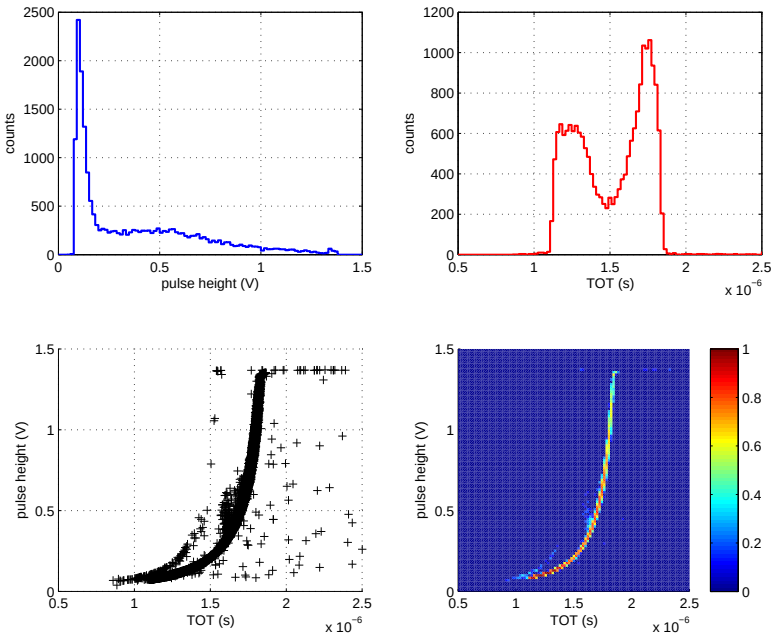


Figure 5.17: Measurement of $S3$ (beam and AmBe source) - amplifier $1\,\mu s$.

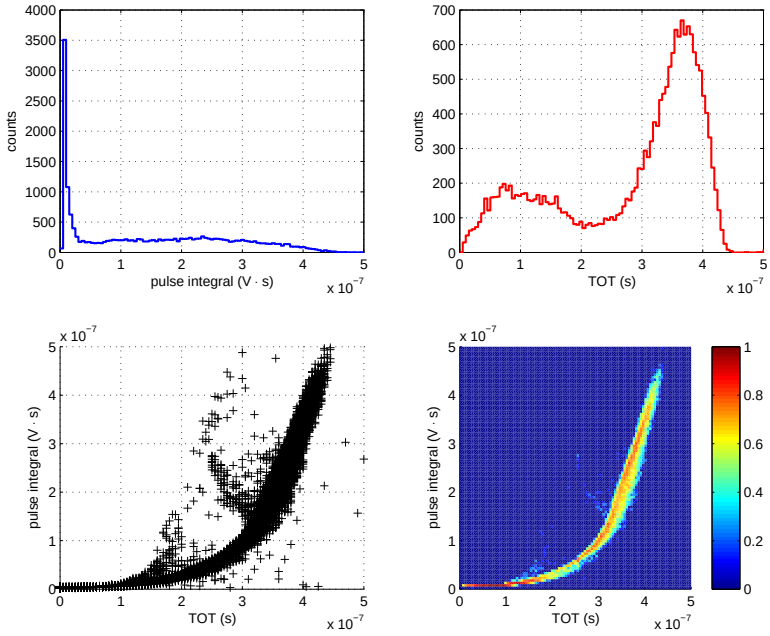


Figure 5.18: Measurement of $S1$ (beam only) - amplifier $3\,ns$.

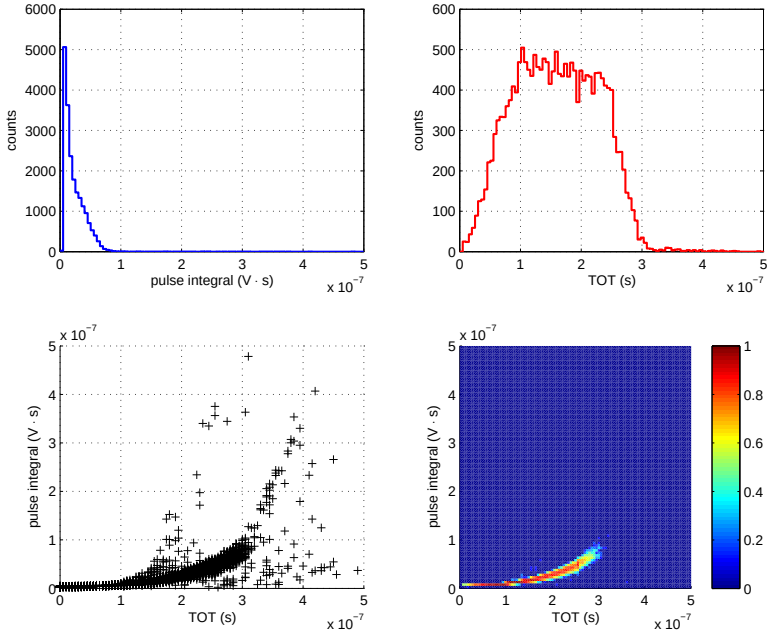


Figure 5.19: Measurement of $S2$ (AmBe source only) - amplifier $3\,ns$.

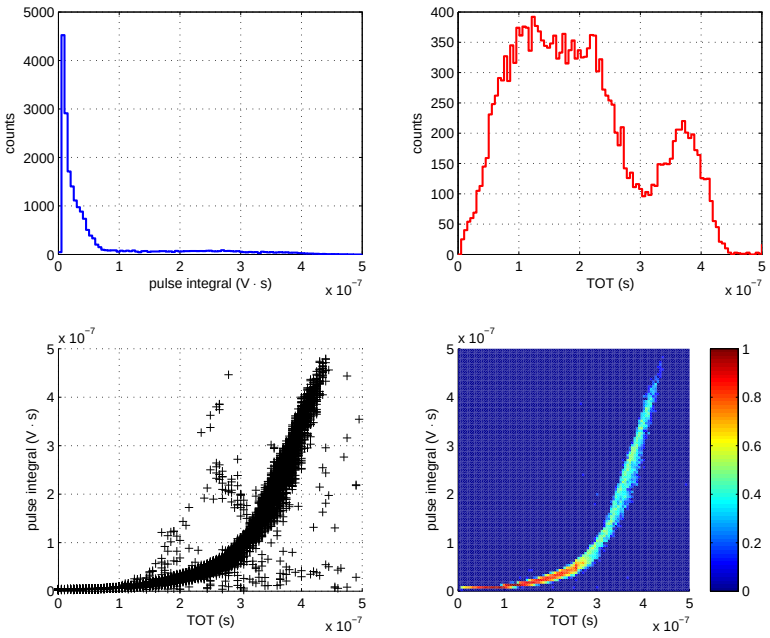


Figure 5.20: Measurement of $S3$ (beam and AmBe source) - amplifier $3\,ns$.

There is no physical difference in the signal shape using the TOT that can be exploited to discriminate against background. The amplitude discrimination remains the best way to reduce $\gamma$-ray sensitivity of neutron detectors based on a solid converter.

# Chapter 6

# The Multi-Blade prototype

I have to thank my group head, Bruno Guérard, who pushed me a lot for the prototype construction and believed in the success of this prototype concept. I also want to thank Jean-Claude Buffet and Sylvain Cuccaro for their important suggestions and the work that made possible the construction of the Multi-Blade prototype.

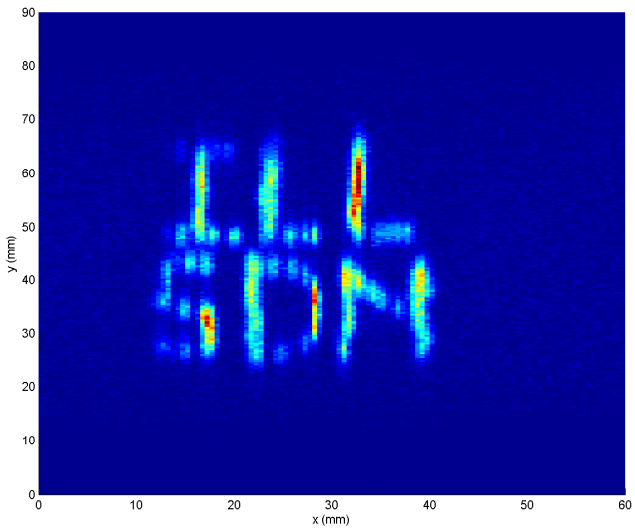

## 6.1 Detectors for reflectometry and Rainbow

Because of its favorable properties, $^3He$ has been the main actor in neutron detection for years. Nowadays its shortage pushes many researchers to investigate alternative ways to efficiently detect neutrons. For large area detectors, i.e. ToF spectrometers, several squared meters in size, it is crucial to find an $^3He$ replacement. At ILL efforts have been made to develop the Multi-Grid [23]. This is a large area neutron detector that exploits up to 30 $^{10}B_4C$-layers in a cascade configuration; its optimization has already been explained in details in Chapter 3. On the other hand, there are several neutron instruments that can work with small detector size. A neutron reflectometer, such as Figaro at ILL needs a detector surface of $400 \times 250\, mm^2$. For these applications a limited amount of $^3He$ is required and its shortage is not the main issue to be addressed.
Neutron scattering science is still growing its instruments' power and together with that the neutron flux a detector must tolerate is increasing. The peak brightness at ESS, the new European Spallation Source, will be higher than that of any of the short pulse sources, and will be more than one order of magnitude higher than that of the World's leading continuous source. The time-integrated brightness at ESS will also be one to two orders of magnitude larger than is the case at today's leading pulsed sources [54], [55].
The Multi-Blade concept wants to address the counting rate capability of $^3He$-based detectors for high flux applications. We want to develop a detector suitable for neutron reflectometry instruments.
The main goal in neutron reflectometry instruments is to achieve a high angular resolution at high counting rates.
A neutron detector for a reflectometry instrument is in general compact in size and the spatial resolution required is of the order of $1\, mm$ in order to achieve the needed angular resolution. Figure 6.1 shows a reflectometry instrument schematic. Neutron reflection by a sample is measured as a function of the momentum transfer $q$, as shown in Section 1.5.4, the value of $q$ can be obtained from Equation 1.88 ($q = \frac{4\pi}{\lambda}\sin(\theta)$). If $\theta$ is kept fixed the reflectometer works in ToF-mode and the neutron beam is chopped to get the ToF information that leads to $\lambda$. If, on the other hand, the neutron beam is monochromatic and $\theta$ is scanned, the reflectometer works in monochromatic-mode. A detector for a reflectometer is characterized by a non-uniform spatial resolution. Referring to Figure 6.1, a high spatial resolution is only needed for the $y$ direction. This is true because for a large number of applications only the specular reflection is needed and the other coordinate ($x$) is generally integrated over.
A PSD (Position Sensitive Detector) is necessary when not only specular reflection occurs but one wants to quantify more sample features, e.g. off-specular reflection arising from the presence of in-plane structures. It is more important to know the actual position of the reflected intensity on the detector to determine $\theta$ for off-specular studies.
In order to give the specifications of a neutron reflectometer we list some features of Figaro at ILL. The neutron wavelength range explored is between 1Å and 30Å. The sample to detector distance can be varied between $1.2\, m$ and $2.9\, m$. The white beam flux before the instrument was recorded as $1.4 \cdot 10^{10}\, neutrons/cm^2 s$; the flux on the sample using the widest chopper pair with collimation slits openings of $0.8 \times 40\, mm^2$ and $0.4 \times 30\, mm^2$ gives a neutron count rate of $4 \cdot 10^4\, neutrons/cm^2 s$ on a sample area of $40 cm^2$. The Figaro detector is a PSD of $400 \times 250\, mm^2$ constructed from a single block of aluminium, with 64 square ($7mm$ side), $25cm$ long channels. Each tube is filled with 8 bars of $^3He$ and 2 bars of $CF_4$ and contains a $15\, \mu m$ Stablohm wire

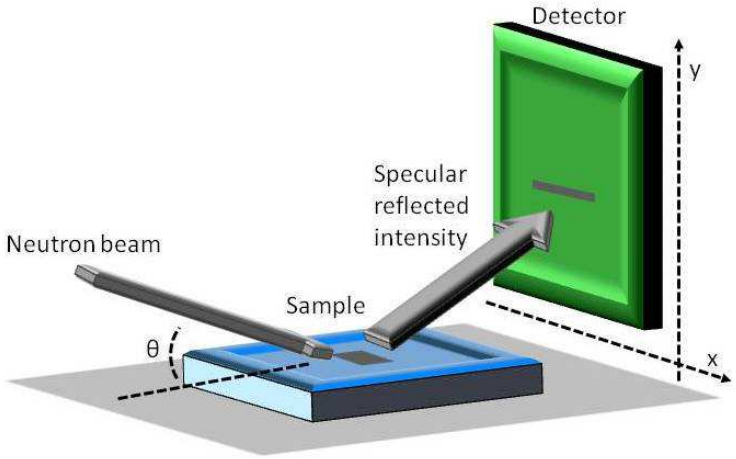


Figure 6.1: A neutron reflectometry instrument schematic.

of 250 $mm$ active length, which detects neutrons by charge division. The vertical position resolution is 2 $mm$ and the horizontal position resolution is 8 $mm$ [56].
In a $^3He$-based detector the counting rate is limited by the space charge effect, as the ions created by each avalanche need more time, compared to electrons, to be evacuated. At high rate they tend to accumulate and consequently they decrease the actual electric field in the gas volume, and as a result the detector loses efficiency. If Figure 6.1 represents the Figaro's detector, the $^3He$-tubes are placed vertically along $y$ in order to split the reflected intensity over several tubes.
Morever, $^3He$ detectors of this type are limited in spatial resolution for two main reasons. The first is that $^3He$-based detectors are gaseous detectors which exploit anode wires for read-out; in one direction wires can not be mounted with a $mm$ spacing because this causes mechanical issues, on the other direction, along the wire, the spatial resolution that can be achieved by a charge division read-out is limited at about 2 $mm$ on a 30$cm$ wire length, i.e. $\sim 0.7\%$. The second reason limiting the spatial resolution is the gas pressure that can be reached. To reduce the particle traces, and thereby increase the spatial resolution, those detectors are operated at high gas pressure, resulting in mechanical constraints. The higher the gas pressure, the more severe are the mechanical problems arising in the detector vessel conception. There is a reasonable limit in the resolution the can be reached with this technique, around 1 $mm$ [57].
In many areas of soft and hard matter research science, the amount of material to investigate is rather limited. Partly because the fabrication of larger samples is too expensive or not feasible, yet, partly because the interesting features depend on the size. The development of a neutron reflectometer optimized for small samples is under study [58]. There is a great deal of interest in expanding the technique of neutron reflectometry beyond static structural measurements of layered structures to kinetic studies [59]. The time resolution for kinetic studies is limited by the available neutron flux.
For both working modes (monochromatic and ToF) a reflectometer is operated, the actual neutron flux reaching the sample is a small fraction of the incoming neutron beam. For monochromatic instruments, this limitation arises from the monochromators used to get a neutron beam of a defined energy. For instruments which use the ToF technique the flux is limited by the

choppers. E.g. the reflectometer D17 [41] at ILL has a transmission of only $10^{-3}$ at about 2 Å if a wavelength resolution $\Delta\lambda/\lambda$ of 1% is needed.
The resolution in momentum transfer $q$ is related to the neutron wavelength $\lambda$ and the angular resolution in $\theta$:

$$\left(\frac{\Delta q}{q}\right)^2 = \left(\frac{\Delta\lambda}{\lambda}\right)^2 + \left(\frac{\Delta\theta}{\theta}\right)^2 \tag{6.1}$$

In ToF, $\Delta\lambda$ is determined by the chopper settings and time resolution, and in a monochromatic approach, by the monochromator resolution. When only considering specular reflection the angular resolution $\Delta\theta$ is determined by collimation and beam divergence.
In [59] and [14] a new instrument layout is presented: Rainbow. This instrument would involve a prism refraction to deduce the wavelength in place of choppers thus providing a large gain in useful neutron flux. Hence, it open the possibility of sub-second kinetic studies. In this new approach, as we will discuss, $\Delta\theta$ in Equation 6.1 is now determined also by the detector spatial resolution and its distance to the sample.
By using the reflectometer D17 [41] at ILL, the actual measurement time of 1 $s$ is only possible by loosening the $q$-resolution of the instrument: between 4% (at about 20 Å) and 10% (at about 2 Å). The advantage of using a prism would be to measure faster and without the cost in resolution. The technique would be of equal value for experiments with sample areas much smaller than can be practically measured at present.
Figure 6.2 shows a schematic of Rainbow. A white and continuous neutron beam is collimated before the sample. A standard distance used between the collimation slits is about $D = 3\,m$. The prism is placed after the sample and is calibrated by passing the direct beam through the prism alone to measure the deflection of the beam due to refraction. The deflected angle $\varphi$ by which a certain neutron wavelength is refracted depends only on the prism angle $\alpha$ and the scattering length density of the prism material. It is given by Snells law: $\varphi = \arccos(n\,\cos(\alpha))$. Where $n$ is refractive index in Equation 1.81 which depends on the neutron wavelength $\lambda$ and $\alpha$ is the angle of the beam to the prism surface.
With a sample in the direct beam, the prism and the detector need to be rotated such that the sample reflection strikes the center of the prism and is refracted. The intensity of the refracted spectrum is measured as a function of the deflection. For specular reflection, not only the incoming beam is well collimated but also the reflected beam before refraction. It then reaches the prism surface and each wavelength is refracted at unique angle $\varphi$.
In a practical situation, we should consider a spread in the incoming angle from the collimation, the imperfect flatness of the prism surface, and the resolution of the detector.
In [14] it has been demonstrated that the detector spatial resolution, in one direction, has to be of about 0.3 $mm$ to reach $\Delta\lambda/\lambda = 5\%$ resolution at 2 Å.
On the actual D17 instrument [41] one can implement the "rainbow" principle. Its detector spatial resolution is $\Delta x = 2\,mm$. In order to get a sufficiently high angular resolution for the reflected beam, the detector is positioned as far as possible from the sample, i.e. about $3\,m$. Due to practical limits in $^3He$ detector resolution and collimation, a resolution of $\Delta\lambda/\lambda < 5\%$ at short wavelengths is probably not practical. Therefore, the development of an area detector with $\Delta x = 0.2\,mm$ required in one dimension only (the other dimension can be summed) is crucial [59].
Although $^3He$ shortage affects scientific research; this is not the main issue for neutron reflectometry applications. A promising alternative, to accomplish the high spatial resolution and the high count rate capability, is to exploit solid $^{10}B$-films employed in a proportional gas chamber.

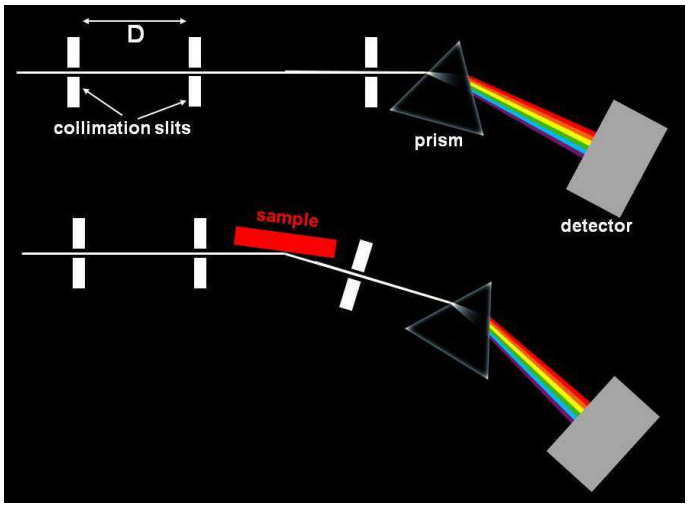


Figure 6.2: Schematic of the reflectometer Rainbow [14] involving a prism to deduce the neutron wavelength by refractive encoding.

The challenge with this technique is to attain a suitable detection efficiency which is about 63% for the Figaro detector at 2.5Å. This can be achieved by operating the $^{10}B$ conversion layer at grazing angle relative to the incoming neutron direction. The Multi-Blade design is based on this operational principle and it is conceived to be modular in order to be adaptable to different applications. A prototype has been developed at ILL and the results obtained on our monochromatic test beam line are presented here. A significant concern in a modular design is the uniformity of detector response. Several effects might contribute to degrade the uniformity and they have to be taken into account in the detector concept: overlap between different substrates, coating uniformity, substrate flatness, parallax errors, etc.

## 6.2 The Multi-Blade concept

The Multi-Blade concept was already introduced at ILL in 2005 [60] and a first prototype was realized in 2012 [61]. Its design is conceived to be modular in order to be versatile to be applied in many applications on several instruments. The Multi-Blade exploits solid $^{10}B$-films employed as a neutron converter in a proportional gas chamber as in [23]. The challenge with this technique is to attain a suitable detection efficiency. This latter can be achieved by operating the $^{10}B$ conversion layer at grazing angle relative to the incoming neutrons direction. Moreover the inclined geometry leads to a gain in spatial resolution and as well in counting rate capability compared to $^{3}He$ detectors.
Figures 6.3 and 6.4 show the Multi-Blade detector schematic, it is made up of several identical units called *cassettes*. Each *cassette* acts as an independent MWPC (Multi Wire Proportional Chamber) which holds both the neutron converter and the read-out system. The fully assembled detector is composed of several cassettes inclined toward the sample position. The angle subtended by each cassette looking at the sample position is kept constant in order to maintain the spatial resolution and the efficiency as uniform as possible.
The cassettes must be arranged taking into account an overlap between them in order to avoid dead space over the whole detector surface. Moreover, once the instrument geometry changes

the cassette arrangement in the detector should also change; if the sample-detector distance changes, the cassettes inclination should change too, if we want to avoid dead spaces.

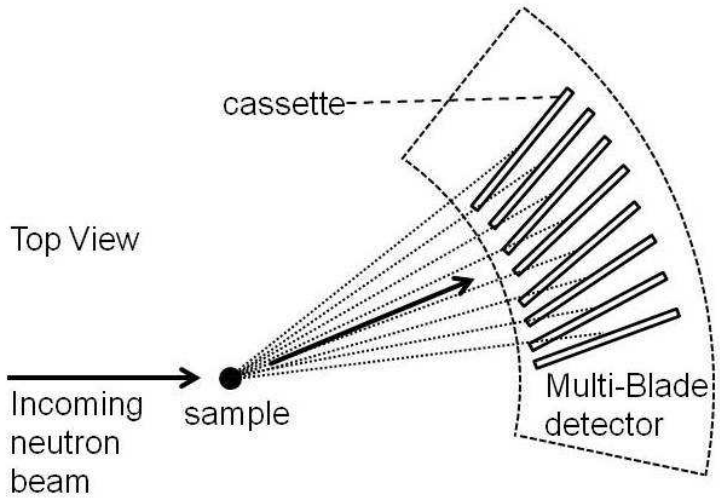


Figure 6.3: The Multi-Blade detector sketch (top view).

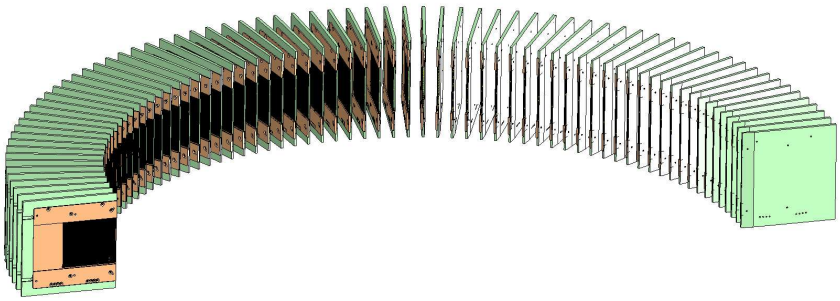

Figure 6.4: Several *cassettes* arranged in a cylindrical configuration around the sample position.

Each cassette should contain one or more neutron converters, e.g. $^{10}B_4C$ layers, and the read-out system that has to assure the two-dimensional identification of the neutron event. Figure 6.5 shows the cross-section of the cassette concept for three different configurations.
In the A and B solutions, in each cassette a single converter layer is facing each read-out system. The read-out is a wire plane and a strip plane placed orthogonally. The space between the strips and the converter is filled with stopping gas at atmospheric pressure to ensure the gas multiplication. The converter layer as well is polarized and together with the strip plane acts as a cathode; the wire plane, on the other hand, acts as an anode plane.

In the C configuration a single wire plane performs the two-dimensional read-out through charge division on resistive wires. A single read-out system is facing two converter layers. The space between the two converters is filled with stopping gas. The two converter layers act as cathodes.

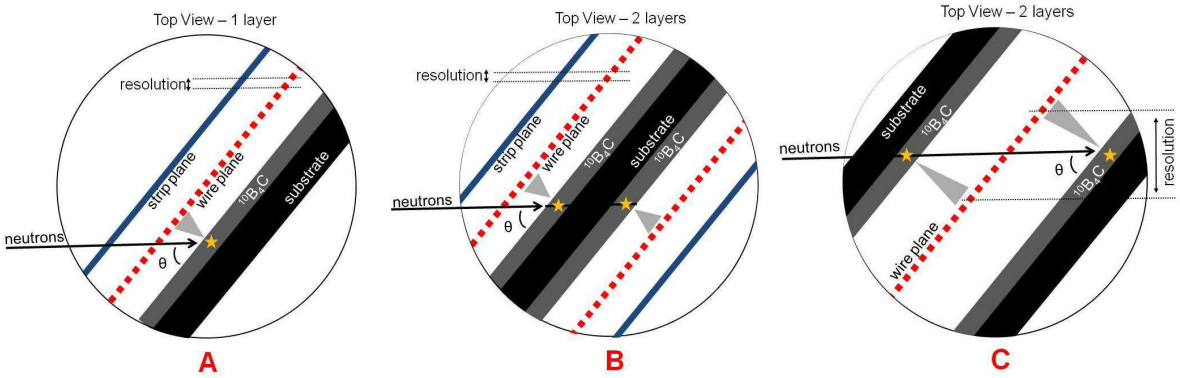


Figure 6.5: Cross-section of one cassette. Three options are shown: A, a single converter layer; B and C, with two converters.

Referring to configurations A and B, the identification of the position of a neutron event is the coincidence of wire and strip hits. The spatial resolution given by the strips does not depend on the inclination of the cassette. The spatial resolution given by the wire plane increases as the angle with the incoming neutron direction decreases. E.g. if the resolution is given by the wire pitch, the actual resolution is improved by a factor about 10 at $\theta = 5°$ $(1/\sin(\theta = 5°) \sim 10)$. Moreover, the actual neutron flux over the detector would be divided by the same factor increasing its counting rate capability; the same flux is shared by several wires.
While the spatial resolution is improved by inclination in both options A and B in Figure 6.5, all the advantage of working at grazing angle is lost in the C configuration. In [27] can be found the actual implementation of such a detector. In options A and B the charge generated by neutron capture fragments in the gas gives a signal on the facing wires and strips. In the solution C, for a given incoming neutron direction there will be two regions on the converters where neutrons are converted. The smaller the angle at which we operate the detector, the larger is the distance between those two regions. The uncertainty on the conversion point is then given by this distance which is much bigger than the wire pitch. On the other hand, option C has half the number of read-out channels as compared to A and B. However, for us, high spatial resolution is crucial.
We decided to concentrate on the implementation of the option A and B.
In Chapter 4 we showed how the solid converter layer efficiency increases as a function of its inclination and how much neutron reflection affects that efficiency. From reflectivity measurements we learnt for a common used neutron wavelength range, e.g. from 1Å to 30Å, that all the effects due to neutron reflection from $^{10}B_4C$ are negligible down to grazing angles of $\theta = 2°$. Therefore reflectivity is negligible for any kind of holding substrate that results into different converter roughness. As a result we decided to operate the Multi-Blade at either $\theta = 10°$ or $\theta = 5°$ in order to maximize the detection efficiency without any reflection concerns and keeping the mechanics simple.
Figure 6.6 shows the detection efficiency for $^{10}B_4C$ layers ($\rho = 2.24\, g/cm^3$) calculated according

to the model developed in Chapter 3 and neglecting neutron reflection. An energy threshold of $100\,KeV$ is applied. We considered two possible configurations: options A and B in Figure 6.5, with one converter or two. On the left we show the neutron detection efficiency, at 2.5Å, as a function of the converter layer thickness for the solutions A and B. While the efficiency shows a maximum for the two layer option, it is saturated over $3\,\mu m$ for the single layer. The single converter option can attain a maximum efficiency of 28% at 10° and 44% at 5° (2.5Å) to be compared with the double-layer efficiency of 37% and 54% respectively. The addition of the second layer, at $\theta = 5°$ leads to an increase of the efficiency of about 10% with respect to the solution A. The advantage of having only one converter is that the coating can be of any thickness above $3\,\mu m$ and the efficiency is not affected, while for the two layer option its thickness should be well calibrated. Moreover, in the two layer configuration the substrate choice is also crucial because it should be kept as thin as possible to avoid neutron scattering and this leads to possible mechanical issues. On the solution A, the substrate choice can be more flexible because it has not to be crossed by neutrons.
On the right in Figure 6.6 we show the efficiency as a function of the neutron wavelength for the the single layer of thickness $3\,\mu m$ (configuration A). The Figaro's detector efficiency [56] efficiency is also plotted, it is a $^3He$-based detector made up of $6.9\,mm$ tubes filled at $8\,bars$. In the plots shown the detector gas vessel Aluminium window is also taken into account as a neutron loss. For the Figaro's detector we used a $5\,mm$ thick window, and, since the Multi-Blade detector will be operated at atmospheric pressure, we used a $2\,mm$ window. $^3He$-based detectors' efficiency can be increased by increasing the $^3He$ pressure in the vessel; on the other hand, for a solid converter based detector the gas acts only as a stopping means, hence its pressure can be kept at atmospheric values. Consequently the gas vessel construction has less constraints.

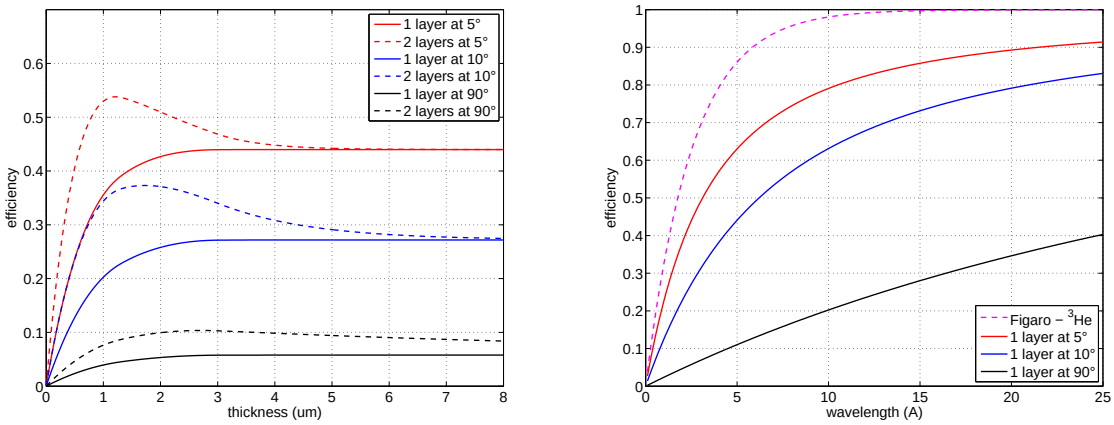


Figure 6.6: $^{10}B_4C$ layers ($\rho = 2.24\,g/cm^3$) detection efficiency at 2.5Å as a function of the layer thickness for the options A and B for three inclinations (left), efficiency as a function of the neutron wavelength for three inclinations of a single $3\,mum$ layer (right). An energy threshold of $100\,KeV$ is applied. The efficiency of the Figaro's detector is shown as well ($6.9\,mm$ tubes filled with $8\,bars$ of $^3He$).

In each of the solutions proposed for the cassette concept, see Figure 6.5, the read-out system has to be crossed by neutrons before reaching the converter. The mechanical challenge in the read-out system construction is to minimize the amount of material on the neutron path to avoid scattering that can cause misaddressed events in the detector.

Figure 6.7 shows four cassettes. They have to overlap to avoid dead spaces and the event loss, due to the zone where we switch the cassette, should be minimized. At the cassette edge electric field distortions and structure holding materials can cause a loss in the efficiency and consequently deteriorate the detector uniformity.
In the prototype realization all these problems have been taken into account, their solutions will be explained in the next Section.

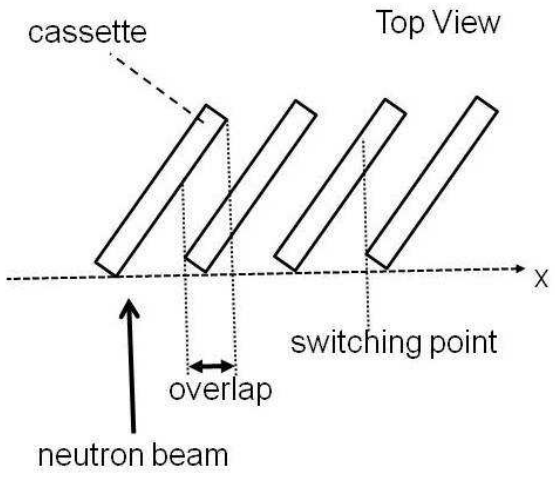


Figure 6.7: Four cassettes disposed one after the other. Their overlap and the switching region between one and an other is an important aspect to be studied.

## 6.3 Multi-Blade version V1

### 6.3.1 Mechanical study

The prototype was conceived to clarify the advantages and disadvantages of the options A and B shown in Figure 6.5.
The detector works as a standard MWPC operated at atmospheric pressure stopping gas such as $Ar/CO_2$ (90/10) or $CF_4$.
Since we want to avoid neutrons to be scattered before reaching the converter layer, we need to minimize the amount of matter that has to be crossed by neutrons: the read-out system and the cassette window.
Figure 6.8 shows a cassette drawing. An Aluminium substrate of thickness $0.5\,mm$ is coated on both sides by a $^{10}B_4C$-layer, i.e. a blade. One layer will work as a back-scattering layer and the second as a transmission layer. The converter is surrounded symmetrically by two polyimide PCBs. Each of them holds a cathode strip plane and a anode wire plane. The converter layer substrate is grounded and it acts as a cathode plane. Therefore a half cassette is a complete MWPC containing one neutron converter layer and a two-dimensional read-out system.
The entire structure is supported by an Aluminium U-shaped holder. The latter shape was conceived to remove any material that can scatter the incoming neutrons. Moreover, each holder presents two gas inlets in order to supply the stopping gas directly inside the gap between the converter and the PCBs. The exhausted gas will flow out from the frontal opening of the cassette

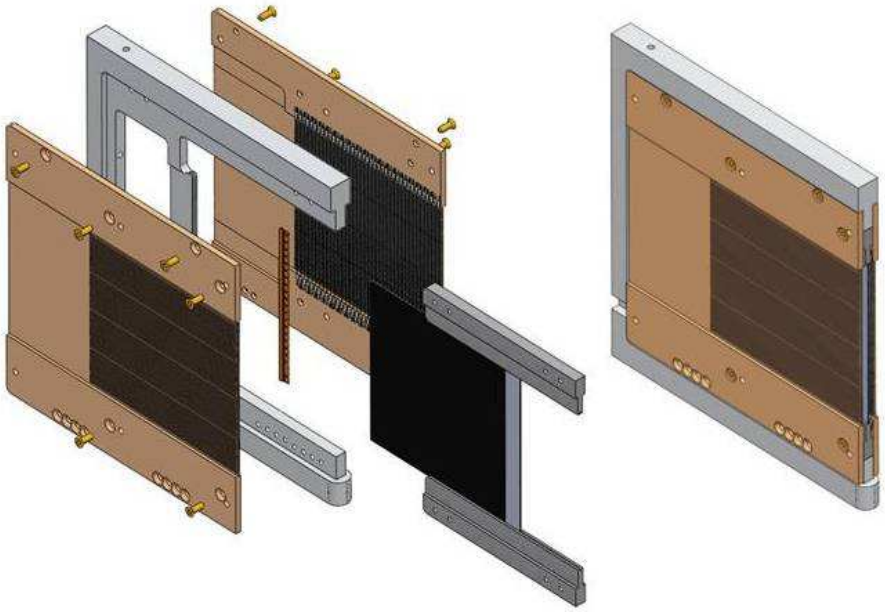

Figure 6.8: Exploded and assembled view of a cassette.

inside the gas vessel.

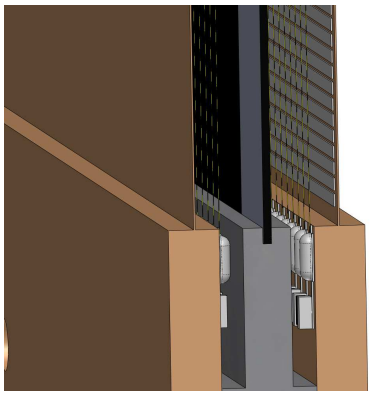

Figure 6.9: Detail of a cassette: the two polyimide PCBs surrounding the coated blade.

Figure 6.9 shows the detail of an assembled cassette. The polyimide PCBs have to be crossed before neutrons can be converted, hence, in order to reduce the amount of material that can induce neutron scattering, and thus misaddressed detected events, those PCBs are as thin as possible according to the mechanical constraints in their inner active region. The strips are deposited on the polyimide and the anode wires are stretched orthogonally over the strip plane. The copper strips are $0.8\,mm$ wide and spaced by $0.2\,mm$; tungsten wires are $15\,\mu m$ thick and they are spaced by $2.5\,mm$. The final electric signal is obtained by gas amplification on the anode wires placed in the gas volume. In order to decrease the number of read-out channels, anode wires and cathode strips are grouped by resistive chain for charge division read-out. Each full *cassette* has then 4 anode outputs and 4 cathodes outputs making 4 charge division read-out

chains. The resistors are placed on the PCBs surface.
The polyimide PCBs are $60\,\mu m$ thick in the inner region: $25\,\mu m$ is the polyimide thickness and $35\,\mu m$ is the copper strips thickness.
The sensitive area of each cassette is $10 \times 9\,cm^2$ but, since it will be oriented at $10\,^\circ$ with respect to the incoming neutron direction, the actual sensitive area offered to the sample is given by $(10\,cm \cdot \sin(10\,^\circ)) \times 9\,cm = 1.7 \times 9\,cm^2$. As a result, the actual wire pitch, at $10\,^\circ$, is improved down to $0.43\,mm$.
The detector will be installed to have the better resolution in the direction of the reflectometry instrument collimation slits; i.e. the cassettes, which can be mounted either horizontally or vertically, will be oriented with the wires parallel to the instrument slits.
Figure 6.10 shows a drawing of 8 cassettes stacked one after the other and placed in the gas vessel.
As already mentioned, the main issue to be addressed in the final detector is the uniformity, as soon as it is made of several units, their arrangement is crucial to get a uniform response in efficiency. A misalignment in one of the modules can give rise to a drop in the efficiency or dead zones.
The cassettes have to be arranged in order to overlap to avoid dead zones. For this reason this detector is suitable for fixed geometry reflectometry instruments, where the distance between sample and detector is kept constant and the arrangement does not change.

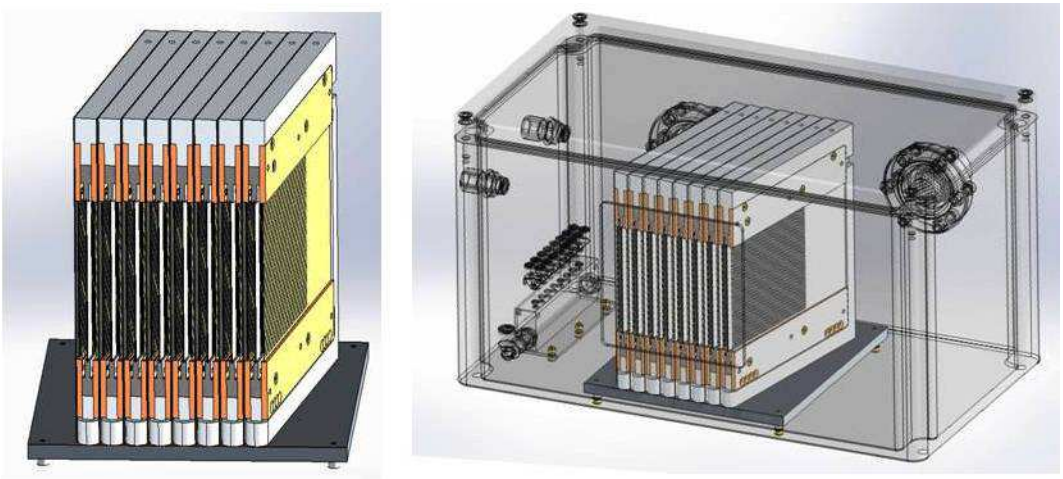

Figure 6.10: A 8-cassettes Multi-Blade in its gas vessel.

The final prototype will be mounted in a gas vessel, see Figure 6.10, together with the gas distribution unit which splits the inlet in the several cassettes, and the electronic connections.
Since the gas is flushed cost effective materials can be used because their outgassing is not an issue.
The presented prototype allows to study both the single layer and the double converter solutions. Its realization, advantages and mechanical issues, will be explained in the following Section.

### 6.3.2 Mechanics

The first prototype (V1) consists of four cassettes operated at $10\,^\circ$. Given the cassette active region size, the prototype active area, considering their overlap is about $6 \times 9\,cm^2$.

Figure 6.11 shows a polyimide PCB. The latter is composed by a stack of three layers: two thick PCBs where in the middle is fixed a $25\,\mu m$ polyimide foil. The inner part is soft and the external part serves as a holder. 86 copper strips are deposited on the surface of the thin region (see Figure 6.12).
39 anode wires (37 active wires and 2 guard wires) are mounted and soldered on pads at $2\,mm$ distance from the cathode plane. Both for anodes and for cathodes a resistive chain is soldered on the rigid PCB. The total resistance is $6\,K\Omega$ for the anode chain and $8\,K\Omega$ for the cathode chain. At the wire plane edge a guard wire was installed to compensate the electric field distortion, hence this wire will not produce any signal.

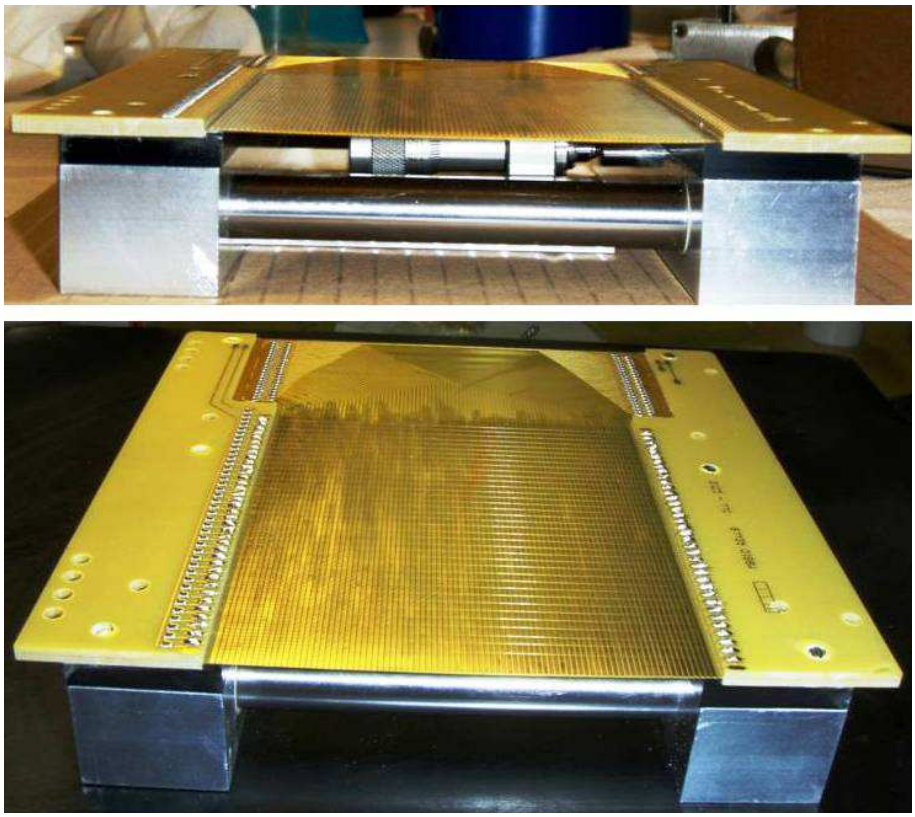

Figure 6.11: A polyimide PCBs where anode wires are mounted orthogonal to the cathode strips.

The total gap between the converter and the cathode plane, i.e. half cassette width, will be about $4\,mm$, thus any deformation of either the substrate or the strip plane will produce a variation in the local electric field produced between the anode plane and cathodes. Consequently where the cathode is closer to the wire plane the detector will manifest a higher gain. This effect mainly degrades the uniformity over the cassette surface. The overall uniformity on the whole detector surface is then degraded by the single cassette uniformity and their arrangement in the space: overlap and switching from one to another.
It is crucial to control the flatness of both the substrate and the PCB. The first manufactured PCB was composed of a thin polyimide held on three sides by the rigid PCB. The provider was not able to assure the polyimide flatness with this design. We changed the PCB design in order to be able to pull on both sides and restore its flatness. The polyimide is held by only two of

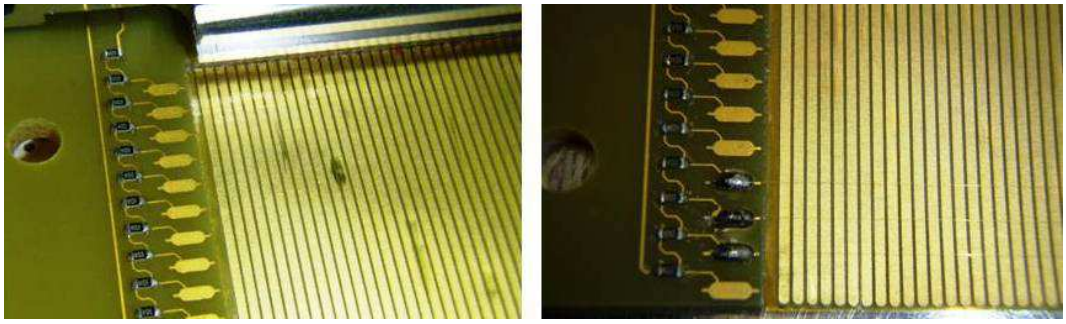

Figure 6.12: Detail of a polyimide PCBs: resistors for charge division link the wire pads where anodes are soldered.

its sides (see Figure 6.11). The PCB is held by a tool (see Figure 6.11) that allows to stretch the foil before being mounted on the Aluminium holder. This tool allows also to mount wires on the PCB keeping the system under tension. The $15\,\mu m$ tungsten wires are mounted on the PCB under a tension of $35\,g$. Once wiring is over, the PCB can be installed on the holder.
Figure 6.13 shows the Aluminium holder where the double side coated substrate with $^{10}B_4C$ [37] is inserted. In order to keep the wire tension, the PCB, without removing the stretching tool, can be placed on the holder. The holder and the PCBs present four different fixation screw shifted by $0.25\,mm$ from each other. The PCB can be screwed on the holder according to its actual size after stretching. This ensures the right tension on the wires and the flatness of the cathode plane.
As for the read-out plane, the converter holding substrate must be flat too. After sputtering, between the $Al$-substrate and the $^{10}B_4C$ coating, a significant residual stress remains due to the difference in the thermal expansion coefficient of $Al$ ($\sim 23.5 \cdot 10^{-6}\,1/K$) and $^{10}B_4C$ ($\sim 5.6 \cdot 10^{-6}\,1/K$). When they are cooled down to room temperature the $Al$ contracts more than $^{10}B_4C$. Experiential evidences of that have been observed: on single side coated substrates, the un-coated side is shorter than the coated side, resulting into a bending of the blade. When a double-side coated blade has to be inserted into the holder (see Figure 6.13) the constraints on the sides makes the blade bend and unstable. On both sides two PCBs have to be installed resulting into two identical and symmetrical MWPC.
We wanted to study both option A and B with this prototype but due to the blade mechanical issue we convert the prototype in a single layer detector.
In order to keep the substrate with the converter flat enough to ensure a uniform electric field, we mounted it on an Aluminium lid placed where a PCB was removed (see Figure 6.14). We used a $3\,\mu m$ thickness $^{10}B_4C$ coating instead. The gap between the wires and the converter was increased up to $6\,mm$, while the gap between the wires and the strips is about $2\,mm$. The MWPC is asymmetric. Figure 6.14 shows the four cassettes equipped with the read-out systems and the converters.
The version V1 of the Multi-Blade detector allowed only to study the single layer configuration A, as mechanical issues had made impossible the initial configuration B realization.
The number of read-out channels per cassette were reduced from 8 to 4: 2 anode and 2 cathode outputs.
Four cassettes were stacked at $10^\circ$ with respect to the beam and parallel to each other. Figure 6.15 shows the detail of the four cassettes stacked from two points of view. We define as the $x$-

Figure 6.13: The Aluminium holder and a blade (substrate coated with $^{10}B_4C$ both sides) inserted.

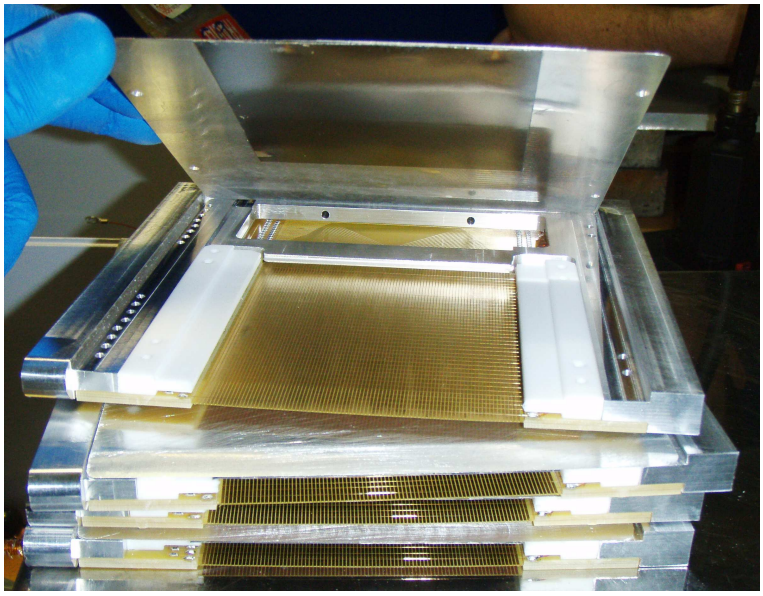

Figure 6.14: Four cassettes assembled. The read-out PCB is installed on the Aluminium holder.

coordinate where the wire pitch is projected at 10 °. The $y$-coordinate is defined by the direction orthogonal to the strips orientation.
The four cassettes were then installed in the gas vessel, see Figure 6.16. Each cassette is supplied by two inlets to let the gas to flow directly inside them. The entrance window of the detector is the one on the right in Figure 6.16.
The front-end electronics of the prototype is connected outside the gas vessel and consists of a decoupling circuit and charge amplifiers. A schematic of the whole front-end electronic chain is shown in Figure 6.17. Both wires and strips are connected in the same way by their resistive chain, the AC signal is decoupled by two capacitors at both ends from the DC component used

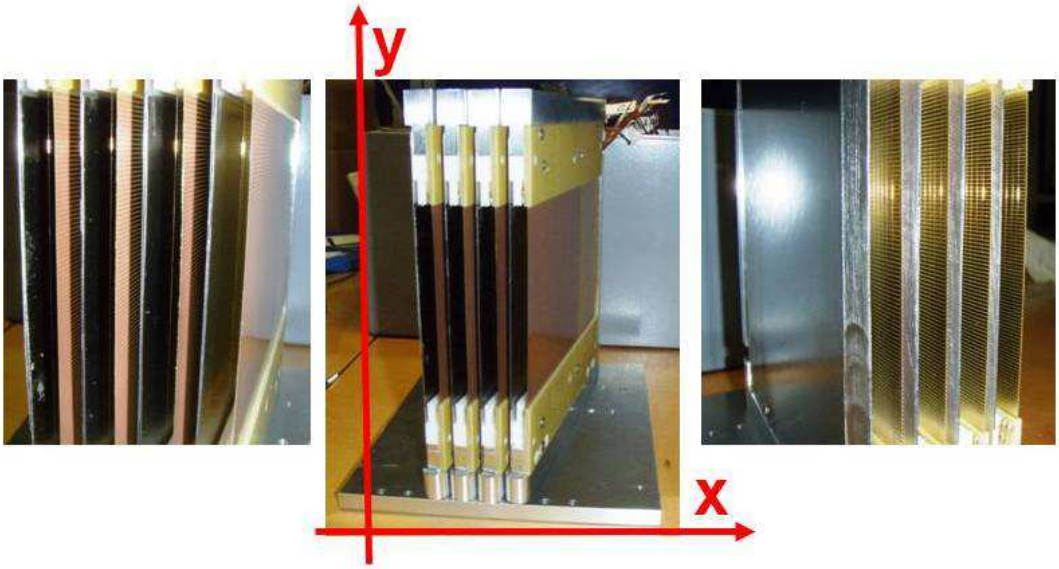


Figure 6.15: Four cassettes stacked one after the other at 10 ° and parallel each other.

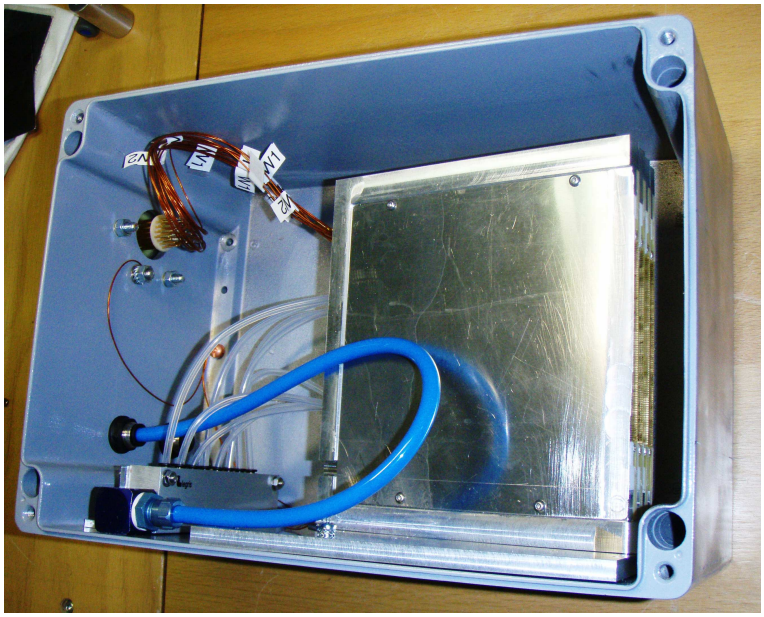

Figure 6.16: The four cassette assembly in the gas vessel. Each cassette is supplied by two gas inlets. The detector entrance window is the one on the right.

to polarize the wires at the HV and the strips to the ground potential.
The charge is amplified by charge amplifiers. We used inverting amplifiers of $6\,V/pC$ and $1\,\mu s$ shaping time for anodes and non-inverting amplifiers of $32\,V/pC$ and $2\,\mu s$ shaping time for cathodes.
Each chain ends into two signal outputs that can be either summed to get the energy information (PHS) or subtracted and divided to get the positional information.

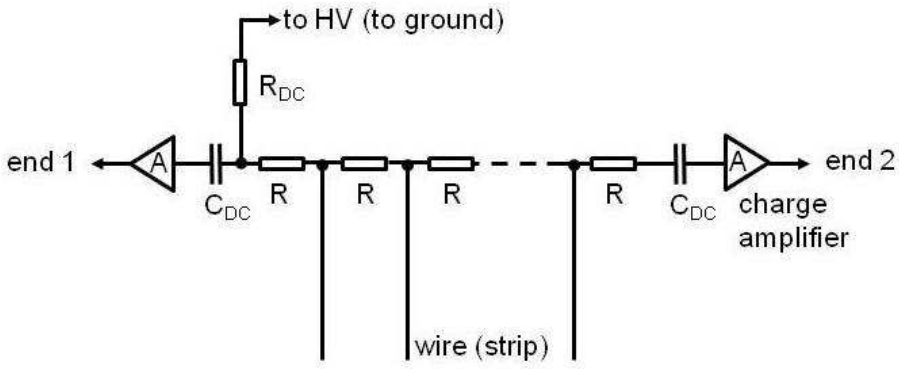


Figure 6.17: The Multi-Blade front-end electronics schematic.

**Polyimide layers characterization**

Transmission measurements on the polyimide layers used in the Multi-Blade prototype have been performed on CT1 (2.5Å neutron beam) at ILL. The neutron beam was collimated and, as shown in Appendix E, it was calibrated to $(122020 \pm 80) Hz$. The polyimide samples were placed after the collimation slit in front of a a two-dimensional $^3He$-based detector (BIDIM) placed at distance $D$. The detector has an efficiency for 2.5Å neutrons of 70%, a spatial resolution of $2 \times 2\, mm^2$ and $26 \times 26\, cm^2$ active area. A single polyimide layer is composed of a stack of $25\, \mu m$ thick polyimide and $35\, \mu m$ thick copper strips.
We place different number of layers in front of the BIDIM in order to simulate the increase of thickness to be crossed by neutrons due to the inclination. An inclination of 10° corresponds to about 6 layers and 5° to about 12 layers.
We repeat the measurement for two distances between detector and sample: $D = 3\, cm$ and $D = 23\, cm$. Diffraction from the samples is not isotropic because of the sample structure itself. Figure 6.18 shows three measurements on a 12 layer sample for the two distances normalized to the incoming neutron flux (the color scale is in $Hz$). The cross arising at $D = 23\, cm$ is due to the diffraction through extended fibers which is the polyimide molecule. Those fibers are placed crossed in the layer manufacturing process.

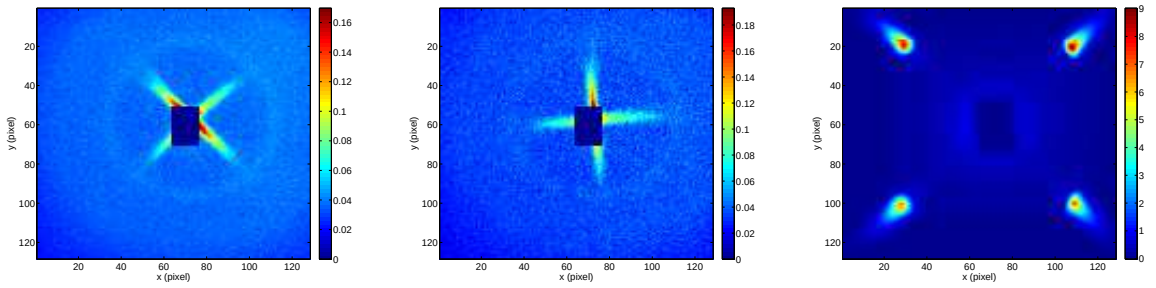


Figure 6.18: Scattered neutrons (2.5Å) by 12 polyimide layers on the BIDIM detector ($26 \times 26\, cm^2$ active area) at $23\, cm$ distance (left and center) and at $3\, cm$ distance. The polyimide layers are rotated by 45° between the left and center plots. The color scale is in $Hz$.

We calculate the scattered beam by the layers, for the two distances, as the ratio of the counting rate on the whole detector surface over the incoming neutron flux. The result as a function of number of layer is shown in Figure 6.19. At $D = 3\,cm$ the detector surface covers a solid angle of $0.398 \cdot 4\pi\,sr$, and at $D = 23\,cm$ of $0.078 \cdot 4\pi\,sr$.

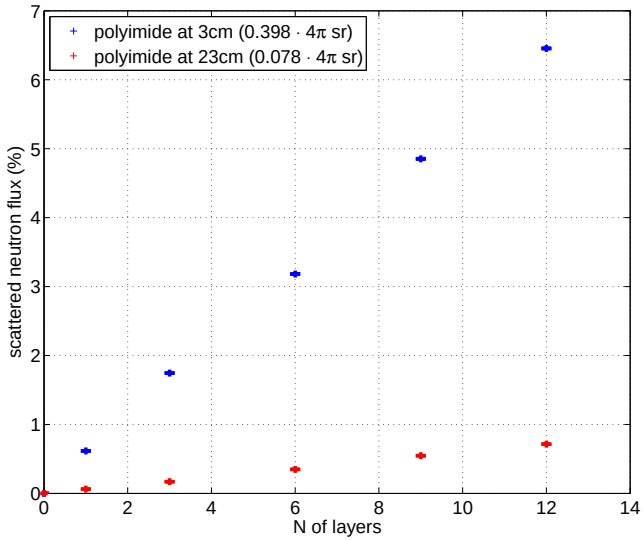


Figure 6.19: Percentage of neutrons (2.5Å) scattered by polyimide as a function of number of layers. At $3\,cm$ distance the detector covers 39.8% of the full solid angle, at $23\,cm$ 7.8%.

At 10° (that equals about 6 layers) we expect to diffuse at most about $\frac{3\%}{0.398} \simeq 7.5\%$ (at 2.5Å) of the beam assuming the same scattering in $4\pi\,sr$.

### 6.3.3 Results

#### Operational voltage

A counting curve was measured in order to set the right bias voltage to be applied to polarize the prototype. Each cassette output was connected to get the energy information and then to measure the PHS. Given the electronic noise, a $25\,mV$ threshold was used for the anode amplifiers; for the cathode amplifiers we used $100\,mV$. Figure 6.20 shows a PHS for both strips and wires, compared with a PHS calculated according to Section 3.6 at $1000\,V$.
The working voltage chosen through the counting curve is $1000\,V$.

#### Gain

The Multi-Blade prototype is operated in proportional mode, its gain has been measured on CT2 at ILL. The neutron flux of $(15280 \pm 20) neutrons/s$ (2.5Å) was quantified using the Hexagonal detector (see Appendix E).
The prototype was polarized at $1000\,V$. Its $3\,\mu m$ $^{10}B_4C$ converter layer was exposed to the beam orthogonally and $\Phi_d = (904 \pm 2) neutrons/s$ were counted. It results into a $\varepsilon = (5.92 \pm 4)\%$ detection efficiency. The current flowing through the detector was measured and it is about

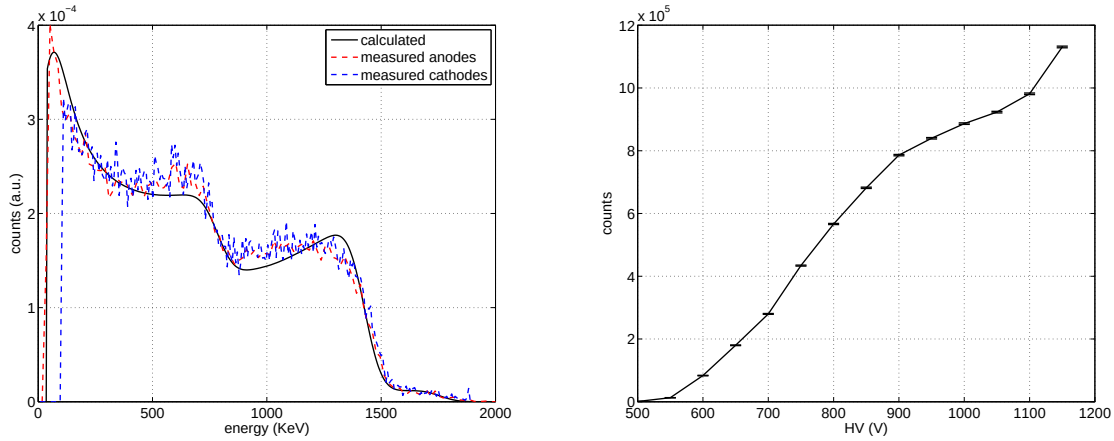


Figure 6.20: PHS measured on strips and wires at $1000\,V$ and calculated PHS (left). The Multi-Blade detector plateau (right).

$I_{prop.} = 180\,pA$.
The detector operational voltage was set to $100\,V$. The measurement of the current output was repeated operating the detector in ionization mode, resulting into $I_{ion.} = 3.1\,pA$.
The average charge created for a detected neutron both proportional and ionization modes are:

$$Q_{prop.} = \frac{I_{prop.}}{\Phi_d} = 199\,fC/neutron, \qquad Q_{ion.} = \frac{I_{ion.}}{\Phi_d} = 3.4\,fC/neutron \tag{6.2}$$

This results into a gain of about $G = 58$ at $1000\,V$.

### Efficiency

Detection efficiency of the Multi-Blade prototype V1 has been measured on CT2 at ILL by using a collimated and calibrated neutron beam of wavelength 2.5Å.
The neutron beam was calibrated using an $^3He$-based detector. The procedure is explained in details in the Appendix E. After the calibration, the neutron flux the Multi-Blade was exposed to is $(15280 \pm 20)\ neutrons/s$ over an area of $2 \times 7\,mm^2$.
The efficiency was measured for the following bias voltages $950\,V$, $1000\,V$ and $1050\,V$. The efficiency was measured on the four cassettes under the angle of 10° and then averaged. The results are listed in Table 6.1.

| $HV(V)$ | $\varepsilon$(at 2.5Å) | Threshold $(KeV)$ | calculated $\varepsilon$(at 2.5 Å) |
|---|---|---|---|
| 950 | $(24.8 \pm 0.2)\,\%$ | 180 | 24.6% |
| 1000 | $(26.2 \pm 0.2)\,\%$ | 120 | 26.3% |
| 1050 | $(27.5 \pm 0.2)\,\%$ | 90 | 27.3% |

Table 6.1: Multi-Blade detection efficiency at 2.5Å for three bias voltages and calculated efficiency for a given threshold.

The result is in a good agreement with what can be calculated from the theory (Chapter 3) by using an energy threshold of $180\,KeV$, $120\,KeV$ and $90\,KeV$ for the three voltages from $950\,V$ to $1050\,V$ respectively.

### Uniformity

The main issue in the Multi-Blade design is the uniformity over its active surface. The cassettes overlap to avoid dead zones, and, in the switching between one cassette to another, a loss in efficiency can occur. There are mainly two reasons that cause the efficiency drop: at the cassette edge the electric field is not uniform and there is some material that scatters neutron on the way to the next cassette. In order to reduce the dead zone at the cassette edge, i.e. any material that can cause scattering, each cassette is cropped (see Figure 6.15) to be parallel to the incoming neutron direction.
Moreover, when a neutron is converted at the cassette edge, it produces a fragment that half of the time travels toward outside of the cassette and half time inward. We expect not to have generated charge for about 50% of the events. In addition to that the electric field at the edge may not be uniform and the guard wire contributes to enlarge the dead zone because it does not generate charge amplification.
We scan with a collimated neutron beam and we register a PHS over the whole prototype surface by using a $1\,mm$ step for the $x$-direction and a $10\,mm$ step for the $y$-direction. We integrate the PHS for each position and we obtain a local counting. We normalize it to 1 on the average efficiency. Figure 6.21 shows the relative efficiency scan over the whole detector. The scan along the cassettes in the position $y = 40\,mm$ is also shown.

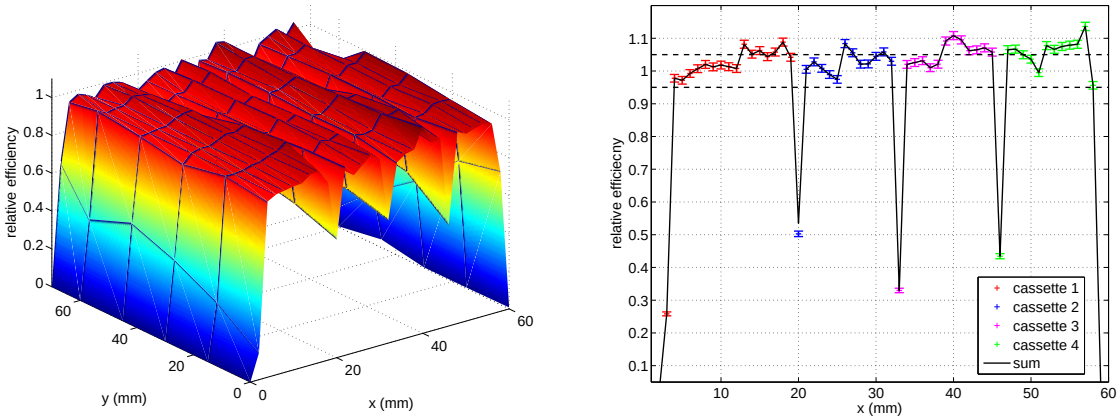


Figure 6.21: Relative efficiency scan over the whole detector surface.

Each cassette shows a quite uniform response along its strips ($y$-direction); the maximum efficiency relative variation is below 2%. On the other hand, in the gap between two cassettes the efficiency drops about 50% in a region which is $2\,mm$ wide.

### Spatial resolution

When we want to calculate a detector spatial resolution one should be careful as to which definition has to be adopted in order to give a meaningful result. If the detector response is a continuous function or discrete the problem should be tackled in a different way.
The spatial resolution is defined as the ability to distinguish between two events as a function of their distance. We have a continuous detector response if a large amount of events that occur

at a certain position on the detector will generate a continuous distribution in space. A widely used criterion is to define the spatial resolution as the FWHM (Full Width Half Maximum) of a distribution of those events. In the particular case the events distribution in space ends up to be gaussian the FWHM is equivalent to $2.35 \cdot \sigma$, with $\sigma$ its standard deviation. In 88% of the cases, for two neutrons hitting the detector at a distance of a FWHM (see Figure 6.22), we will identify them on "the right side". We will identify them with 12% probability to be on the wrong side.

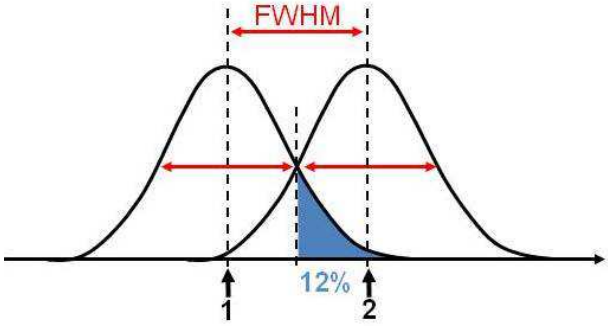


Figure 6.22: Two neutrons hitting a detector at a FWHM distance. We identify them with 12% probability to be on the wrong side.

When the detector response can be considered continuous, the spatial resolution as the FWHM represents a suitable definition. This happens when the pixel size is much smaller than the resolution. On the other hand it is not possible to define the spatial resolution as a parameter of a distribution if the events are discretely distributed over a few pixels. That is when the granularity of the detector is comparable with the spatial resolution.
As example, let's imagine a detector read-out system made up of strips. Imagine that their width is a few $mm$. A gas volume faces the strip plane. If the ionizing particle ranges in gas is order of a few $cm$, the induced charge on the strips results in a continuous distribution over the strips with charge centroid in the center of the resulting gaussian distribution.
On the contrary, if the particle ranges in the gas were much shorter, $\sim 1\,mm$, the strip response would be not any more gaussian, but almost an individual strip will participate to the induction process.
We consider a MWPC of wires spaced by a few $mm$ and particle tracks comparable to the wire pitch. The detector response to a single event is not continuous. As most of the charge is originated in the multiplication region thanks to the avalanche process close to the wire, each wire acts as an independent detector. Each wire acts as a electromagnetic lens focusing the charge for a certain detector segment. Thus, the detector is segmented and, thus, discrete. If the primary charge is only generated in the influence cell of a single wire, only this wire will generate a signal; on the other hand, if a ionization process covers two segments two wires will be involved. In this case the spatial resolution is not given by the wire pitch because there can be situations where two wires reacts to the single event. Moreover, spatial resolution is neither two wire pitch because there are cases when only one wire reacts. In fact, by putting forward that the detector has a two wire pitch resolution we were asking to be able to discriminate between events with a precision of 100%. That is not incongruent with out FWHM resolution definition to get a 88% precision.
We should reformulate the spatial resolution definition for a more general case.

In order to do that, one can refer to the Shannon information theory [62]. If we consider two streams of neutrons hitting the detector in two different positions we will get, according to its resolution, two resulting response distributions that can either be completely separate, can overlap partially or can be indistinguishable. The resolution definition is based on the probability to correctly assign an event to its real neutron original stream, i.e. to the right distribution.
This problem can be treated as a lossy communication channel. In a binary communication channel the bit 0 or 1 can be sent and, in presence of noise, it can be received correctly or flipped.
That is the same as determining the probability to assign a neutron that belonged to one of two distributions to the right one.
We define as the mutual information $I(X;Y)$ the information that the receiver get in a noisy channel, i.e. the detection process when 1 bit of information was sent. $X$ is the received message if $Y$ was sent. If the mutual information is 1, no loss in the channel is present.
In the detector case four possibilities are possible: a 0 was sent and 0 is received, a 0 was sent and a 1 is received, and similar for a 1 is sent.
The mutual information is operationally defined as:

$$I(X;Y) = \frac{1}{2}\sum_{x=0}^{1}\sum_{y=0}^{1} p(x|y)\log_2 \frac{p(x|y)}{\frac{1}{2}(p(x|0)+p(x|1))} \tag{6.3}$$

where $p(x|y)$ is the conditional probability to send y and get x.
$I$ represents the information we have obtained from a single neutron impact about the point source from which it originates. By resolution we can then understand the distance between two neutron hits needed in order to reach a given threshold of information $I$.
We can define, in the case of a symmetric distribution, as $a$ the probability to make the right reception of the message; i.e. we send 0 and we get 0 or we send 1 and we get 1. This probability is naturally symmetric for the neutron labels 0 or 1. The resulting probability $1-a$ would be the probability to make the wrong reception; i.e. to assign a neutron to the wrong stream. In the gaussian continuous case, at one FWHM distance, those probabilities correspond to $a = 88\%$ and $1-a = 12\%$. Hence, if we calculate the mutual information for this case we get 0.47 bits of information. Therefore, the probability of 88% to make the right reception corresponds to an information of 0.47 bits (in the symmetric and continuous case).
As a result, a way to define the resolution which is independent from any spatial distribution is to calculate the mutual information and asking to get a minimum threshold value of 0.47 bits. This definition is suitable as well for discrete response, when the detector granularity is comparable to the resolution we want to calculate as for the continuous case where it will become the FWHM definition if the distribution is gaussian. As a matter of fact, a scan over several neutron streams has to be performed to determine the lowest mutual information obtained.
Going back to the MWPC example, in the case the detector response involves either one or two wires according to the particle track position, the mutual information will be higher for higher spacing between distributions because their overlap is smaller.
The value to take as the detector resolution is the one that gives the spacing to achieve a mutual information of at least 0.47 bits.

**Spatial resolution: x** The version V1 of the Multi-Blade prototype is operated at 10° between the neutron incoming direction and the detector converter layer. We recall that the wire plane

is projected on the neutron incoming direction. An improvement by a factor $\sin(10^\circ) \sim 0.17$ is achieved on the horizontal spatial resolution with respect to an orthogonal incidence. E.g. if the spatial resolution, before projection, were a wire pitch (in our prototype $2.5\,mm$) this results in an actual resolution of about $0.45\,mm$.
In Figure 6.23 is shown the charge division response of the wire plane by using either a diffuse beam or a collimated beam down to $1\,mm$ footprint (2.5Å).

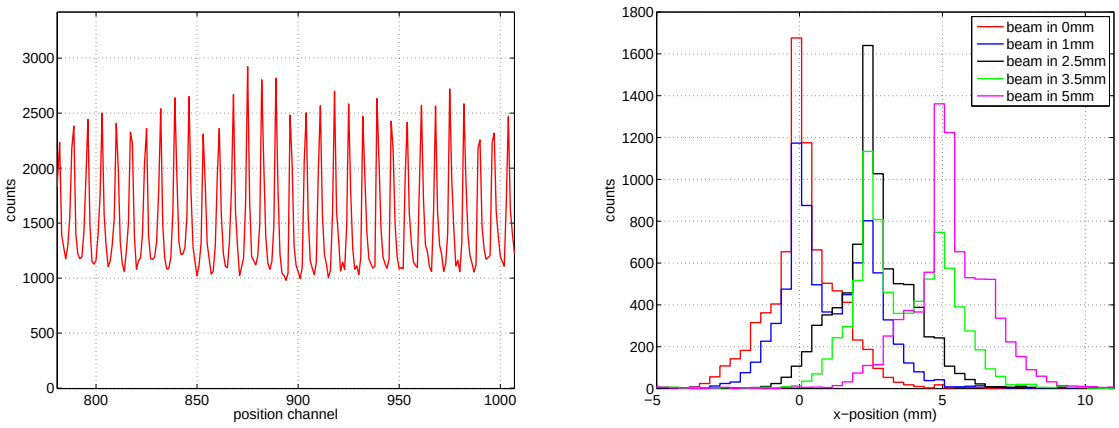


Figure 6.23: Diffuse beam wire response in charge division (left), collimated neutron beam response as a function of the beam position (right).

The charge division method is able to identify each wire anode position; when a collimated beam is in one position we can either get a single wire reacting or two. This effect is due to the fact that the wire plane splits the gas volume into almost independent cells, thus the charge generated by primary ionization in one cell makes its associated wire react. In our case, since we are using a mixture of $Ar/Co_2$ (90/10) at atmospheric pressure the $^{10}B$ neutron capture reaction fragment ranges make a few $mm$. Therefore, if the track is contained in one single wire cell, only a single wire reacts; on the other hand if the track travels across two cells we get a two wire response. Since the wire plane is read-out in charge division, if two wires react, the hit will be identified to be in between the two wires, corresponding to the charge centroid. The response distribution, for a given hitting position, will have tails corresponding to these events. Figure 6.23 shows the resulting distribution as the neutron beam moves along the detector. One can wonder now in what is the actual spatial resolution in this situation. In order to quantify it is necessary to apply the informational-theoretical approach explained above.
We calculate the mutual information between the distribution in Figure 6.23 for all the possible combinations and we will take as resolution the worse result at an information threshold level of 0.47 bits.
Figure 6.24 shows the mutual information as a function of the distance of the neutron distribution response of our detector. We notice that in the worst case we end up with $3.4\,mm$; which translates into a spatial resolution of $0.6\,mm$ at $10^\circ$.
Note that the spatial resolution lies in between a single wire pitch ($2.5\,mm$) and two; because we are asking the detector to be able to discriminate between two neutrons that hit the detector at one resolution distance with a confidence level of 88%.

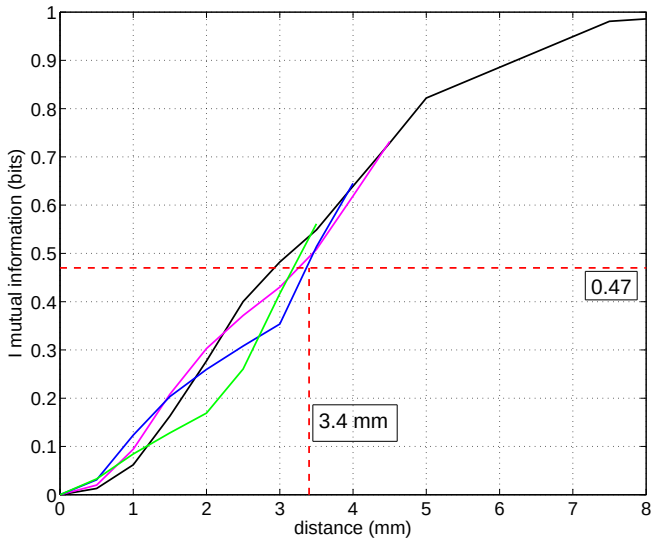


Figure 6.24: Mutual information as a function of the distance between the response distributions of the neutron detector. The horizontal line defines an information of 0.47 bits that corresponds to a 3.4 $mm$ spatial resolution (before projection) in the worse case.

**Spatial resolution: y** As already mentioned, particles tracks in gas make few $mm$. Since the cathodes read-out strips are 0.8 $mm$ wide and they are spaced by 0.2 $mm$ and the read-out is performed by a charge division chain, there are several strips that are involved in the induction process per each event. The charge division makes the charge centroid along the $y$-direction in the detector.
For the cathodes the response can be considered continuous and the FWHM method is suitable. Figure 6.25 shows the strip response as a function of the position of the collimated beam hitting the detector. By performing a gaussian fit we obtain a spatial resolution (FWHM) for the vertical direction $y$ of about 4.4 $mm$.

### Images

To validate the results we want to generate an image with our prototype. In order to do that we acquire both anode and cathode signals and we reconstruct an event using their time coincidence. Figure 6.26 shows an image reconstructed with the Multi-Blade obtained by placing a Cd mask in order to get a pattern. The mask consists of 80 holes of 1 $mm$ size spaced by 5 $mm$ along $x$ and by 1 $cm$ along $y$.
The number of bins on the image is set to be equal to the number of wires (37) for the $x$-direction and is 256 bins for the $y$-direction.
Due to the neutron beam divergence the spots on the image appear much wider than the detector resolution.
In the reconstructed image we observe the intensity that drops at the cassettes edges.

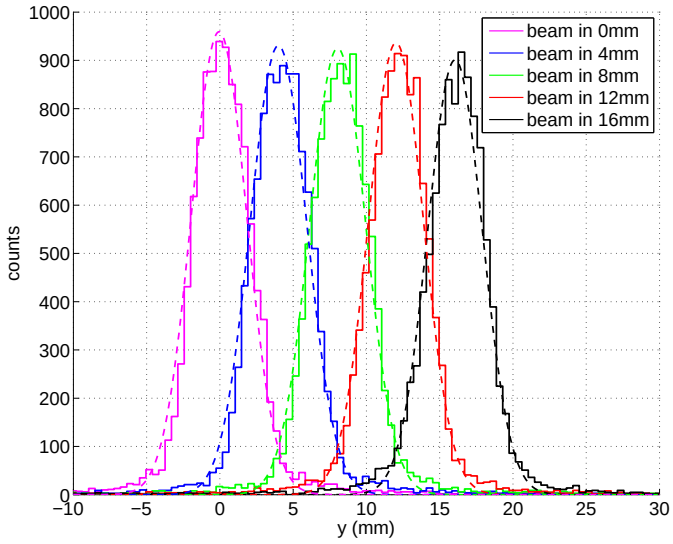


Figure 6.25: Fine beam neutron scan along the strip cathodes. The spatial resolution is given by the FWHM and corresponds to 4.4 $mm$.

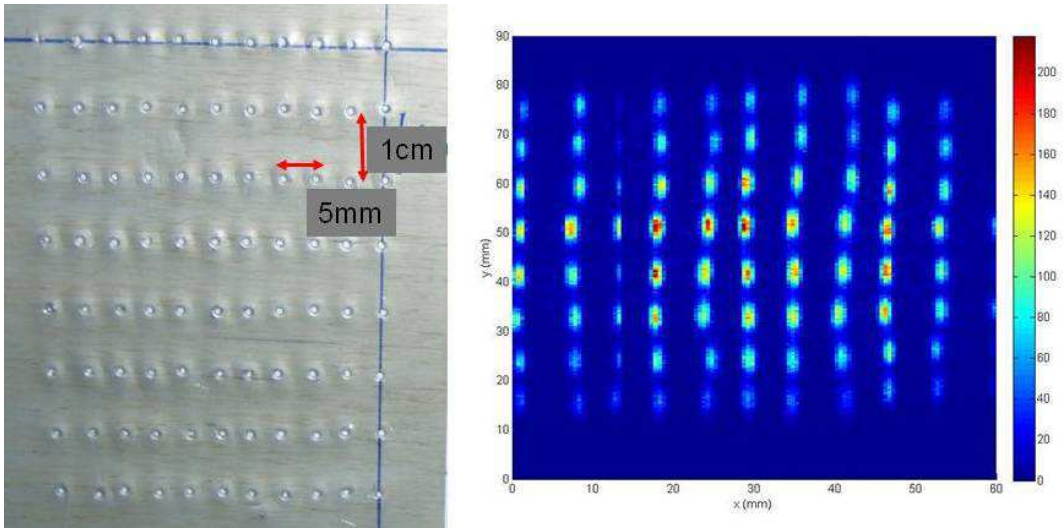


Figure 6.26: The Cd mask (left) used to generate the image on the right.

## 6.4 Multi-Blade version V2

### 6.4.1 Mechanical study

We learned from the Multi-Blade version V1 that the single layer configuration (option A) presents less mechanical constraints. Moreover, the substrate holding the converter has not to be crossed by neutrons that makes its manufacture easier.
The converter layer can be thick because the efficiency is saturated above 3 $\mu m$; the substrate can be thick also because it has not to be crossed by neutrons to hit a second converter. Hence,

the substrate can be an integrated part of the cassette holder, the converter layer can be directly deposited over its surface. The read-out system used is the same as in version V1. Neutrons have still to cross the PCBs before being converted. Figure 6.27 shows a cassette and a stack of them conceived for the single layer option.

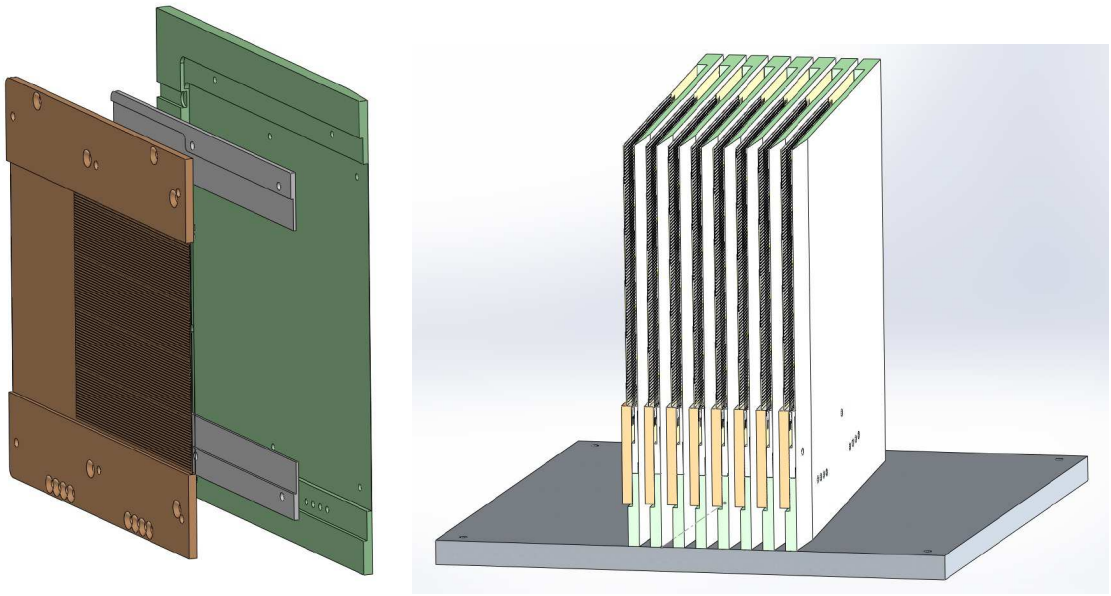

Figure 6.27: A cassette conceived to hold one converter layer (left) and a stack of several cassette (right).

The cassettes are oriented at $5\,^\circ$ with respect to the incoming neutron direction. The sensitive area of each cassette is $10 \times 9\,cm^2$ but, the actual sensitive area offered to the sample is given by $(10\,cm \cdot \sin(5\,^\circ)) \times 9\,cm = 0.9 \times 9\,cm^2$. As a result, the actual projected wire pitch is improved down to $0.22\,mm$.

### 6.4.2 Mechanics

The second prototype (V2) consists also of four cassettes but we operate them at $5\,^\circ$. At this inclination the expected efficiency at 2.5Å is about 43% if we employ the sputtered coating of the version V1 [37]. The cassettes are the ones shown in Figure 6.27, conceived to study the single converter layer option. A rigid substrate is directly coated with the converter material. The cassette width in the version V1 was about $12\,mm$, in the version V2 we reduce their actual size to $6\,mm$. Consequently the MWPC gap, between the converter and the cathodes, is $4\,mm$. With respect to the version V1 the wire plane is closer to the converter.
The prototype active area, considering the cassette overlap, is about $3.2 \times 9\,cm^2$.
The read-out PCBs are those used in the version V1.
Figure 6.28 shows a cassette substrate both coated and un-coated.
Since the efficiency is saturated as the thickness of the layer exceeds $3\,\mu m$, we study the possibility to use different converters. We can deposit a painting containing $^{10}B$ grains and make a coating a few hundreds of microns thick. A thick layer also functions as an integrated collimator. Any neutron that comes from the sides of the detector has less probability to be detected and is more likely absorbed in the outer layers. Hence, only neutrons which impinge the detector from

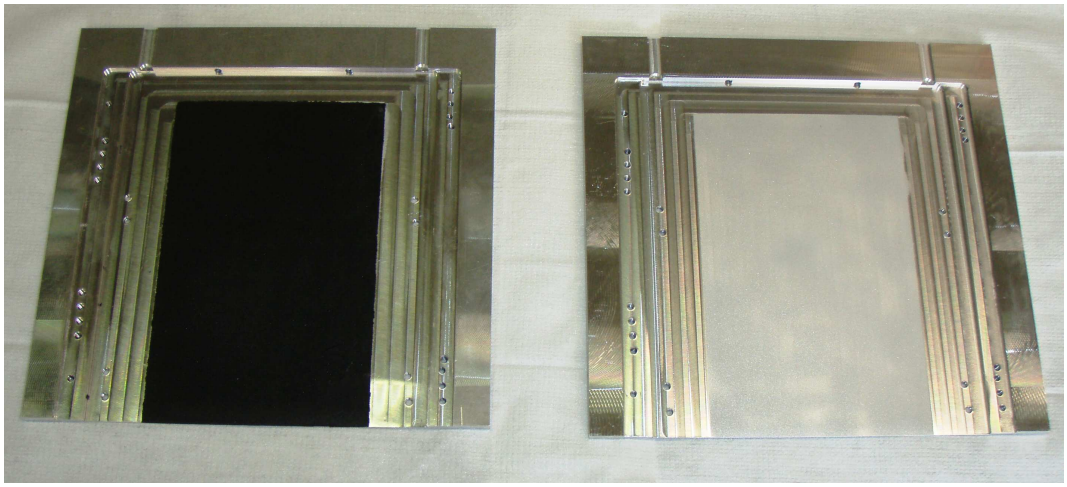

Figure 6.28: A cassette V2 coated and un-coated with $^{10}B$ painting.

the front have a serious chance to generate a signal. Neutron background is then decreased.
The uniformity of the coating, even in the single layer configuration, is an important aspect to guarantee the converter flatness. The latter has to ensure the precision of the neutron incidence angle, in fact if it varies slightly the efficiency changes widely. Furthermore, a deviation from the converter flatness also induces the variation of the electric field and then the local gain of the detector changes.
The roughness of the converter should be below the neutron capture fragment ranges, which is of the order of a few $\mu m$ for $^{10}B$. In fact, the gain in efficiency due to an inclination comes from the fact that the neutron path travels close to the surface. If the surface is irregular (on the $\mu m$ scale or more), that can be seen as equivalent for a neutron to hit a surface perpendicularly, there is not much gain in efficiency. It is crucial that the size of our grains, in the painting, is less than the particles ranges, i.e. their size should be below the micron scale for $^{10}B$.
The conductivity of the painting can be an issue. If the resistivity is too large the charge evacuation is not guaranteed and consequently the actual electric field is affected. We mix a glue with $^{10}B$ grains of sizes $< 10\mu m$, the layer resistivity was measured to be about $50\,M\Omega \cdot m$ and we make a $0.5\,mm$ layer. As the grain size is not smaller than the fragment ranges we know that there can be an efficiency issue. We did not have access to a finer-grained $^{10}B$ powder: our grinding technique resulted in $\sim 10\,\mu m$ grain size. We used this powder.
Figure 6.29 shows two PHS: one is taken with a $3\,\mu m$ thick $^{10}B_4C$ layer [37] and the other with the $^{10}B$ painting both installed in a MWPC. Both at normal incidence and with a 2.5Å neutron beam. The variation in gain on the two spectra is due to the difference in the gas gap between the wire plane and the converter, since the painting is a few $mm$ closer to the wires than the sputtered layer.
The painting efficiency is 1.5% lower than the sputtered coating.
In order to investigate if the resistivity of the painting is not to large to avoid the evacuation of the charges, we place the painting layer on a very intense beam of $560\,KHz$ and we measure the counting rate as a function of time. There are no losses after several hours. The resistivity of the $^{10}B$ painting seems to be acceptable.
The painting is suitable for single layer application supposed that we can control the flatness of

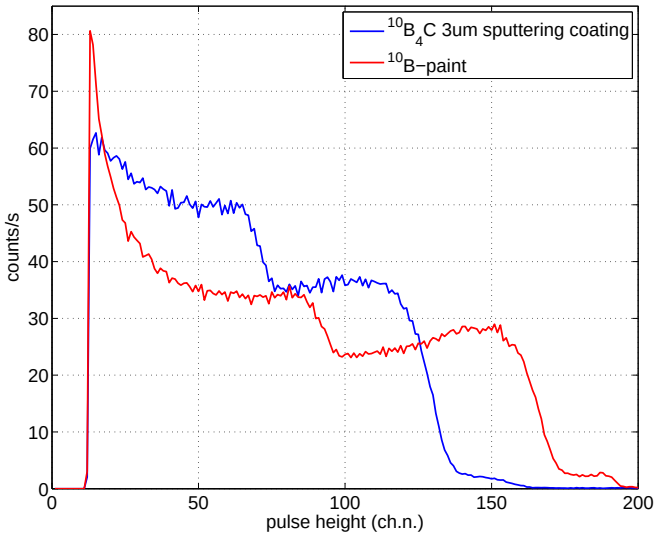


Figure 6.29: Comparison between the PHS of the sputtered coated layers [37] and the $^{10}B$ painting.

the layer and to use smaller grains. We do not guarantee the sputtered layers efficiency under an angle because of the size of the grains we used in the painting.
The converter painting was not optimized, hence we expect some problems due to its not perfect regularity. This effect will be more evident at the edge of each cassette where the flatness affect to a greater extent the electric field glitches.
We mount the prototype using the painting. Four cassettes were assembled. Figure 6.30 and 6.31 show the cassettes and the installation in the gas vessel for testing.
The electronics used is the same as in the version V1 of the Multi-Blade.

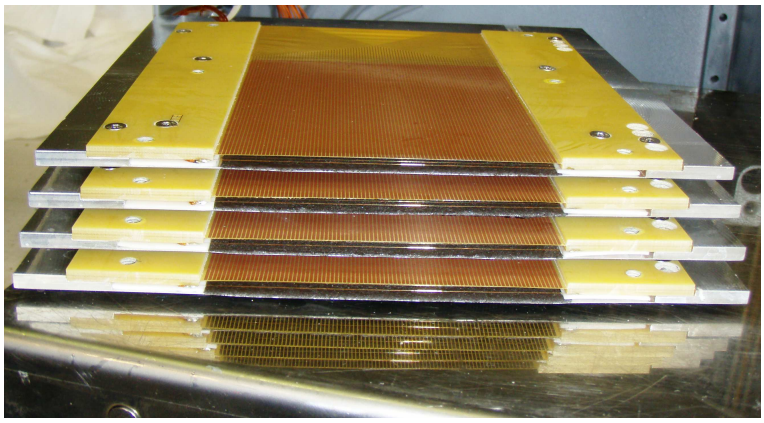

Figure 6.30: Four fully assembled cassettes for the Multi-Blade version V2.

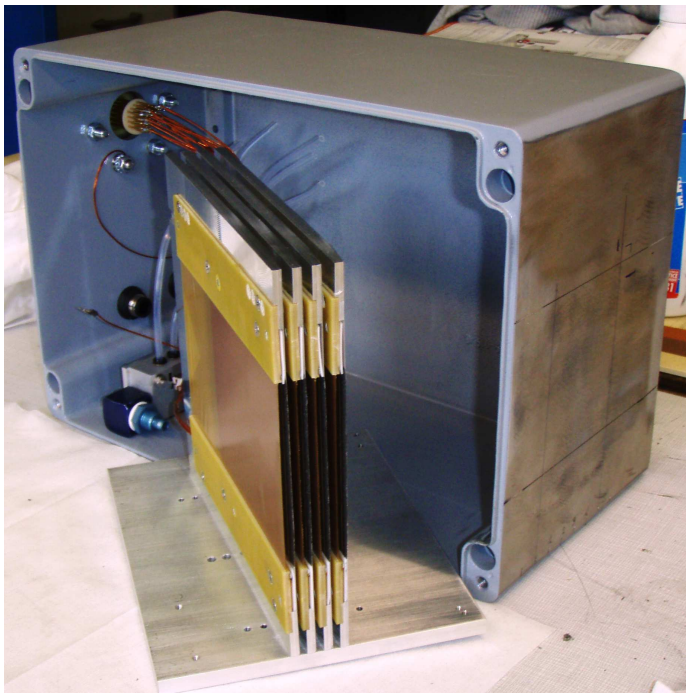

Figure 6.31: The four cassettes installed at 5 ° with respect to the detector window being installed in the gas vessel.

### 6.4.3 Results

#### Operational voltage

The measure of the counting curve gives the bias voltage of $800\,V$.
The operational voltage is lower than the one used for the first prototype because the gap between anodes and cathodes was reduced in the new design. For this reason the PHS is degraded also because the maximum path in $Ar/CO_2$ of an $\alpha$-particle makes almost $9\,mm$ it is more likely in the version V2 to hit the opposite cathode before depositing its entire energy in the gas volume.

#### Efficiency

Detection efficiency of the Multi-Blade prototype V2 has been measured on CT2 at ILL by using a collimated and calibrated neutron beam of wavelength 2.5Åusing the procedure explained in details in the Appendix E.
The neutron flux used is $(12010 \pm 20)$ $neutrons/s$ over an area of $2 \times 6\,mm^2$.
The efficiency was measured for the operational voltage $800\,V$. The efficiency was measured on the four cassettes under the angle of 5° and then averaged. The results is:

$$\varepsilon\left(\text{at } 2.5\text{Å}\right) = (8.32 \pm 0.05)\,\% \tag{6.4}$$

The expected efficiency for a sputtered layer of which the roughness is widely below the $\mu m$ scale is about 43% (at 2.5Å). Having an angle only increases the efficiency by a few percent because of the grains size. The surface irregularity makes the inclination effect vanish. Neutrons only

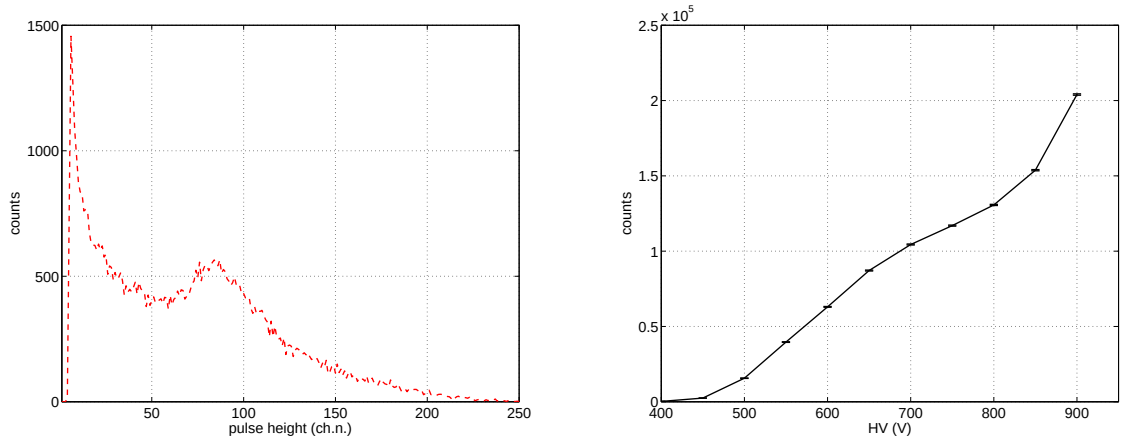


Figure 6.32: PHS measured on wires at $800\,V$ (left). The Multi-Blade detector plateau (right).

impinge almost perpendicular on the microscopic grain structure.
At 5° neutron reflection by the surface is negligible. Hence, by using a sputtered layer or, if one can better control the painting flatness and have smaller grain size, there should be no reason not to get the calculated efficiency.

### Uniformity

In the version V2 of the Multi-Blade the mechanics is more compact in order to avoid dead zones in the overlap between the cassettes. It has been discussed that the two issues which degrade the uniformity are those dead zones and the electric field at each cassette edge.
Even though the mechanics design is more efficient in the version V2, the electric field issue remains.
Moreover, the coating done by the painting was slightly irregular mostly at the edges of each cassette. This diminishes the precision by which we switch between one and the following. A large amount of converter material at the edge will absorb most of the neutrons without generating any signal.
Figure 6.33 shows the relative efficiency scan over the detector surface. Compared with the version V1 uniformity is worse. The gap between the converter and the wire plane is $2\,mm$, hence any irregularity on the layer surface will affect the local gain of the detector. Even along each cassette ($y$-direction) the gain varies by about 10% while in the sputtered version it only varied of about 2%.
Moreover, now looking at the $x$-direction, at the cassettes edge the efficiency now drops more than 50%. This is due to the amount of converter at the edge that does not generate signal but only absorbs neutrons.
The version V2 is in principle more compact and if the coating would be precise the uniformity was expected to be better than in the version V1.

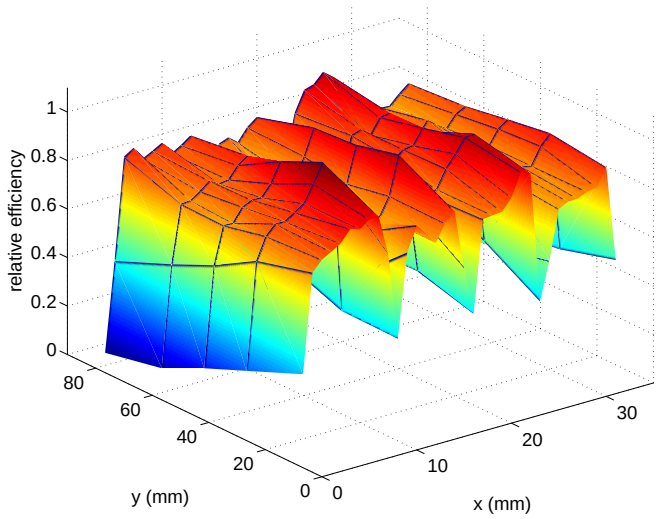


Figure 6.33: Relative efficiency scan over the whole detector surface.

### Spatial resolution

The spatial resolution was calculated as already shown for the Multi-Blade version V1. By using a very collimated beam, of about $0.2 \times 10\,mm^2$, we scan one cassette and a half of the detector. Each step is $0.9\,mm$ along the $x$-direction. The cassette 1 is from $x = 0\,mm$ to $x = 10\,mm$, the cassette 2 starts at $x = 10\,mm$. Figure 6.34 shows the reconstructed image and its projection on the $x$-direction obtained by adding together all the images taken in the scan.
For each step either a wire or two are firing. A the switching point between the two cassette we observe the drops in the counts.

**Spatial resolution: x** We quantify the spatial resolution along the $x$-direction in the same way as for the version V1.
We scan the detector surface to obtain the events distribution to calculate the mutual information which is shown in Figure 6.35. We use the threshold of $0.47\,bits$ which corresponds to the standard FWHM resolution definition and we obtain a value of $3.16\,mm$.
This value is slightly better of the one found for the version V1 because in the version V2 the gap between wires and converter is diminished. It is the first part of the ionization path, on average, that gives more signal and it is closer to the fragment emission point, this improves the spatial resolution.
Since the detector is inclined at 5° the actual spatial resolution is given by the projection: $3.16\,mm \cdot \sin(5°) = 0.275\,mm$.

**Spatial resolution: y** The spatial resolution given by the strips is also enhanced thanks to the narrower gas gap.
Figure 6.36 shows a scan performed along $y$. The spatial resolution is given by the FWHM and is $4\,mm$.

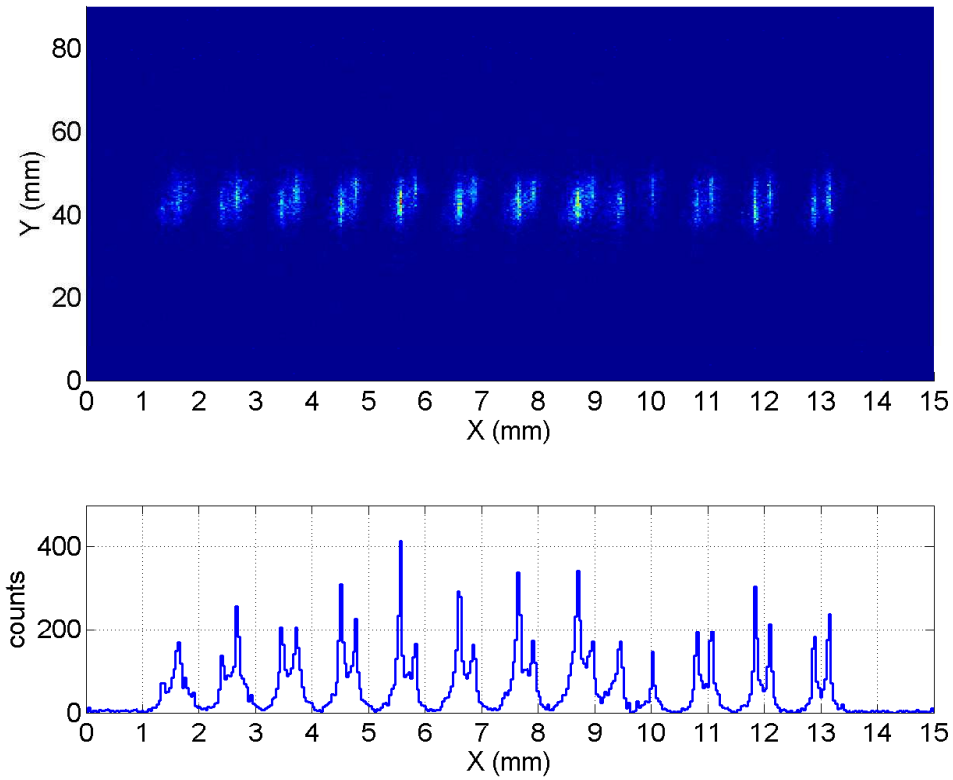


Figure 6.34: An image and its projection on the $x$ axis taken with the prototype. Each slit is $0.2\,mm \times 10\,mm$ large and it is spaced by $0.9\,mm$.

### Dead time

The intrinsic dead time of a detector is due to its physical characteristics; here we measure the entire dead time from the detector to the end of the whole electronic chain. It is the detector plus electronics dead time we measure.
Neutrons arrive at the detector according to an exponential distribution assuming the process to be Poissonian. A way to measure dead time is to record the difference in the arrival time between two successive neutrons on the detector; in principle their distribution should follow an exponential:

$$f(t) = \frac{1}{\tau} e^{-t/\tau} \tag{6.5}$$

where the time $\tau$ represents the average time is in between two events; $\nu = 1/\tau$ is the counting rate.
In practice the detector is characterized by a dead time $t_D$ which is the minimum time interval that separates two correctly recorded events. As a result the distribution measured with the detector should move away from the theoretical behavior near and below $t_D$. Moreover, if the detector is ideally non-paralyzable, the distribution has to show a sharp cutoff at $t_D$ because the probability of measuring an event between $t = 0$ and $t = t_D$ is zero.
In a paralyzable case the passage is smoother.
Figure 6.37 shows the measured times between neutrons on the detector. The two anode outputs

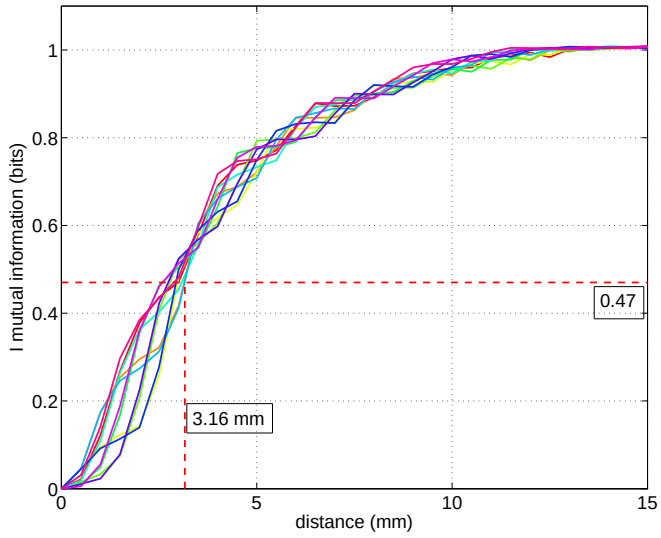


Figure 6.35: Mutual information as a function of the distance between the response distributions of the neutron detector. The horizontal line defines an information of 0.47 bits that corresponds to a 3.16 $mm$ spatial resolution (before projection) in the worse case.

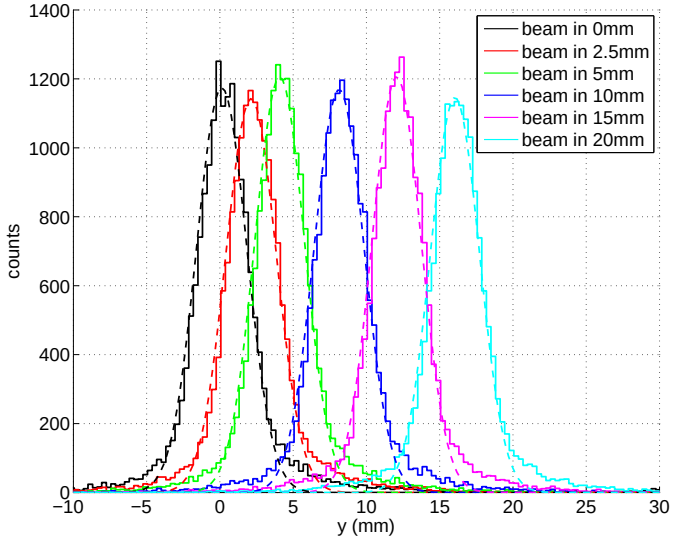


Figure 6.36: Fine beam neutron scan along $y$. The spatial resolution is given by the FWHM and corresponds to 4 $mm$.

of a single cassette where added and the resulting signal discriminated. The time between every couple of discriminated events was recorded for $T = 300\,s$.
The measurement was performed by using two kind of amplifiers. One is the standard Multi-Blade amplifier of $1\,\mu s$ shaping time and the second is a fast amplifier with $3\,ns$ shaping time. The fits in Figure 6.37 represent the theoretical behavior.

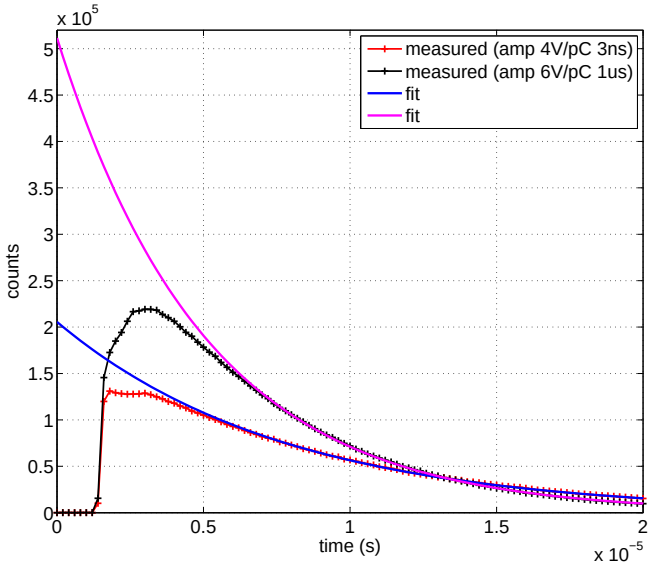


Figure 6.37: Time distribution of neutron events recorded with the Multi-Blade, the fit shows the theoretical behavior. Two anode amplifiers have been used.

The value for $\tau$, for both the measured distributions, was obtained by the calculation of the maximum likelihood estimator for the exponential distribution. It is:

$$\tau = \frac{\sum_i n_i(t_i - t_s)}{\sum_j n_j} \tag{6.6}$$

where $t_s$ is the minimum time for which we consider the measured distribution to behave as expected. We can assume that a time $t_s$ exists above which the measured distribution follows the exponential behavior. We assume $t_s = 7\,\mu s$.
By knowing $\tau$ and the measurement duration $T = 300\,s$, the total number of neutrons that have generated a signal in the detector but, due to dead time, have not all been recorded, is given by:

$$N_0 = \frac{T}{\tau} \tag{6.7}$$

If we integrate instead the measured distribution we obtain the number of events recorded $N_m$. The dead time is simply given by:

$$t_D = \frac{N_0 - N_m}{N_0}\tau = \frac{\frac{T}{\tau} - N_m}{T}\tau^2 \tag{6.8}$$

For the $1\mu s$ amplifier we obtain $t_D = (1.58 \pm 0.08) \cdot 10^{-6}\,s$, the fast amplifier gives $t_D = (1.5 \pm 0.1) \cdot 10^{-6}\,s$.

### Images

Figure 6.38 shows an image reconstructed with the Multi-Blade version V2 obtained by placing the Cd mask with holes in front of the detector. We repeat the mask consists of 80 holes of

$1\,mm$ size spaced by $5\,mm$ along $x$ and by $1\,cm$ along $y$.
The number of bins on the image is set to equal the number of wires (37) for the $x$-direction and is 256 bins for the $y$-direction.
Due to the neutron beam divergence the spots on the image appear much wider than the detector resolution.

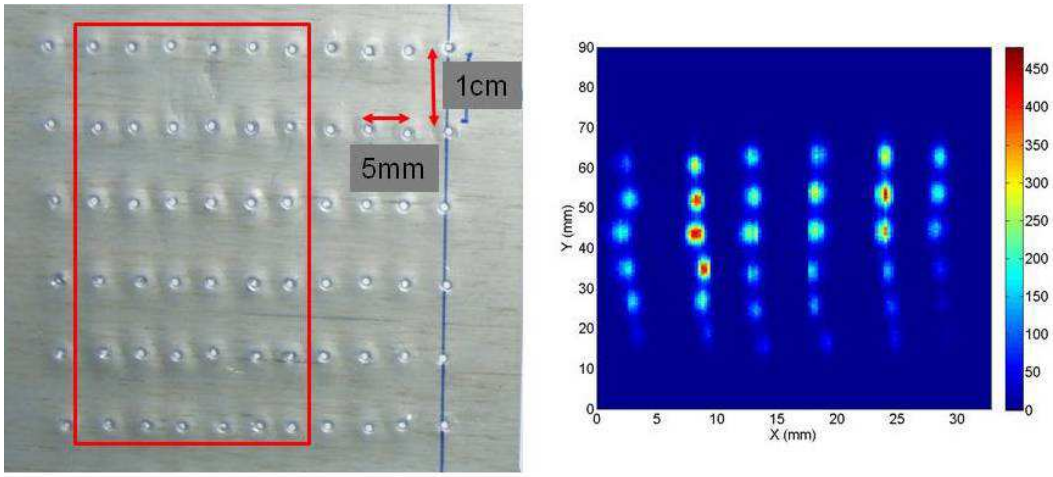


Figure 6.38: The Cd mask (left) used to generate the image on the right.

In the reconstructed image we observe the intensity that drops according to the cassettes edges. We observe that any deviation of an hole position on the mask is perfectly reproduced on the image.

# Conclusions

Although $^3He$ has been the main actor in thermal neutron detection, the World is now experiencing a shortage of $^3He$. The main issue to be addressed for large area neutron detectors (several square meters) is to find an alternative technology to detect neutrons because this rare isotope of Helium is not available anymore in large quantities. This is not the main concern for small area detectors ($\sim 1\,m^2$) where the main effort is focused on the performances. There is a great interest in expanding the detector performances because for instance $^3He$ detectors are limited in spatial resolution and counting rate capability.
The detectors developed and implemented at ILL are based on $^{10}B$ layers used as neutron converter in a gas proportional chamber. In particular we used $^{10}B_4C$-layers deposited by magnetron sputtering technique on holding substrates.
The Multi-Grid is a large area detector that has been developed at ILL to face the $^3He$ shortage problem. It employs up to 30 $^{10}B_4C$-layers in a cascade configuration.
The concept of the Multi-Blade was introduced at ILL in 2005 but it has never been implemented until 2012. The Multi-Blade prototype is a small size detector for application in neutron reflectometry instruments based on single $^{10}B_4C$ layers. The goal of the Multi-Blade is to go beyond the limits of $^3He$-based detectors in terms of spatial resolution (which is about $1\,mm$ for $^3He$ gaseous detectors) and counting rate capability.
For both applications there are several aspects that we investigated in order to validate this alternative technology.
Although the physical process behind the neutron conversion through solid converter is well known, the theoretical modeling for these new detectors can open further developments. We elaborated analytical expressions and equations to help the detector design.

In a neutron facility a detector is always exposed to other kinds of radiation that we consider as a background to be suppressed. The detection of a background event (mostly $\gamma$-rays) can give rise to misaddressed events in a neutron detector. Generally the $\gamma$-ray background can be a few orders of magnitude more intense than the neutron signal. This has been proved by the measurement of the typical background in a Multi-Grid prototype detector installed on the time-of-flight spectrometer IN6 at ILL. The low $\gamma$-ray sensitivity of a neutron detector is then a key feature and it must be determined to validate the $^{10}B$ technology. While for $^3He$ detectors there is a clear energy separation between neutron and $\gamma$-ray events, this is not the case for solid converter based detectors. The neutron Pulse Height Spectrum (PHS) for a $^{10}B$ detector is extended in a continuum down to zero energy. In addition to that a $^{10}B$-based detector should in principle show a higher sensitivity to $\gamma$-rays because of the larger amount of material it is composed of with respect to a standard $^3He$ detector.
We quantified the $\gamma$-ray sensitivity of $^{10}B$ and $^3He$ detectors by using a set of calibrated $\gamma$-ray

sources. For $^{10}B$-based detectors we confirm that the energy spectrum given by $\gamma$-rays mostly involves the low energy region of the spectrum. A suitable $\gamma$-ray rejection, below $10^{-6}$, can be achieved by using a discrimination on the energy level. The method consists of an energy threshold, as is the case for $^3He$ detectors. We demonstrated that a limited efficiency price of only about 0.5% has to be paid in neutron detection if a strong $\gamma$-ray rejection is necessary, below $10^{-6}$.
However, contrary to $^3He$ detectors, there is no clear separation between the neutron Pulse Height Spectrum (PHS) and the $\gamma$-ray PHS. Therefore, we investigate another method to separate neutron from photon events trying to improve the discrimination; but since it turned out that there is no physical difference in the signal shape using the Time Over Threshold method (TOT), this can not be exploited to discriminate against background. The amplitude discrimination remains the best and simpler way to reduce $\gamma$-ray sensitivity of neutron detectors based on a solid converter.
The Multi-Grid detector appears a promising replacement of $^3He$-based large area detectors. We can conclude that such detectors' $\gamma$-ray sensitivity is comparable to that of $^3He$ detectors.

In a multi-layer detector the arrangement of those layers is crucial to optimize the performances. We studied solid converter films based detectors from the theoretical point of view. With the magnetron sputtering deposition method both sides of a substrate are coated with the same thickness of converter. The suite of equations we developed demonstrates that this method is also suited to make optimized blades. In fact, for a single blade the same converter thickness for both sides of a substrate has to be chosen in order to maximize the efficiency. We demonstrated this result to be valid in the case the optimization is done for a single neutron wavelength and in the more general case when we deal with a distribution of wavelengths. If the absorption of the substrate is not negligible we also calculated the deviation from an ideal transparent substrate. We showed that also in a multi-layer detector all the blades have to hold two layers of the same thickness in order to maximize the detection efficiency. The demonstration is valid for a single neutron wavelength and for whichever distribution of wavelengths. On the other hand, the thicknesses of different blades can be distinct and they can be optimized. The optimization procedure to be implemented has been developed for both the monochromatic case and for the case of a distribution of wavelengths.
The blade-by-blade optimization in the case of a multi-layer detector for a single neutron wavelength can achieve a few percent more efficiency over the best detector with identical blades but this can lead to several blades less in the detector. In the case of a distribution of wavelengths, the optimization does not give important improvements in the overall efficiency compared with a monochromatic optimization done for the barycenter of that distribution. On the other hand, the optimization of the efficiency for a neutron wavelength distribution is often more balanced between short and long wavelengths than the barycenter optimization.
Since the $\gamma$-ray discrimination is an important feature of a neutron detector and it is strictly related to its PHS shape, we calculated the PHS analytical expression based on very simple assumptions and we showed it is in a good agreement with measurements. Thanks to this model, we understood the overall shape of the PHS which can be an important tool if one wants to improve the $\gamma$-ray to neutron discrimination in neutron detectors.
In a solid converter-based detector both the PHS shape, for $\gamma$-ray sensitivity, and the efficiency have to be taken into account in its optimization. Both of them are influenced by the choice of the layer thicknesses.

Theoretical modeling was a useful tool to develop the Multi-Blade detector of which we constructed two prototypes in order to demonstrate its feasibility. The Multi-Blade employs $^{10}B_4C$ layers operated at grazing angle with respect to the neutron incoming direction. The read-out is performed by a standard gas amplification process implemented by a plane of wires. There are at least three advantages in operating the detector at grazing angle. The detection efficiency increases, the spatial resolution and the counting rate capability are improved. Thanks to the inclination the detector active surface is projected over the incoming neutron beam. The effective wire pitch is then smaller than the pitch of the finest possible wire mounting and the same local neutron flux is shared among several wires.

In order to get a suitable detection efficiency, compared with $^3He$, the converter layers must be operated at an angle of 10° or below. By approaching lower and lower angles, neutrons can be reflected by the barrier potential of the converter surface and are then lost for detection. We studied the reflection process by strongly absorbent surfaces and we developed a model that we have compared with our experiments carried out at ILL. This model indicates that even for a strong neutron absorber, the reflectivity measurement does not depend on the technique used. A monochromatic scan over the angle or a Time of Flight (ToF) measurement lead to the same result. This is confirmed by experiments.
The theoretical equations derived to optimize the solid converter-based detectors have been corrected for neutron reflection for $^{10}B_4C$ in the neutron wavelength range from 1 to 30 Å. Above 2° there is no need to correct for neutron reflection even if the layer is smooth at the $nm$ scale. We observed that a too small converter roughness drastically increases neutron reflection below 2°. A suitable roughness can help to diminish neutron reflection. Since the ranges of the neutron capture fragments in $^{10}B_4C$ are about a few $\mu m$, the layer irregularity should never exceed the $\mu m$ scale. A larger roughness cancels the gain in efficiency in operating the layer at grazing angle. Our theoretical model about neutron reflection on strong absorbers allowed us to fit the measured profiles that led to the determination of the scattering length density of the used $^{10}B_4C$ layers, it is about $(2.5 - 1.1\,i) \cdot 10^{-6}\,\text{Å}^{-2}$.

We studied two approaches to be used in the Multi-Blade implementation: either with one or with two converters. The latter has more technical issues that makes its realization more difficult. The single layer detector is finally the choice to make to keep the mechanics reasonably simple. The extra advantage of having only one converter is that the coating can be of any thickness above $3\,\mu m$ without affecting the efficiency, while for the two layer option its thickness should be chosen carefully. Moreover, in the two layer configuration the substrate choice is also crucial because it should be kept as thin as possible to avoid neutron scattering and this leads to mechanical issues. In a single-layer detector it can be integrated in the holding structure.
We conceived a detector to be modular in order to be versatile: it is composed of modules called *cassettes*. We operated the two Multi-Blade prototypes at either $\theta = 10°$ and $\theta = 5°$. In each of the solutions proposed for the cassette concept the read-out system has to be crossed by neutrons before reaching the converter. The mechanical challenge in the read-out system construction is to minimize the amount of material on the neutron path to avoid scattering that can cause misaddressed events in the detector. The choice fell on polyimide substrates; they induce a few percent scattering of the incoming neutrons. It can be eventually replaced with more suitable materials.
The detector is operated at atmospheric pressure. This makes it suitable to be operated in

vacuum. Moreover, cost effective materials can be used inside the detector because outgassing is not an issue.
Since the detector is modular the main issue is its uniformity. In the presented prototype we got a 50% drop in efficiency in the overlap region between cassettes.
The presented Multi-Blade showed a very high spatial resolution, it was measured to be about $0.3\,mm$ in one direction and about $4\,mm$ in the other one.
We measured the neutron detection efficiency for both prototypes at 2.5Å neutron wavelength. The first prototype has an efficiency of about 28% employing sputtered $^{10}B_4C$-layers inclined at 10°. This result is in a perfect agreement with the expected efficiency we can calculate by using our theoretical model we developed for solid neutron converters. Since the efficiency, in the single layer option does not depend on the converter thickness above $3\,\mu m$, in the second prototype we investigated a different deposition method: a $^{10}B$ glue-based painting. This thick painted layer functions also as an integrated collimator inside the detector. The resistivity of the $^{10}B$ painting is larger than the sputtered $^{10}B_4C$-layers but it seems to be acceptable and does not cause issues to the charge evacuation. We measured the efficiency of the second prototype operated at 5° and we only got about 8%. The coarse granularity of the painting makes the inclination effect vanish. The expected efficiency for a sputtered layer of which the roughness is widely below the $\mu m$ scale is about 43% (at 2.5Å). There is no reason not to get the calculated efficiency.
We measured the detector dead time, including the read-out electronics, to be about $1.5\,\mu s$.
The single layer option represents a good candidate to go beyond the performances of $^3He$ detectors. Further studies need to address the uniformity problems. If a simple coating technique is found, e.g. painting containing grains of a suitable size that assures a uniform layer, the Multi-Blade could be a cost-effective and high performance alternative. Its production in series is easy to be implemented.

We have reached a profound insight in the principles of solid converters in neutron detection by successfully confronting our theoretical investigations with experiment.
We investigated several technological aspects of $^{10}B$-based detectors by prototyping the Multi-Blade idea. Some explored avenues are very promising while others indicate technological difficulties which need to be resolved. Nevertheless, the results are sufficiently encouraging to foresee a relatively simple construction.

# Appendix A

# The stopping power law

## A.1 Classical derivation

Consider a heavy particle with charge $ze$, mass $M$ and velocity $v$ passing through a medium and suppose there is an atomic electron at some distance $b$ from the particle trajectory (see Figure A.1). We assume that the electron is free and at rest, and that it only moves slightly during the interaction so that the position where the electric field acts in the collision can be considered constant.

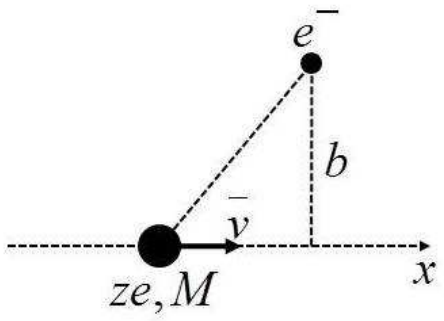


Figure A.1: Collision of a heavy particle with an atomic electron.

Let's calculate the energy gained by the electron by finding the momentum impulse it receives from the collision with the heavy particle:

$$\Delta p = \int F\,dt = e\int E_\perp \frac{dt}{dx}dx = e\int E_\perp \frac{dx}{v} \tag{A.1}$$

where $E_\perp$ is the normal component of the electric field to the particle trajectory. By using the Gauss' law on a infinitely long cylinder of radius $b$ and centered on the particle trajectory:

$$\Phi(E_\perp) = \int E_\perp 2\pi b\,dx = 4\pi ze \qquad \Longrightarrow \qquad \int E_\perp dx = \frac{2ze}{b} \tag{A.2}$$

hence:

$$\Delta p = e\int E_\perp \frac{dx}{v} = \frac{2ze^2}{bv} \tag{A.3}$$

The energy gained by the electron results to be:

$$\Delta E(b) = \frac{(\Delta p)^2}{2m_e} = \frac{2z^2e^4}{m_e b^2 v^2} \tag{A.4}$$

If we consider $n_e$ the number density of electrons, the energy lost to all the electrons located at a distance between $b$ and $b + db$ in a thickness $dx$ is:

$$-dE(b) = \Delta E(b)\, n_e\, dV = \frac{2z^2e^4}{m_e b^2 v^2}\, n_e\, (2\pi b\, db\, dx) = \frac{4\pi z^2 e^4}{m_e v^2} n_e \frac{db}{b}\, dx \tag{A.5}$$

The total energy loss in $dx$ is obtained by integration over $db$ of the Equation A.5 in the interval $[b_{min}, b_{max}]$. It has to be pointed out that if we integrate between 0 and $+\infty$ this is contrary to our original assumptions. E.g. collisions at very large $b$ would not take place over a short period of time, thus the impulse calculation in Equation A.1 would not be valid. On the other hand, for $b = 0$, Equation A.4 gives an infinite energy transfer. Thus:

$$-\frac{dE}{dx} = \frac{4\pi z^2 e^4}{m_e v^2} n_e \ln\left(\frac{b_{max}}{b_{min}}\right) \tag{A.6}$$

To estimate $b_{min}$ and $b_{max}$ we should advance some physical arguments. The maximum energy transferable, classically, is in a head-on collision where the electron obtains an energy of $\frac{1}{2}m_e(2v)^2$. If we take relativity into account this becomes $2\gamma^2 m_e v^2$, where $\gamma = (1-\beta^2)^{-1/2}$ and $\beta = \frac{v}{c}$. From Equation A.4 we find:

$$\frac{2z^2e^4}{m_e b_{min}^2 v^2} = 2\gamma^2 m_e v^2 \qquad \Longrightarrow \qquad b_{min} = \frac{ze^2}{\gamma m_e v^2} \tag{A.7}$$

For $b_{max}$, we should recall that the electrons are not free but bound to atoms with some orbital frequency $\nu$. In order for the electron to absorb energy, the perturbation caused by the passing particle must take place in a time short compared to the period $\tau = \frac{1}{\nu}$ of the bound electron, otherwise the perturbation is adiabatic and no energy is transferred. The typical interaction time is $t \simeq \frac{b}{v}$, which relativistically becomes $t' = \frac{t}{\gamma} = \frac{b}{v\gamma}$, thus:

$$\frac{b}{v\gamma} \leq \tau = \frac{1}{\nu} \qquad \Longrightarrow \qquad b_{max} = \frac{\gamma v}{\nu} \tag{A.8}$$

Where $\nu$ should be considered as the mean frequency averaged over all bound states because there are several bound electron states with different frequencies.
Finally, by substituting A.7 and A.8 in Equation A.6, we obtain:

$$-\frac{dE}{dx} = \frac{4\pi z^2 e^4}{m_e v^2} n_e \ln\left(\frac{\gamma^2 m v^3}{ze^2\nu}\right) \tag{A.9}$$

This is the Bohr's classical formula and it gives a reasonable description of the energy loss for very heavy particles.

## A.2 The Bethe-Bloch formula

The correct quantum-mechanical calculation leads to the Bethe-Bloch formula:

$$-\frac{dE}{dx} = 2\pi N_A r_e^2 m_e c^2 \rho \frac{Z}{A}\frac{z^2}{\beta^2}\left(\ln\left(\frac{2m_e\gamma^2 v_2 W_{max}}{I^2}\right) - 2\beta^2 - \delta - 2\frac{C}{Z}\right) \tag{A.10}$$

where:

| | | | |
|---|---|---|---|
| $r_e$ | classical electron radius | $\rho$ | absorbing material density |
| $m_e$ | electron mass | $z$ | charge of the incident particle |
| $N_A$ | Avogadro's number | $\beta$ | $= v/c$ incoming particle velocity |
| $I$ | mean excitation potential | $\gamma$ | $= (1-\beta^2)^{-1/2}$ |
| $Z$ | atomic number of absorbing material | $\delta$ | density correction |
| $A$ | atomic weight of absorbing material | $C$ | shell correction |
| $W_{max}$ | max energy transferred in a single collision | | |

The maximum energy transfer is that produced by a head-on collision; for an incident particle of mass $M$:

$$W_{max} = \frac{2m_e c_2 \beta^2\gamma^2}{1 + 2\frac{m_e}{M}\sqrt{1+\beta^2\gamma^2} + \frac{m_e^2}{M^2}} \tag{A.11}$$

The mean excitation potential $I$ is directly related to the average orbital frequency $\nu$.
The quantities $\delta$ and $C$ are correction at high and low energies respectively. The density factor, $\delta$, arises from the fact that the electric field of the incoming particle also tends to polarize the atoms along its path. The shell correction, $C$, accounts the effect which arise when the velocity of the incident particle is comparable, or smaller, than the orbital velocity of the bound electrons. A qualitative behavior of the Bethe-Bloch formula is shown in Figure 1.3 as a function of both particle energy $E$ and track length $x$, respectively. The point where $\frac{dE}{dx}$ has a minimum in energy is known as *minimum ionizing*.

# Appendix B

# Connection with Formulae in [4]

The relations between the formulae in [4] and the expression used in Chapter 3, Section 3.2 are the following:

- the particle ranges $R$ are denoted by $L$;
- the branching ratios of the $^{10}B$ reaction (expressed by $F_p$) are $F_1 = 0.94$ and $F_2 = 0.06$;
- the thickness of the layer is $d = D_F$.

Hence, the relation between the expressions 3.12, 3.14, 3.16 and the formulae in [4] is:

$$\begin{aligned} \varepsilon_T(d_T) &= 0.94 \cdot \varepsilon_T(R_1^{94\%}, R_2^{94\%}) + 0.06 \cdot \varepsilon_T(R_1^{6\%}, R_2^{6\%}) \\ &= S_1(D_F, L_1, 0.94) + S_1(D_F, L_2, 0.94) + S_2(D_F, L_1, 0.06) + S_2(D_F, L_2, 0.06) \end{aligned} \tag{B.1}$$

Valid for both equations (18$a$) ($D_F \leq L_i$) and (18$b$) ($D_F > L_i$) in Section 4.2 of [4]. In the case of the back-scattering mode, equations (25$a$) and (25$b$) in [4], we consider one layer of converter and we replace $\varepsilon_T(d_T)$ into $\varepsilon_{BS}(d_{BS})$ in the expression B.1.
In a different way, for both equations (18$a$) and (18$b$), we can also write:

$$F_p \cdot \varepsilon_T = S_p(D_F, L_1, F_p) + S_p(D_F, L_2, F_p) \tag{B.2}$$

# Appendix C

# Connection with Formulae in [26]

The relations between the formulae in [26] and the expression used in Chapter 3, Section 3.6 are the following:

- the macroscopic cross-section ($\Sigma$) is expressed in terms of mean free path $\Sigma = \frac{1}{l}$;
- the variable $u$ is denoted by its cosine $u = \cos(\theta)$;

The formulae (4) in [26] corresponds to the Equation 3.64, except for a factor $\frac{1}{2}$, where $l = \frac{1}{\Sigma}$. The formulae (3) in [26] corresponds to the Equation 3.66.

# Appendix D

# Highly absorbing layer neutron reflection model

The model used to fit the reflectivity profile for a strong neutron absorber, such as $^{10}B_4C$, is the one shown in the Equations 4.11 in Chapter 4. $R$ and $A$ are the reflectivity and the absorption of an absorbing layer deposited on a substrate. These quantities depend on $q$ by $q = \frac{4\pi}{\lambda}\sin(\theta)$. In order to fit the reflectivity and absorption profiles we calculate the reduced chi-square:

$$\chi^2 = \frac{1}{(2N-p)} \sum_{n=1}^{N} \left[ (R_{meas.}(q_n) - R_c(q_n))^2 + (A_{meas.}(q_n) - A_c(q_n))^2 \right] \tag{D.1}$$

where $N$ is the number of points in each set of measurements and $p$ is the number of parameters we used in the fit. In our specific case they are $p = 8$: $\theta_{over}$, $\theta_{shift}$, $^{10}B_4C$ scattering length density (real and imaginary parts), layer roughness $\sigma_r$, layer thickness $d$, Ge-detector efficiency $\varepsilon_{Ge}$ and an overall normalization $M$.
Before the sample the neutron beam is collimated by two slits. Even if the beam divergence is known it is not easy to calculate the exact beam footprint at the sample position. In addition to that, the beam can be not uniform, even after collimation, and the samples do not have sharp edges. $\theta_{over}$ corrects for these effects in the horizontal direction. However, the remaining effect in the vertical direction will introduce a modification of the normalization. This is why we introduce the normalization factor $M$. Generally it has values close to 1.
To model the layer roughness we used the Equation 1.87 applied to the Fresnel coefficients (Equation 4.8) in the case of absorption.
In Equation D.1, $R_{meas.}$ and $A_{meas.}$ are the measured raw curves; $R_c$ and $A_c$ are the reflectivity and the absorption as a function of $q$ predicted by our theoretical model after applying the instrumental corrections.
The overillumination correction is a factor $I_{over}$ that has to be applied to the data to consider the finite extension of the sample. This correction is $I_{over} = 1$ for all the $\theta$ for which the sample projection is larger than the beam size (the full beam hits the sample), and it is less than 1 for the values of $\theta$ for which the sample projection is smaller (only a part of the beam hits the sample). This function has also to be smoothed using a smoothing filter (a 3 points moving average filter) to include the non uniform beam intensity and the instrumental resolution. It is:

$$I_{over} = \begin{cases} \frac{\sin(\theta)}{\sin(\theta_{over})} & \text{if } \theta < \theta_{over} \\ 1 & \text{otherwise} \end{cases} \tag{D.2}$$

The misalignment of the instrument is included in the angle $\theta_{shift}$. This affects the actual value for the angle used to calculate the reflectivity and absorption:

$$\theta_c = \theta + \theta_{shift} \tag{D.3}$$

The values for the profiles once applied the instrumental corrections can be calculated by:

$$R_c = M \cdot I_{over} \cdot R(\theta_c), \qquad A_c = M \cdot \varepsilon_{Ge} \cdot I_{over} \cdot A(\theta_c) \tag{D.4}$$

We recall the quantities $R$ and $A$ depend on the fitting parameter $d$, the layer scattering length density, the reflection angle $\theta_c$ and the layer roughness $\sigma_r$.

# Appendix E

# Neutron flux measurement

It is commonly useful to know the actual neutron flux of a beam line, e.g. CT1 at ILL. By knowing the neutron flux, for example, the efficiency of a prototype can be estimated. In order to perform an accurate neutron flux measurement, the so-called *Hexagonal detector* is used. The latter, shown in Figure E.1, is a multi-tube $^3He$-based gaseous detector composed of 37 7 $mm$-diameter tubes. Each of them acts as a proportional chamber; the drift voltage is common to the 37 hexagonal shaped tubes and they are read-out individually. Thus, the neutron detected in each tube can be quantified.

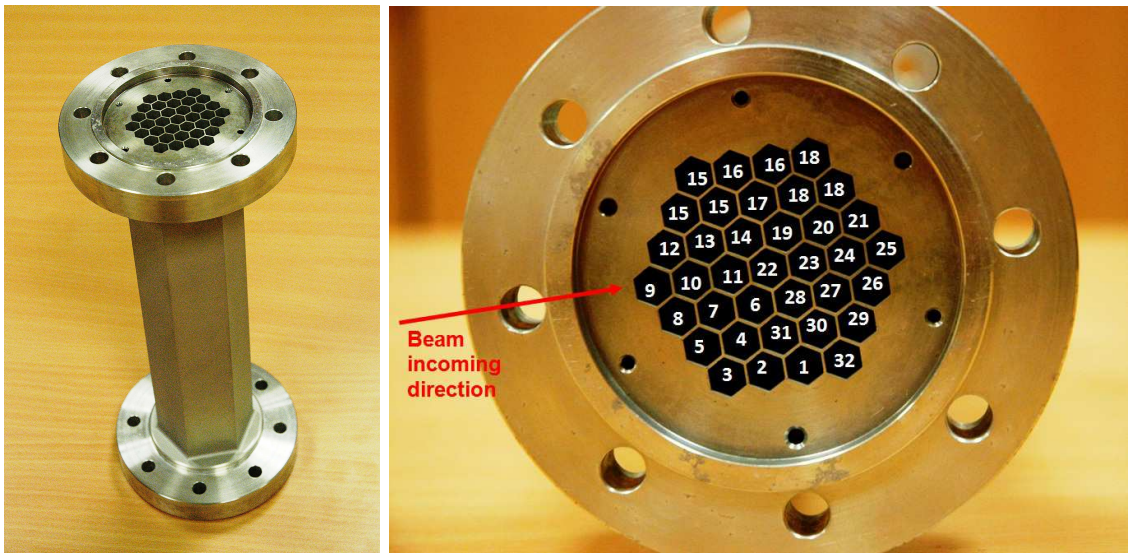


Figure E.1: Hexagonal $^3He$-tubular detector used to measure the actual neutron flux (the red arrow shows the neutron beam direction and the number are the channel number of each tube, some tubes are connected together).

We start by setting each channel (tube) threshold above the noise level; it is not problematic to have some gain difference between the channels, because further adjustment can be done later by software.
The beam is collimated at a size which is smaller than the single tube diameter. By counting the detected neutrons per tube, we scan the detector in order to find the position where the central seven tubes are aligned on the neutron trajectory (see Figure E.1). The additional tubes

on the two sides allow to help in the alignment.
Once alignment is over, we record a PHS for each tube in a given time $T$ which is long enough to get a small statistic error (relative errors below 1% can be archived in few minutes).
We repeat the measure in the same conditions but without the beam in order to quantify the background that has to be subtracted from the measurement with the beam on.
In Figure E.2, on the left, is shown the seven $^3He$-PHS relative to the central tubes and the dashed line represent the threshold, added by software, used to calibrate the detector efficiency. Hence, we integrate, from the threshold to the end, the PHS and we obtain the counting per tube that has to be divided by the measurement time $T$ to get the counting rate. We cumulate the rates of the seven central tubes in order to get the plot shown in Figure E.2 on the right. This represents the number of neutron detected per second in a detector made up of 1, 2, ..., $N$ tubes.

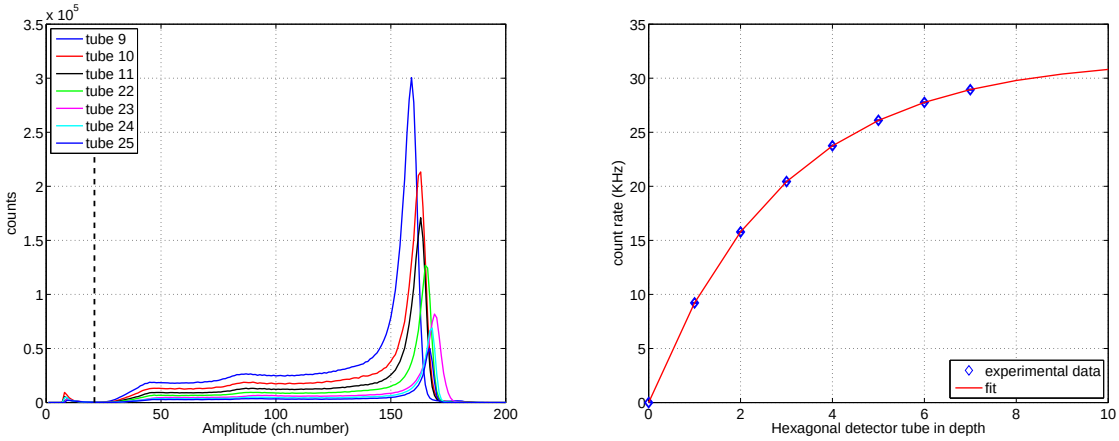


Figure E.2: Hexagonal detector PHS (left) and neutron cumulative flux across the 7 central tubes of the detector (right).

One can now imagine to arrange an infinite number of $^3He$-tubes on the beam path, ideally each neutron is counted, if it is not lost before by scattering out of the beam direction.
Therefore, by performing a fit of the plot in Figure E.2, the asymptotic value gives the actual neutron flux at the neutron wavelength it was measured.

# Bibliography


[1] R. Leo William, *Techniques for Nuclear and Particle Physics Experiments*. Springer, Berlin, 1994.

[2] J. F. Ziegler et al., *SRIM - The stopping and range of ions in matter (2010)*, Nuclear Instruments and Methods in Physics Research Section B: Beam Interactions with Materials and Atoms, Volume 268, Issues 1112, 2010, Pages 1818-1823, ISSN 0168-583X, 10.1016/j.nimb.2010.02.091.

[3] J. F. Ziegler et al., *RBS/ERD simulation problems: Stopping powers, nuclear reactions and detector resolution*, Nuclear Instruments and Methods in Physics Research Section B: Beam Interactions with Materials and Atoms, Volume 136138, Issues 0, 1998, Pages 141-146, ISSN 0168-583X, 10.1016/S0168-583X(97)00664-2.

[4] D. S. McGregor et al., *Design considerations for thin film coated semiconductor thermal neutron detectors—I: basics regarding alpha particle emitting neutron reactive films*, Nuclear Instruments and Methods in Physics Research Section A: Accelerators, Spectrometers, Detectors and Associated Equipment, Volume 500, Issues 13, 11 March 2003, Pages 272-308, ISSN 0168-9002, 10.1016/S0168-9002(02)02078-8.

[5] G. nelson and D. Reilly, *Gamma-Ray Interactions with Matter*.

[6] G. F. Knoll, *Radiation Detection and Measurement* - third edition. John Wiley & Sons, Inc. 2000.

[7] C. Cohen-Tannoudji, *Quantum Mechanics*. Wiley-VCH Verlag GmbH, 1992.

[8] L. I. Schiff, *Quantum Mechanics* - third edition. McGraw-Hill, Inc. 1955.

[9] G. L. Squires, *Introduction to the theory of thermal neutron scattering*. Cambridge univertisty press, 1978.

[10] V. F. Sears, *Neutron scattering lengths and cross sections - Special Feature*, Neutron News, Volume 3, Issue 3, 1992, Pages 29-37.

[11] E. Fermi and W. H. Zinn, *Reflection of neutrons on mirrors*, Los Alamos National Laboratory, U.S. Atomic Energy Commission, 1946.

[12] R. Cubitt et al., *Chapter 2.8.3 - Neutron Reflection: Principles and Examples of Applications*, Scattering, Roy Pike and Pierre Sabatier, Academic Press London, 2002, Pages 1198-1208, ISBN 978-0-12-613760-6, 10.1016/B978-012613760-6/50065-6.

[13] V. Ignatovich et al., *Optical potential and dispersion law for long-wavelength neutrons*, Physical Review B, Volume 55, Issue 22, June 1997, Pages 14774-14783, 10.1103/PhysRevB.55.14774.

[14] R. Cubitt et al., *Refraction as a means of encoding wavelength for neutron reflectometry.* Nuclear Instruments and Methods in Physics Research Section A: Accelerators, Spectrometers, Detectors and Associated Equipment, Volume 558, 2006, Pages 547 - 550, 10.1016/j.nima.2005.12.045.

[15] F. Sauli, *Principles of operation of multiwire proportional and drift chambers.* Lectures given in the Academic Training Programme of CERN, Geneva, 1977.

[16] W. Shockley, *Currents to Conductors Induced by a Moving Point Charge.* Journal of Applied Physics, Volume 9, Issue 10, October 1938, Pages 635-636, 10.1063/1.1710367.

[17] S. Ramo, *Currents Induced by Electron Motion.* Proceedings of the IRE, Volume 27, Issue 9, September 1939, Pages 584-585, 10.1109/JRPROC.1939.228757.

[18] Z. He, *Review of the Shockley-Ramo theorem and its application in semiconductor gamma-ray detectors.* Nuclear Instruments and Methods in Physics Research Section A: Accelerators, Spectrometers, Detectors and Associated Equipment, Volume 463, Issue 1-2, 2001, Pages 250-267, ISSN 0168-9002, 10.1016/S0168-9002(01)00223-6.

[19] T. W. Crane and M. P. Baker, *Neutrons Detectors.*

[20] P. Convert, J. B. Forsyth, *Position Sensitive Detection of Thermal Neutrons*, Academic Press (London), 1983

[21] D. A. Shea and D. Morgan, *The Helium-3 Shortage: Supply, Demand, and Options for Congress.* Congressional Research Service, 22 December 2010.

[22] R. T. Kouzes, *The 3He Supply Problem.* Technical Report 11-753, US Government Accountability Office 2011.

[23] J. Birch et al., *$^{10}B_4C$ Multi-Grid as an Alternative to $^3He$ for large area neutron detectors*, IEEE Transactions on Nuclear Science, Volume PP, Issue 99, 17 January 2013, Pages 1-8, ISSN 0018-9499, 10.1109/TNS.2012.2227798.

[24] J. Correa et al., *10B4C Multi-Grid as an alternative to 3He for Large Area Neutron Detectors*, PhD thesis, 2012, Universidad de Zaragoza.

[25] Z. Wang et al., *Multi-layer boron thin-film detectors for neutrons*, Nuclear Instruments and Methods in Physics Research Section A: Accelerators, Spectrometers, Detectors and Associated Equipment, Volume 652, Issue 1, 1 October 2011, Pages 323-325, ISSN 0168-9002, 10.1016/j.nima.2011.01.138.

[26] D.J. Salvat et al., *A boron-coated ionization chamber for ultra-cold neutron detection*, Nuclear Instruments and Methods in Physics Research Section A: Accelerators, Spectrometers, Detectors and Associated Equipment, Volume 691, 1 November 2012, Pages 109-112, ISSN 0168-9002, 10.1016/j.nima.2012.06.041.

[27] M. Henske et al., *The 10B based Jalousie neutron detector − An alternative for 3He filled position sensitive counter tubes*, Nuclear Instruments and Methods in Physics Research Section A: Accelerators, Spectrometers, Detectors and Associated Equipment, Volume 686, 11 September 2012, Pages 151-155, ISSN 0168-9002, 10.1016/j.nima.2012.05.075.

[28] K. Tsorbatzoglou et al., *Novel and efficient 10B lined tubelet detector as a replacement for 3He neutron proportional counters*, Symposium on Radiation Measurements and Applications (SORMA) XII 2010, Nuclear Instruments and Methods in Physics Research Section A: Accelerators, Spectrometers, Detectors and Associated Equipment, Volume 652, Issue 1, 2010, Pages 381-383, ISSN 0168-9002, 10.1016/j.nima.2010.08.102.

[29] J. L. Lacy et al., *Boron-coated straws as a replacement for 3He-based neutron detectors*, Nuclear Instruments and Methods in Physics Research Section A: Accelerators, Spectrometers, Detectors and Associated Equipment, Symposium on Radiation Measurements and Applications (SORMA) XII 2010, Volume 652, Issue 1, 2011, Pages 359-363, ISSN 0168-9002, 10.1016/j.nima.2010.09.011.

[30] J. L. Lacy et al., *One meter square high rate neutron imaging panel based on boron straws*, Nuclear Science Symposium Conference Record (NSS/MIC), 2009 IEEE, Pages 1117-1121, ISSN 1095-7863, 10.1109/NSSMIC.2009.5402421.

[31] M. Klein et al., *CASCADE, neutron detectors for highest count rates in combination with ASIC/FPGA based readout electronics*, Nuclear Instruments and Methods in Physics Research Section A: Accelerators, Spectrometers, Detectors and Associated Equipment, VCI 2010 Proceedings of the 12th International Vienna Conference on Instrumentation, Volume 628, Issues 1, 2011, Pages 9-18, ISSN 0168-9002, 10.1016/j.nima.2010.06.278.

[32] M. Shoji et al., *Development of GEM-based detector for thermal neutron*, Journal of Instrumentation, Volume 7, C05003, May 2012, doi:10.1088/1748-0221/7/05/C05003.

[33] F. Piscitelli et al., *Analytical modeling of thin film neutron converters and its application to thermal neutron gas detectors*, Journal of Instrumentation, Volume 8, P04020, April 2013, 10.1088/1748-0221/8/04/P04020.

[34] K. Andersen et al., *10B multi-grid proportional gas counters for large area thermal neutron detectors*, Nuclear Instruments and Methods in Physics Research Section A: Accelerators, Spectrometers, Detectors and Associated Equipment, 20 December 2012, ISSN 0168-9002, 10.1016/j.nima.2012.12.021.

[35] A. Khaplanov et al., *Multi-Grid Boron-10 detector for large area applications in neutron scattering science*, Presented at the ICANS-XX conference, March 2012, arXiv:1209.0566.

[36] A. Athanasiades et al., *Straw detector for high rate, high resolution neutron imaging*, Nuclear Science Symposium Conference Record, 2005 IEEE, Volume 2, Pages 623-627, 10.1109/NSSMIC.2005.1596338.

[37] C. Höglund et al., *$B_4C$ thin films for neutron detection*, Journal of Applied Physics, Volume 111, Issue 10, 23 May 2012, Pages 10490-8, ISSN 0168-9002, 10.1063/1.4718573.

[38] T. Bigault et al., *10B multi-grid proportional gas counters for large area thermal neutron detectors*, Neutron News, Volume 23, Issue 4, 2012, Pages 20-25, 10.1080/10448632.2012.725329.

[39] J. B. Hayter. and H. A. Mook, *Discrete thin-film multilayer design for X-ray and neutron supermirrors*, Journal of Applied Crystallography, Volume 22, Issue 1, 1989, Pages 35-41, ISSN 1600-5767, 10.1107/S0021889888010003.

[40] H. Zhang et al., *Grazing incidence prompt gamma emissions and resonance-enhanced neutron standing waves in a thin film*, Phys. Rev. Lett., Volume 72, Issue 19, 1994, Pages 3044-3047, 10.1016/j.physb.2007.02.085.

[41] R. Cubitt et al., *D17: the new reflectometer at the ILL*, Journal of Applied Physics A, Springer-Verlag, Volume 74, Issues 1, 1 December 2002, Pages s329-s331, 10.1007/s003390201611.

[42] A. Devishvili et al., *SuperADAM: Upgraded polarized neutron reflectometer at the Institut Laue-Langevin*, AIP Review of Scientific Instruments, Volume 84, Issue 2, 2013, Pages 025112, 10.1063/1.4790717.

[43] C. Höglund, *Growth and Phase Stability Studies of Epitaxial Sc-Al-N and Ti-Al-N Thin Films*, PhD Thesis 2010, Linköping University - Institut of Technology.

[44] A. Khaplanov et al., *Investigation of gamma-ray sensitivity of neutron detectors based on thin converter films*. Submitted to Journal of Instrumentation.

[45] J. Birch et al., *In-beam test of the B-10 Multi-Grid neutron detector at the IN6 time-of-fight spectrometer at the ILL* submitted to IOP Conference Series.

[46] GEANT4, http://geant4.cern.ch.

[47] R. T. Kouzes et al., *Neutron detection gamma ray sensitivity criteria*. Nuclear Instruments and Methods in Physics Research Section A: Accelerators, Spectrometers, Detectors and Associated Equipment, Volume 654, 2011, Pages 412 - 416, ISSN 0168-9002, 10.1016/j.nima.2011.07.030.

[48] R. T. Kouzes et al., *Neutron detection alternatives to 3He for national security applications*. Nuclear Instruments and Methods in Physics Research Section A: Accelerators, Spectrometers, Detectors and Associated Equipment, Volume 623, Issue 3, 2010, Pages 1035-1045, ISSN 0168-9002, 10.1016/j.nima.2010.08.021.

[49] H. Schroer, *The solid angle through the vertical rectangle*, 2006.

[50] H. Schroer, *The solid angle through the inclined rectangle*, 2006.

[51] H. Schroer, *Luminous Flux and Illumination*,english and german edition, Wissenschaft und Technik Verlag Berlin, 2001, ISBN 3896855212 9783896855213.

[52] A. R. Spowart, *Measurements of the gamma sensitivity of granular and glass neutron scintillators and films*. Nuclear Instruments and Methods, Volume 82, 30 May 1970, Pages 1-6, ISSN 0029-554X, 10.1016/0029-554X(70)90317-4.

[53] C. L. Morris et al., *A digital technique for neutron-gamma pulse shape discrimination.* Nuclear Instruments and Methods, Detectors and Associated Equipment, Volume 137, Issue 2, 1976, Pages 397-398, ISSN 0029-554X, 10.1016/0029-554X(76)90353-0.

[54] S. Peggs, *ESS Technical Design Report* ESS-doc-274, 23 April 2013. ISBN 978-91-980173-2-8.

[55] B. Gebauer et al., *Towards detectors for next generation spallation neutron sources*, Proceedings of the 10th International Vienna Conference on Instrumentation, Nuclear Instruments and Methods in Physics Research Section A: Accelerators, Spectrometers, Detectors and Associated Equipment, Volume 535, Issues 1-2, 2004, Pages 65-78, ISSN 0168-9002, 10.1016/j.nima.2004.07.266.

[56] R. A. Campbell et al., *FIGARO: The new horizontal neutron reflectometer at the ILL*, The European Physical Journal Plus, Springer-Verlag, Volume 126, Issue 11, 2011, Pages 1-22, 10.1140/epjp/i2011-11107-8.

[57] F. Ott et al., *RefloGrad/GradTOF: Neutron energy analysis for a very high-flux neutron reflectometer*, Proceedings of the Sixth International Workshop on Polarised Neutrons in Condensed Matter Investigations, Physica B: Condensed Matter, Springer-Verlag, Volume 397, Issues 1-2, 2007, Pages 153-155, ISSN 0921-4526, 10.1016/j.physb.2007.02.085.

[58] J. Stahn et al., *Focusing specular neutron reflectometry for small samples.* Eur. Phys. J. Appl. Phys., Volume 58, 2012, 10.1051/epjap/2012110295.

[59] R. Cubitt et al., *Neutron reflectometry by refractive encoding*, The European Physical Journal Plus, Springer-Verlag, Volume 126, Issues 11, 11 November 2011, Pages 1-5, 10.1140/epjp/i2011-11111-0.

[60] J. C. Buffet et al., *Advances in detectors for single crystal neutron diffraction*, Nuclear Instruments and Methods in Physics Research Section A: Accelerators, Spectrometers, Detectors and Associated Equipment, Volume 554, Issues 13, 1 December 2005, Pages 392-405, ISSN 0168-9002, 10.1016/j.nima.2005.08.018.

[61] J.C. Buffet et al., *Study of a 10B-based Multi-Blade detector for Neutron Scattering Science*, Nuclear Science Symposium and Medical Imaging Conference (NSS/MIC), Transaction Nuclear Science Conference Record IEEE - Anaheim, 2012, PAGES 171-175, ISSN 1082-3654, 10.1109/NSSMIC.2012.6551086.

[62] P. Van Esch et al., *An information-theoretical approach to image resolution applied to neutron imaging detectors based upon discriminator signals*, Proceeding of ANNIMA, 2013, arXiv:1307.7507.